# *Investigation of the Materials Properties of Polyvinyl Alcohol for Soluble Unit Dose Laundry Pods*

CRESSWELL, JAMES,DANIEL

# Investigation of the Materials Properties of Polyvinyl Alcohol for Soluble Unit Dose Laundry Pods


James Cresswell

St Mary's College, Durham University

A thesis submitted for the degree of Doctor of Philosophy

Michaelmas Term 2024

**Abstract**

Soluble unit dose (SUD) laundry pods are a recent innovation in the home and laundry care sector, offering enhanced consumer convenience, reducing excess consumption, and enabling compartmentalised reagents for improved laundry performance. Polyvinyl alcohol (PVA) forms the film used to encapsulate laundry products, but the processes involved in pod manufacture and film adhesion are not well understood. This lack of understanding can lead to product failures, such as poor dissolution in low-temperature wash cycles or premature seal failure, which negatively impacts consumer satisfaction. This thesis investigates the polymer properties—specifically chain dimensions, aggregation behaviour, and phase stability—in model PVA systems similar to those used in commercial products. Techniques including small angle neutron scattering (SANS), dynamic light scattering (DLS), and rheology were employed to study these properties.

Key findings from this work include solution state SANS which revealed that partially hydrolysed PVA shows aggregation behaviour and provided chain dimension data across concentrations ranging from 0.25 to 30 w/w%. Solid state SANS further demonstrated that the interaction parameter between polymers in a blend increases with the difference in hydrolysis levels between the two polymers, while also characterising the chain dimensions of PVAc in the solid state. Fluorescence recovery after photobleaching (FRAP) analysis indicated that the degree of hydrolysis significantly influences the diffusion rate of PVA in thin plasticised films, with polymers of lower degree of hydrolysis diffusing faster than those with higher hydrolysis. Diffusion coefficients were extracted for use in diffusion models. Ion beam analysis, including Particle Induced X-ray Emission (PIXE) and Rutherford Backscattering Spectrometry (RBS), was used to visualise and quantify the interfaces in two-layer PVA films, simulating the seal structure of an SUD pod. These results showed that the interface was sharper for higher degrees of hydrolysis, with less diffusion at the interface, while greater interdiffusion was observed in less hydrolysed polymers, which aligns with FRAP findings.

This thesis makes contributions to the understanding of PVA film properties, including chain dimensions and the Flory-Huggins interaction parameter, in well-defined PVA series with consistent degree of polymerisation. Additionally, it demonstrates the novel application of the FRAP technique for observing diffusion in synthetic polymers, extending its typical use from biomolecules. The results offer insights that could improve computational models of interface behaviour in PVA film systems, advancing both material properties and manufacturing processes for SUD laundry pods.

**Acknowledgements**

Firstly, I would like to thank Professor Clare Mahon for being the most supportive, encouraging, and fun supervisor I could have hoped for. It has been an honour to be the first PhD student in your group and a privilege to watch the lab flourish under your guidance. I am deeply grateful for your endless support throughout my time at Durham. I would also like to thank Professor Richard Thompson for being such a knowledgeable and kind co-supervisor. Your insight and humour made challenging situations so much easier to manage. A sincere thank you to my industrial collaborator Procter & Gamble for part-funding this research, and specifically to Dr Florence Courchay for her support throughout this project. Kate, thank you for always being my cheerleader and for the endless chats and laughter. Some of the ideas for this thesis originated in those conversations and I could not have written this without you. Josie, thank you for supporting me through all-nighters at the neutron beam, and for the many laughs we've shared. Your friendship has been invaluable. Ed, you've been the most supportive boyfriend I could wish for. You've been there for me through the highs and lows of this journey, and your love and patience have been my anchor. Steve & Maria, thank you for providing a safe haven to visit on weekends when I needed a break, and for all the trips to Betty's. Mum & Dad, thank you for supporting me through every stage of my education, from school to university and now this PhD. Nan and Grandad, thank you for always taking an interest in my work and for making me smile with your repeated "when will my laundry pods not stick to my cardigan?" questions. Lastly, to my wonderful Nanny Shirley. You were always a pillar of strength for me growing up. Thank you for being on the end of the phone for a chat, for taking such an interest in my life, and for always telling me how proud you were of me. Your love and support were a constant source of motivation during this PhD. This is for you.

**Declaration**

The following people contributed to this body of work:

In Chapter 2, the contribution of Dr Juan A. Malavia, Head of the Solution State NMR Service at Durham University, was instrumental in setting up and conducting the NMR spectroscopy for the deuterated polymerisations. His expertise and time were critical to the successful completion of this work. The staff at the ISIS Neutron and Muon Source provided essential support for the SANS component of this project. Dr Gregory Smith and Dr Robert Dalgliesh were directly involved with the LARMOR instrument, while Dr Stephen King and Dr Najet Mahmoudi facilitated the use of the SANS2D instrument, assisting in both the measurement process and subsequent data analysis. In Chapter 3, Dr Catia Costa, Dr Matthew Sharpe, and Dr Vladimir Palitsin from the UKNIBC carried out the analysis during the project visit. Dr Costa and Dr Sharpe were responsible for the extraction and preparation of the data, while the synthesis, preparation, interpretation, and presentation of the results were handled by myself. In Chapter 4, Professor John Girkin, from the Durham University Department of Physics, provided access to his confocal microscope and contributed valuable insights into the optimal approach for data analysis.

**List of Abbreviations**

| Abbreviation | Definition |
|---|---|
| $\frac{d\Sigma}{d\Omega}$ | absolute differential scattering cross section |
| $\vec{R}$ | root mean square distance |
| $\dot{\gamma}$ | shear strain rate |
| ABD | 7-amino-2,1,3-benzoxadiazol-4-yl |
| AIBN | azobisisobutyronitrile |
| ATRP | atom transfer radical polymerisation |
| *b* | scattering length |
| CLSM | confocal laser scanning microscope |
| CTA | chain transfer agent |
| Đ | dispersity, $M_w/M_n$ |
| DA | degree of acetylation |
| DH | degree of hydrolysis |
| $D_H$ | hydrodynamic diameter |
| DLS | dynamic light scattering |
| DP | degree of polymerisation |
| dPVAc | deuterated PVAc |
| dRI | differential refractive index |
| DTT | dithithreitol |
| ERDA | elastic recoil detection analysis |
| ESI | electrospray ionisation |
| EtPAX | 2-(ethoxycarbonothioyl)sulfanyl propanoic acid |
| FRAP | fluorescence recovery after photobleaching |
| FRP | free radical polymerisation |
| FTIR | Fourier transform infrared |
| *G'* | storage modulus |
| *G''* | loss modulus |
| GPC | gel permeation chromatography |
| GuHCl | guanidinium chloride |
| *h* | Planck's constant |
| I | intensity |
| IBA | ion beam analysis |
| ICT | intramolecular charge-transfer |
| IR | infrared |
| *J* | coupling constant |
| *k* | kinetic rate constant |
| *l* | bond length |
| LCA | life cycle analysis |
| LCST | lower critical solution temperature |
| LDPE | low density polyethylene |
| LRMS | low resolution mass spectrometry |
| LUMO | lowest unoccupied molecular orbital |
| LUT | lookup table |
| LVER | linear viscoelastic region |
| m.p. | melting point |
| MADIX | macromolecular design by interchange of xanthate |
| MMA | methyl methacrylate |
| $M_n$ | number average molecular weight |
| MS | mass spectrometry |

| | |
|---|---|
| $M_w$ | weight average molecular weight |
| NA | numerical aperture |
| NBD | nitrobenzofurazan |
| NMP | nitroxide mediated polymerisation |
| NMR | nuclear magnetic resonance |
| NR | neutron reflectivity |
| PEG | polyethylene glycol |
| PEO | polyethylene oxide |
| PES | polyether sulfone |
| PET | photo single electron transfer |
| PET | polyethylene terephthalate |
| PIPS | passivated implanted planar silicon |
| PIXE | particle induced X-ray emission |
| ppm | parts per million |
| PVA | polyvinyl alcohol |
| PVA/c | polyvinyl alcohol–co–vinyl acetate |
| PVAc | polyvinyl acetate |
| ϕ | volume fraction |
| $Q$ | scattering wave vector |
| RAFT | reversible addition-fragmentation chain transfer |
| RBS | Rutherford backscattering spectrometry |
| RDRP | reversible deactivation radical polymerisations |
| $R_g$ | radius of gyration |
| RH | relative humidity |
| RI | refractive index |
| RPA | random phase approximation |
| $S(Q)$ | single particle shape factor |
| SANS | small-angle neutron scattering |
| SEC | size exclusion chromatography |
| SESANS | spin echo small angle neutron scattering |
| sld | scattering length density |
| SUD | soluble unit dose |
| TCEP | tris(2-carboxyethyl)phosphine |
| THF | tetrahydrofuran |
| ToF | time of flight |
| UCST | upper critical solution temperature |
| $v$ | velocity |
| VAc | vinyl acetate |
| $v_m$ | unit volume of cell |
| $W_i$ | weight fraction of species *i* |
| XRD | X-ray diffraction |
| γ | shear strain |
| δ | chemical shift |
| $\eta$ | viscosity |
| θ | incident angle |
| λ | wavelength |
| $\rho$ | scattering length density |
| σ | shear stress |
| $\tau$ | characteristic recovery time |
| $\chi$ | Flory Huggins interaction parameter |

# Contents

# Chapter 1: Introduction

## 1.1 Laundry and consumer goods

Since washing machines gained popularity in the 1950s, the formulated consumer products industry has continually enhanced the performance of detergents and fabric softeners to meet consumer demands.[1] Recently, there has been a shift towards washing at lower temperatures and reducing product overconsumption. A recent life cycle analysis (LCA) by Ariel,[2] a Procter & Gamble brand, revealed that up to 60% of a fabric care product's carbon footprint comes from its 'in-use' phase (Figure 1.1), mainly from heating water. In comparison, only 20% originates from ingredient manufacturing. The consumer can minimise the 'in-use' carbon footprint by washing at lower temperatures and using less water during wash cycles, necessitating more effective and robust cleaning products to maintain the same performance under these more stringent conditions. A recent report by the European Commission finds by reducing the temperature of a wash from 40 °C to 30 °C, the global warming potential is reduced by 19%.[3] This is the equivalent saving of 27.2 kg $CO_2$ per appliance, per year, based on an average of 220 wash cycles/year.[3]

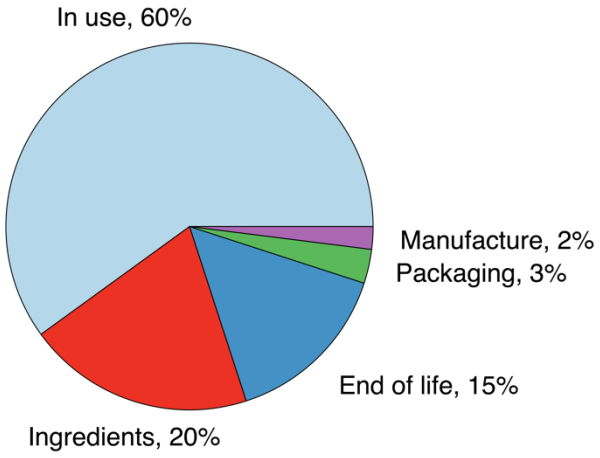


Figure 1.1: Simplified LCA break-down from Ariel.[2]

## 1.2 The design of laundry pods

Soluble unit dose (SUD) detergent capsules are a relatively recent innovation in the home and laundry care sector, first introduced by Procter & Gamble with the Ariel pod in 2012.[4] Earlier attempts at SUD

products were in the form of compressed powder tablets. However, these possess a significant drawback in their poor water solubility. These powder-based tablets are slow to dissolve, and with variable washing temperatures and durations, it is difficult to predict whether the product will dissolve to provide sufficient detergent to the load. Because of these complexities, liquid detergents are used in the modern iteration of the SUD capsules (Figure 1.2). These pods offer a convenient alternative to traditional bottled liquid or powder detergents by containing highly concentrated liquid ingredients in a single, pre-measured packet. The capsule's outer shell is made from a water-soluble polymer, typically polyvinyl alcohol (PVA),[5] which dissolves during the laundry cycle to release the detergent mixture. SUD pods quickly gained popularity and are now widely available in many global markets. They are designed for consumer convenience, preventing the mess of pouring from a bottle and the risk of overdosing associated with traditional detergents.

The polymer film used to construct the capsules can create separate compartments to prevent premature mixing of multiple liquid components, such as detergents and enzymes, before the wash cycle. This separation is crucial, as mixing ingredients in the bottle can significantly impact their efficacy, particularly for enzymes that may degrade if combined with certain surfactants too early. By segregating liquid detergents and enzymes within chambers divided by PVA film, each component can deliver maximum impact when combined during the wash. The films are developed to dissolve fully in the wash process, even in cold water cycles, ensuring optimal performance. Poor dissolution of the polymer film can result in a late or absent dose of detergent. Modification of the polymer structure, as well as the inclusion of additives and variation in film thickness, can influence the film's dissolution while maintaining a robust capsule during storage and handling. To ensure safety and avoid spillage, the soluble film is designed not to dissolve when touched with wet hands or put into the mouth, resist compression, and trigger an adverse reaction in case of oral contact. These safety features are mandated for liquid laundry detergent capsules in the EU under Regulation (EU) 1297/2014.[6]

Figure 1.2: Soluble unit dose (SUD) laundry pods, showing three distinct compartments enclosed in a PVA film. (Image Credits: Licensed from Adobe Stock - Roman Samokhin).

One challenge resulting from reduced wash temperatures is a perceived decline in cleaning performance by consumers.[7] Therefore, existing products must continue to perform well at lower temperatures and shorter wash cycles. A particular issue with shorter and cooler wash cycles is that SUD laundry pods sometimes fail to dissolve fully, preventing the complete release of their contents. Additionally, incomplete dissolution of the capsule can result in the casing being deposited onto garments (Figure 1.3), reducing customer satisfaction and necessitating further wash cycles to remove the residue.

Figure 1.3: SUD pod residue resulting from incomplete dissolution during the wash cycle.[8]

An issue associated with SUD pod manufacture is the poor diffusion of the polymer film into the opposing polymer layer which can lead to the premature breakage of the seal and subsequent leakage of detergent. Various factors can compromise the integrity of the PVA film, leading to rupture and

leakage. A significant factor affecting the dissolution and diffusion properties of the PVA film is humidity. High humidity during storage and transportation can cause the film to become tacky as the polymer chains become hydrated.[9] As a result, the polymer chains become more mobile and have the potential to disentangle,[10] causing the seal to fail before it reaches the washing machine. Additionally, mechanical stresses during handling,[11] packing, and transportation can impose pressure on the pods which can cause them to burst. Minor abrasions or punctures to the PVA film can result in leakage and,[12] ultimately, wastage of the product. The PVA film is also susceptible to the detergent formulation itself. As the ingredients are almost always liquids, it is important that they do not inadvertently interact with and structurally affect the film, which is typically achieved by keeping the water content of the liquid components as low as possible.

### 1.3 Industrial manufacturing methods

Industrially, SUD pods are produced on mass by vacuum forming a layer of PVA film to a metal mould, after which the concentrated liquid detergent is dosed into the cavity (Figure 1.4). Water is then applied to the rim of the cavity to enable polymer chain diffusion, and a second layer of PVA film is applied and pressed onto the lower film, sealing the detergent inside. In a two-layer PVA film system such as that shown in Figure 1.4, polymer swelling, chain mobility, interdiffusion, and entanglement collectively influence the film's structural integrity and functionality. Upon absorbing water, the PVA swells as its hydrophilic chains form hydrogen bonds with water molecules, increasing chain mobility, particularly in amorphous regions. This enhanced mobility promotes interdiffusion, where chains from one layer penetrate the other, strengthening interfacial adhesion. Furthermore, chain entanglement across the interface improves the film's mechanical properties. These processes, driven by swelling and diffusion, are crucial for optimising the performance of multi-layered PVA films. This initial seal process occurs on a timescale of a few seconds, meaning polymers must migrate and entangle at an appropriate speed to ensure the seal formed is robust. The product is then left for several days, allowing the seal to continue strengthening as the polymers diffuse and entangle, and as the water

diffuses away from the interface. If the polymer chains are not sufficiently entangled, the seal will likely fail, leading to a loss of containment of the liquid detergent. This can potentially compromise the PVA films of other pods in the pack, ruining the entire product. The depth of the entanglement is not currently well described, nor is the impact of polymer properties (molecular weight, degree of hydrolysis (DH)) on the diffusion depth or the diffusion rate. While there is not much literature regarding specifically PVA interfaces, there is research into both polymer-polymer[13] and also polymer-surfactant interfaces.[14]

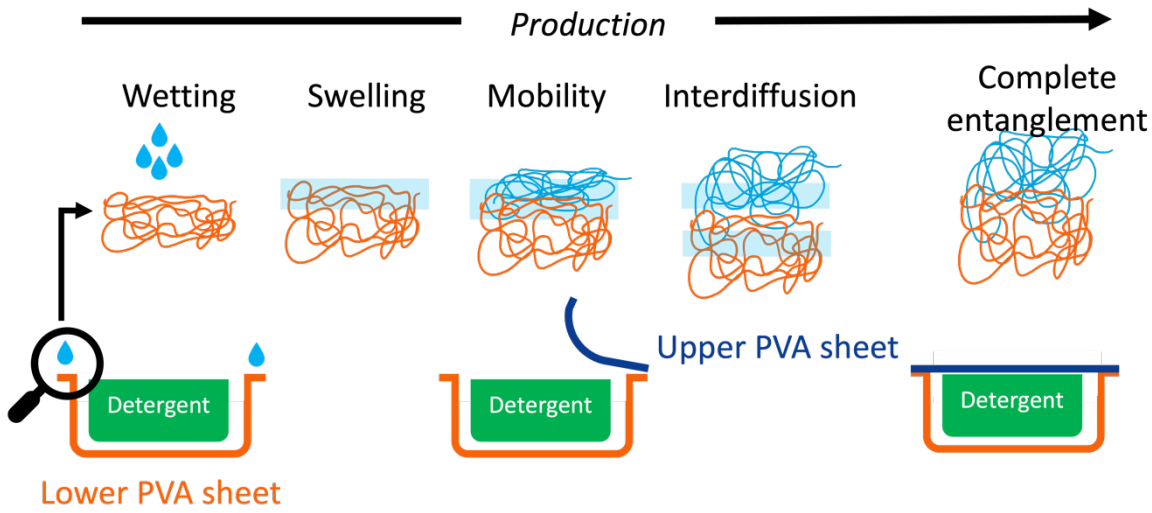


Figure 1.4: A depiction of the industrial SUD pod manufacturing process with polymer chain interdiffusion and entanglement shown. Typical timescale for production line process is of the order of several seconds. Pods are aged for several days while the entanglement process continues.

## 1.4 The chemistry of PVA

PVA may be assumed to be prepared by the polymerisation of vinyl alcohol; however, since this monomer is unstable and readily tautomerises to acetaldehyde at room temperature, alternative methods are necessary.[15] Consequently, PVA is typically produced through the alkaline hydrolysis of the corresponding polyvinyl acetate (PVAc) (Figure 1.5b), the acetate ester of PVA. After removing all acetate functionality, 'fully hydrolysed' PVA is obtained (Figure 1.5d). In contrast, when only partial removal of acetate functionality is achieved, the resultant polymer is 'partially hydrolysed' PVA (Figure

1.5c) – strictly speaking, the product of this partial hydrolysis is a vinyl alcohol – vinyl acetate copolymer (PVA/c); however, it is also commonly referred to as PVA.

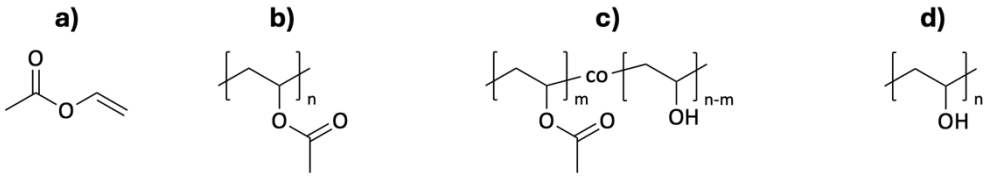


Figure 1.5: a) Vinyl acetate monomer, b) polyvinyl acetate, c) polyvinyl alcohol-co-polyvinyl acetate, d) polyvinyl alcohol.

First synthesised in 1924 by Herrmann and Haehnel,[16] PVA is found in various commercial products thanks to its excellent film-forming properties, resistance to oil and solvents, and gas barrier properties to oxygen and carbon dioxide.[17] The PVA industry initially grew with the production of Vinylon[5] – a synthetic fibre produced using PVA, anthracite coal, and limestone as raw materials – which was developed two years after DuPont introduced Nylon in 1939.[18] The material originated in North Korea, where winter temperatures plummet, and sufficient cotton or wool for clothing cannot be produced.

PVA has also been used as a binder in the paper industry since the early 1950s due to its excellent adhesion.[19] Additionally, the push for secondary fibre usage means most paper grades now include some percentage of recycled fibre. However, the continued use of reclaimed fibres reduces the overall strength of the paper due to the reduction in fibre length from repeated refining and a decrease in the fibres' ability to swell due to repeated drying operations.[20] Adding PVA to the sheet's surface imparts tensile strength and provides resistance to oils, greases, and organic solvents.[5, 20] PVA primarily contributes to the development of higher-grade specialised paper products, such as silicone-coated release liners, cigarette filter tip papers, food-grade boards, and high-brightness printing papers.[5] Today, the food packaging segment dominates the global PVA market, accounting for 32.4% of the total share.[21] The increasing demand for bio-compatible and non-toxic packaging solutions in the food and beverage industry is expected to further drive this growth. PVA is particularly well-suited for such applications due to its excellent biocompatibility and non-toxic nature. PVA is commonly used in

medical and pharmaceutical applications, including wound dressings and drug delivery systems, due to its safe interaction with biological systems.[22] Its non-toxic degradation products make it a desirable material for packaging, as it poses minimal risk to human health and the environment. This further enhances its potential as a sustainable alternative to conventional packaging materials in various sectors, including food and beverage.

The water solubility of PVA depends primarily on the DH and, to a lesser extent, the degree of polymerisation (DP).[5] Varying the DH has two counteracting effects on the polymer's solubility, which can be understood through both thermodynamic and kinetic considerations. Thermodynamically, at low DH, the presence of acetate groups reduces the overall hydrophilicity, leading to lower absolute solubility in water. However, as the DH increases, the number of hydroxyl groups on the polymer rises, enhancing hydrophilicity and seemingly increasing solubility. Kinetically, the rate of dissolution is hindered by strong inter- and intra-chain hydrogen bonding, particularly in more crystalline regions of high DH, which slows the dissolution process (Figure 1.6).[23] Consequently, while higher DH makes the polymer more thermodynamically compatible with water, the crystalline structure can significantly impede the dissolution rate.

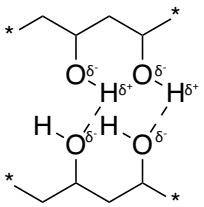

Figure 1.6: Hydrogen bonding between two chains of PVA.

Increasing the amount of acetylation on the polymer (decreasing DH) results in fewer hydrogen bonds due to the reduction in hydroxyl groups, resulting in a less crystalline material (Figure 1.7b).[24] These polymers are soluble in water at lower temperatures (~10 °C).[25] Minge *et al*.[26] report that the optimum cold-water solubility is achieved with a DH of 87 – 89% when DP is between 600 and 2400. Julinová *et al*.[27] further report that the solubility of PVA is reliant on DH, with PVA DH = 95% insoluble in cold water

and soluble in water at 65 – 70 °C. However, reducing the DH below 80% results in polymer precipitation from a solution below 35 °C due to the hydrophobicity of the acetate groups on the chain. PVA with DH less than 50% are insoluble in water even at elevated temperatures.

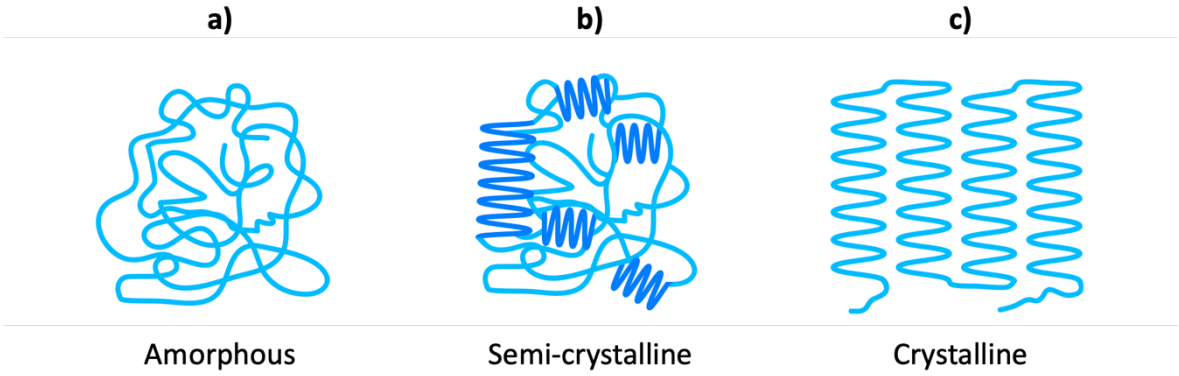


Figure 1.7: Diagram displaying amorphous, semi-crystalline and crystalline polymer chain packing structure; increasing the DH of PVA results in higher crystallinity and decreasing the DH results in a more amorphous structure.

When using PVA, it is essential to consider the impact of the DP and the DH in relation to the end application. Figure 1.8 illustrates the effects of varying DH and molecular weight (proportional to DP) on the polymer's material properties. Generally, a higher DP results in higher solution viscosity, increased initial grab of the adhesive, and greater film strength but lower water solubility than a lower DP PVA.[5] Higher DH PVA (97-99%) exhibits slightly lower solution viscosity, greater film strength, and reduced water solubility than lower DH (87-89%) alternatives. Highly hydrolysed PVA (99%+) offers greater water resistance due to closer polymer chain packing from increased crystallinity.[28] For remoistenable adhesives, partially hydrolysed grades are preferable due to their ease of wetting, which is attributed to reduced chain packing and crystallinity compared to higher DH PVA. The tackiness of the adhesive can be enhanced by adding boric acid,[29] which acts as a cross-linker.

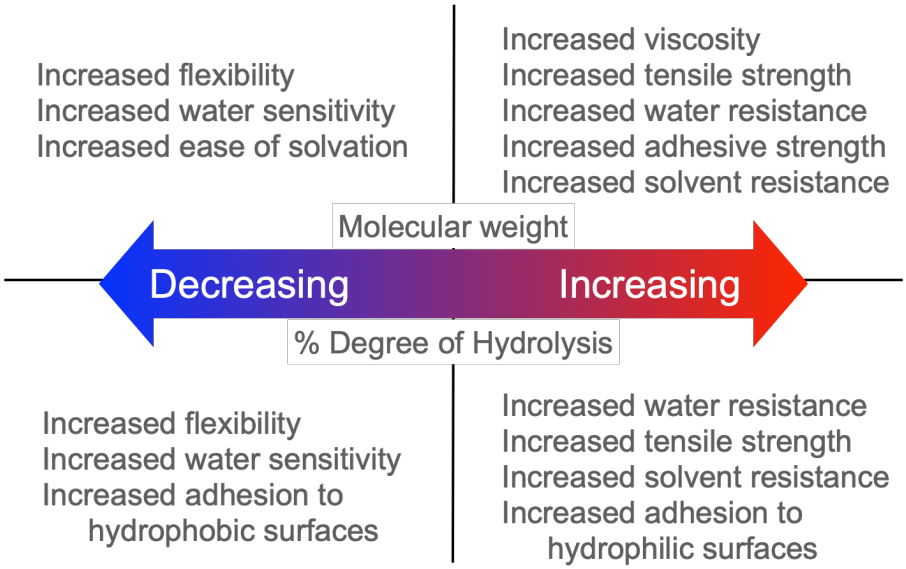


Figure 1.8: Impact of varying the molecular weight and DH on the material properties of polyvinyl alcohol.

### 1.5 Issues with PVA laundry detergent pods

Despite the success of the SUD pod, further development of the polymer film is required. Structural parameters of PVA, such as DH and polymer crystallinity, should be optimised to balance rapid dissolution in cold water wash cycles with maintaining sufficient film integrity to prevent premature dissolution. Additionally, the film must remain stable during transportation and storage, particularly in conditions of uncontrolled humidity, to minimise the risk of polymer chain mobility and disentanglement, which can lead to leaks and product spoilage. Industrially, modifications to the polymer, such as secondary monomer incorporation and plasticisation, are used to create a film that performs in these stringent environments. Copolymerisation with the standard PVA can affect factors such as crystallinity and viscosity, whereas plasticiser will facilitate more flexible and easily handleable films while also enhancing polymer chain mobility.

As the polymer casing should ideally dissolve fully during the wash cycle, all the polymer used to create the SUD pod is discarded into the sewage system. It is crucial, therefore, that these polymers are biodegradable. PVA is recognised as one of the few vinyl polymers that is water soluble and subject to complete biodegradation in the presence of suitable microorganisms. There are comprehensive

reviews on the biodegradability of PVA,[26, 30-33] which conclude that PVA films used for SUD laundry pods can be biodegraded, but the extent of this biodegradation depends on several factors, including environmental conditions and the presence of specific microorganisms. High levels of biodegradation have been observed in aqueous environments containing bacterial species commonly found in PVA-contaminated waste streams and sewage sludge.[30] However, these bacteria, which have adapted to metabolise PVA, may not be present in waste streams that have not previously been exposed to the polymer.[27] Once in the sewage water, PVA does not accumulate in the environment in its polymer form but is gradually broken down into non-toxic by-products, such as water and carbon dioxide by the microbial activity present. However, in systems with insufficient microbial adaptation, there is a risk of failed degradation until acclimated bacteria are present.[32]

### 1.6 Issues with studying PVA

Industrially prevalent PVA available to researchers typically comes in two main varieties, DH = 99%+ and DH = 88%, with a range of molecular weights. These polymers are often characterised by broad dispersity (Đ), meaning the molecular weight distribution is wide, which is common to many polymers produced via free radical polymerisation (FRP). This broad Đ, due to radical termination events and limited synthetic control, complicates the interpretation of structure-property relationships, hindering research into the effects of specific polymer characteristics. Additionally, the limited commercial selection of PVA grades makes it challenging to isolate the impact of parameters such as DH on material properties, as available grades seldom share the same molecular weight or come from the same batch of PVAc, making it difficult to maintain consistent backbone lengths. Beyond DH and DP, another important factor is the "blockiness" of partially hydrolysed PVA, which varies depending on the production method and influences material properties. Blockiness refers to the distribution of pendent groups, with like pendent groups neighbouring each other repeatedly being termed blocky PVA. This further complicates the study of PVA, as DH and DP alone are insufficient to fully describe a material's characteristics.

### 1.7 Structural parameters of polymers

A polymer may be defined as a molecule with high molecular mass containing repeating monomers joined by covalent chemical bonds.[34] A molecule is said to have high molecular mass if the removal or addition of one repeat unit has a negligible effect on the molecular properties. The repeat monomer units which form the polymer chain are usually arranged linearly, and the number of repeating units can range from several hundred to millions. For example, if A is a monomer molecule, -A- is the repeat unit, and n is the DP, then the molecular structure of the polymer is represented by:

$$\left[\text{A}\right]_n$$

One would assume the molar mass, *M*, of the homopolymer can be calculated:

$$M = M_0 * DP \qquad \text{(Equation 1)}$$

where $M_0$ is the molar mass of the repeat unit.

However, with very few exceptions, there is no single DP value for all polymer chains; instead, a distribution of molecular weights is observed. It is convenient to characterise the distribution of molar masses in terms of averages. These are usually defined by considering the nature of the distribution in which macromolecules exist, *i.e*. Discrete fraction, 'i' containing $N_i$ molecules of molar mass $M_i$.

The number average molecular weight, $M_n$, is defined as the sum of products of the molar mass of each fraction multiplied by its mole fraction:

$$M_{\text{n}} = \frac{\sum N_i M_i}{\sum N_i} \qquad \text{(Equation 2)}$$

The number average molecular weight does not account for the mass of the polymer chains in the sample and favours all masses equally. It is often more convenient to use weight fractions rather than numbers of molecules to describe the polymer distribution. The weight fraction, $w_i$, is defined as the mass of molecules of molar mass $M_i$ divided by the total mass of all the molecules present, *i.e*.

$$w_i = \frac{N_i M_i}{\sum N_i M_i} \qquad \text{(Equation 3)}$$

The weight average molecular mass $M_w$ is defined as the sum of the products of the molar mass of each fraction multiplied by its weight fraction, *i.e*.

$$M_w = \sum w_i M_i \quad \text{(Equation 4)}$$

By combining this equation with Equation 3, $M_w$ can be expressed in terms of the number of molecules

$$M_w = \frac{\sum N_i M_i^2}{\sum N_i M_i} \quad \text{(Equation 5)}$$

The ratio of $M_n/M_w$ must be >1 for a polymer sample that is polydisperse. The ratio, known as Đ, of the polymer population and is used as a measure of the breadth of the molar mass distribution.

$$Đ = \frac{M_w}{M_n} \quad \text{(Equation 6)}$$

Typically, Đ is in the range of 1.2 – 2.0 for most polymers, although there are many polymers where the value is smaller or larger (Figure 1.9). The Đ affects the mechanical properties of the polymer; a narrow Đ of chain lengths is desirable for controlling the physical and mechanical properties. It is often preferred if the distribution of molecular weights is uniform, especially when investigating structure-property relationships.

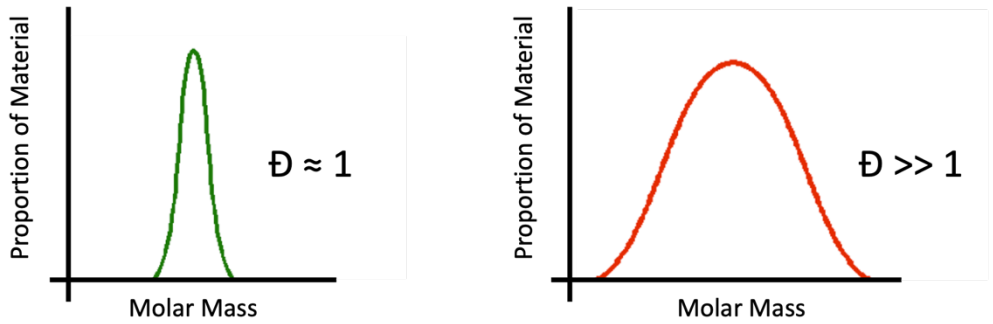


Figure 1.9: Comparison of narrow (left) and broad (right) polymer distribution.

In 1953, Paul Flory first defined two main classes of synthetic polymerisations: step growth and chain growth.[35] In step-growth polymerisations, the molecular weight of polymer chains increases gradually.[35] These reactions are driven by the condensation of small molecules, and require

bifunctional starting materials like diacids, diamines, and diols. They are classified as polymers which contain fewer atoms than are present in the monomer from which they are formed. Notable polymers produced through this method include polyethylene terephthalate (PET), formed from the condensation of terephthalic acid and ethylene glycol, and Nylon 66 which is produced from hexamethylenediamine and adipic acid, a process discovered by Wallace Carothers at DuPont in 1935.[36] Step growth polymerisations typically result in broad molecular weight distributions.[37] For low DP, Đ can exceed 2 due to the large presence of small oligomers. As the reaction proceeds, Đ approaches a value of 2 as the molecular weight distribution becomes more uniform, and eventually, Đ converges at 2, which is a characteristic feature of an ideal step growth polymerisation.[38]

Alternatively, synthetic polymers can be formed by chain growth polymerisation, named so because the reaction mechanism is a chemical chain reaction. These reactions characterised by polymers that contain repeat units of molecular formulae identical to those of the monomers from which they are formed. During such reactions, there must be an initiation step, forming an active centre, either radical or ionic, from which monomers can be sequentially added to form the polymer during the rapid propagation stage. These reactions must usually also include a termination step, although this is not the case in some examples. Unlike step growth polymerisation, chain growth polymerisations are known to rapidly form polymers of high molecular weight.[39]

### 1.8 Radical polymerisation

Free radicals are species that possess an unpaired electron, and are usually highly reactive and short-lived.[40] A carbon-based free radical is usually $sp^2$ hybridised, and the unpaired electron exists in the unhybridised p-orbital (Figure 1.10).[40]

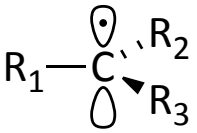

Figure 1.10: A carbon-based free radical with $sp^2$ hybridisation and the carbon atom bearing the unpaired electron in an unhybridised p-orbital. $R_1$, $R_2$, and $R_3$ represent atoms or molecular fragments attached to the carbon bearing the radical.

FRP is a widely employed type of chain growth polymerisation and is known for its versatility and synthetic ease. For this reason, it is utilised extensively in the polymer industry. Polymerisations of this type are highly tolerant of a wide variety of functional groups, meaning they can be utilised in the production of a range of polymers without the need for protection of monomer functionality.[41] This type of polymerisation undergoes rapid chain growth, leading to high molecular weight species, but the fast, uncontrolled growth of chains and frequent termination events means there is little uniformity in their length.[42] The unpredictable reaction kinetics can be attributed to radical transfer from the polymer to solvent, monomer, initiator or other polymer chains, sometimes causing irreversible termination.[39] In radical polymerisation, the reaction can be divided into three distinct stages: initiation, propagation, and termination.[39, 42]

During the initiation stage of a radical polymerisation the first free radical active centres are formed. This generally takes place over two stages: the generation of a free radical from an initiator species (Scheme 1.1 top) and the addition of a free radical to a monomer molecule (Scheme 1.1 middle).

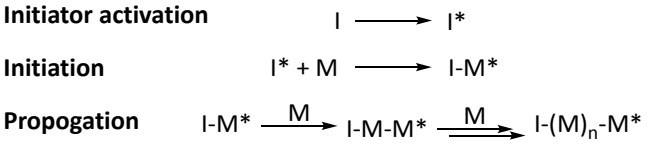


Scheme 1.1: Initiator activation, initiation and propogation of monomer M.

Initiator molecules create free radicals via two main processes: (i) homolytic scission of a single bond in which the two bonding electrons each go onto the two atoms comprising the original bond, producing two free radical species in the process, and (ii) transfer of a single electron to or from an ion

or molecule, known as single-electron transfer process, some of which only produce a single free radical species.

Homolysis can be driven by the application of heat, giving rise to a class of initiators known as thermal initiators. Many compounds undergo thermolysis at useful rates above 50 °C, typically containing peroxide (-O-O-) or azo (-N=N-) linkages. Common initiators of this kind include benzoyl peroxide, lauryl peroxide, azobisisobutyronitrile (AIBN).

Homolysis can be driven by the application of heat, giving rise to a class of initiators known as thermal initiators.[43] Many compounds undergo thermolysis at useful rates above 50 °C, typically containing peroxide (-O-O-) or azo (-N=N-) linkages.[44] The rate refers to the speed at which the initiators decompose to generate free radicals, with a half-life typically ranging from minutes to hours at these temperatures. For example, the half-life of benzoyl peroxide at 60 °C is typically around 10–30 minutes, while AIBN has a half-life of approximately 30 minutes to 1 hour at the same temperature.[44, 45] These rates are considered useful in polymerisations as they allow for controlled initiation of the polymerisation process within practical timeframes.

An activated radical initiator then reacts with the C=C bond of a monomer molecule (Scheme 1.1 middle), resulting in a reactive monomer. Following the reaction of this activated monomer with additional monomer units, the propagation stage begins. During propagation, polymers are formed by the successive addition of unsaturated monomer units to an activated or initiated form of the monomer (Scheme 1.1 bottom).[46] The growing chain radical attacks the $\pi$-bond of a monomer molecule, resulting in homolytic cleavage of the unsaturated monomer C=C bond (Scheme 1.2).

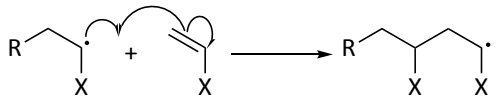


Scheme 1.2: Reaction mechanism for the propogation of polymer chains through free radical polymerisation.

The movement of a single electron from the $\pi$-bond joins with the unpaired electron from the terminal carbon of the chain radical, creating a new bond to the methylene carbon of the C=C bond; the other $\pi$-bond electron moves to the other C=C carbon atom, becoming the new active radical site. Upon every monomer addition, the active centre is transferred to the newly formed chain end.

The propagation stage continues until all monomer is consumed, or a termination event occurs, deactivating the reactive end group and stopping polymerisation. For radical polymerisation, chain termination can occur via chain combination (Scheme 1.3 top), or via disproportionation (Scheme 1.3 bottom), both of which result in deactivated polymer chains which can no longer propagate. Radical combination can occur between any two radical species, such as an initiator fragment radical or another propagating chain. The result is a product containing a broad distribution of polymer molecular weights, which can be undesirable in some applications. Vinyl acetate polymerisations are known to suffer from disproportionation termination events more so than combination events, due to the high reactivity of the propagating polymeric radical species.[47, 48]

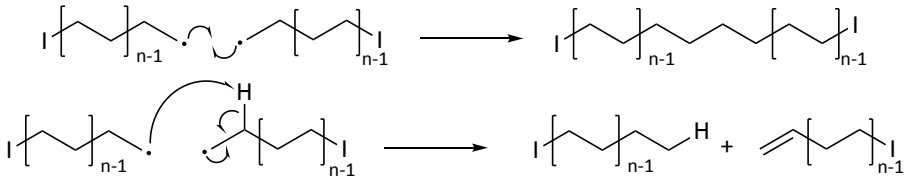


Scheme 1.3: Radical combination between two terminal radicals resulting in a dead polymer chain of length 2n+2 (top) and intermolecular hydrogen abstraction between a terminal radical and a neighbouring chain also resulting in dead chains (bottom).

Intramolecular hydrogen abstraction, also known as backbiting, can occur when the reactive radical terminus of the polymer reacts with a hydrogen atom on a preceding repeat unit (Scheme 1.4). The

rearrangement of the polymer structure results in the radical being migrated from the end of the chain back to some point within the chain, causing a branch point in the structure. This phenomenon is observed in the polymerisation of ethylene, causing short-chain branching and resulting in the low-density material known as LDPE.[39]

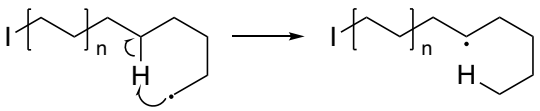


Scheme 1.4: Intramolecular hydrogen abstraction showing transfer of the active radical from the polymer terminus to the preceding repeat unit causing a branch point.

### 1.8.1 Reversible-deactivation radical polymerisation

Reversible-deactivation radical polymerisation (RDRP) aims to address the limitations of traditional free radical polymerisations discussed above,[49] such as imprecise molecular weight control and high Đ. Various techniques have been developed to achieve this control, all of which work by decreasing the number of active radical species in the reaction or making the radicals less 'free' and reactive. Since the likelihood of termination events is proportional to the square number of radicals in the system,[39] reducing the concentration of radicals lowers the probability of these events, thereby enhancing control over the polymer structure. This is achieved by reversibly deactivating the free radical, meaning it is only active during monomer addition for short bursts of time.

Living polymerisations are characterised by continuous chain propagation until the monomer is fully consumed, without chain transfer or irreversible chain termination.[50] Unlike conventional FRP, reversible addition-fragmentation chain transfer (RAFT) polymerisation approaches these conditions by lowering the number of active radicals present at any given time.[51] Although this reduction does not eliminate termination events due to radical-radical interactions, RAFT demonstrates living characteristics and can be described as pseudo-living.[51] IUPAC recommended a new term, RDRP, to describe techniques like RAFT, nitroxide-mediated polymerisation (NMP), and atom transfer radical

polymerisation (ATRP), which exhibit living characteristics but still experience some termination events.[52]

### 1.8.2 Reversible addition-fragmentation chain transfer polymerisation

The RAFT process was introduced in 1998 by the Commonwealth Scientific and Industrial Research Organisation (CSIRO) in Melbourne, Australia.[53, 54] RAFT polymerisations are highly compatible with functional monomers, such as vinyl acetate and acrylic acid, allowing them to polymerise with some living characteristics such as reduced termination and pseudo first order reaction kinetics. RAFT polymerisation employs thiocarbonylthio chain transfer agents (CTAs) to control chain growth through a kinetic strategy, enabling precise control over molecular weight and polymer architecture. Following Graeme Moad's presentation at Macromolecules '99: Polymers in the New Millennium,[55] a paper titled "Living free radical polymerisation reversible addition-fragmentation chain-transfer (the life of RAFT)" was published in Polymer International in 2000.[56] Since then, literature on polymerisation with thiocarbonylthio-bearing molecules has rapidly grown.[51, 57-61]

The aim of RAFT is to create polymers with minimal and controlled imperfections by reducing the likelihood of termination events during polymerisation. Although radical terminations are not completely eliminated, their frequency is significantly minimised relative to the number of growing polymer chains. This is achieved by reversibly trapping the propagating polymeric radical using the CTA, forming a dormant species in the form of the poly-RAFT agent (Scheme 1.5c). The propagating radical adds to the thiocarbonyl sulfur centre of the dithioester to produce an intermediate carbon-centred radical. This radical intermediate can then undergo β-scission, either reforming the propagating radical or liberating a new carbon-centred radical, the leaving group, R.

The RAFT process is shown in Scheme 1.5, with the structure of a typical RAFT agent represented in Scheme 1.5a. This functions through a two-step addition-fragmentation. Scheme 1.5a features a

reactive C=X bond, with X typically being sulphur. The Z group is selected to ensure the RAFT agent's C=S bond has suitable reactivity concerning the monomer and stability of the RAFT-adduct radical (Scheme 1.5b). The chain transfer product, Scheme 1.5c, is the poly-RAFT agent, which allows for further chain extension in the presence of monomer and a radical source. For living characteristics, the poly-RAFT agent must have an activity that is similar to or greater than that of the original small molecule RAFT agent (Scheme 1.5a). The rate of addition to the RAFT agent is given by $k_{add}$, which is typically favoured over the opposite removal reaction, i.e. $k_{add} > k_{-add}$. This is achieved through radical stabilisation discussed later. $k_{\beta}$ is the rate of β-scission, which is typically close to equal to $k_{add}$ to ensure a rapid exchange and uniform chain growth in the system.

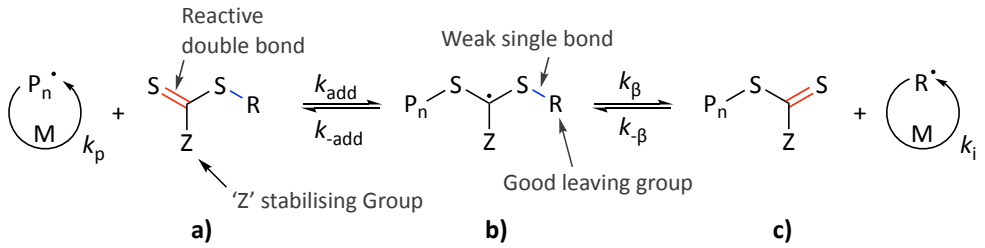


Scheme 1.5: Entrapment of the propagating radical species with a RAFT agent forming a RAFT adduct radical. Subsequent beta scission releases the R group for further initiation. a) small molecule RAFT agent, b) RAFT-adduct radical, c) poly-RAFT agent.

R is a radical leaving group and must be effective at reinitiating polymerisation and be converted to a propagating species at a sufficient rate ($k_{add}$ must be large). The R group of a RAFT agent is selected for its ability to readily undergo β-scission from the RAFT adduct radical favourably over the propagating radical, while still being capable of reinitiating polymerisation. This ensures that the initial RAFT agent quickly transforms into the poly-RAFT agent, and the R$^{\bullet}$ radicals convert into additional propagating species. As a result, an equilibrium is eventually established between the polymeric propagating radicals and the dormant poly-RAFT species (Scheme 1.6). When selecting a RAFT agent, it is important to take care to ensure a balance is met between the leaving ability and the reinitiation efficiency. If the rate of β-scission is slow relative to the rate of propagation, then retardation of polymerisation is likely to result. The RAFT-radical adducts are then more susceptible to side reactions.

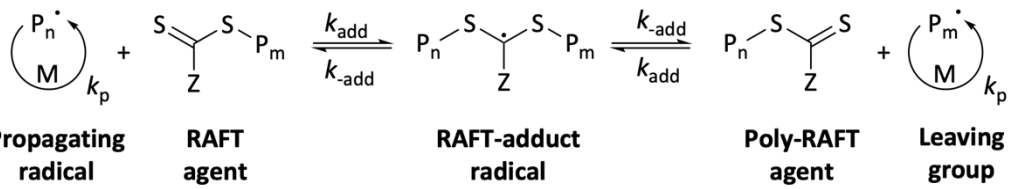


Scheme 1.6: Equilibrium achieved between propagating radicals and dormant species for two different propagating chains, $P_m$ and $P_n$. $k_p$ is the rate of propogation, $k_{-add}$ is the rate of fragmentation.

The selection of appropriate R and Z groups is essential for the success of polymerisation. For efficient polymerisation, several conditions must be met: both the initial and poly-RAFT agents need a highly reactive C=S bond (*i.e*. $k_{add}$ is large); the radicals generated should fragment quickly and without side reactions (*i.e*. $k_\beta$ is large, S-R bond is weak); the RAFT adduct radical intermediate should favour product formation (*i.e*. $k_\beta \geq k_{-add}$); and the eliminated R· radicals must efficiently reinitiate (*i.e*. $k_i \geq k_p$). The rate coefficient for the addition to the thiocarbonyl group ($k_{add}$) is strongly influenced by the structure of the stabilising group, Z (Figure 1.11). Thiocarbonylthio compounds include those with aromatic (**a**) and aliphatic (**d**) dithioesters, trithiocarbonates (**b**), dithiocarbamates (**c** and **f**) and xanthates (**e**). The rate of addition ($k_{add}$) and transfer decreases, and rate of fragmentation ($k_{-add}$) increases through the series from left to right.

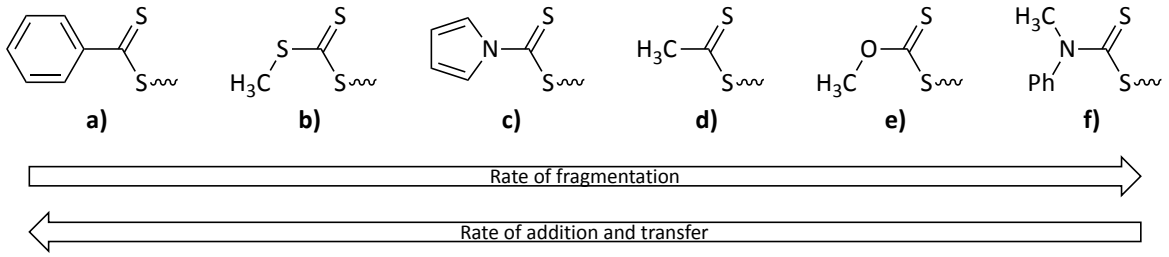


Figure 1.11: Various Z group substituents used to change the reactivity of the C=S bond.

The Z group can be used to activate or deactivate the C=S bond and to modify the stability of the intermediate radicals. A Z group should be chosen which does not stabilise the intermediate RAFT-adduct radical more than necessary, meaning the radical must be stable enough to allow for $k_{add}$ to be high, otherwise, there is risk that the rate of propagation, $k_p$, exceeds the addition rate, resulting in

poor polymerisation control. Conversely, if the Z group provides so much stabilisation that the RAFT adduct radical becomes slow to react or unreactive, large inhibition periods in polymerisation are observed, as the RAFT agent acts as a radical sink. When the radicals are 'stuck' in this RAFT-adduct form, they risk undergoing cross-termination reactions with propagating radicals.[43] Electron-withdrawing substituents on Z can be used to enhance the reactivity of the RAFT agent by making the thiocarbonyl sulphur more electrophilic, enhancing the rate of addition to the C=S bond.

The R group should be chosen as a better homolytic leaving group than the propagating radical. β-scission is favoured when R· has substantial stability and steric bulk. Usually, secondary or tertiary alkyl species are chosen as reinitiating groups, with electron withdrawing groups typically added to further stabilise the radical. These groups are usually similar to those found in radical initiators for the same reasons of radical stability and reinitiation capability.

### 1.8.3 Initiator selection

The conventional RAFT process does not generate radicals independently and thus requires a radical source in the form of an initiator. Typically, in a polymerisation, the amount of initiator is a minority component as increasing the amount of initiator increases the number of radicals in the system, thus increasing the probability of a termination event.[58] In an ideal polymerisation, all chains are initiated at the start of the reaction, grow uniformly, and remain active throughout the polymerisation process. When initiation is rapid relative to propagation, narrow molecular weight distribution is obtainable. It is important to consider the reactivity of the initiator radicals. If a less active RAFT agent is used, initiator-derived radicals will likely react preferentially with the monomer, meaning some polymer chains in the system will contain an initiator fragment at their end, with the subsequent reaction of the propagating chain with a RAFT agent providing a RAFT capped dormant chain.

As with conventional radical polymerisation, RAFT-polymerisations are air-sensitive. Both propagating macro-radicals and intermediate radicals are prone to react with oxygen, necessitating precautions to exclude air during these reactions. This is typically achieved through an inert gas sparge or a freeze-pump-thaw process. If air enters the polymerisation, it can cause the reaction to stall completely or result in poor control and broad molecular weight distributions due to dead chains in the population.

### 1.8.4 Macromolecular design by interchange of xanthate (MADIX) polymerisation

Macromolecular design by interchange of xanthate (MADIX) and RAFT are based on identical processes that involve the addition of a small amount of chain transfer agent polymerisation. Rhodia chemists initially gave the term MADIX during the development of xanthates for the industrial production of block copolymers, which was later covered in a patent alongside trithiocarbonates and dithioesters for the same purpose.[62, 63] CSIRO also filed in the area, with their patent covering trithiocarbonates and dithioesters but not xanthates (Figure 1.12).[53] RAFT and MADIX are polymerisation control techniques based on identical mechanisms,[62] with the only difference being the nature of the CTA. RAFT applies to CTAs Z–C(=S)–S–R in general, whereas MADIX refers exclusively to xanthates, where R = OZ'. The two original patents from Rhodia and CSIRO cover the same thiocarbonylthio derivatives, with CSIRO omitting xanthates from their patent.[53]

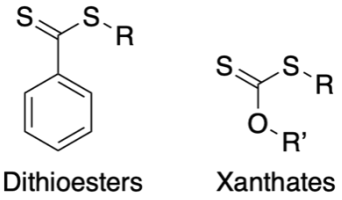


Figure 1.12: Generic structure of a dithioester and a xanthate. *N.B*. Xanthate is the trivial name for an *O*, *S*-dithiocarbonate.

For some applications, xanthates may be favoured over trithiocarbonates and dithioesters for the following two reasons: 1) Cost and availability – potassium and sodium *O*-ethyl xanthate salts which are required to produce the xanthate chain transfer agents are commodity chemicals utilised in the

mineral extraction industry as collectors in froth floatation of ores. As a result, these precursors to xanthate chain transfer agents are produced on a large scale, with the global market for xanthates estimated at $424.3 million in 2020.[64] 2) Xanthates are effective – for vinyl esters such as vinyl acetate, *O*-ethyl xanthates offer excellent control.[65] The polymerisation of methyl methacrylate (MMA) is poorly controlled by *O*-ethyl xanthates, but replacing the ethyl with a trifluoro ethyl group allows polymerisation control of MMA.[62] Conversely, dithioesters and trithiocarbonates are poor at controlling vinyl esters irrespective of the specific Z groups but can control polymerisation of MMA.

In 2000, MADIX was the first reported controlled radical polymerisation technique to successfully control polymerisation of vinyl acetate.[66] Vinyl acetate does not exhibit conjugation between the vinyl double bond and the pendant group, making it less reactive.[67] As a result, chain transfer reactions occur more frequently than with conjugated counterparts due to a lack of resonance stabilisation,[68] making polymerisation harder to control. Living radical polymerisation of vinyl acetate is typically challenging, and techniques such as ATRP and NMP fail to provide adequate control. Initial studies in the RAFT field demonstrated that it was possible to achieve molecular weight control of vinyl acetate polymerisation using specific xanthates,[66, 69] as well as less activated dithiocarbamates.[69, 70] Conversely, the use of other common RAFT agents, such as dithioesters and trithiocarbonates, results in inhibition during the polymerisation, which has been attributed to the relative stability of the RAFT-adduct radical.[57, 69, 71] This arises due to the propagating vinyl acetate radicals being poor leaving groups. The propagating radical of vinyl acetate is characterised by a lack of steric bulk and low radical stabilisation, resulting from the absence of conjugation within the monomer. Consequently, it is a highly reactive yet ineffective homolytic leaving group. This leads to a scenario in which the fragmentation products are less stable than the intermediate radical adduct, causing slow fragmentation and, ultimately, ineffective polymerisation control. It is, therefore, essential that the reactivity of the RAFT/MADIX agent is adjusted to sufficiently destabilise the intermediate radical, enabling the formation of propagating radical species at appropriate rates.

The choice of the Z-group for polymerisation of vinyl acetate is of particular importance, with the *O*-alkyl substituent playing a critical role.[72, 73] Common substituents include *O*-methyl, *O*-ethyl, *O*-isopropyl, and *O*-aryl xanthates, whereas *O*-tert-butoxyl is unsuitable due to the increased stability of the tertiary carbon radical.[73] The oxygen-bound alkyl group must be a poor homolytic leaving group relative to the intended S-R cleavable group to ensure that cleavage is favoured at the S-R site over the *O*-alkyl group. The use of alkyl groups is advantageous in this context, given the inherent instability of the primary alkyl radical.[51] The mechanism of a MADIX polymerisation is the same as that for RAFT, with activation of an initiator and subsequent reaction of the active initiating species with a monomer forming the first step of polymerisation (Scheme 1.7a). The pre-equilibrium stage (Scheme 1.7b) follows with the reaction of the propagating polymer radical and the CTA, consuming the initial CTA. Once the CTA has been consumed, the poly-RAFT agent enters the main equilibrium (Scheme 1.7d), where the chain transfer between dormant CTA-terminated polymers and propagating species commences. This is the equilibrium responsible for the controlled addition of monomer units to the propagating chain.

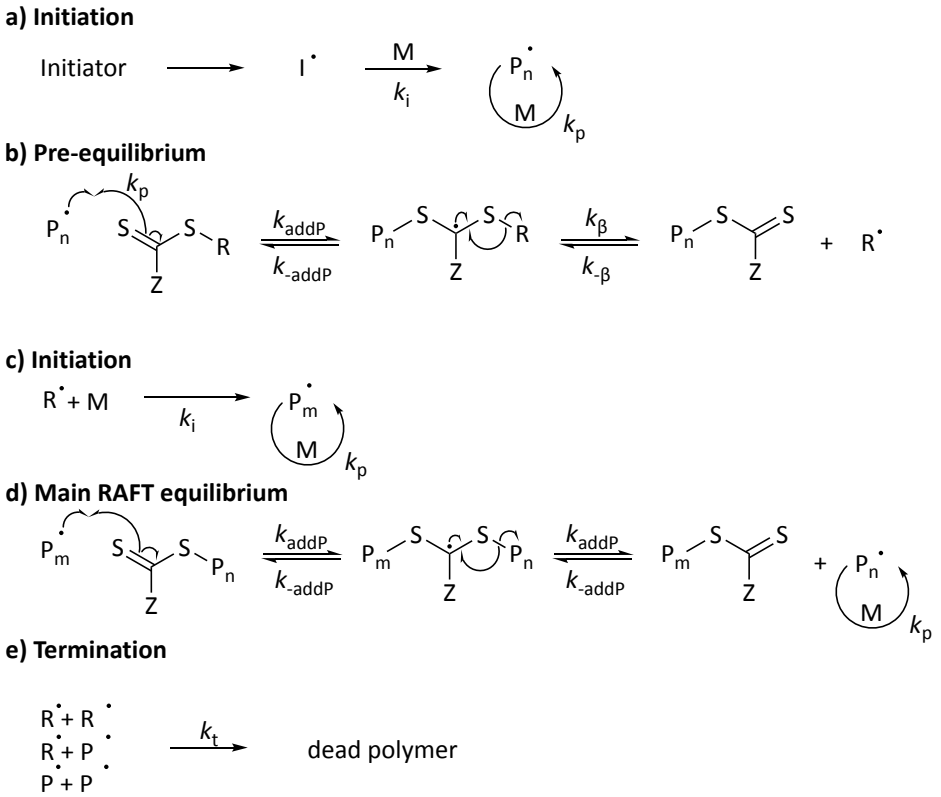


Scheme 1.7: General mechanism of RAFT/MADIX polymerisation.

Ideally, there is a rapid exchange in the main equilibrium stage (Scheme 1.7d), meaning all polymer chains have an equal chance to grow, with each chain spending a comparable amount of time in the active propagating state, ensuring a narrow molecular weight distribution. Most polymer chains retain the xanthate at the end group after consumption of all monomer units or when quenched. In contrast, the α end group bears the R group from the original xanthate. This means that the end groups can be used in subsequent reactions, such as reducing the dithiocarbonate to a thiol to exploit sulfur chemistries or radical reinitiation and adding a secondary monomer to produce block copolymers.

### 1.8.5 Photo initiated polymerisation techniques

Earlier approaches to polymerisation usually involved thermally initiated radical sources such as AIBN and peroxides (e.g. lauroyl peroxide, benzoyl peroxide), which required elevated reaction temperatures to cleave and initiate polymerisation. More recently, photoinduced reactions have been integrated into radical polymerisation methods, offering a low-cost and energy-efficient route to

initiate various types of polymerisation processes.[74] In the field of RAFT/MADIX, the use of light as a means of initiation has allowed new processes such as photo RAFT and photoinduced single electron transfer (PET) RAFT/MADIX[75] methods to be explored. This methodology is beneficial as it reduces the need for excessive heating during processes that often require flammable solvents, and for which monomers or polymers may thermally degrade if exposed to heat for prolonged periods. It also opens avenues to explore switchable radical generation methods by varying the wavelength of the light source.[76]

Although photo-RAFT and PET-RAFT both use light to initiate polymerisation, the methods differ in the mechanism by which the light initiates polymerisation (Scheme 1.8). In photo-RAFT, the chain transfer agent is also the initiator, with the weak S–R bond being cleaved homolytically by irradiation to generate a pair of radicals (Scheme 1.8). The R· species then acts as the initiating radical and reacts with a monomer unit to begin the propagation process. This process has the advantage of initiating all polymer chains with the same group, rather than conventional RAFT, where a small minority of chains are initiated with the initiator fragment. This is useful should the $\alpha$ terminus contain a reactive handle for post-polymerisation modification, such as a carboxylic acid functionality, as $\alpha$-end-group fidelity is maximised. Typically, ultraviolet (UV) light is used for such activations, with the earliest example reported in 1982 by Otsu *et al*. for polymerisation of methyl methacrylate with a dithiocarbamate.[77] It was also reported that other common thiocarbonylthio compounds respond to UV irradiation in this way, allowing polymerisation in the absence of a traditional azo or peroxide initiator.[78] The issue, however, with direct UV irradiation is the eventual degradation of the CTA beyond just the R–S bond, eventually leading to loss of control and, thus, broader molecular weight distributions.[79] To overcome this issue, visible light can be used, although this is only suitable for specific CTAs which have low bond dissociation energies cleavable with light in the visible region. There are examples of this;[80-82] however, it is typically more effective to utilise a photocatalyst and subsequent energy/electron exchange to

fragment the CTA R–S group to improve the energy transfer efficiency. This process is known as PET-RAFT.

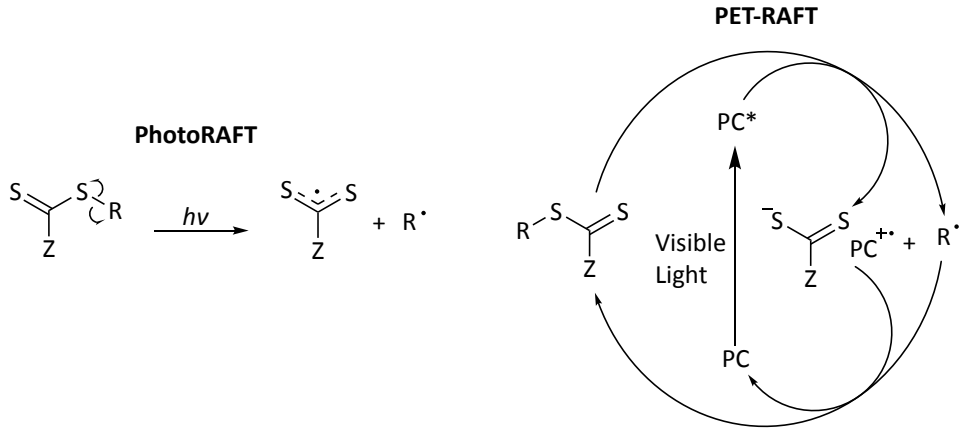


Scheme 1.8: L) PhotoRAFT showing photolysis of RAFT agent dithiocarbonate radical and R radical; R) PET-RAFT showing excitation of photocatalyst (PC) and subsequent electron transfer forming photocatalyst radical cation, thiocarbonylthio anion and R radical.

PET-RAFT is a method of polymerisation mediated by photoredox catalysis upon irradiation with light.[83] Boyer *et al.*[84] discovered that an initiating species can be generated via electron transfer from a photoredox catalyst to a chain transfer agent. Original PET-RAFT photocatalysts were based on transition metal complexes such as iridium tris(bipyridine) and metalloporphyrins.[85, 86] The excitation of a photocatalyst under visible light irradiation causes an electron transfer to the thiocarbonylthio moiety, which in turn cleaves to alleviate R or $P_n$ radicals, which can, in turn, go on to take part in the conventional RAFT/MADIX process. Additionally, a thiocarbonylthio anion species and a photocatalyst cation species are produced, which may interact with a radical species, either R· or $P_n$·, to complete the cycle.[85, 87]

A recent report[88] using bismuth derivatives as visible-light-driven photocatalysts has sparked interest in their use as components in PET-RAFT/MADIX.[89-91] The narrow band gap of 2.85 eV in α-$Bi_2O_3$ and 2.58 eV in β-$Bi_2O_3$ allows the promotion of an electron by irradiation with visible light (Figure 1.13) – the excitation wavelength corresponds with that present in white light from a domestic fluorescent light bulb. Of the variety of narrow band gap semiconducting materials, commercially available $Bi_2O_3$

powder (a mixture of α-$Bi_2O_3$ and β-$Bi_2O_3$) has been reported as an efficient heterogeneous visible light-activated photocatalyst.[92] Moreover, this study demonstrated that $Bi_2O_3$ was highly effective in the polymerisation of vinyl acetate, highlighting its potential for broad applicability in PET-RAFT/MADIX systems. $Bi_2O_3$ also has the benefit of low toxicity, low cost, and ease of removal from the reaction post-polymerisation due to its heterogeneous nature.

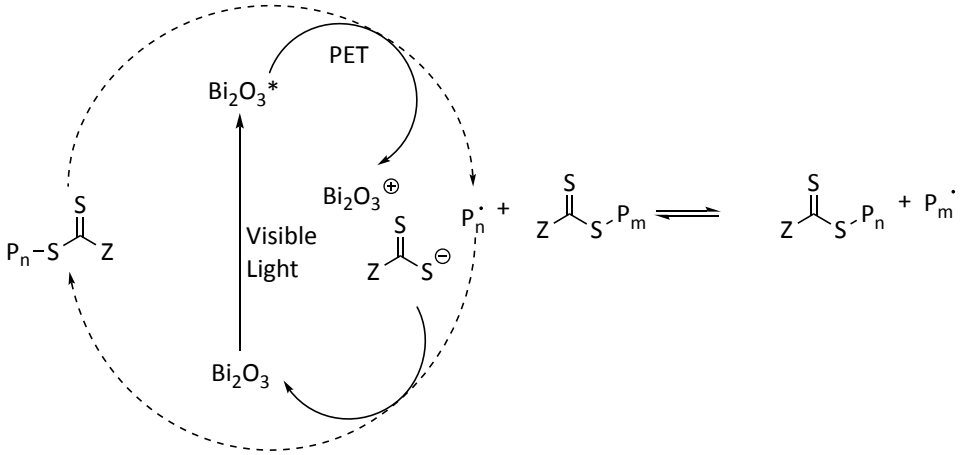


Figure 1.13: Scheme showing the method of radical generation via photoexcitation of a single electron in bismuth oxide photocatalyst followed by electron transfer to the dithiocarbonate. Reproduced with permission from Hakobyan et al.[89]

## 1.9 Project aims

This project is driven by the significant industrial importance of improving the performance of homecare products under more environmentally friendly conditions (i.e. lower wash temperatures, shorter wash cycles). With this focus, the aim is to study the material properties of PVA, with precise control over its polymer structure and, where required, end-group functionality. A key objective is to design a method for synthesising well-defined, industrially relevant model PVAs, while conducting experiments to explore the polymer's structure-property relationships. Specifically, the main goal of this work is to investigate the effect of the degree of acetylation in PVA on key polymer properties such as polymer size, phase stability, and diffusion characteristics.

Chapter 2 seeks to characterise the dimensions of PVA both in its solid and solution states. This will provide experimental validation for existing computational predictions and support the development of industrially relevant polymer diffusion models. The chain dimensions of PVA/c will be examined using small-angle neutron scattering (SANS) in aqueous solutions at varying concentrations, as well as in the melt state. Additionally, the study will explore the phase separation tendency in a two-component system as the degree of hydrolysis between the two polymer species varies. This will be assessed by fitting for the Flory-Huggins interaction parameter. For this purpose, deuterated PVAc analogues and PVA with controlled degrees of acetylation and dispersity will be synthesised using the PET-MADIX technique.

Chapter 3 will investigate the depth of polymer interdiffusion in an aged two-component film system, which serves as a model for the seals used in soluble unit dose detergent pods. Ion Beam Analysis (IBA) will be employed to analyse the diffusion characteristics. A variety of PVA polymers with different degrees of hydrolysis will be synthesised, with multiple methods for incorporating heavy atom labels explored. The study will utilise proton beam and backscattered X-ray analysis to achieve detailed profiling of the polymer interdiffusion in the aged seal system.

Chapter 4 aims to assess the rate of polymer diffusion in thin films using Fluorescence Recovery After Photobleaching (FRAP). A library of PVAs with varying degrees of hydrolysis will be produced via PET-MADIX, with the thiol end group of the polymer used for the attachment of a fluorescent, photo-bleachable dye molecule to each polymer chain. Different fitting models will be evaluated to provide both qualitative and quantitative insights into the relative and absolute diffusion rates within the polymer library.

This work ultimately aims to improve understanding of how structural modifications in PVA influence its behaviour in industrial applications, particularly in relation to diffusion and phase behaviour, thereby providing a valuable basis for optimising materials for homecare products.

## 1.10 References


1. L. T. T. Ho, *Formulating Detergents and Personal Care Products: A Guide to Product Development*, AOCS Press, 2000.
2. P&G, The life cycle assessment – the backbone of Ariel's commitment to reduce its carbon footprint, https://www.ariel.co.uk/en-gb/about-ariel/sustainability/ariel-life-cycle-assessment, (accessed 25/07/2024).
3. A. Villanueva, I. Hook, F. Alborzi, M. Cordella, K. Graulich, N. Espinosa, A. Boyano, I. Rüdenauer and R. Stamminger, *Ecodesign and energy label for household washing machines and washer dryers – Preparatory study - final report*, European Commission

Joint Research Centre, 2017.

4. *M. Jennewein, World Pat.,* WO2010141301A1, 2010.
5. C. A. Finch, *Polyvinyl Alcohol: Developments*, Wiley, Hoboken, NJ, 1992.
6. Classification, labelling and packaging of substances and mixtures, http://data.europa.eu/eli/reg/2014/1297/oj, (accessed 18/03/23).
7. Electrolux, *The Truth About Laundry*, Elecrtrolux, 2021.
8. iFixIt, Redit, SUD pod residue resulting from incomplete dissolution during the wash cycle, https://www.reddit.com/r/fixit/comments/n7srij/laundry_detergent_pod_did_this_to_my_wifes/ (accessed 31/07/2024).
9. K. R. Rajeesh, R. Gnanamoorthy and R. Velmurugan, *Mat. Sci. Engineer. A*, 2010, **527**, 2826-2830.
10. R. S. Porter and J. F. Johnson, *Chem. Rev.*, 2002, **66**, 1-27.
11. N. Jain, V. K. Singh and S. Chauhan, *J. Mech. Behav. Mater.*, 2017, **26**, 213-222.
12. B. Liu, J. Zhang and H. Guo, *Membranes*, 2022, **12**, 347.
13. L. Leger and C. Creton, *Philos. Trans. R. Soc. A*, 2008, **366**, 1425-1442.
14. A. Briddick, R. J. Fong, E. F. D. Sabattie, P. Li, M. W. A. Skoda, F. Courchay and R. L. Thompson, *Langmuir*, 2018, **34**, 1410-1418.
15. S. K. Lin and J. March, *March's Advanced Organic Chemistry: Reactions, Mechanisms, and Structure, 5th Edition*, Wiley-Blackwell, Chichester, UK, 2001.
16. I. Sakurada, *Polyvinyl Alcohol Fibers*, Taylor & Francis, New York, 1985.
17. M. Lim, D. Kim and J. Seo, *Polym. Int.*, 2016, **65**, 400-406.
18. *W. H. Carothers, US Pat.,* 2,130,948, 1937.
19. O. Olabisi and K. Adewale, *Handbook of Thermoplastics*, Taylor & Francis, 1997.
20. E. R.L. and S. K., *TAPPI J.*, 1993, **76**, 143-146.
21. *Polyvinyl Alcohol (PVA) Market Share & Growth Report, 2030*, Grand View Research, 2023.
22. D. Verma, A. Bhatia, S. Chopra, K. Dua, P. Prasher, G. Gupta, M. M. Tambuwala, D. K. Chellappan, A. A. A. Aljabali, M. Sharma and D. N. Kapoor, in *Advanced Drug Delivery Systems in the Management of Cancer*, 2021, DOI: 10.1016/b978-0-323-85503-7.00003-1, pp. 351-358.
23. C. H. Lee and W. H. Hong, *J. Membrane Sci*, 1997, **135**, 187-193.
24. H. Ochiai, H. Fujii, M. Watanabe and H. Yamamura, *Polym. J.*, 1974, **6**, 396-402.
25. *S. Nii, D. M. Lee and J. Childers, World Pat.,* WO2016160116A1, 2016.
26. M. Amann and O. Minge, in *Synthetic Biodegradable Polymers*, eds. B. Rieger, A. Künkel, G. W. Coates, R. Reichardt, E. Dinjus and T. A. Zevaco, Springer, Berlin, Heidelberg, 2012, pp. 137-172.
27. M. Julinova, L. Vanharova and M. Jurca, *J. Environ. Manag.*, 2018, **228**, 213-222.
28. F. L. Marten, in *Encyclopedia of polymer science and technology*, Wiley, Hoboken, NY, 2002.
29. *W. Zimmermann and G. Pospich, European Pat.,* EP0032572A1, 1982.
30. E. Chiellini, A. Corti, S. D'Antone and R. Solaro, *Prog. Polym. Sci.*, 2003, **28**, 963-1014.
31. F. Kawai and X. Hu, *Appl. Microbiol. Biotechnol.*, 2009, **84**, 227-237.

32. D. Byrne, G. Boeije, I. Croft, G. Hüttmann, G. Luijkx, F. Meier, Y. Parulekar and G. Stijntjes, *Tenside Surfact. Det.*, 2021, **58**, 88-96.
33. N. Ben Halima, *RSC Adv.*, 2016, **6**, 39823-39832.
34. A. D. Jenkins, P. Kratochvíl, R. F. T. Stepto and U. W. Suter, *Pure Appl. Chem.*, 1996, **68**, 2287-2311.
35. R. J. Young and P. A. Lovell, *Introduction to Polymers, Third Edition*, Taylor & Francis, Boca Raton, FL, 2011.
36. M. E. Hermes, *Enough for One Lifetime: Wallace Carothers, Inventor of Nylon*, American Chemical Society and the Chemical Heritage Foundation, USA, 1996.
37. J. K. Stille, *J. Chem. Educ.*, 1981, **58**, 862-866.
38. Y. H. So, *Acc. Chem. Res.*, 2001, **34**, 753-758.
39. C. Barner-Kowollik, P. Vana and T. P. Davis, in *Handbook of Radical Polymerization*, Wiley, Hoboken, NJ, 2002, pp. 187-261.
40. J. March and M. Smith, in *March's Advanced Organic Chemistry*, Wiley-Blackwell, Chichester, UK, 2006, pp. 32-105.
41. M. F. Cunningham and R. Hutchinson, in *Handbook of Radical Polymerization*, Wiley, Hoboken, NJ, 2002, pp. 333-359.
42. K. Matyjaszewski, in *Handbook of Radical Polymerization*, Wiley, Hoboken, NJ, 2002, pp. 361-406.
43. G. Moad and C. Barner-Kowollik, in *Handbook of RAFT Polymerization*, Wiley, Hoboken, NJ, 2008, ch. 3, pp. 51-104.
44. B. Yamada and P. B. Zetterlund, in *Handbook of Radical Polymerization*, Wiley, Hoboken, NJ, 2002, pp. 117-186.
45. J. Brandrup, *Polymer handbook*, Knovel, Norwich, NY, 4 edn., 2005.
46. D. J. Walton and J. P. Lorimer, *Polymers*, OUP, Oxford, UK, 2000.
47. J.-L. Gustin and F. Laganier, *OPR&D*, 2005, **9**, 962-975.
48. B. L. Funt and W. Pasika, *Can. J. Chem.*, 1960, **38**, 1865-1870.
49. A. Bagheri, S. Boniface and C. M. Fellows, *Chem. Teach. Internat.*, 2021, **3**, 19-32.
50. M. Szwarc, *Nature*, 1956, **178**, 1168-1169.
51. S. Perrier, *Macromolecules*, 2017, **50**, 7433-7447.
52. S. Penczek and G. Moad, *Pure Appl. Chem.*, 2008, **80**, 2163-2193.
53. *T. Le, G. Moad, E. Rizzardo and S. Thang, World Pat.,* WO1998001478, 1998.
54. G. Moad and E. Rizzardo, *Polym. Int.*, 2020, **69**, 658-661.
55. A. Amass, *Polym. Int.*, 2000, **49**, 911-911.
56. G. Moad, J. Chiefari, Y. K. Chong, J. Krstina, R. T. A. Mayadunne, A. Postma, E. Rizzardo and S. H. Thang, *Polym. Int.*, 2000, **49**, 993-1001.
57. G. Moad, E. Rizzardo and S. H. Thang, *Aust. J. Chem.*, 2005, **58**, 379-410.
58. G. Moad, *Aust. J. Chem.*, 2006, **59**, 5559-5562.
59. J. Chiefari and E. Rizzardo, in *Handbook of Radical Polymerization*, Wiley, Hoboken, NJ, 2002, pp. 629-690.
60. C. Barner-Kowollik, T. P. Davis, J. P. A. Heuts, M. H. Stenzel, P. Vana and M. Whittaker, *J. Polym. Sci. A*, 2002, **41**, 365-375.
61. M. Semsarilar and V. Abetz, *Macromol. Chem. Phys.*, 2020, **222**, 2000311.
62. S. Z. Zard, *Macromolecules*, 2020, **53**, 8144-8159.
63. *P. Corpart, D. Charmot, T. Biadatti, S. Zard and D. Michelet, World Pat.,* WO1998058974, 1998.
64. marketresearch.com, *Xanthates*, 2021.
65. S. Perrier and P. Takolpuckdee, *J. Polym. Sci. A*, 2005, **43**, 5347-5393.
66. D. Charmot, P. Corpart, H. Adam, S. Z. Zard, T. Biadatti and G. Bouhadir, *Macromolecular Symposia*, 2000, **150**, 23-32.
67. A. Rudin and P. Choi, *The Elements of Polymer Science & Engineering*, Academic Press, Boston, Third edn., 2013.

68. T. Kanazawa, T. Nishikawa and M. Ouchi, *Polym. J.*, 2021, **53**, 1167-1174.
69. E. Rizzardo, J. Chiefari, R. T. A. Mayadunne, G. Moad and S. H. Thang, in *Controlled/Living Radical Polymerization*, American Chemical Society, USA, 2000.
70. M. Destarac, D. Charmot, X. Franck and S. Z. Zard, *Macromol. Rapid Commun.*, 2000, **21**, 1035-1039.
71. A. Favier and M. T. Charreyre, *Macromol. Rapid Commun.*, 2006, **27**, 653-692.
72. M. H. Stenzel, L. Cummins, G. E. Roberts, T. P. Davis, P. Vana and C. Barner-Kowollik, *Macromol. Chem. Phys.*, 2003, **204**, 1160-1168.
73. M. L. Coote and L. Radom, *Macromolecules*, 2003, **37**, 590-596.
74. N. Zaquen, J. Yeow, T. Junkers, C. Boyer and P. B. Zetterlund, *Macromolecules*, 2018, **51**, 5165-5172.
75. S. Dadashi-Silab, S. Doran and Y. Yagci, *Chem. Rev.*, 2016, **116**, 10212-10275.
76. J. Xu, C. Fu, S. Shanmugam, C. J. Hawker, G. Moad and C. Boyer, *Angew. Chem. Int. Ed.*, 2017, **56**, 8376-8383.
77. T. Otsu, M. Yoshida and T. Tazaki, *Macromol. Rapid Commun.*, 1982, **3**, 133-140.
78. T. G. McKenzie, Q. Fu, M. Uchiyama, K. Satoh, J. Xu, C. Boyer, M. Kamigaito and G. G. Qiao, *Adv. Sci.*, 2016, **3**, 1500394.
79. J. F. Quinn, L. Barner, C. Barner-Kowollik, E. Rizzardo and T. P. Davis, *Macromolecules*, 2002, **35**, 7620-7627.
80. T. G. McKenzie, Q. Fu, E. H. H. Wong, D. E. Dunstan and G. G. Qiao, *Macromolecules*, 2015, **48**, 3864-3872.
81. C. Ding, C. Fan, G. Jiang, X. Pan, Z. Zhang, J. Zhu and X. Zhu, *Macromol. Rapid Commun.*, 2015, **36**, 2181-2185.
82. K. Jung, C. Boyer and P. B. Zetterlund, *Polym. Chem.*, 2017, **8**, 3965-3970.
83. V. Bellotti and R. Simonutti, *Polymers*, 2021, **13**, 1119.
84. J. T. Xu, K. Jung, A. Atme, S. Shanmugam and C. Boyer, *J. Am. Chem. Soc.*, 2014, **136**, 5508-5519.
85. J. Phommalysack-Lovan, Y. Chu, C. Boyer and J. Xu, *Chem. Commun.*, 2018, **54**, 6591-6606.
86. S. Shanmugam, J. Xu and C. Boyer, *J. Am. Chem. Soc.*, 2015, **137**, 9174-9185.
87. Y. Lee, C. Boyer and M. S. Kwon, *Chem. Soc. Rev.*, 2023, **52**, 3035-3097.
88. O. O. Fadeyi, J. J. Mousseau, Y. Feng, C. Allais, P. Nuhant, M. Z. Chen, B. Pierce and R. Robinson, *Org. Lett.*, 2015, **17**, 5756-5759.
89. K. Hakobyan, T. Gegenhuber, C. S. P. McErlean and M. Mullner, *Angew. Chem. Int. Ed.*, 2019, **58**, 1828-1832.
90. K. Hakobyan, C. S. P. McErlean and M. Müllner, *Macromolecules*, 2020, **53**, 10357-10365.
91. K. Hakobyan, C. S. P. McErlean and M. Müllner, *Macromolecules*, 2021, **54**, 7732-7742.
92. M. Ratova, R. Marcelino, P. de Souza, C. Amorim and P. Kelly, *Catalysts*, 2017, **7**, 283.

# Chapter 2: Investigation of chain dimensions and phase separation behaviour of well-defined polyvinyl alcohol materials and their solutions

## 2.1 Introduction

PVA plays a crucial role in water-soluble unit dose technologies, where its ability to interdiffuse and entangle under humid conditions is essential for forming sealed joins that encapsulate surfactants. Understanding this interdiffusion process, which occurs over a timescale of seconds and at nanometre distances, is vital for optimising the industrial application of PVA. However, traditional measurement techniques such as neutron reflectivity (NR), infrared spectroscopy (IR), and nuclear magnetic resonance (NMR) spectroscopy are either too slow or lack the resolution to capture this behaviour in wet films. In this work, small angle neutron scattering (SANS) was used to examine how PVA microstructure, specifically the degree of hydrolysis (DH), and environmental factors such as solution concentration influence chain dimensions. Additionally, PVA is synthesised through the hydrolysis of PVAc, where residual acetate groups suppress crystallisation and enhance solubility, though the compatibility between PVA and PVAc remains poorly understood. By combining SANS analysis with rheological studies of terminal relaxation time and studying blends of deuterium-labelled d-PVAc and PVAc with varying degrees of hydrolysis, this work aims to elucidate the interdiffusion behaviour and structural interactions within PVA-based systems. The determination of an interaction parameter will provide insight into the influence of DH on phase separation of PVA.

### 2.1.1 Small angle neutron scattering

SANS is a useful technique to probe the morphology of various materials. It can be used to investigate samples of length scales from the molecular size (fractions of nanometres) to the macroscopic (micrometre) size.[1] This scale encompasses the sizes of polymer chains (tens of Å) and their aggregates (hundreds of nanometres) as well as biological macromolecules,[2-5] ceramics[6-10] and metallic materials.[11-15]

The ability to substitute hydrogen for deuterium in macromolecular samples to achieve contrast makes SANS a valuable technique for probing the structure property relationships of polymeric materials as

well as biological systems such as membranes. Certain parts of the macrostructure can be selectively deuterated to enable their study without requiring the addition of molecular tags to visualise the area of interest.

Unlike other analytical techniques such as NMR spectroscopy, SANS plots typically contain few prominent features. As a result, SANS relies heavily on modelling the scattering intensity on an absolute scale. For macromolecular systems such as polymers, previous work by the likes of Flory[16] (Gaussian chains), Kuhn[17] (polymer chain stiffness), Zimm[17] (dilute polymer solutions) and de Gennes[18] (random phase approximations, scaling ideas) has enabled accurate prediction of their scattering behaviour. SANS has shown that polymer coils follow random walk behaviour when in the bulk state, meaning that monomer units along the chain are screened by surrounding chains, *i.e.* the chain can pass areas in space it has previously occupied as the chain has little correlation between distant points on the same polymer chain, except for a probability distribution that defines their most likely distance of separation. In the case of polymer solutions, a self-avoiding walk behaviour is more appropriate due to solvent polymer interactions and their attractive or repulsive nature.[1] When models are not available for a specific polymer systems, generic SANS methods are able to provide information on the nature of the sample configuration. For example, a gradient of -2 in a log[*I(Q)*] vs log(*Q*) is indicative of ideal polymer chains, while a gradient of -4 indicates smooth surfaces on objects which are large compared to the neutron wavelength.[1, 19]

### 2.1.2 Neutron scattering

Neutron scattering is a powerful tool in the study of soft matter. The low energies of neutrons coupled with their deep penetrating nature in most materials makes them an excellent non-destructive probe for most samples.[20] A neutron is a subatomic particle which also behaves as a wave, with its wavelength, λ, given by the de Broglie relationship,

$$\lambda = \frac{h}{mv} \qquad \text{(Equation 7)}$$

where *h* is Planck's constant, and *m* and *v* are the mass and velocity of the neutron respectively.

For scattering techniques, including light scattering, X-ray diffraction (XRD) and neutron scattering, it is convenient to convert the angular dependence of scattering to momentum transfer vector, *Q*. The scattering vector has units of inverse length and can be helpful to enable comparison between behaviour using different scattering techniques. *Q* is defined as the difference between the momentum of the incident wave ($k_i$) and the final wave ($k_f$), described by Equation 8 and Equation 9, and depicted in Figure 2.1.

$$|k_i| = |k_f| = \frac{2\pi}{\lambda} \quad \text{(Equation 8)}$$

$$Q = |k_i - k_f| = \frac{4\pi}{\lambda}\sin\left(\frac{\theta}{2}\right) \quad \text{(Equation 9)}$$

Substituting Equation 9 into Bragg's Law, Equation 10, gives Equation 11 which shows the relationship between size of the scattering object and the momentum transfer vector.

$$n\lambda = 2dsin\theta \quad \text{(Equation 10)}$$

$$Q = \frac{2\pi}{d} \quad \text{(Equation 11)}$$

where *n* is the atomic plane, *d* is the spacing of diffracting planes and θ is the incident angle.

Neutron scattering is characterised by coherent and incoherent contributions to scattering. Coherent scattering depends on *Q* and is therefore the part that contains information about scattering structures, whereas SANS incoherent scattering is featureless (*Q* independent) and contains information about the scattering material's density only.[21] Here, only coherent scattering is considered.

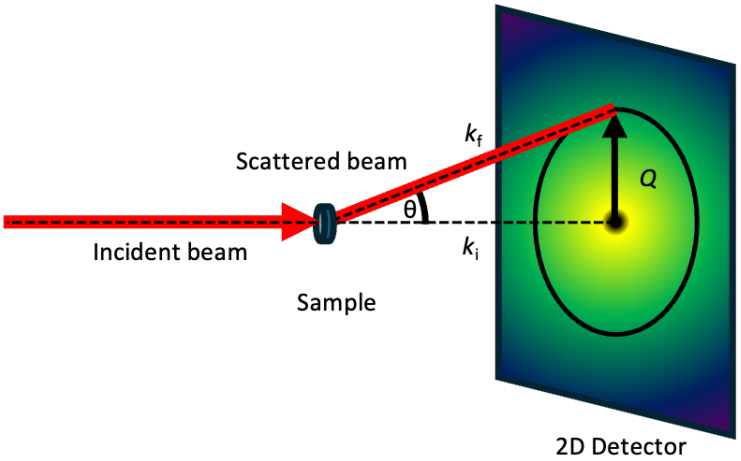


Figure 2.1: Schematic of elastic neutron scattering. $k_i$ is the momentum of the incident wave. $k_f$ is the momentum of the final wave. θ is the scattering angle relative to the incident beam.

The interaction strength between the neutron and nuclei is determined by the scattering length of the nucleus, *b*. The scattering length varies seemingly randomly with atomic number and is independent of momentum transfer, *Q*. This is beneficial for deuterium labelling in isotopic analogous materials as the scattering lengths for hydrogen and deuterium are wildly different ($b_H$ = -3.739 x $10^{-13}$ cm and $b_D$ = 6.671 x $10^{-13}$ cm respectively, Figure 2.2). The negativity of $b_H$ indicates that the scattered neutron wavefunction is out of phase with respect to the incident neutron wavefunction. When investigating large-scale structures such as polymer chains, the length scales are much greater than those of atoms, meaning it is helpful to define the scattering length density (s.l.d), *ρ*, of the material. *ρ* is calculated according to Equation 12.

$$\rho = \frac{\sum_{i=1}^{n} b_i}{v_m} \text{ where } v_m = \frac{M}{D} \qquad \text{(Equation 12)}$$

$b_i$ are the scattering length contributions of each atom in a unit cell of volume $v_m$. *M* and *D* represent the molar mass and density of the material respectively.

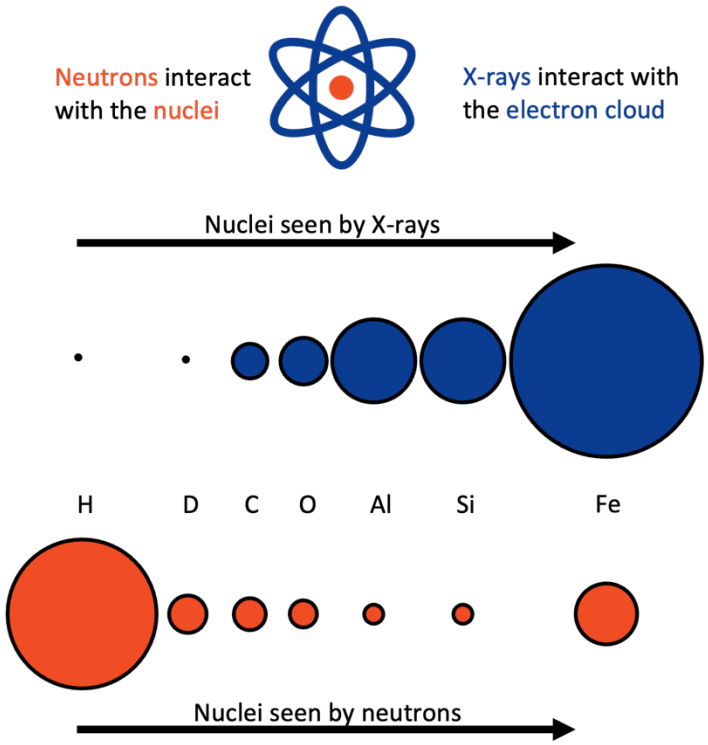


Figure 2.2: Comparison of scattering cross sections of nuclei for X-ray and neutron scattering techniques.

In a SANS experiment, *I(Q)* is measured, which is defined as the absolute differential scattering cross section $\frac{d\Sigma}{d\Omega}$. *I(Q)* has units of reciprocal centimetres and represents the probability that a neutron of wavelength λ is scattered, per unit solid angle, at that *Q* value.[22] The dependence of scattering length density on the constituent atoms' scattering length contributions, as well as the densities and molecular weights of the materials these atoms form, allows *ρ* to be tuned to either match or contrast other materials in the sample, which can help simplify analysis of the resultant scattering (Figure 2.3).

Other advantages of neutron scattering include the fact that neutrons have high penetration (*i.e.* low absorption) for most elements, making neutron experiments great for looking at the bulk of a sample. This is due to neutrons interacting through nuclear interactions, rather than electromagnetic interactions (as is the case with techniques such as X-ray scattering), or electrostatic interactions (as with electron beam measurements). Further to this, a wide range of neutron wavelengths are

achievable, enabling the interrogation of subjects from near Å to near micron length scales. This approach is ideal for characterising polymer chains, which are typically tens of angstroms in coil radius.

Exploiting the difference in scattering length of deuterium and hydrogen is the origin of contrast in this technique and what enables us to observe polymer chains in the sample. Below (Figure 2.3) is an example of the various types of contrast achievable with SANS. During this work, finite contrast (Figure 2.3a) was utilised.

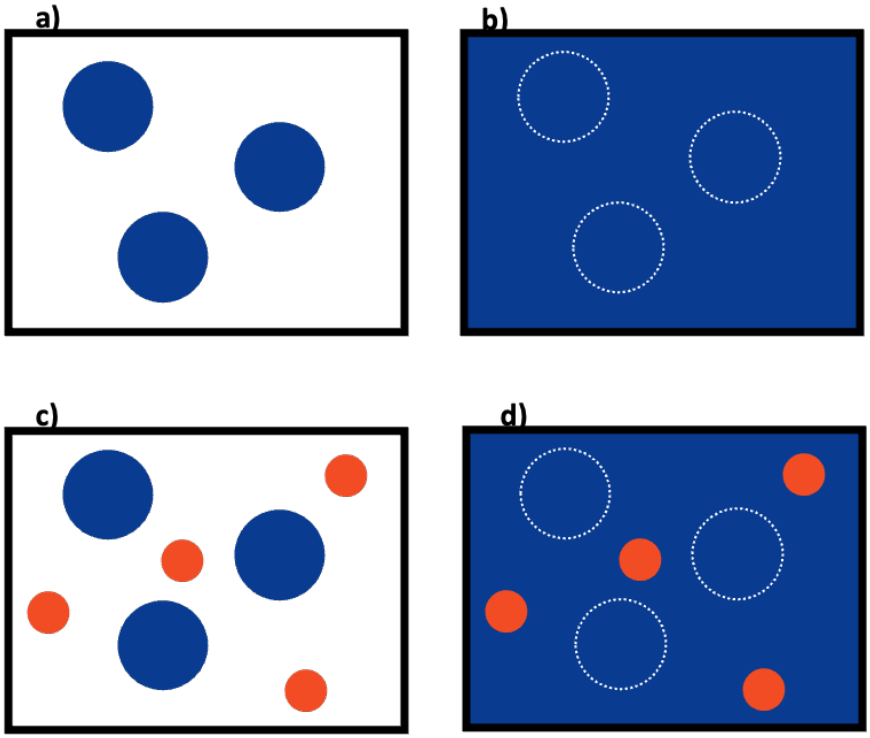


Figure 2.3: Various neutron contrast conditions: a) finite contrast, b) zero contrast, c) multiple contrasts and d) contrast matched (with respect to blue spheres).

### 2.1.3 Random coil conformations of polymer chains

Each bond in a polymer can adopt various conformations when solvated or in the melt state; many of these conformations will lead to an overall polymer form of a loosely coiled ball while very few will result in the chain being elongated. If all these conformations have equal probability, then it is far more likely that a polymer chain will be in a coiled (Figure 2.4a) conformation than a linear one (Figure

2.4b).[23] A theta solvent is one in which a solution of polymer in such solvent forms an ideal mixture, meaning it has equal interactions between monomer-monomer, solvent-solvent and monomer-solvent.[24] The size of a polymer chain in a melt or in a theta solvent can be described by its root mean square distance ($\vec{R}$) or its radius of gyration ($R_g$). For both measures, the chain dimension is proportional to the square root of the DP. This relationship can be expressed as:

$$\vec{R} \text{ or } R_g \propto \sqrt{DP} \qquad \text{(Equation 13)}$$

In a melt or a theta solvent, the polymer behaves similarly to an ideal chain, meaning the interactions between different parts of the chain either cancel out or are minimal. Therefore, the polymer assumes a random coil conformation where its dimensions scale as the square root of the number of monomers, the root mean square distance, $\vec{R}$. The root mean square distance can be calculated by Equation 14:

$$\vec{R} = l\sqrt{DP} \qquad \text{(Equation 14)}$$

where *l* is the bond length and DP is the degree of polymerisation.

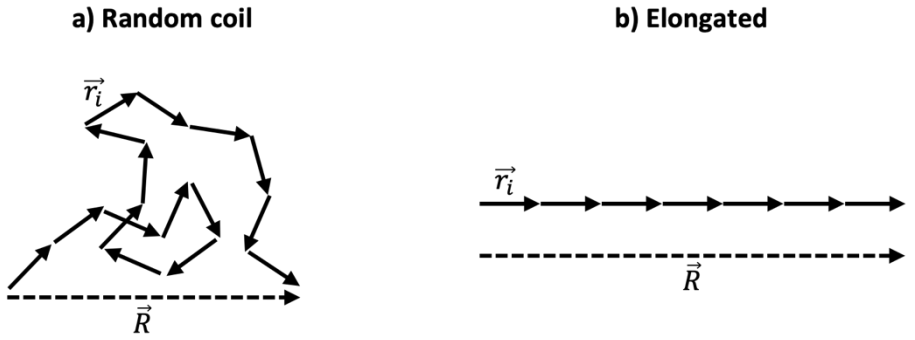


Figure 2.4: A schematic ilustration showing the calculation of root-mean-square separation for a) randon polymer coil and b) elongated polymer chain. $r_i$ is the end to end vector of a monomer, $\vec{R}$ is the total end to end vector, also known as root mean square distance.

Another convenient measure of polymer size is the $R_g$, which is the radius of a hollow sphere that has the same moment of inertia as a molecule of the same mass. For a one-dimensional random coil, radius of gyration is given by Equation 13, however for a three-dimensional coil, it is given by:

$$R_g = \left(\frac{DP}{6}\right)^{1/2} l \qquad \text{(Equation 15)}$$

where DP is the number of units of monomer each of length *l*.

The expected radius of gyration is always smaller for three dimensional systems due to the extra dimensions allowing the coil to be more compact.

The random coil model ignores the role of a solvent, hence the caveat of melt state or theta solvent conditions, where the polymer is likely to have its natural dimensions. This is important as poor solvents will typically cause the coil to tighten to reduce solute-solvent interactions, reducing the polymer size. A good solvent does the opposite of this. It is therefore beneficial to view results of calculations based on these models as lower bounds for a polymer in a good solvent and upper bounds for a polymer in a poor solvent.

### 2.1.4 Polydisperse Gaussian coil model

To fit the neutron data of solution state samples, and allow extrapolation of parameters from the obtained fit, a polydisperse Gaussian coil model can be employed. The model describes the scattering from polydisperse polymer chains in theta solvents or in a polymer melt.[23, 25, 26]

The scattering is described by Equation 16:

$$\mathrm{I(Q)} = \mathrm{scale} \cdot I_0 \cdot P(Q) + \mathrm{background} \qquad \text{(Equation 16)}$$

where

$$I_0 = \phi_{poly} \cdot V \cdot \left(b_{poly} - b_{solv}\right)^2$$

$$P(Q) = 2[(1+UZ)^{-\frac{1}{U}} + Z - 1]/[(1+U)Z^2]$$

$$Z = [(QR_g)^2]/(1+2U)$$

$$U = (M_w/M_n) - 1 = Đ - 1$$

$$V = M/(N_A\delta).$$

Here, *P(Q)* is the single particle (form) factor, $\phi_{poly}$, is the volume fraction of polymer, *V* is the volume of a polymer coil, *M* is the molecular weight of the polymer, $N_A$ is Avogadro's Number, δ is the bulk density of the polymer, $b_{poly}$ is the s.l.d. of the polymer, $b_{solv}$ is the s.l.d. of the solvent, and $R_g$ is the radius of gyration of the polymer coil. The parameters available to fit in the model are shown in Table 2.1. The 1D plot of default parameters takes the following form:

Table 2.1: Parameters for polydisperse Gaussian coil model.

| Parameter | Description | Units | SasView Default value |
|---|---|---|---|
| Scale | Scale factor or volume fraction | None | 1 |
| Background | Source background | $cm^{-1}$ | 0.001 |
| $I_0$ | Intensity at Q=0 | $cm^{-1}$ | 70 |
| $R_g$ | Radius of gyration | Å | 75 |
| Đ | Polymer $M_w/M_n$ | None | 2 |

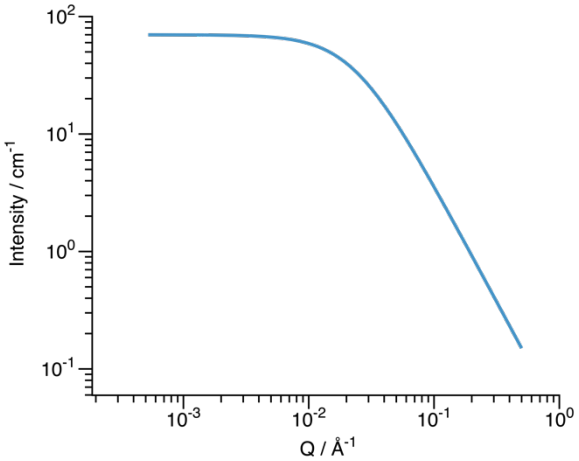


Figure 2.5: 1D plot of default model parameters for polydisperse Gaussian coil model.

### 2.1.5 Power law model

The power law model is based on a simple exponential with a flat background. This model is usually used to fit to spherical particle scattering. Scattering from fractal systems, *i.e.* those that are "self-similar" under a change of scale can be used to provide information about the surface roughness of the particles in the system. It is needed for this work to encompass the scattering of aggregate particles in the system and is combined with other models to improve the description of experimental scattering by the model.

The scattering is described by Equation 17:

$$\mathrm{I(Q)} = \mathrm{scale} \cdot Q^{-\mathrm{power}} + \mathrm{background} \qquad \text{(Equation 17)}$$

Table 2.2. Parameters used in SasView analysis software[27] and default values for power law model.

| Parameter | Description | Units | SasView Default value |
|---|---|---|---|
| Scale | Scale factor or volume fraction | None | 1 |
| Background | Source background | $cm^{-1}$ | 0.001 |
| Power | Power law exponential | None | 4 |

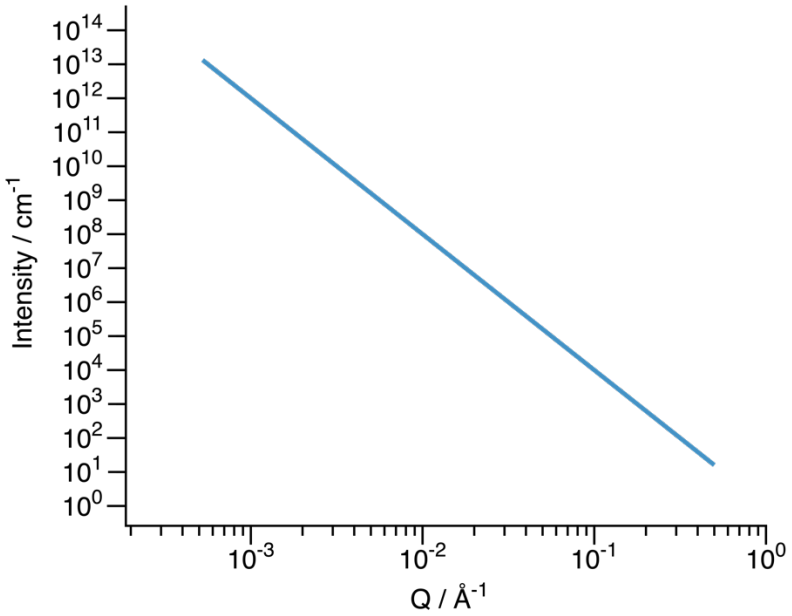

Figure 2.6: 1D plot of the power law model with default parameters.

### 2.1.6 Phase separation in polymer systems

Mixtures of homopolymers from different species typically form separate phases.[28] This common behaviour arises because the enthalpy of mixing, which refers to the change in energy associated with the formation of new intermolecular interactions between different species (e.g. species A and species B), is often positive. In such cases, the A-B interactions between the different polymer species are less favourable than the A-A interactions within each homopolymer, promoting phase separation.[29] The positive enthalpy of mixing reflects the physical reality that these mixtures tend to form distinct phases due to the unfavourable nature of the new intermolecular forces. Additionally, the entropy of mixing for large macromolecules is usually insufficient to counterbalance the enthalpic contribution.

Temperature plays a crucial role in determining polymer miscibility. Many polymers exhibit a temperature-dependent phase behaviour that can be understood in terms of critical solution temperatures, such as the Lower Critical Solution Temperature (LCST) and Upper Critical Solution Temperature (UCST). Polymers with an LCST, such as poly(*N*-isopropylacrylamide), become immiscible with their solvent above a certain temperature, leading to phase separation.[30, 31] Conversely, polymers with a UCST, such as poly(*N*-acryloyl glycinamide)

phase separate below a certain critical temperature.[31-33] These phenomena arise due to the balance between enthalpic and entropic contributions to mixing, which shift with temperature. The temperature dependence of polymer-solvent interactions, especially the hydrophilic or hydrophobic nature of the polymer, is key in determining the behaviour of polymer solutions near these critical temperatures.

In the context of the modelling of PVA SUD packaging, it is therefore crucial to investigate the extent, if any, of polymer demixing as PVAc is gradually hydrolysed, turning into PVA in a two-polymer system. In SUD pods, the polymers within the film must not phase separate, given the necessity of polymer mixing during the interdiffusion and entanglement process. This tendency to demix can be quantified by the Flory-Huggins interaction parameter ($\chi$). The dimensionless parameter $\chi$ quantifies the energetic interaction between different components in a polymer blend, such as polymer-polymer or polymer-solvent interactions. Derived from the Flory-Huggins theory of polymer solutions,[34, 35] $\chi$ helps determine whether a mixture of polymers will remain miscible or undergo phase separation.[29] A positive $\chi$ value indicates repulsive interactions between the components, leading to phase separation if the molecular weights are sufficiently large, while a negative or low value suggests attractive interactions, promoting miscibility regardless of molecular weight.

The magnitude and sign of the Flory-Huggins interaction parameter, $\chi$, are strongly dependent on temperature and the specific chemical interactions between polymers, such as hydrogen bonding. As $\chi$ typically varies with temperature, polymer miscibility becomes temperature dependent. At higher temperatures, entropic contributions to mixing increase, typically improving miscibility. In contrast, at lower temperatures, phase separation is usually more likely to occur due to the dominance of enthalpic contributions. The temperature dependence of $\chi$ can be described by several models, with the simplest form being $\chi=(A+B)/T$, where $A$ and $B$ are positive constants, and $T$ is temperature in Kelvin.[36] However, this empirical relationship may be modified to include additional terms, such as a $C/T^2$ term,

particularly when directional interactions (e.g., hydrogen bonding) are significant.[36] This flexibility in the temperature dependence of $\chi$ is a key feature of polymer blends, where $\chi$ can either increase or decrease with temperature, depending on the specific interactions at play. In the context of phase behaviour, polymers can exhibit two distinct regimes: the strong and weak segregation regimes. In the strong segregation regime, $\chi$ is large and the system tends towards phase separation, while in the weak segregation regime, $\chi$ is small, and polymers are more likely to mix.[37, 38] Additionally, the presence of crystalline regions within a polymer can create a separate phase that hinders miscibility. Crystalline polymers with strong intramolecular forces resist mixing with other polymers, whereas amorphous polymers are generally more miscible. This again highlights the motivation for choosing PVAc for this work, as opposed to PVA, which is semi-crystalline in nature and less likely to show miscibility with other species.

The power law scattering observed in small-angle scattering experiments can be indicative of phase-separated domains or distinct bubbles formed by polymers or other components, such as gas bubbles. This scattering pattern is expected when these distinct phases or regions emerge due to demixing. Understanding the Flory-Huggins interaction parameter is crucial for predicting the thermodynamic behaviour of polymer blends and their phase stability. $\chi$ can be determined experimentally by various techniques, including enthalpies of mixing, phase separation boundaries and light scattering.[39] More recent work utilises small angle scattering techniques to determine the interaction parameter of polymer blends, including SANS.[28, 40, 41]

The Random Phase Approximation (RPA) polymer model is a theoretical framework used to describe the thermodynamics of polymer blends and copolymers. Initially developed to interpret small-angle scattering data from non-crystalline, single-phase polymer mixtures,[42] it provides insights into the phase behaviour of these systems by accounting for both entropic and enthalpic contributions to mixing. In the RPA model, the collective response of polymer chains to composition fluctuations is

analysed, allowing the calculation of the structure factor *S(Q)*, which helps predict phase separation or miscibility. The model is particularly useful for its ability to link light scattering data of intensity *I* vs. scattering vector *Q* to structural information given by the structure factor *S(Q)*,[42] offering a simplified but powerful method to study complex polymer interactions at various length scales.

The structure factor, *S(Q)*, describes how the polymers are spatially arranged in the blend and provides insight into the degree of phase separation or miscibility, although the RPA is only strictly valid for single phase systems. The RPA can be experimentally tested and solved using SANS on polymer blends. SANS provides direct access to the structure factor by the relationship shown in Equation 18. As SANS measures the scattering intensity *I(Q)* as a function of the scattering vector *Q*, which corresponds to the spatial scale of composition fluctuations in the polymer blend, the intensity *I(Q)* is related to the structure factor *S(Q)* through:

$$I(Q) = S(Q) * \frac{(b_B - b_A)^2}{v} \qquad \text{(Equation 18)}$$

The right-hand term is a factor dependent on the contrast of the polymers in the blend. In essence, it depends on the difference in the neutron scattering length densities of the two polymers (in this case, dPVAc (deuterated PVAc) and hPVA/c (hydrogenous part hydrolysed PVA/c)) and the volume of polymer in the beam. For a binary polymer blend, the structure factor *S(Q)* can be determined using the RPA expression:

$$S^{-1}(Q) = \frac{1}{[N_A \phi_A g_D(R_{gA}, Q)]} + \frac{1}{[N_B \phi_B g_D(R_{gB}, Q)]} - 2\chi_S \qquad \text{(Equation 19)}$$

where $g_D$ is a single chain Debye function:

$$g_D\left(R_{g_i}, Q\right) = 2\frac{R_{g_i}^2 Q^2 + \exp\left(-R_{g_i}^2 Q^2\right) - 1}{R_{g_i}^4 Q^4} \qquad \text{(Equation 20)}$$

In the above expressions, *v* is a reference volume, $b_i$ is the scattering length of monomeric unit *i*, which can be calculated from known values, and $R_g$ is the radius of gyration of polymer molecule *i*, which can

be simultaneously determined by SANS, $N_A$ is Avogadro's constant and $\phi_i$ is the volume fraction of polymer *i*, which is known by mass fraction of polymer in the blend.

The SANS measurements of *I(Q)* vs *Q* are fit to the RPA model. By comparing the experimental scattering intensity *I(Q)* with the RPA-predicted structure factor *S(Q)*, the unknown parameters, particularly the Flory-Huggins interaction parameter $\chi$, can be extracted. Additionally, the $R_g$ can be determined from the fitting as other parameters are known values and the polymers are well characterised in terms of molecular weight and Đ.

### 2.1.7 Dynamic light scattering (DLS)

To study polymer particles above the upper size limit of a SANS experiment, alternative techniques can be employed. DLS is a particle sizing technique used to measure particles in the nanometre to micron regime. DLS and SANS are complementary techniques often used together to characterise the size and structure of particles or macromolecules in solution. For this work, DLS was employed to analyse the aggregation behaviour of polymer chains in solution where the size of particles was above the upper limit for the SANS instrument. DLS cannot be utilised to gain the same information of a SANS measurement, due to the limitation of the wavelength of light compared to the neutron wavelength. DLS does not probe individual polymer chains in the same way a SANS measurement does but instead can be used to investigate aggregates formed by multiple polymer chains. In a DLS instrument, a laser is directed at the sample, and as the particles move, light is scattered in various directions (Figure 2.6). The intensity of scattered light fluctuates with time due to the movement of the particles caused by Brownian motion. By fitting the correlation function, DLS determines the diffusion coefficient, *D*, of the particles, which is related to their size through the Stokes-Einstein Equation (Equation 21).

$$D_H = \frac{k_B T}{3\pi \eta D} \qquad \text{(Equation 21)}$$

where $k_B$ is the Boltzmann constant, $T$ is the temperature of the sample, $\eta$ is the viscosity and $D_H$ is the hydrodynamic diameter. If viscosity and temperature remain constant, smaller particles move faster than larger ones.

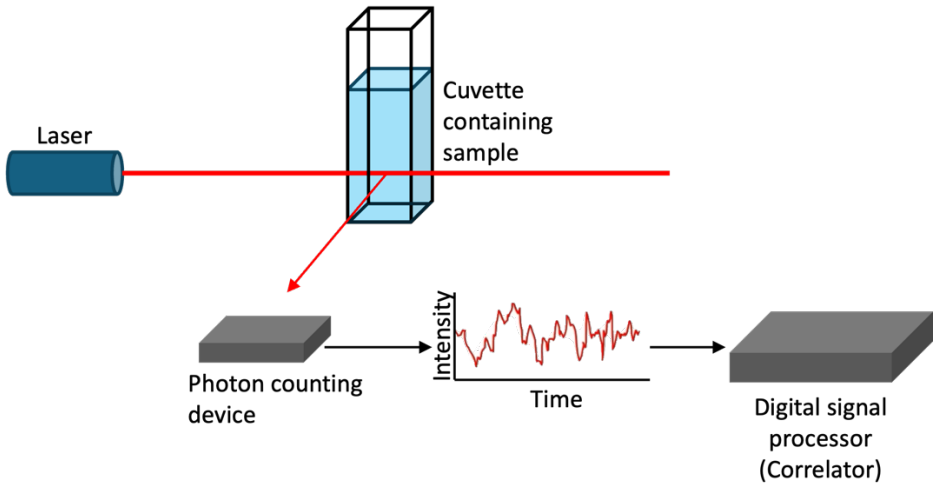


Figure 2.6: Diagram of DLS instrument with single right angle light scattering (RALS) detector.

Size analysis with DLS is only valid for single scattered light, meaning samples of high solute concentration (generally above 1-2 w/v%) are unsuitable for DLS due to the large proportion of multiply scattered light. To ensure valid data and reliable particle size distributions, samples must be highly diluted to ensure only singly scattered light is emitted from the sample. Additionally, in non-dilute solutions, the viscosity of the solution can deviate from that of the pure solvent, particularly when the volume fraction of particles is significant or charged particles are involved. These factors can alter particle diffusion, leading to an incorrect perception of the hydrodynamic size. The increased interactions between particles in concentrated solutions affect the diffusion coefficient, which may result in skewed DLS measurements if not accounted for properly.

In dynamic light scattering there are many different methods of describing particle size. The distribution of the sample describes the probability of encountering a certain variable. When looking at particle sizing, there are three main types of distribution obtained. The number distribution displays the number of particles in different size bins. The volume distribution shows the total volume of

particles in the different size bins. The intensity distribution describes the amount of light scattered by the particles in each size bin. These distributions are all different and defined in Equations 22-24.

In a system with two particle sizes, species one with radius *a* and species two with radius *b*, if there are $N_a$ particles with radius *a* and $N_b$ particles with radius *b* then their relative contribution compared to the other particle in terms of number is given by Equation 22.

$$\%N_a = \frac{100*N_a}{N_a+N_b} \quad \text{(Equation 22)}$$

where $\%N_a$ is the relative number of the particle with radius *a*.

If one assumes these particles are spherical, the particle volume is proportional to the size to the third power. Therefore, in terms of volume, the relative contribution from *a* is

$$\%V_a = \frac{100*N_a a^3}{N_a a^3+N_b b^3} \quad \text{(Equation 23)}$$

where $\%V_a$ is the relative volume of the particle size.

For small isotropic particles the scattering intensity from a spherical particle is proportional to the radius to the sixth power, or volume squared. Therefore, in terms of intensity, the relative contribution from a is

$$\%I = \frac{100*N_a a^6}{N_a a^6+N_b b^6} \quad \text{(Equation 24)}$$

where $\%I_a$ is the relative intensity of the particle with size *a*.

This typically means that intensity distributions emphasise the larger particles in the population, whereas the number distributions emphasise the smaller particles in a population. To compare DLS data with other sizing techniques, the detection mechanism of the other technique should be

considered. For neutron scattering, an intensity of scattered neutrons is reported and so it is most appropriate to compare SANS data to DLS intensity data.

### 2.1.8 Rheology

Rheology is defined as the study of flow and deformation of matter, describing the interrelation between force, deformation, and time. It can be used to investigate both the deformation of solid-like samples and the flow properties of liquid-like materials. There are two basic types of flow: shear flow and extensional flow. In shear flow, fluid components move past one another, while in extensional flow, fluid components move away from or towards each other. The most common and easily measured flow type on a rotational rheometer is shear flow, as it allows the sample's shape to remain unchanged, simplifying both the experimental procedure and analysis. In contrast, extensional flow often involves significant deformation of the sample's shape, making the setup and interpretation more complex. Shear flow will be discussed further in this chapter.

Shear flow can be thought of as layers of fluid sliding over one another, with each layer moving faster than the one beneath it (Figure 2.7). The layer in contact with the moving plate experiences the highest velocity, while the bottom layer experiences the least. For shear flow to exist, an external force, known as shear force, must be applied to the sample—typically by the rotation of a metal plate in a mechanical rheometer. This force, denoted as $F$ in Figure 2.17, acts over an area $A$, resulting in shear stress, σ (Equation 25). As a result of this force, the uppermost layer moves a distance $x$, while the bottom layer remains stationary, creating a displacement gradient across the sample ($x/h$). This displacement gradient is constant in simple laminar flow and is referred to as the shear strain ($\gamma$) (Equation 26). For fluid-like materials where the constituents can move relative to each other, the shear strain will continue to increase while the stress is applied, leading to a velocity gradient, known as the shear rate (or strain rate), which describes the rate of change of strain over time (Equation 27).

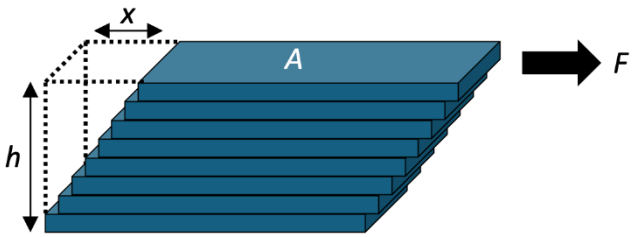


Figure 2.7: Quantification of shear rate and shear stress for fluid layers sliding one on top of the other.

$$\sigma = \frac{F}{A}\ (Pa) \qquad \text{(Equation 25)}$$

$$\gamma = \frac{x}{h} \qquad \text{(Equation 26)}$$

$$\dot{\gamma} = \frac{d\gamma}{dt}\ (s^{-1}) \qquad \text{(Equation 27)}$$

When a shear stress is applied to a fluid, momentum from the rotating plate is transferred to the upper layer of the sample. This momentum transfer occurs due to collisions and interactions between fluid components, which oppose the flow. In the linear regime and under constant flow, both the viscosity and kinetic energy remain constant. The coefficient of proportionality between shear stress and shear rate is known as the shear viscosity, $\eta$ (Equation 28), which is a quantitative measure of the internal fluid friction. Although viscosity is associated with resistance to flow and the dissipation of energy, in this regime, the system reaches a steady state where the rate of kinetic energy loss is balanced, ensuring both viscosity and kinetic energy are maintained at constant values.

$$\eta = \frac{\sigma}{\dot{\gamma}} \qquad \text{(Equation 28)}$$

For a Newtonian fluid, such as water, the shear stress is linearly related to the shear rate, meaning viscosity is independent of shear rate or shear stress. Non-Newtonian fluids show variation in viscosity as a function of shear rate, such as shear thinning liquids, which display a reduction in viscosity as shear rate is increased. Shear thinning is a result of micro-structural rearrangements in the plane of

the applied shear. It is commonly observed in polymer solutions and melts as well as dispersion systems. At low shear rates materials typically maintain their irregular order with a high zero shear viscosity as a result of particle or molecular interactions (Figure 2.8a). When a shear force is applied to the system with high enough energy, the shear rate may exceed the rate at which polymer chains can relax. Under these circumstances, the polymer chains align to the direction of the applied force, which usually results in a lower resistance to flow (Figure 2.8b).

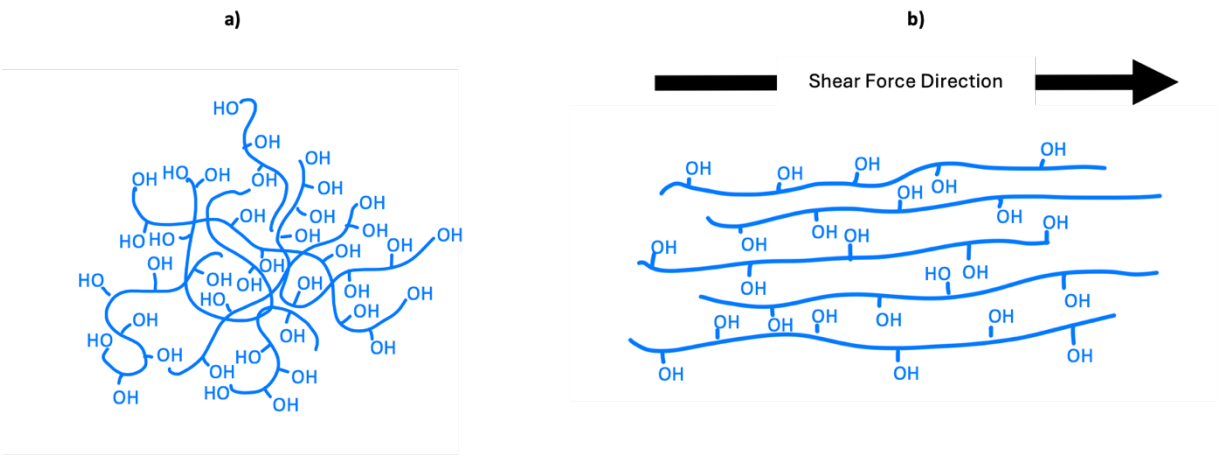


Figure 2.8: a) PVA at rest with no shear – chains are entangled; b) PVA under shear force- chains alligned to direction of shear.

Typical parameters used to quantify material properties in rheology are G’ and G’’, the storage and loss moduli respectively. G' represents the elastic, or solid-like, behaviour of the material. It indicates how much energy is stored and recovered during deformation. G'' reflects the viscous, or liquid-like, behaviour of the material. It indicates how much energy is dissipated as heat during deformation.[43, 44] A frequency sweep reveals how G' and G’’ change with the rate of deformation (frequency).

The phase angle (δ) is the phase difference between the applied strain and the resulting stress, and it provides insight into whether the material's behaviour is more elastic or viscous. If δ = 0°, the material is purely elastic (G' dominant); if δ = 90° the material is purely viscous (G'' dominant); if 0° < δ < 90°, the material is viscoelastic, with both elastic and viscous components.[43-46] The phase angle gives indication as to whether the material behaves more like a solid or a liquid at different frequencies.

## 2.2 Aims

This chapter aims to investigate key aspects of PVA in both the melt and solution states, focusing on how the DH and concentration influence polymer chain dimensions and phase behaviour. It is of particular interest to understand the relationship between the molecular structure of PVA and the interaction parameters that govern phase separation in multi-component systems. To achieve this, custom polymers were synthesised to allow precise control over molecular weight and DH, with deuterated polymers included for solid state SANS measurements to enhance contrast between components. The insights gained from these investigations will contribute to improving computational models for predicting polymer interdiffusion behaviour, which is critical to the SUD manufacturing process.

## 2.3 Results and discussion

### 2.3.1 Synthesis of polymers for SANS experiments

To synthesise commercially relevant PVA materials, partial acetylation was required. The majority of PVA used industrially is not fully hydrolysed in order to enhance its mechanical properties and solubility. Fully hydrolysed PVA is brittle and difficult to dissolve due to its high degree of crystallinity.[47] As solution-state SANS could be applied to predominantly hydroxyl functionalised materials, while solid-state SANS required mostly acetylated materials, different methods were developed to achieve the desired composition.

Synthesis of PVAc was conducted via PET-MADIX, following a method by Hakobyan *et al.*,[48] involving the use of a bismuth oxide photocatalyst and domestic fluorescent lightbulb to polymerise vinyl acetate. The method is highly effective and gave good control over polymer molecular weight and Đ to high polymer conversions (>70%, for calculation, see chapter 2 experimental section), as exhibited in Figure 2.9. This method of polymerisation is used throughout this thesis.

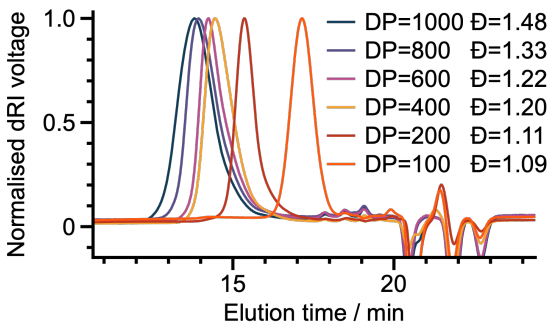


Figure 2.9: GPC chromatogram (dRI) for series of PVAc polymers synthesised via the method of Hakobyan *et al.*, using $Bi_2O_3$ photocatalyst and domestic light bulb. 1 mL/min, THF, 35 °C, Triple detection with universal calibration.

For solution-state measurements, which required mostly hydrolysed PVA, the approach involved fully hydrolysing PVAc to PVA and then re-acetylating the material (Scheme 2.1). It was necessary to be able to target specific degrees of re-acetylation to synthesise materials for SANS experiments. A method adapted from Congdon *et al.* was employed to modify the PVA.[49] This method utilised an acid-catalysed Fischer esterification between acetic acid and PVA to introduce acetate functionality onto the hydroxyl pendant groups, and it is known to result in random placement of the acetate groups along the polymer chain.[50]

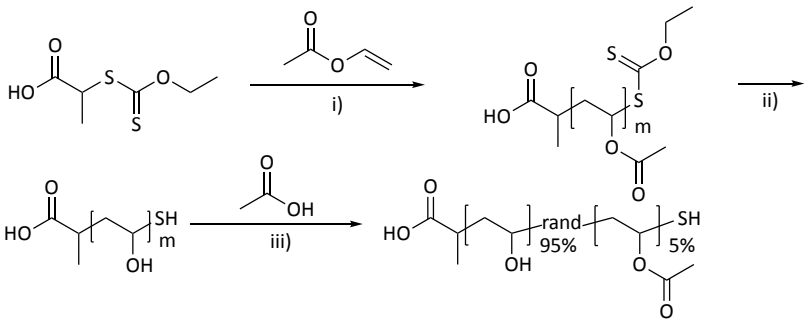


Scheme 2.1: Synthesis of part acetylated PVA via reacetylation of fully hydrolysed PVA. i) $Bi_2O_3$, h$\nu$ 15 W Fluorescent tube, 1010 lm, DMSO, inert atm, ii) NaOH (200 µL, 1 M) in MeOH (2 mL), iii) HCl (200 µL, 1 M), 50 °C.

A series of experiments was conducted to determine the relationship between volume fraction of acetic acid and the resultant degree of acetylation achieved on the polymer chain. It was found that when neat acetic acid (with HCl catalyst) was used, the highest degree of acetylation achieved was 77% (as determined by $^1$H NMR spectroscopy by comparing the integrals of the PVA α-H (δ= 4.00 ppm)

and $-CH_3$ shifts (δ= 2.00 ppm) of the purified copolymers), indicating this method is unsuitable for full reacetylation of PVA to PVAc. The fit of acetic acid volume percentage to achieved acetylation incorporation to a quadratic equation (Figure 2.10) allowed rough targeting of the DA% for a given volumetric ratio of acetic acid and water. A full summary of results are shown in Table 2.3. The polymers synthesised via Scheme 2.1 for use in the solution state SANS experiment are shown in Table 2.4.

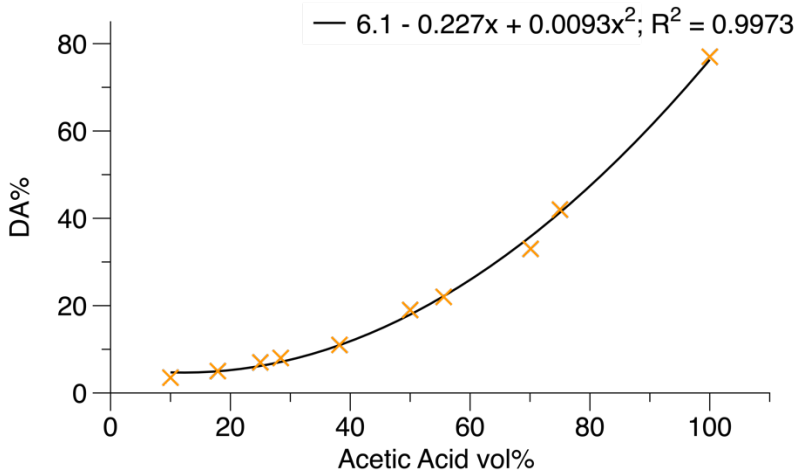


Figure 2.10: Experimentally achieved degree of acetylation as determined by $^1$H NMR spectroscopy as a function of acetic acid concentration in reacetylation solution. 100 mg/mL polymer concentration.

Table 2.3: Summary of achieved acetylation content for partially hydrolysed PVA via acid catalysed esterification with acetic acid.

| Sample | Acetic Acid Vol% | DI $H_2O$ Vol% | 3M HCl Vol% | Acetylation%[a] |
|---|---|---|---|---|
| **1** | 10 | 90 | 10 | 3.5 |
| **2** | 18 | 82 | 10 | 5 |
| **3** | 25 | 75 | 10 | 7 |
| **4** | 28 | 72 | 10 | 8 |
| **5** | 38 | 62 | 10 | 11 |
| **6** | 50 | 50 | 10 | 19 |
| **7** | 56 | 44 | 10 | 22 |
| **8** | 70 | 30 | 10 | 33 |
| **9** | 75 | 25 | 10 | 42 |
| **10** | 100 | 0 | 10 | 77 |

[a]Determined by $^1$H NMR spectroscopy.

Table 2.4: Summary of partially acetylated PVA synthesised for solution state SANS experiment. Unhydrolysed PVAc: $M_n$[a] 28,500 g mol$^{-1}$, DP 331.[a] $M_n$[b] 29,700, $M_w$[b] 37,400, Đ[b] 1.26

| **Polymer** | **Targeted DA** | **Achieved DA[a]** | **$M_n$[a] / gmol$^{-1}$** | **$M_n$[c] / gmol$^{-1}$** | **$M_w$[c] / gmol$^{-1}$** | **Đ[c]** | **Structure** |
|---|---|---|---|---|---|---|---|
| **P1** | 0% | - | 14,600 | 17,900 | 21,100 | 1.18 | 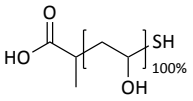 |
| **P2** | 5% | 4% | 15,100 | 20,800 | 25,100 | 1.21 | 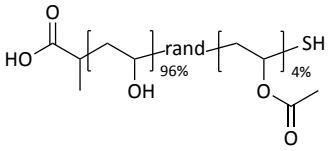 |
| **P3** | 10% | 10% | 16,000 | 23,700 | 28,800 | 1.22 | 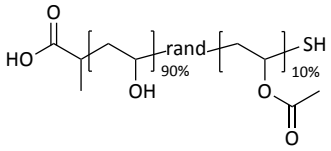 |
| **P4** | 15% | 16% | 16,800 | 32,900 | 37,400 | 1.14 | 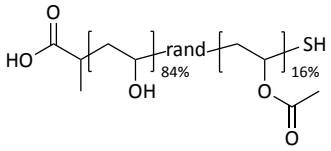 |

[a]Determined by $^1$H NMR spectroscopy. [b]Determined by THF GPC, 1 mL/min, Universal calibration. [c]Determined by aqueous GPC 10 mM $NaNO_3$, 1 mL/min, Narrow standard calibration.

Due to the inability of this method to achieve higher than 77% DA, an alternative synthetic route was required to produce the materials necessary for solid-state SANS experiments, which were predominantly acetylated. A controlled hydrolysis was employed, using dilute base to remove a small portion of pendent acetate groups from the polymer chain, resulting in a low degree of hydrolysis. Table 2.5 summarises the quantities of base added to achieve the desired DH for the experimental samples. This method still proved difficult to control, and the achieved DH slightly exceeded that of the target for some samples. However, the samples still formed a series of polymers suitable for the planned experiment. This approach produced blocks of hydroxyl groups along the chain, unlike reacetylation, which results in a random distribution of pendent groups.[50, 51] A representative hydrolysis of this kind is shown in Scheme 2.2.

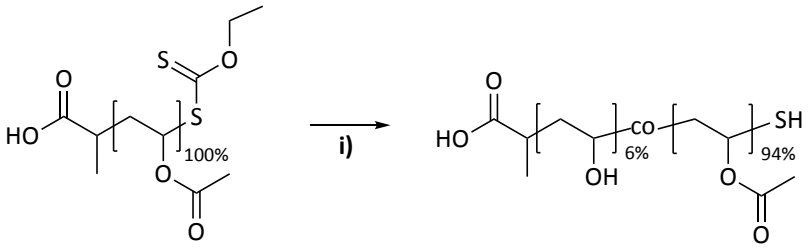


Scheme 2.2: Partial hydrolysis of PVAc. i) PVAc (300 mg) in MeOH (3 mL), NaOH (50 µL, 0.1.M), 60 °C, 16 h.

Table 2.5: Summary of partially hydrolysed PVAc synthesised for solid state SANS experiment. Unhydrolysed PVAc **P5** $M_n$[a] 28,500 g mol$^{-1}$, DP 331.[a] $M_n$[b] 28,900 $M_w$[b] 35,900 Đ[b] 1.24.

| **Polymer** | **Targeted DH** | **Volume base added / µL** | **Achieved DH[a]** | **Structure** |
|---|---|---|---|---|
| **P6** | 5% | 50 | 6% | 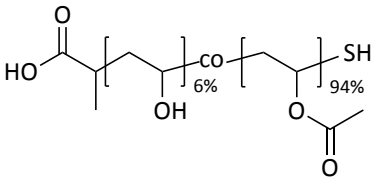 |
| **P7** | 10% | 150 | 16% | 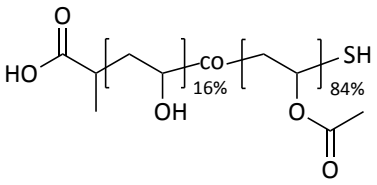 |
| **P8** | 15% | 350 | 21% | 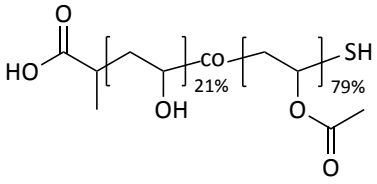 |
| **P9** | 20% | 400 | 25% | 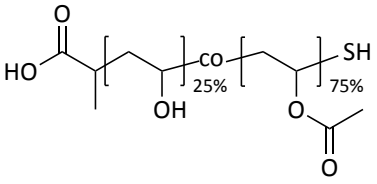 |

[a]Determined by $^1$H NMR spectroscopy. [b] Determined by THF GPC, 1 mL/min, Universal calibration.

Deuterated PVAc to blend with the above materials was synthesised in the same way as regular PVAc (Scheme 2.3), however, considerations were made to enable analysis with $^2$H NMR spectroscopy. DMF-$d_7$ was used as an internal standard to enable conversion analysis via comparison of the vinyl C-D singlet with the integral of the DMF C(O)-D resonance. NMR samples were made up in $CHCl_3$. The spectrometer was locked at the beginning of the day prior to analysis with a $CDCl_3$ sample. The shims

were set using the t=0 sample. The PET-MADIX method reported by Hakobyan *et al.*[48] also performed well with deuterated monomer, allowing the production of well controlled dPVAc (**P10**) for SANS experiments (Figure 2.11).

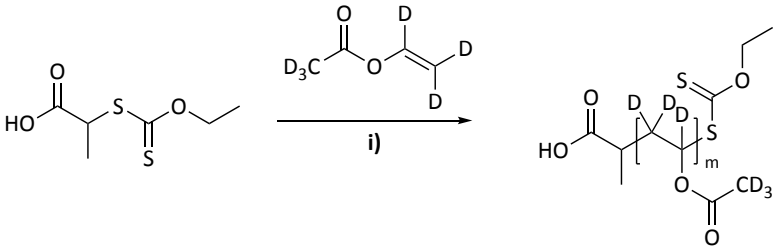


Scheme 2.3: Synthesis of dPVAc **P10** via PET-MADIX using hydrogenous chain transfer agent. i) $Bi_2O_3$, h*v* 15 W Fluorescent tube, 1010 lm, DMSO, inert atmosphere. DP: 334,[a] conversion 90%.[a]
[a]Determined by $^2H$ NMR spectroscopy.

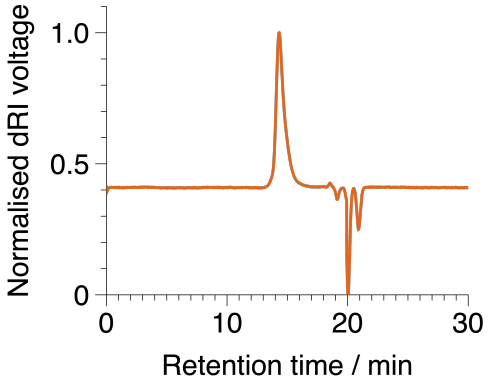


Figure 2.11: GPC chromatogram (dRI) 1 mL/min, THF, 35 °C, Triple detection with universal calibration **P10**. $M_n$: 27,900 $M_w$: 33,800 Đ: 1.21.

### 2.3.2 Solution state PVA chain dimension in relation to packaging films

An industrially relevant series of incompletely hydrolysed PVA was synthesised for analysis via SANS. The PVA series was reacetylated to the range of 100% ≥ DH ≥ 85%. Reacetylation of PVA is known to give rise to a more random structure compared to partial hydrolysis.[50, 51] All the polymers were derived from the same batch of PVAc, meaning the DP was constant between all samples, and molecular weights and Đ were well characterised. No previous report of chain dimensions has been found in the literature for a series of partially acetylated PVAs with the same DP.

The chain dimensions for a series of PVA polymers with varying degrees of acetylation and constant degree of polymerisation were investigated in a single component solution state SANS experiment. The structures are illustrated in Figure 2.12.

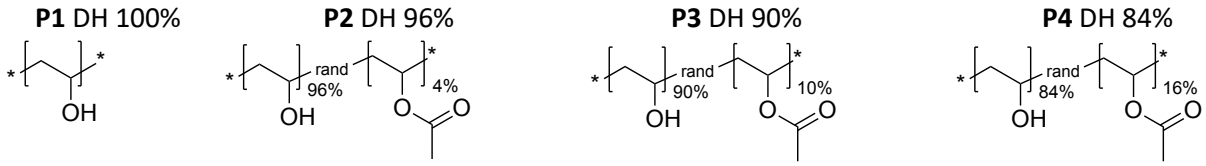


Figure 2.12: Part hydrolysed PVA series for solution state SANS experiments.

Intensity information is recorded for a 2D area corresponding to intensity in *Q* space (Figure 2.13a). The data was reduced to subtract the blank $D_2O$ cell measurements as well as apply the direct beam transmission run to absolutely scale the data. The beam stop support arms are also excluded from the reduction by a mask. Radial averaging and viewing the data on a 1D plot makes the scattering features more apparent (Figure 2.13b). The 1D data can then be fit to a model.

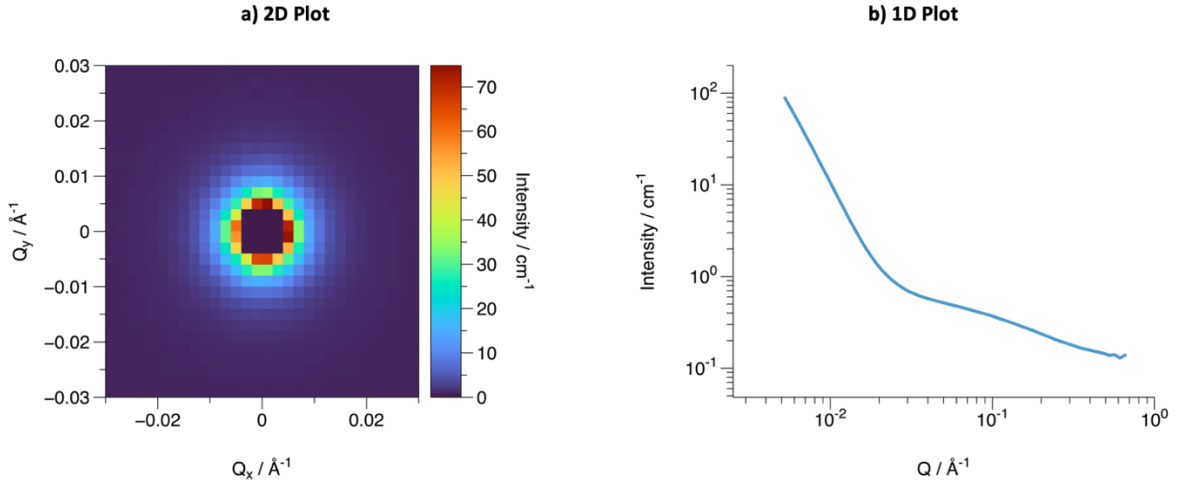


Figure 2.13: a) 2D intensity map of part acetylated PVA solution. Note that the beamstop in the centre of the detector causes the black square (zero intensity detected) at $Q \sim 0$ Å$^{-1}$ ; b) 1D radial intensity average of part acetylated PVA solution.

All SANS plots for this sample series are shown below, with Figure 2.14 grouping by DH and Figure 2.15 grouping by concentration to highlight the impact of each parameter on scattering profiles. It is observed that for all degrees of hydrolysis the scattering observed for all concentrations did not resemble a typical polydisperse Gaussian coil model (Figure 2.5) with a plateau in intensity at low *Q*.

Instead, two correlation lengths are observed. A high intensity feature is observed at low *Q*, which appears to dwarf subtle Debye scattering arising from Gaussian polymer chains in solution at higher *Q* values. This result was unexpected and suggests there is long range order present in the sample. This kind of scattering is typically observed in gel systems, with high intensity low *Q* scattering indicative of large structures within the system.[52]

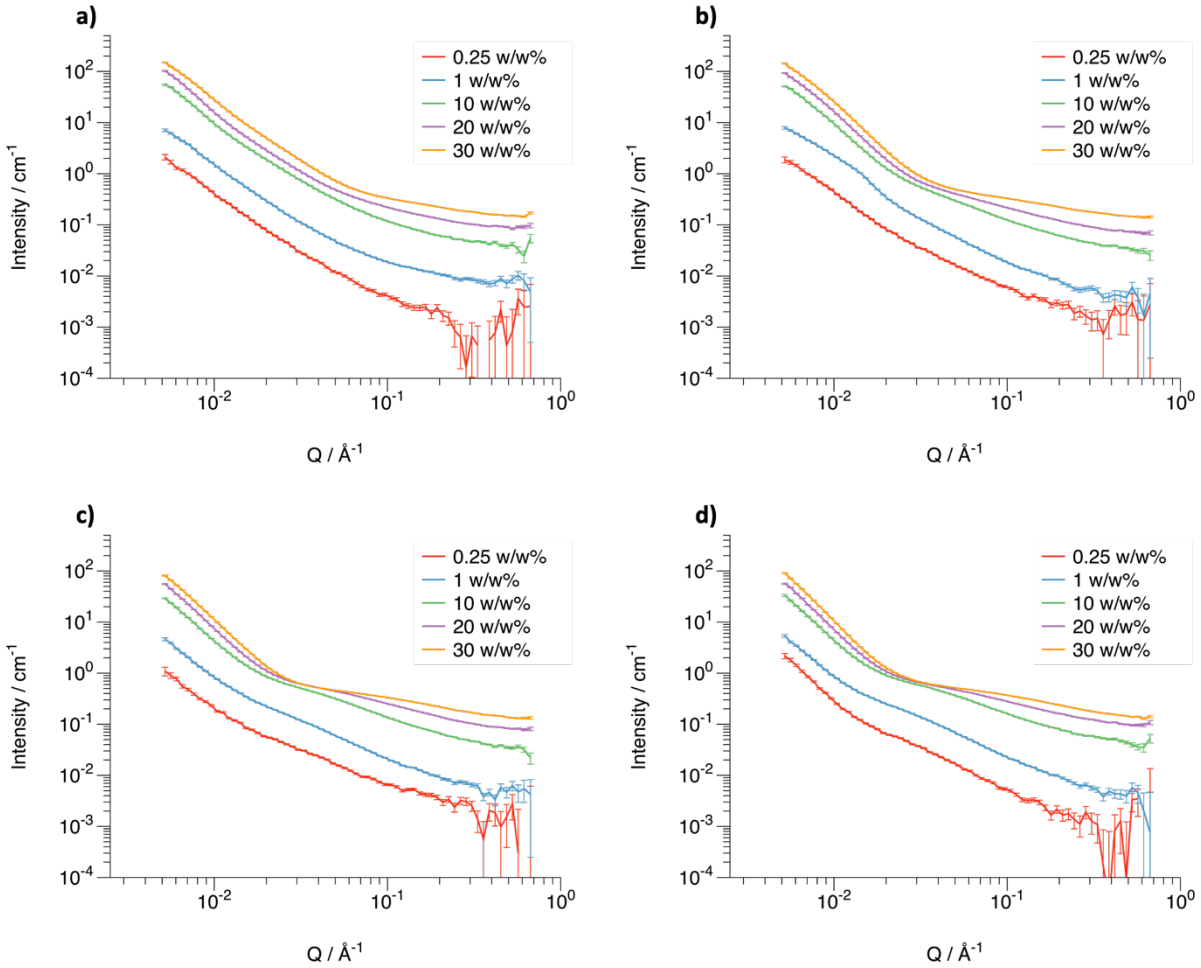


Figure 2.14: Concentration dependence of SANS intensity plots grouped by DH%. a) **P1** DH 100%, b) **P2** DH 95%, c) **P3** DH 90%, d) **P4** DH 85%.

The concentration grouped dataset is seen to be of a lower background at lower polymer concentration which is due to the higher amount of $D_2O$ in these samples. It is noted that the 0.25 w/w% dataset is of significantly poor quality due to the low polymer concentration, and error bars are large at high *Q* values. It is clear from observation, however, that as concentration is increased, the low

Q scattering feature increases in gradient, implying a change in the nature of the structural properties of the aggregate. This observation is explored further once the data is fitted.

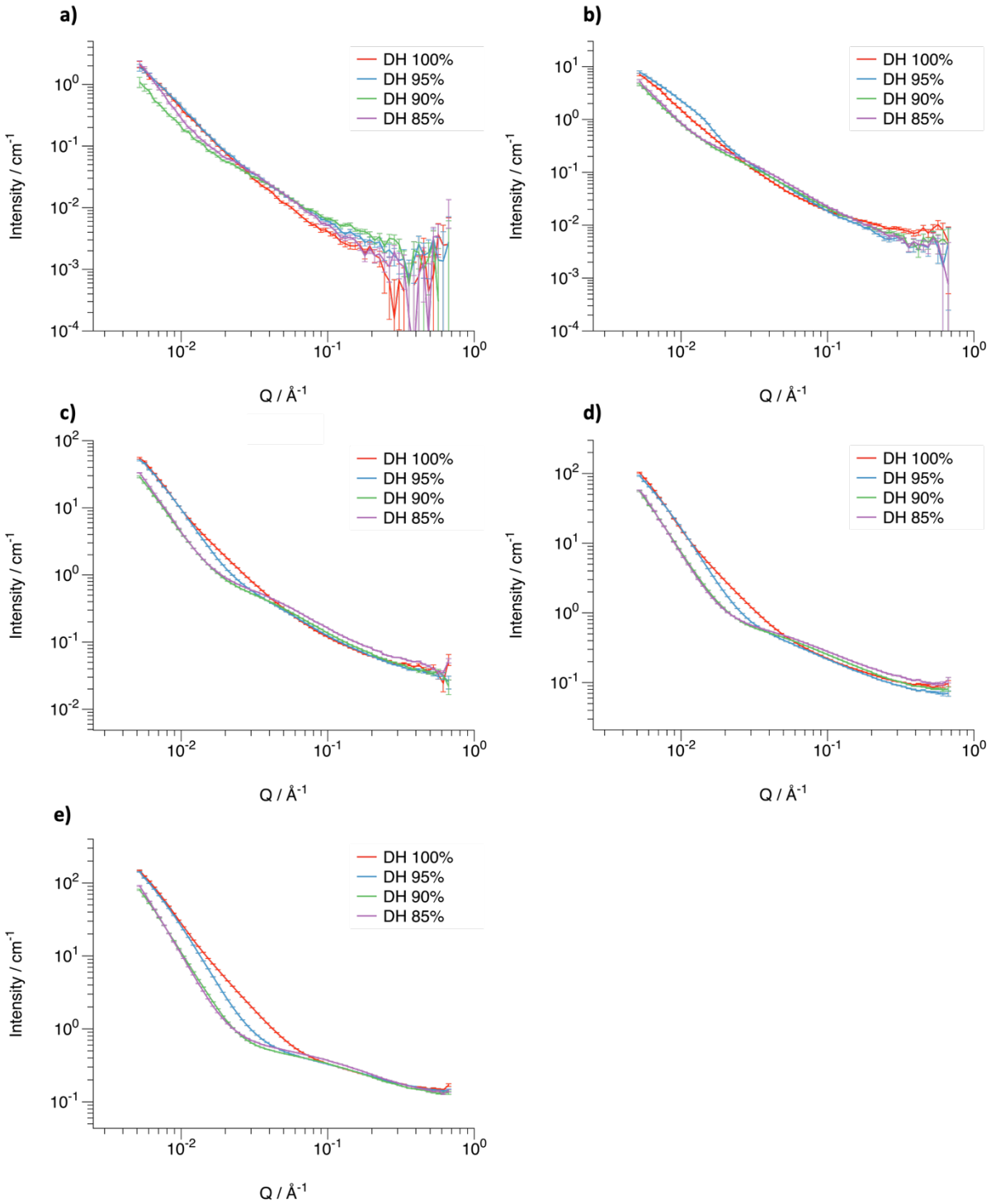


Figure 2.15: Degree of hydrolysis dependence of SANS intensity plots grouped by solution concentration. a) 0.25 w/w%, b) 1.0 w/w%, c) 10 w/w%, d) 20 w/w%, e) 30 w/w%.

To enable the data to be fit, a combined power law and polydisperse Gaussian coil model was created to capture both the high *Q* scattering from polymer chains as well as the low *Q* scattering from larger order artefacts in the system. The models were added together in the SasView software[27] to create a custom model of the form:

$$I(Q) = \text{scale}_a \cdot I_0 \cdot S(Q) + \text{scale}_b \cdot Q^{-\text{power}} + \text{background} \qquad \text{(Equation 29)}$$

The red component is from the polydisperse Gaussian coil, and the blue component is from the power law model. To allow the variation of the contributions from each component of the mode, two scale factors are included which are independently floatable. The experimental data can be fit well to the combined model as shown from Figure 2.16 below. Fitting the data to the polydisperse Gaussian coil was able to be achieved if the fit range was limited to exclude the low *Q* scattering feature, however, fits were of greater quality when the combined model was utilised. Contributions of each component of the combined fit are shown in Figure 2.17.

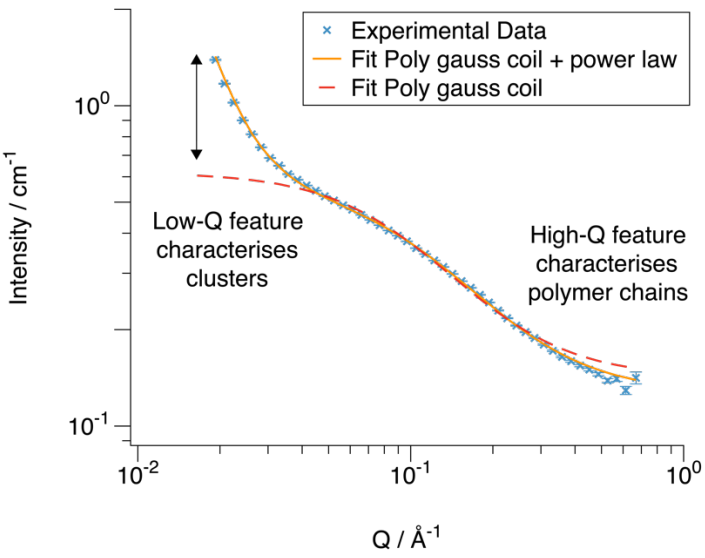


Figure 2.16: Comparison of experimental SANS data from 30 w/w% in $D_2O$.
**P4** PVA DH 85%, expected polydisperse Gaussian coil model fit for polymer chains in solution (red dashed line) and combined polydisperse Gaussian coil + power law fit (solid orange line) emphasising the deviation from the predicted scattering at low Q.

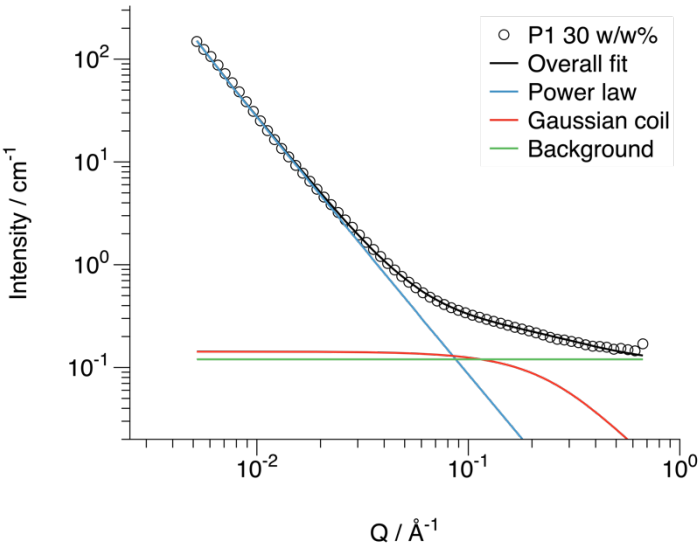


Figure 2.17: Fit contributions shown for a combined power law + polydisperse Gaussian coil fit to **P1** 30 w/w%. Power law contribution shown in blue, Gaussian coil contribution shown in red, background contribution shown in green.

It is observed that as the degree of hydrolysis (DH) increases from 85% (**P4**) to 100% (**P1**), the gradient of the low Q scattering decreases for all solution concentrations, typically shifting from around 3.4 to 2.5 (Figure 2.18). This trend in scaling exponents suggests that interfacial roughness increases with higher DH, as indicated by the lower exponent values—generally, a lower exponent signifies a rougher surface. This change in roughness may be linked to an increase in hydrophobicity as the degree of hydrolysis decreases (and acetylation increases), leading to less favourable interactions at the interface. A sharper and more defined interface might be expected with lower hydrolysis, as a less compatible phase boundary tends to form between the hydrophilic and hydrophobic regions. This is visualised in Figure 2.19, where a smoother, sharper interface is seen in systems with higher acetylation. The transition between phases could become more abrupt, contributing to the lower scattering exponents. This sharpness could reflect a more distinct separation between phases, with the hydrophobic regions possibly forming more compact, organised structures at the interface, as opposed to the more diffuse, disordered interface observed in systems with higher hydrolysis. These changes in interface sharpness could further influence the material's overall structural properties and behaviour.

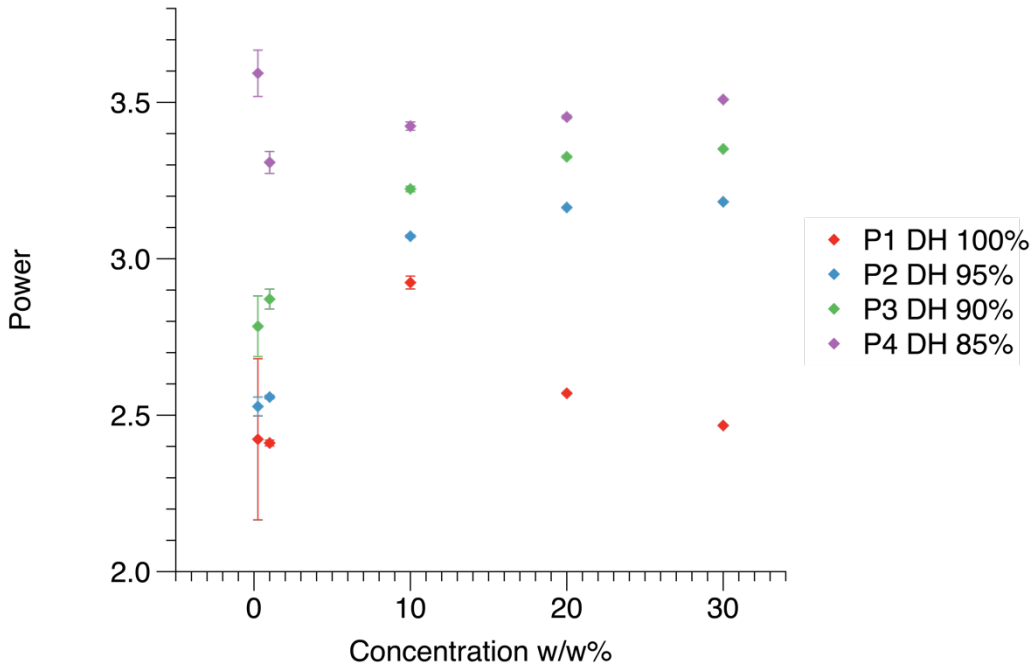


Figure 2.18: Variation of SANS derived power law exponent with concentration at various DH.

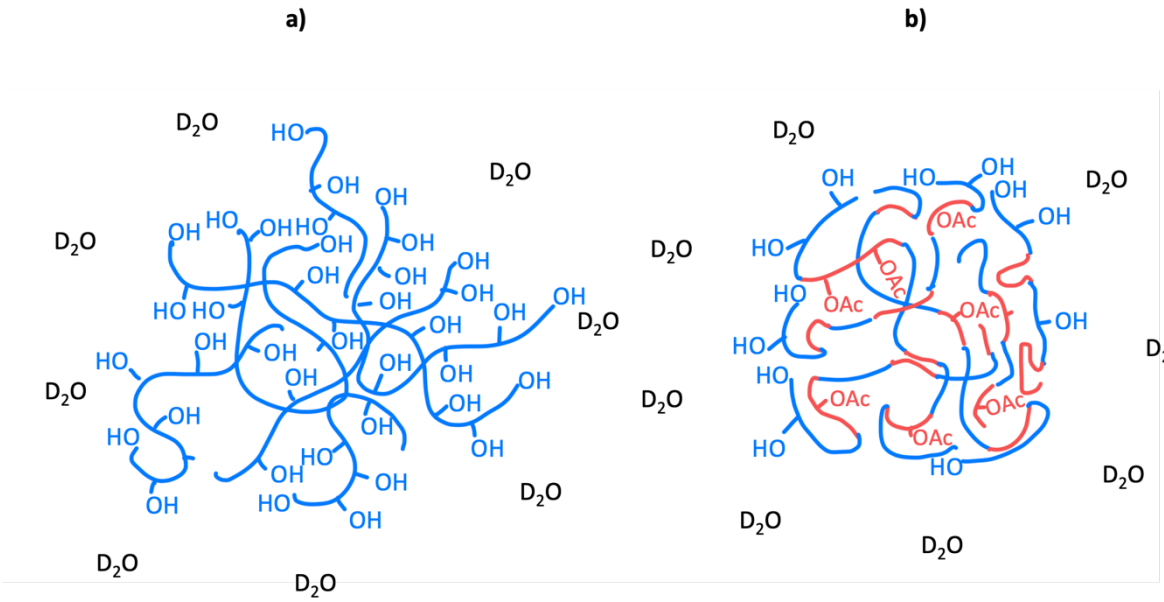


Figure 2.19: Cartoon of a) PVA DH 100% in $D_2O$ solution; b) PVA/c DH <100% in $D_2O$ solution. A more diffuse structure is shown for PVA, whereas a more compact smooth structure is depicted for partially hydrolysed PVA.

The trend for the fully hydrolysed (**P1** DH 100%, Figure 2.18 red plot) would appear to contain an outlier in exponential value at 10 w/w% concentration. Excluding that point, there appears to be little impact of concentration on the exponential for this sample, remaining at around 2.5 for all

concentrations, implying that particle smoothness is unaffected by concentration. This could be the result of some kind of association or aggregation within the sample.

For other partially acetylated samples in the series, there appears to be an increase in the exponent as concentration increases, with the greatest concentration dependence observed for the most partially acetylated sample (**P2** DH 95%). One possible explanation is that the low degree of acetylation in the DH 95% sample may result in particles that appear rougher at low concentrations, where mostly -OH bearing chains form loosely connected particles in the $D_2O$ medium (Figure 2.20a). The small amount of acetylation could be arranged to minimise interactions with the aqueous solvent. As concentration increases, the particles may pack more tightly, leading to closer packing of the diffuse PVA chains and a smoother overall surface (Figure 2.20b and c). However, this change in exponent could also stem from factors such as variations in surface characteristics (*e.g.* smoothness/diffusivity of the corona) or particle size distribution, which could evolve as concentration changes.

As DH decreases and the polymer becomes more solvent-phobic, it can minimise contact area with the solvent by forming sharper interfaces and by aggregating. This phase segregation is likely to occur at lower solution concentrations as the DH decreases (*i.e.* acetate content increases) due to the reduced availability of -OH regions. The random placement of acetate groups on the polymer chain, resulting from the synthetic method, may further contribute to why at lower DH the exponential value remains high for all concentrations. One would expect to observe that at low polymer solution concentrations the aggregates are not present. However, even at low solution concentrations of 0.25 w/w% the high intensity low *Q* scattering is present, indicating there are still large order structures in solution. It may be that attractive interactions between polymer chains persists at low concentrations.

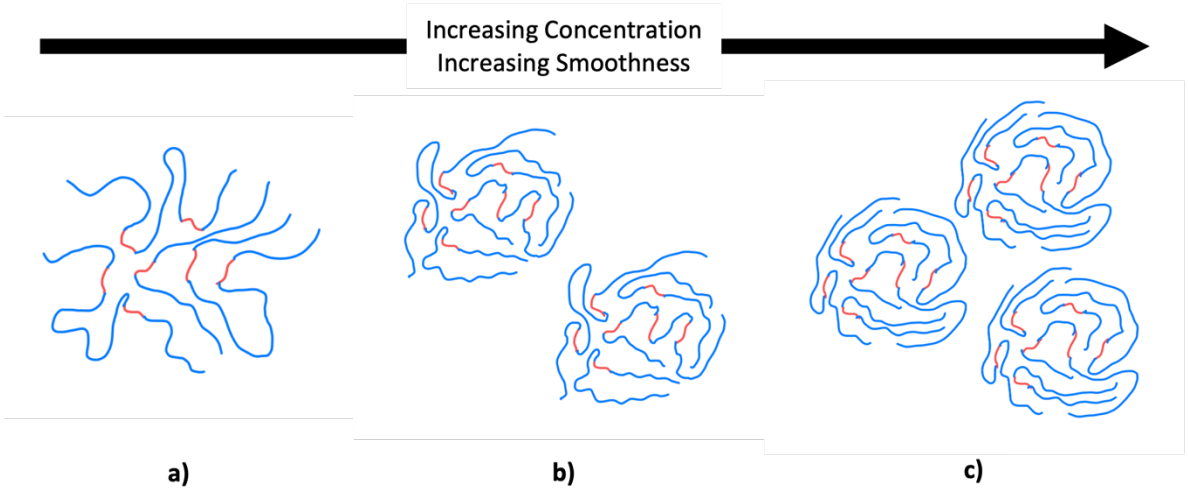


Figure 2.20: Depiction of increasing particle smoothness observed for partially hydrolysed PVA. **a)** low concentration, diffuse hydrophilic regions present, **b)** medium concentration, -OH bearing regions less diffuse, **c)** high concentration, sharp interface between aggregates.

The $R_g$ values were also determined from the fit data (Figure 2.21). As the DH increases, there is a general decrease in the $R_g$ of individual polymer chains, which can be attributed to the removal of bulky acetate groups, allowing the chains to occupy a smaller volume. Interestingly, despite the hydrophobic nature of the acetate groups, which might be expected to cause the chains to collapse due to hydrophobic interactions, this collapse is not observed. Instead, the introduction of acetyl groups, due to their steric bulk, prevents the polymer chains from packing as closely as they would with hydroxyl (-OH) groups, inhibiting the chains from folding into crystal nuclei and resulting in poorer packing ability and a reduction in crystallinity.

Furthermore, the introduction of additional acetate groups likely disrupts the network of hydrogen bonds that would normally form between the -OH groups on adjacent polymer chains. These hydrogen bonds are crucial for stabilising the chain structure and facilitating crystal formation. By replacing -OH groups with -OAc groups, the potential for hydrogen bonding is reduced, further hindering the chains' ability to align and pack into a crystalline lattice. This disruption of hydrogen bonding, alongside the steric effects, likely contributes to the overall decrease in crystallinity. However, it should be noted that

these interpretations are speculative, and further investigation would be required to confirm the exact mechanisms at play.

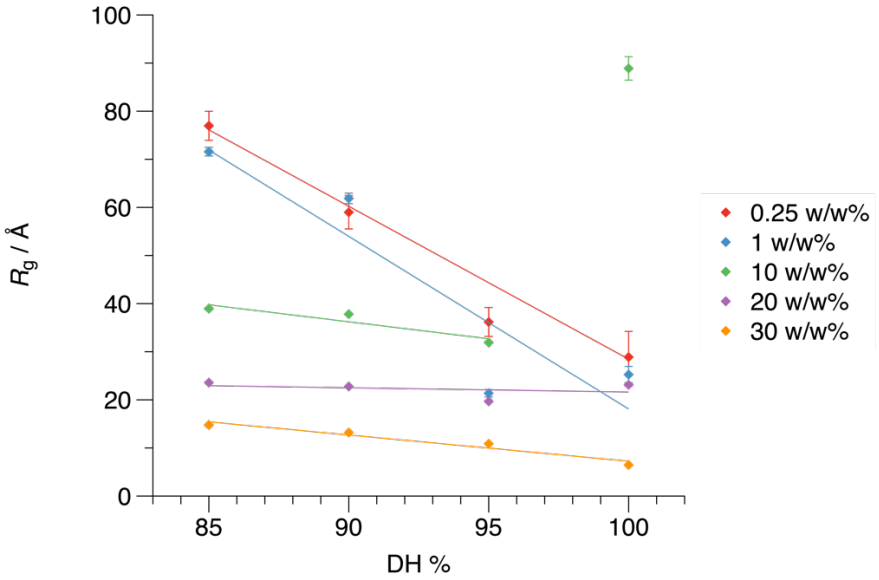


Figure 2.21: Variation of SANS derived $R_g$ with DH at various concentrations. DH 100% 10% w/w outlier excluded from linear fits.

At high concentrations >1 w/w% it appears that DH has little impact on the $R_g$ for each concentration series. This would imply that at these higher concentrations, polymers are no longer behaving as single chains in solution but are a part of a larger order structure. As concentration is increased, the average $R_g$ decreases for all DH samples, to the point at which the value is unrealistically low.[53] It is hypothesised that at this high concentration regime the reported $R_g$ is actually the inter-cluster distance, and not the isolated polymer chain dimension. The results are summarised in Table 2.6 below.

Table 2.6: Summary of Power and $R_g$ extracted from fitting PVA solution SANS data.

| Sample | Temp / °C | DH% | Conc w/w% | Power | Error Power | $R_g$ / Å | Error $R_g$ / Å |
|---|---|---|---|---|---|---|---|
| **P1** | 25 | 100 | 0.25 | 2.423 | 0.257 | 28.9 | 5.3 |
| | 25 | | 1 | 2.411 | 0.009 | 25.3 | 1.7 |
| | 25 | | 10 | 2.924 | 0.021 | 88.9 | 2.4 |
| | 40 | | 10 | 3.173 | 0.054 | 129.0 | 7.5 |
| | 25 | | 20 | 2.570 | 0.003 | 23.1 | 0.3 |
| | 25 | | 30 | 2.467 | 0.001 | 6.5 | 0.1 |
| **P2** | 25 | 95 | 0.25 | 2.528 | 0.030 | 36.2 | 3.0 |
| | 25 | | 1 | 2.558 | 0.006 | 21.4 | 0.8 |
| | 25 | | 10 | 3.072 | 0.005 | 31.9 | 0.2 |
| | 40 | | 10 | 3.008 | 0.007 | 35.6 | 0.3 |
| | 25 | | 20 | 3.164 | 0.003 | 19.7 | 0.1 |
| | 25 | | 30 | 3.182 | 0.002 | 10.9 | 0.1 |
| **P3** | 25 | 90 | 0.25 | 2.784 | 0.097 | 59.0 | 3.5 |
| | 25 | | 1 | 2.871 | 0.032 | 61.9 | 1.1 |
| | 25 | | 10 | 3.223 | 0.009 | 37.8 | 0.2 |
| | 40 | | 10 | 3.250 | 0.030 | 44.8 | 0.5 |
| | 25 | | 20 | 3.326 | 0.004 | 22.8 | 0.1 |
| | 25 | | 30 | 3.351 | 0.003 | 13.2 | 0.1 |
| **P4** | 25 | 85 | 0.25 | 3.593 | 0.074 | 77.0 | 3.0 |
| | 25 | | 1 | 3.308 | 0.035 | 71.6 | 0.9 |
| | 25 | | 10 | 3.424 | 0.013 | 39.0 | 0.2 |
| | 25 | | 20 | 3.453 | 0.006 | 23.6 | 0.1 |
| | 25 | | 30 | 3.509 | 0.003 | 14.8 | 0.0 |

Hammouda *et al.* have investigated similar examples of clustering for polyethylene oxide (PEO) and polyethylene glycol (PEG) systems.[54-56] High intensity low-*Q* scattering is observed for these polymers, as well as high-*Q* scattering for polymer chains in solution. It is hypothesised that the end groups of the PEG/PEO polymers play a role in the aggregation behaviour; if a hydrophilic -OH group is present, the end group is well solvated in aqueous media, whereas if an -OMe group is present, it arranges to minimise interactions with solvent molecules and shields near a $CH_2$ group, resulting in the network behaviour. In a similar way, PVA has hydrophobic $CH_2$ and CH groups, and hydrophilic -OH groups, as well as hydrophobic -OAc groups in partially hydrolysed samples. Additionally, the scattering from polymers that associate primarily through their end groups resembles that of star polymers, which scatter in a manner not qualitatively different from simple linear polymers.[57] It is also observed for

PEG/PEO systems that varying the concentration influences the aggregation, whereas for the PVA system, there appear to be large aggregates present even at low concentrations.

Even when the samples were measured on another neutron scattering instrument, SANS2D, in a 12 m sample-to-detector configuration, which can reach $Q_{min}$ of 0.0015 Å$^{-1}$, the behaviour persisted (Figure 2.22, red plots). This suggests that the SANS method was only capturing the tail of these large-scale structures. This result indicates that the low $Q$ feature is larger than the practical measurable range of SANS. Consequently, alternative techniques, such as DLS, were employed to further investigate the nature of these clusters.

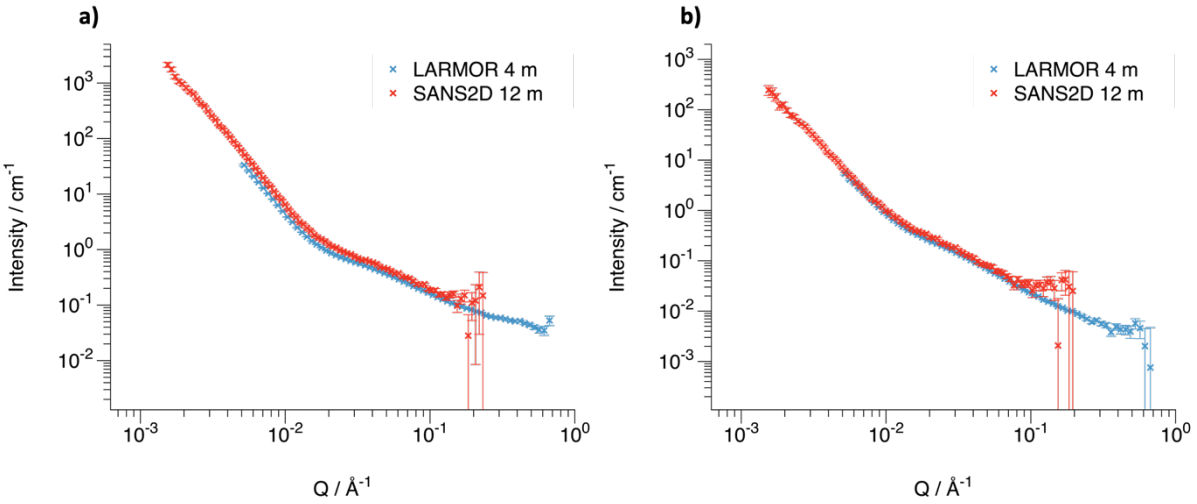


Figure 2.22: Comparison of LARMOR and SANS2D SANS data of a) 10 w/w% **P4** DH 85% PVA/c and b) 1 w/w% **P4** DH 85% PVA/c. LARMOR sample to detector distance 4 m, SANS2D sample to detector distance 12 m. The slight difference in intensity between the two instruments likely arises as a result of slightly different solution concentrations as measurements were taken on different days using freshly made solutions.

### 2.3.3 Temperature dependence of polymer chain dimensions in solution

For some samples in the series, analysis was carried out at an elevated temperature of 40 °C. It was observed that for all samples, the $R_g$ slightly increased with increased temperature, while the low-$Q$ exponential remained unchanged (Figure 2.23 and Table 2.7). This behaviour can be explained by considering the crystallinity of the system. As temperature increases, it begins to disrupt crystallinity

between chains, allowing them to rearrange and become more solvated and diffuse in nature, occupying a larger area in solution. This is consistent with the general trend observed for many polymers, whether semi-crystalline or not, where an increase in temperature leads to a corresponding increase in $R_g$, as the polymer chains experience greater freedom of movement and expansion due to overcome intermolecular forces at higher temperatures.[58, 59]

Interestingly, PVA does not exhibit lower critical solution temperature (LCST) behaviour like PEO, which undergoes phase separation at higher temperatures. Instead, PVA tends to display upper critical solution temperature (UCST) behaviour, where it becomes more soluble as temperature increases,[47] supporting the observation of a slightly larger $R_g$ at elevated temperatures. This effect is similar to that observed when varying the DH, as lower DH samples are less crystalline and exhibit a larger $R_g$ across all concentrations compared to more hydrolysed samples at the same concentrations. It should be noted that modified polyvinyl alcohols copolymers do exhibit LCSTs.[49]

This temperature-dependent behaviour of PVA is distinct from that of other water-soluble polymers like PEO, which become less miscible with water as temperature increases. For example, Hammouda showed that the single-chain correlation length (size) of PEO decreases with increasing temperature, while another correlation length (cluster size) increases.[54] Compared to his data, the PVA samples are remarkably insensitive to temperature at the range studied, maintaining a consistent increase in $R_g$ without any significant changes in other structural parameters. Additionally, as temperature increases, the density of the polymer solution may decrease due to thermal expansion. However, the observed increase in $R_g$ for PVA at elevated temperatures appears to be more influenced by the structural rearrangement of the polymer chains than by any significant change in the solution's density.[59, 60]

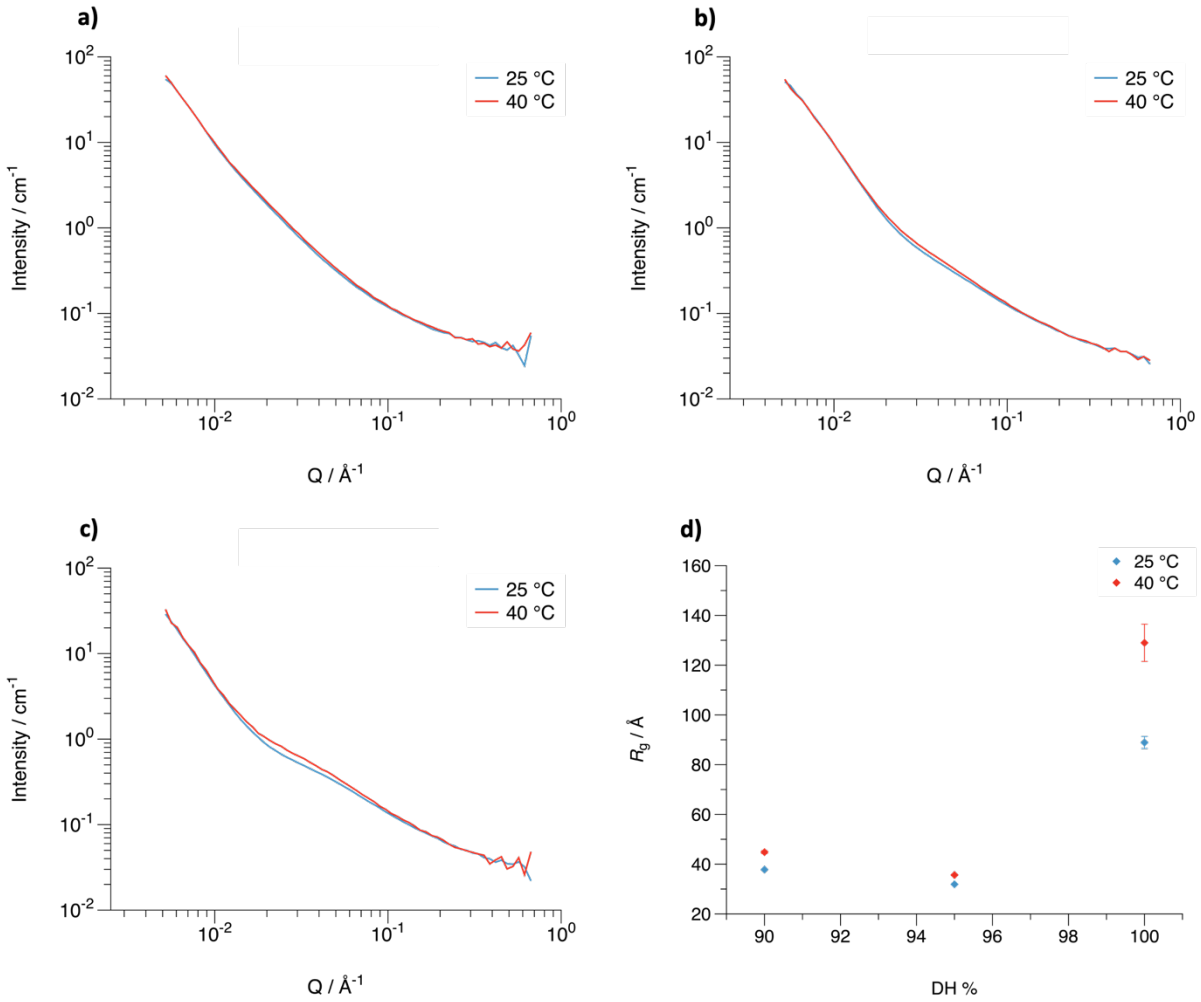


Figure 2.23: SANS scattering intensity plots of various DH PVA/c at 10 w/w% concentration at 25 and 40 °C – a) **P1** DH 100%, b) **P2** DH 95%, c) **P3** DH 90%; d) Fit generated $R_g$ values. Error bars omited for clarity on SANS plots.

Table 2.7: Comparison of Power and $R_g$ obtained from fits of 25 and 40 °C of selected 10 w/w% samples.

| Sample | Temp / °C | DH | Power | Error Power | $R_g$ / Å | Error $R_g$ / Å |
|---|---|---|---|---|---|---|
| **P1** | 25 | 100 | 2.924 | 0.021 | 88.885 | 2.424 |
| | 40 | | 3.173 | 0.054 | 128.990 | 7.499 |
| **P2** | 25 | 95 | 3.072 | 0.005 | 31.898 | 0.199 |
| | 40 | | 3.008 | 0.007 | 35.643 | 0.305 |
| **P3** | 25 | 90 | 3.223 | 0.009 | 37.821 | 0.175 |
| | 40 | | 3.250 | 0.030 | 44.829 | 0.544 |

### 2.3.4 Dynamic Light Scattering (DLS)

To better study the nature of the larger structures in solution, DLS analysis was carried out on the samples (Figure 2.24). All polymers analysed in the SANS measurement were recovered via

lyophilisation and made up to 1 w/w% solutions in MilliQ water and passed through a 0.2 µm polyether sulfone (PES) syringe filter upon loading into the cuvette. Commercial PVA was also analysed to compare with the samples prepared via PET-MADIX polymerisation.

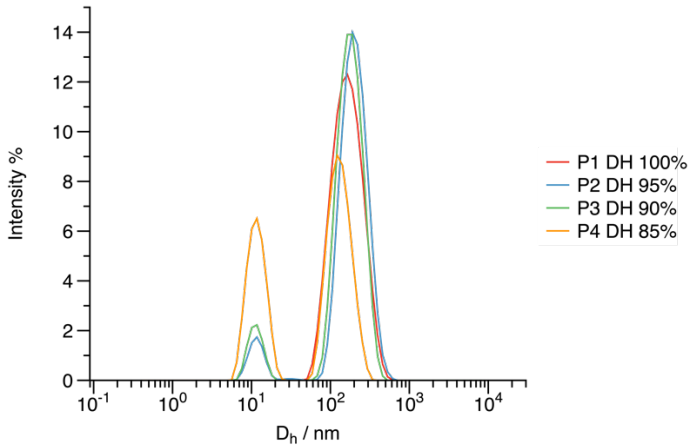


Figure 2.24: DLS intensity plots of part hydrolysed PVA series **P1** – **P4** analysed via SANS. 1 w/w% polymer solutions measured at 25 °C.

All polymers analysed exhibited a large particle size, approximately 200 nm in diameter. Additionally, partially acetylated polymers—unlike fully hydrolysed PVA—displayed a smaller distribution, around 10 nm in diameter, which aligns with the predictions from SANS data. The intensity of the 10 nm peak was observed to increase as the degree of hydrolysis (DH) decreased. This suggests that, in more acetylated samples, the larger structures constitute a smaller proportion of the overall sample compared to those with lower acetyl content. This observation further supports the hypothesis that polymers with higher acetylation are less crystalline and less capable of forming large aggregates compared to those with higher hydroxyl content and lower acetylation.

To further investigate, commercial PVA (Sigma Aldrich, 89 – 98 kDa, DH 99%+) was analysed as a 1 w/w% solution in D2O using SANS2D. The results indicated that this commercial PVA did not exhibit the characteristic low-Q scattering feature observed in the other samples. Instead, the data was well fitted by a polydisperse Gaussian coil model, without the need for a power law model (Figure 2.25a). The polymer's $R_g$ was determined to be approximately 200 Å by fitting the SANS data (Figure 2.25a),

whereas DLS reports a hydrodynamic diameter of around 15 nm (150 Å) (Figure 2.25b), leading to a hydrodynamic radius of 7.5 nm (75 Å). It is unlikely that the commercial PVA contains a carboxyl (COOH) end group, as no chain transfer agents are used in the synthesis of this commercial PVA. Therefore, it is expected that the polymer contains only initiator end groups, likely from azo or peroxide fragments, rather than COOH groups.

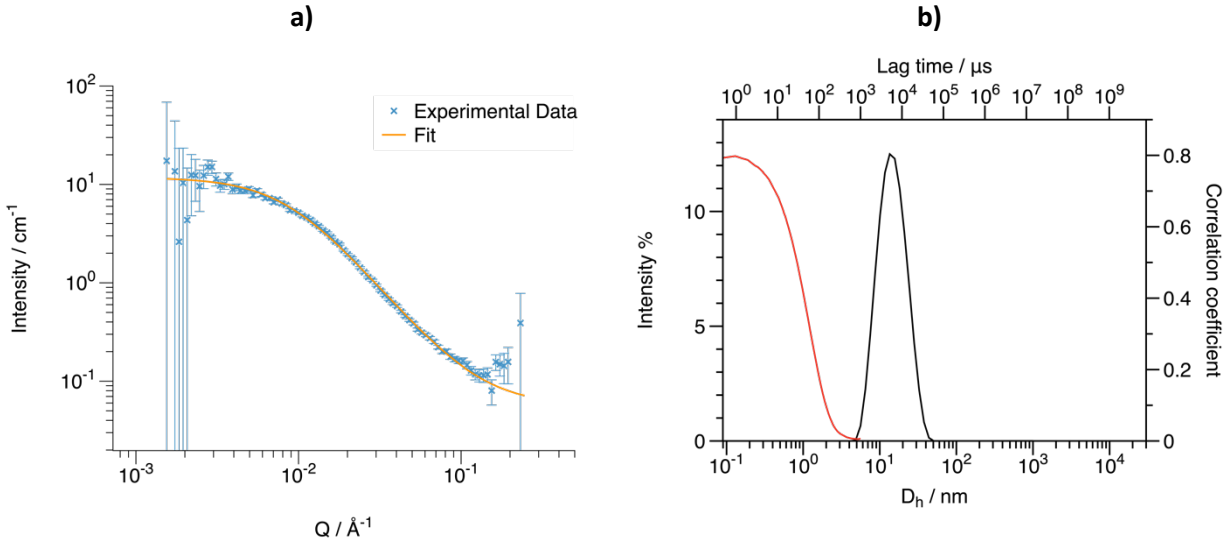


Figure 2.25: 1% w/w commercial PVA 89 – 98 kDa 99%+ DH, 25 °C a) SANS2D SANS data with fit to polydisperse Gaussian coil model, showing no low Q scattering observed. b) DLS intensity plot and corellogram showing particle sizes in the order of 10 nm.

The polymers used in this study have carboxylic acid end groups (Figure 2.26a). To investigate the impact of these end groups, a new PVA without a carboxylic acid end group was synthesised (**P1-iso**), following reports by Hammouda *et al.* that highlighted the influence of end groups on aggregation behaviour in PEG/PEO systems analysed by SANS. The new PVA was synthesised to match the original PVA closely in terms of molecular weight and Đ (Figure 2.26b). To isolate the effect of the end group, only fully hydrolysed PVA was examined. The isopropyl-terminated PVA (**P1-iso**) was analysed exclusively via DLS.

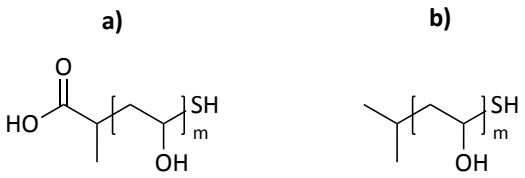


Figure 2.26: Original PVA **P1** studied in the SANS experiment, b) non carboxylate containing **P1-iso** to investigate end group on clustering behaviour. DP a) =330, DP b)= 282.

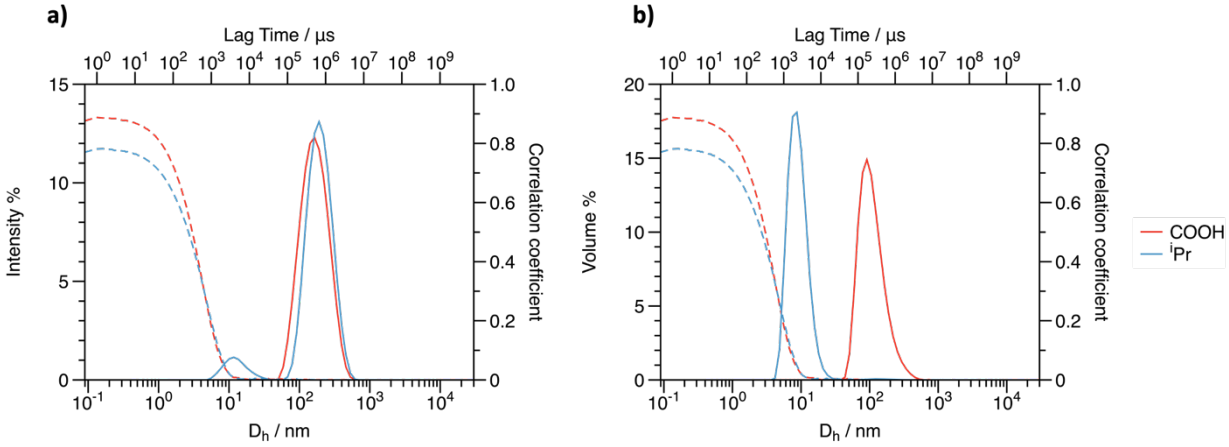


Figure 2.27: a) Intensity profile of **P1-iso** (blue) compared to COOH-PVA **P1** (red) with corellogram; b) volume profile of **P1-iso** (blue) compated to COOH-PVA **P1** (red) with corellogram (dashed lines). 1 w/w% polymer solutions measured at 25 °C.

DLS intensity (Figure 2.27a) and volume (Figure 2.27b) plots of both polymers show the persistence of the large structures in the range of 100 – 200 nm for **P1-iso**, as well as a new lower size observed indicating smaller particles also present in the system around 10 nm in diameter, indicating individual polymer chains are observable. The volume contribution from the larger component in the intensity plot is so small (<0.001%) that it is no longer displayed due to the sixth power relationship intensity scattering has relative to the number of particles in the sample (Equation 24), while volume contributions only have a third power relationship to intensity (Equation 23). It would be desirable to also complete this analysis with SANS however we can conclude that there appears to be some influence of end groups on the dimensions of polymer particles in solution.

The structure of the hydrogen bonding network within the sample can be hypothesised to take the following form (Figure 2.28), with hydrogen bonding possible between pendent hydroxyl groups (Figure 2.28b) as well as the chain terminal carboxylic acid group (Figure 2.28a and c). One can imagine

that where the number of repeat units, m, is large, the opportunity for inter and intra chain bonding becomes large. When considering the case of the $^{i}$Pr PVA, only pendent – pendent interactions are plausible (Figure 2.28e), which may explain the appearance of the secondary distribution in the intensity plot corresponding to smaller particles in solution of approximately 10 nm.

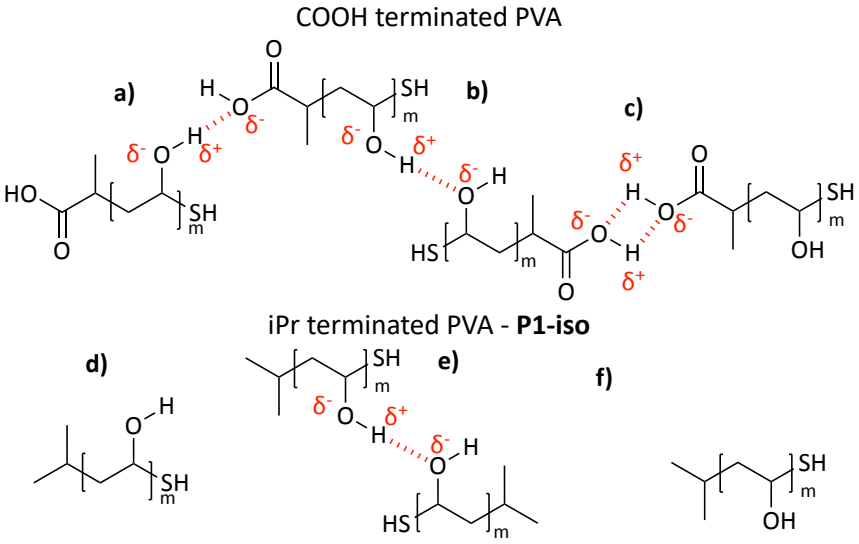


Figure 2.28: Proposed hydrogen bonding network with multiple options of bonding for COOH terminated PVA **P1**: **a)** pendent – terminus, **b)** pendent – pendent and **c)** terminus – terminus dimer; and for $^{i}$Pr terminated PVA **P1-iso** where terminus hydrogen bonding is removed **d)** and **f)**. **e)** only pendent – pendent hydrogen bonding remains.

### 2.3.4.1 Concentration dependence of PVA solutions on aggregate size

Comparing partially hydrolysed PVA (**P3**, DH 90%) at 1 and 10 w/w% concentrations via DLS revealed that increasing concentration of polymer in solution results in a larger particle presence in the order of 2000 nm diameter (Figure 2.29a). It would appear that as concentration is increased, the size of the polymer cluster also increases and is now outside the size window accessible via SANS even with low *Q* instruments such as SANS2D. Volume distributions (Figure 2.29b) of the same samples show that the dominant species in the solution relative to volume are the ~10 nm particles for the 1 w/w% and the 2000 nm particles in the 10 w/w% sample. It should be noted that the sample at 10 w/w% concentration is reaching the limits of the DLS instrument due to the high polymer concentration increasing the probability of scattered light being subsequently rescattered by other particles in the sample. However, it is crucial to be very careful about any assumptions regarding viscosity, just as much

as with multiple scattering effects. Consideration of the limits and validity of the DLS method is essential for accurate interpretation of the results.

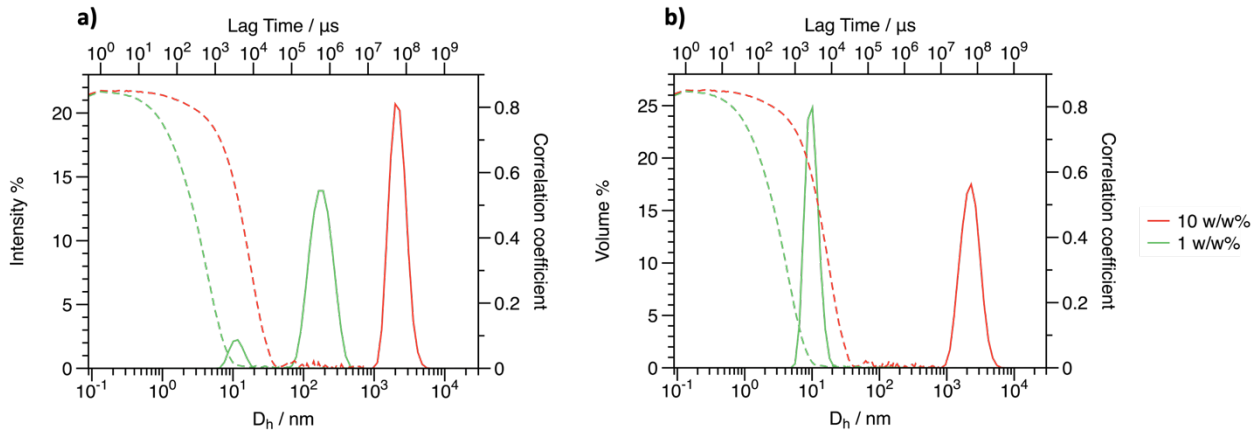


Figure 2.29: a) DLS Intensity trace and b) volume trace of part acetylated PVA DH 90% **P3** at 1 w/w% (green trace) and 10 w/w% (red trace) with corresponding corellograms (dashed lines).

### 2.3.4.2 Disruption of hydrogen bonding with guanidinium chloride

To test the hypothesis that polymer clusters were formed as a result of inter- and intramolecular hydrogen bonding, fully hydrolysed PVA (**P1**) samples were made up in both MilliQ $H_2O$ and also 12M guanidinium chloride (GuHCl). Typically, these high concentrations are utilised in biochemistry research to ensure full disruption of hydrogen bonds present. GuHCl is a strong protein denaturant that disrupts hydrogen bonding by itself being a strong hydrogen bond donor.[61] In protein samples it is used to disrupt the folding structure resulting in randomly coiled peptide chains. In this instance it was hoped that it would competitively bind to pendent hydroxyl groups, preventing them from forming hydrogen bonds between themselves and other polymer chains (Figure 2.30). It is shown that the addition of GuHCl at room temperature reduces the scattering intensity correlated to the largest particles in the sample but does not completely eradicate them (Figure 2.31a). The formation of a new peak of low particle diameter >1 nm appears. Increasing the temperature to 60 °C was found to entirely remove the 100 nm scattering particles from the sample (Figure 2.31b), with only two peaks corresponding to sub nanometre and ~ 10 nm particles present.

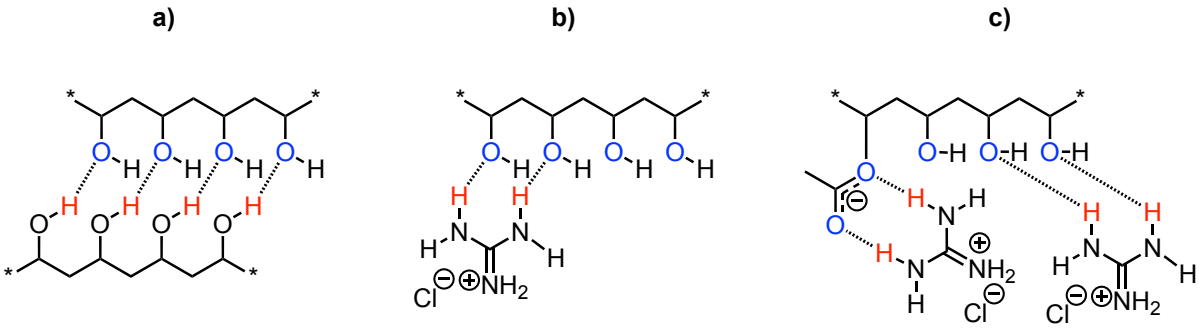


Figure 2.30: a) proposed formation of PVA interchain hydrogen bonding which is thought to be responsible for aggregates observed in SANS and DLS; b) Interaction of GuHCl with PVA; c) Interaction of GuHCl with PVA/c. *N.B.* HCl omited for clarity.

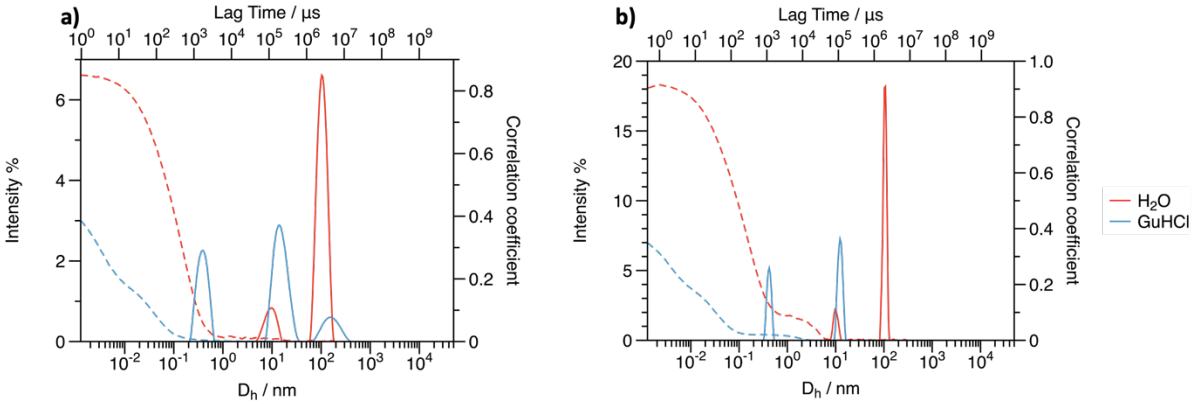


Figure 2.31: DLS intensity profiles of 1 w/w% **P1** at a) 25 °C and b) 60 °C in Milli Q $H_2O$ (red trace) and 12M GuHCl (blue trace) with corresponding corellograms (dashed lines).

The results indicate that hydrogen bonding plays a significant role in the formation of large polymer clusters. The reduction in scattering intensity with the addition of GuHCl, coupled with the complete removal of larger particles at elevated temperatures, supports the hypothesis that inter- and intramolecular hydrogen bonds are key drivers in the clustering process. However, the persistence of smaller 10 nm particles even in the presence of GuHCl suggests that other interactions, possibly related to polymer chain configuration, may also contribute to the system's behaviour.

### 2.3.4.3 Use of additives to probe aggregation behaviour

To investigate whether any other polymer components were contributing to the clustering behaviour a variety of additives were tested to determine whether they impacted clustering behaviour. Additives were chosen to either encourage or discourage polymer association. Tris-(2-carboxyethyl)phosphine

hydrochloride (TCEP·HCl) was chosen for its ability to reduce disulfide bonds between polymer chain termini, which are known to form creating polymer dimers.[62] Ethylenediaminetetraacetic acid (EDTA) was selected to competitively chelate any residual ions that may be in solution,[63] or any other metal ions that may be present in the water source, although this is unlikely as MilliQ water was used for all experiments. $CaCl_2$ was used to encourage divalent metal bridging between hydroxyl groups which was thought to promote aggregation.[64]

No observable change in the DLS intensity response was found, indicating the aggregate nature is not influenced by disulfide formation or divalent ions in solution, Figure 2.32.

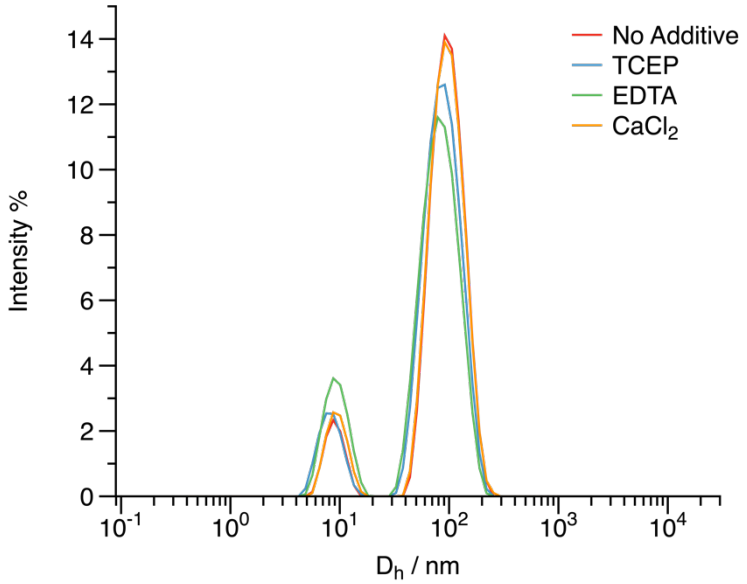


Figure 2.32: DLS intensity plots of 0.1 w/w% **P1-iso** with various 10 w/v% additive, 25 °C.

The impact of pH on aggregation behaviour was also investigated on 0.1 w/w% $^{i}$Pr-PVA solutions (Figure 2.33). A sample of polymer solution was prepared before three aliquots were taken. One aliquot was adjusted to pH 14, one to pH 1 and one to pH 7. It is seen that large species are formed at both low and high pH but are not present at neutral pH.

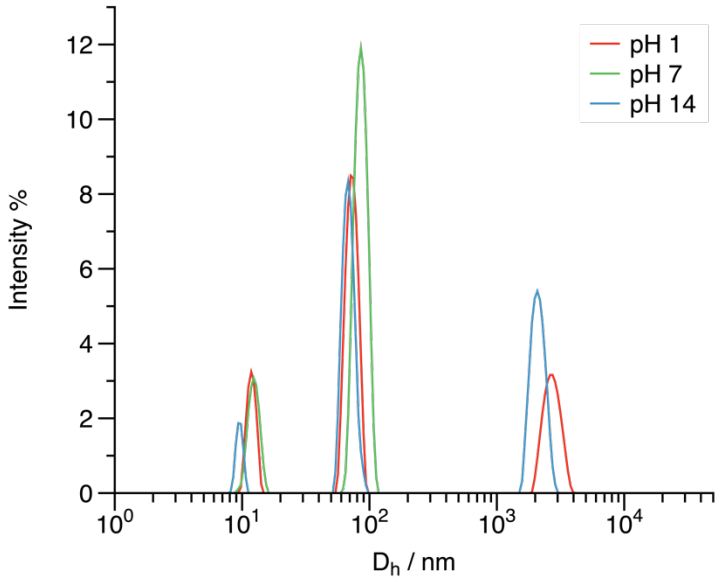


Figure 2.33: DLS Intensity plots of 0.1 w/w% **P1-iso** at pH 1 (red), pH 14 (blue), and pH 7 (green), 25 °C.

Pendent hydroxyl groups are able to lose or gain protons to become $-O^-$ or $-OH_2^+$.[65] While charge can reduce the likelihood of aggregation among chains, it also causes them to expand due to repulsion between same charged pendent groups, occupying more volume and potentially hindering their diffusion past one another.[65, 66] Consequently, if the charge on the particles inhibits diffusion, they may appear larger than their actual size.

### 2.3.5 Rheological analysis of PVA polymers

To further investigate the properties of the samples analysed via SANS, mechanical rheology was employed to examine the viscoelastic behaviour of 30 w/w% polymer solutions. This concentration was selected to ensure an adequate response from the rheometer, as the polymers were not particularly viscous, especially at the highest DA. It was also the maximum concentration used in SANS experiments and approaching the limit of solubility, requiring considerable effort to dissolve the polymers. A strain sweep (at fixed frequency), a frequency sweep (at fixed strain), and a flow sweep were performed during the analysis. This concentration was also chosen to provide the best chance of observing a crossover point. The crossover point reveals the polymer terminal relaxation time, which,

when combined with the chain dimensions from SANS, allows for the calculation of diffusion constants for the polymers.

Strain sweeps were carried out to identify the linear viscoelastic region (LVER) of the materials (Figure 2.34), *i.e.* the range of strain where the material's response remains proportional to the applied strain. In this region, the material's structure is not significantly disrupted by the applied strain, and its intrinsic viscoelastic properties can be measured accurately. At low strains, the material remains in the LVER, where its moduli (storage modulus G' and loss modulus G'') remain constant. Beyond a critical strain, the material begins to deform non-linearly, and the moduli start to change, indicating the transition out of the LVER. For the frequency sweep to be accurate, it must be conducted within the LVER, where the material's response is stable and representative of its intrinsic properties.[43-46] Strain sweeps revealed that a strain of 0.5% was within the LVER for all samples, and so frequency sweeps were carried out at this strain. For the **P4** sample (Figure 2.35d), G' appeared to decrease with increasing strain at all amplitudes, but 0.5% was used because a much smaller strain would make it difficult to obtain data within the sensitivity of the instrument.

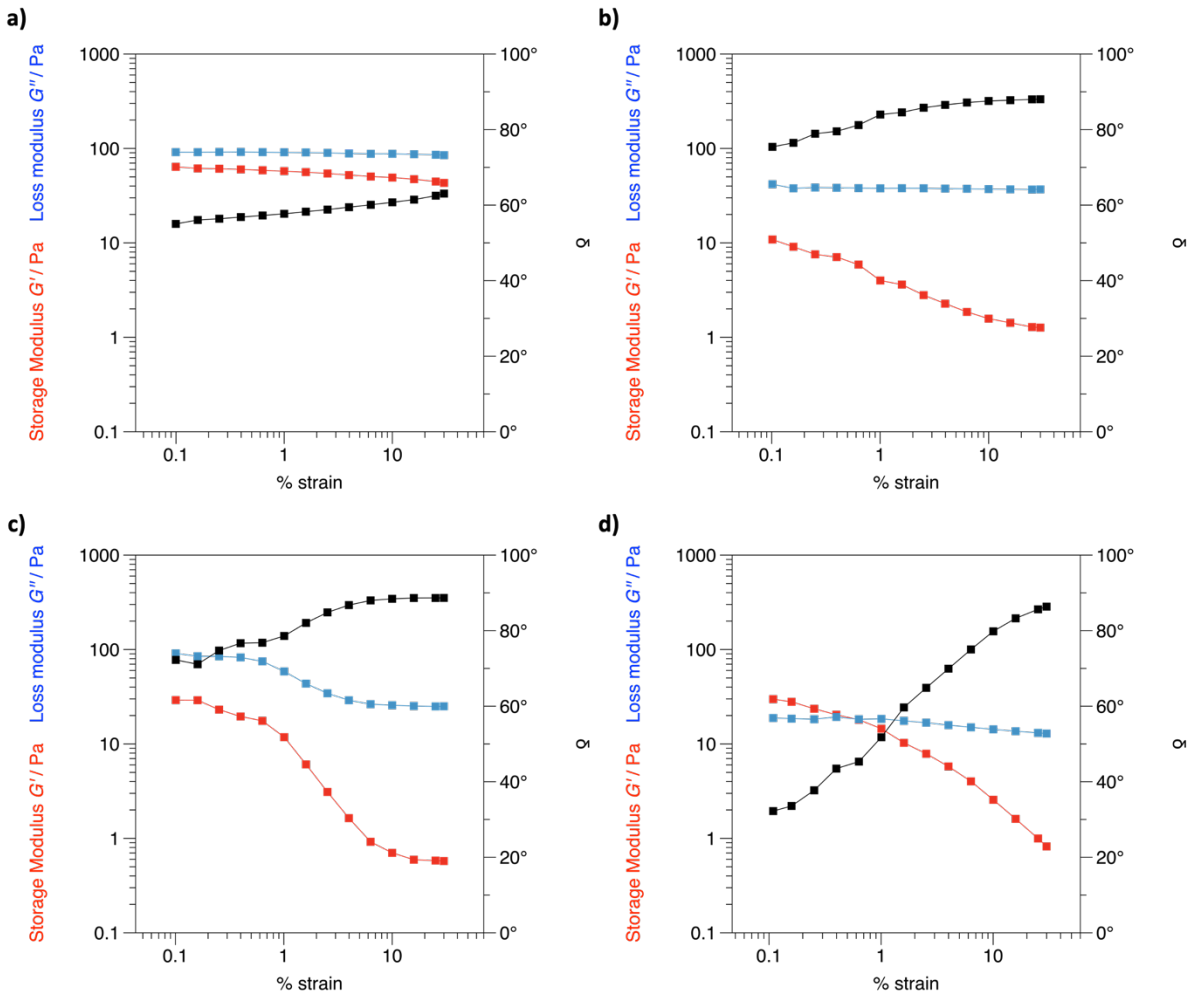


Figure 2.34: Strain sweeps at 25 °C 1 Hz for 30 w/w% solutions of a) **P1** DH 100%, b) **P2** DH 95%, c) **P3** DH 90%, d) **P4** DH 85%.

Frequency sweeps (Figure 2.35) provide insight into the viscoelastic properties of the polymer samples by measuring its response to deformation across a range of frequencies. For all samples the phase angle increases with frequency, tending towards 90°, indicating a shift towards a purely viscous material.[43-46] A frequency sweep can also identify transitions in the material's behaviour, such as the crossover point, where G' and G'' cross each other at a certain frequency. This indicates a transition from viscous-dominated to elastic-dominated behaviour (or *vice versa*). This is often seen in polymer melts and the crossover frequency provides information about the material's relaxation time. This relaxation time would then be used to calculate the polymer diffusion rate, in conjunction with $R_g$ established via SANS. As there was no reliable crossover point observed for the samples, potentially due to the low viscosity of the solutions as a result of the relatively low polymer molecular weight,

other techniques such as FRAP (discussed in Chapter 4) were utilised to determine the polymer diffusion coefficients for a similar series of materials.

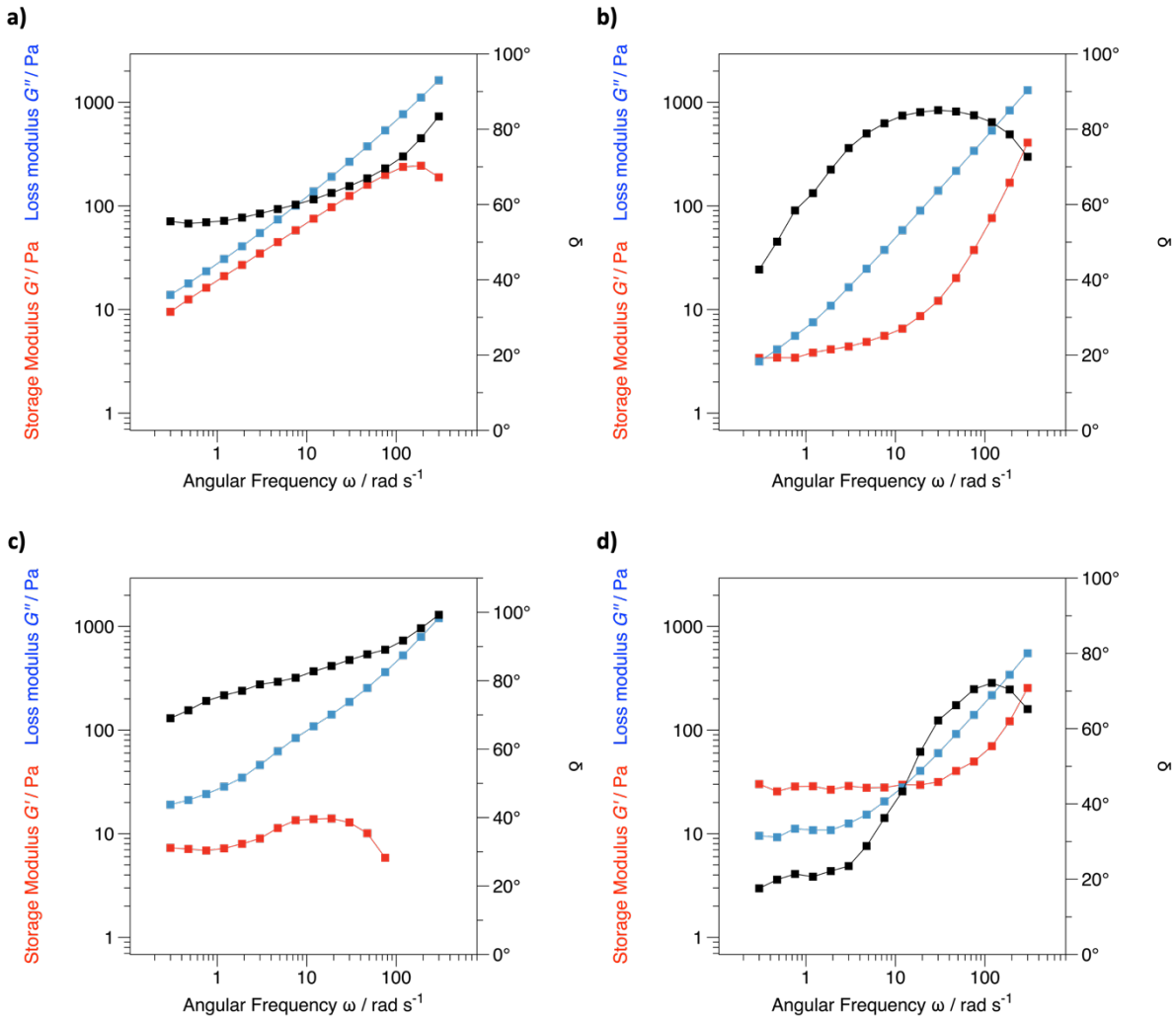


Figure 2.35: Frequency sweeps at 25 °C 0.5% strain for 30 w/w% solutions of a) **P1** DH 100%, b) **P2** DH 95%, c) **P3** DH 90%, d) **P4** DH 85%.

Stepped flow experiments (Figure 2.36) demonstrated that fully hydrolysed PVA exhibits shear-thinning behaviour, characterised by higher viscosity at lower shear rates, which decreases as the shear rate increases. This indicates that the material becomes less resistant to flow under greater stress. As the DH% decreases, meaning as the polymer becomes more acetylated, the overall viscosity reduces. While this result might appear suprising given the suggestion of network behaviour for the most acetylated sample, it is in fact consistent with this sample being most susceptible to disruption in the

strain-sweep experiments. The shear-thinning behaviour also diminishes with increased acetylation. This reduction in both viscosity and shear-thinning behaviour is likely influenced by the increased presence of acetyl groups, which disrupt the polymer's crystallinity. Furthermore, acetylation reduces the number of hydroxyl groups available for hydrogen bonding between polymer chains. Hydrogen bonding is a key factor in maintaining the viscosity and structural integrity of PVA, and its reduction weakens the intermolecular forces between chains, making the polymer less viscous and reducing its shear-thinning properties. Consequently, higher levels of acetylation result in a more amorphous structure and reduced resistance to flow under stress. This result provides further evidence for factors which may contribute to a larger overall structure, as observed by solution state SANS measurements, being present in the sample.

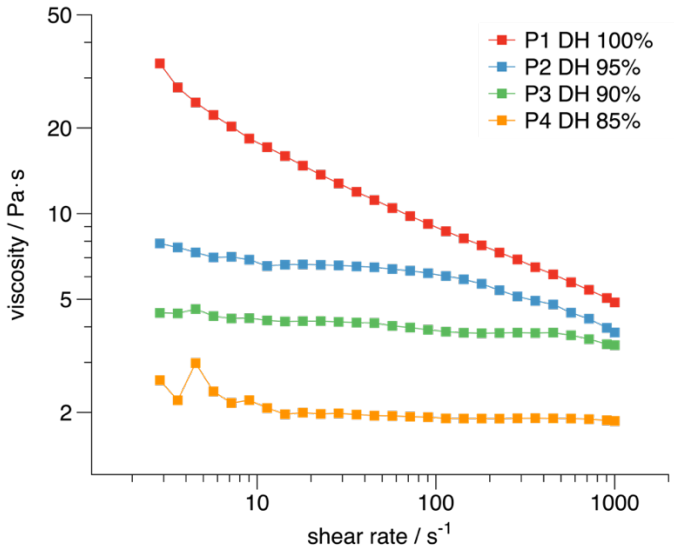


Figure 2.36: Stepped flow sweeps of **P1** – **P4** 30 w/w%, 25 °C, 0.1 rad/s – 35.0 rad/s, 25 mm 2° cone geometry.

### 2.3.6 Solid state PVAc chain dimension and interaction parameter elucidation

As introduced in Chapter 1, vinyl alcohol cannot be polymerised directly and PVA is synthesised by hydrolysing PVAc. For most uses, the hydrolysis is incomplete, leaving residual acetate groups. While these groups are not inherently hydrophilic, they help reduce crystallisation and enhance the copolymer's solubility.[67] Interestingly, no direct measure of the compatibility between PVAc and PVA

appears in the literature, despite the importance of understanding this to predict the material's solubility and interdiffusion behaviour. To address this, this work utilises SANS to study well-defined blends of deuterium-labelled dPVAc with hydrogenous hPVAc. The deuterated polymer remains fully acetylated for all experiments, and hydrogenous polymers, all with the same degree of polymerisation, have systematically varied levels of hydrolysis. To investigate tendency for polymer chains to phase separate due to disparity between the two polymer samples (in this instance, differences in DH%) the interaction parameter between vinyl alcohol and vinyl acetate groups, which represent the extent of phase separation, was investigated. Materials utilised for this work are shown in Figure 2.37.

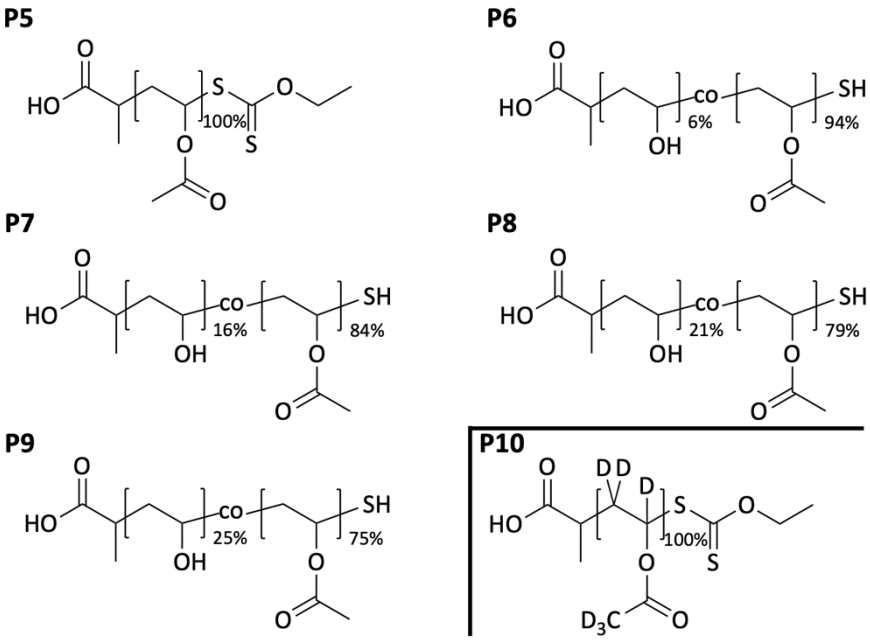


Figure 2.37: Structures of hPVAc and dPVAc polymers. DP hPVAc: 331,[a] dPVAc: 334.[b] [a]as determined by $^{1}$H NMR spectroscopy, [b]as determined by $^{2}$H NMR spectroscopy.

In this study, the interaction parameter, $\chi$, between dPVAc and hPVAc was determined using SANS and fitting to the modified RPA + power law model. Initially, the system consisted of dPVAc and fully hydrogenous hPVAc. To investigate the chain dimensions and interaction parameters of partially hydrolysed PVAc systems in the solid state, a library of partially hydrolysed PVA polymers (degree of hydrolysis 0–23%, Figure 2.37, Table 2.8) was synthesised from a single parent PVA (ensuring a consistent DP across all samples) while the dPVAc remained chemically unchanged. As this study was

conducted in the solid state, where crystallisation could complicate the fitting of SANS data, the samples were prepared with a high degree of acetylation (low DH) to suppress crystallisation. It is known that partial hydrolysis results in a less randomly distributed polymer product than reacetylation of PVA as was utilised for solution state SANS.[50, 51, 68] It was preferable to conduct a controlled hydrolysis rather than an incomplete reacetylation due to the high acetylation content required for these samples as well as the synthetic challenge of achieving high but not fully acetylated PVAc via the reacetylation method. As a result, the polymers used in this work are blockier than those used in the solution state SANS work. In this work, dPVAc was synthesised to closely match the DP of the hydrogenous material. Two different blend compositions were created (D:H mass ratios of 75:25, and 25:75) to determine whether $\chi$ varied with the sample composition (Table 2.9). For each composition, a reference sample was made where no interaction parameter should exist—blends of dPVAc with hPVAc. As hydrolysis is introduced into the hydrogenous chains, but not the deuterated chains, it is expected that the blends will begin to show a tendency for demixing.

Table 2.8: Summary of polymers synthesised for solid state SANS chain dimension and interaction parameter work. GPC analysis of parent PVAc and dPVAc conducted pre hydrolysis. dPVAc $M_n$: 27,900, $M_w$: 33,800, Đ: 1.21. PVAc $M_n$: 26,200, $M_w$: 32,500, Đ: 1.24.

| **Polymer** | **H/D** | **DP[a]** | **$M_n$ / gmol$^{-1}$ [a]** | **DH%[a]** |
|---|---|---|---|---|
| **P5** | H | 336 | 28,900 | 0 |
| **P6** | H | 336 | 28,000 | 6 |
| **P7** | H | 336 | 26,700 | 16 |
| **P8** | H | 336 | 26,000 | 21 |
| **P9** | H | 336 | 25,600 | 25 |
| **P10** | D | 331 | 30,500 | 0 |

[a]as determined by $^1$H or, where appropriate, $^2$H spectroscopy.

Table 2.9: Summary of hPVAc/dPVAc blends used for solid state SANS interaction parameter experiments. Volume fraction, $\phi$,calculated based on mass used and $\rho_{PVAc}$ = 1.19 and $\rho_{dPVAc}$=1.27.

| D:H | Blend | hPVAc | $\phi$ hPVA/c | Total Sample mass / mg | Sample Thickness / mm |
|---|---|---|---|---|---|
| 75:25 | **B1** | **P5** | 0.26 | 20.0 | 0.053 |
| | **B2** | **P6** | 0.26 | 14.0 | 0.037 |
| | **B3** | **P7** | 0.26 | 53.7 | 0.144 |
| | **B4** | **P8** | 0.25 | 19.6 | 0.052 |
| | **B5** | **P9** | 0.26 | 62.4 | 0.167 |
| 25:75 | **B6** | **P5** | 0.76 | 65.9 | 0.176 |
| | **B7** | **P6** | 0.75 | 48.8 | 0.131 |
| | **B8** | **P7** | 0.77 | 102.1 | 0.273 |
| | **B9** | **P8** | 0.76 | 76.7 | 0.205 |
| | **B10** | **P9** | 0.76 | 64.9 | 0.174 |

All polymer blends were solution cast to quartz windows ⌀ = 20 mm. Thickness calculated assuming sample density of 1.19 g $cm^{-3}$. To achieve absolute scaling of the scattering data, it is essential to know the thickness of material within the beam path. This enables accurate determination of an interaction parameter and allows for reliable comparisons between samples. In this study, samples were analysed at room temperature to prevent them from exceeding their glass transition temperature ($T_g$), which would cause the polymers to flow off the quartz window and out of the beam path. During a previous analysis, samples were heated above their $T_g$ (at 80, 100, 120, and 140 °C), causing the polymers to flow out of the beam path. Lack of knowledge of sample thickness meant that the interaction parameter could not be established, this was the motivation for repeat analysis of these samples directly coated onto quartz and analysed at room temperature.

Similar to the solution-state samples, these samples exhibited a low-*Q* scattering feature, suggesting the presence of larger ordered structures. This may be due to trapped solvent within the solid, which would likely evaporate during an annealing process. To address the need for a combined power law model and a two-component blend polymer model, Microsoft Excel's Solver function was used to fit the data. SasView does not currently allow for the combination of plugin models (such as the binary blend model) with default models (such as the power law model).

The samples were fit as follows. First, blends of hPVAc and dPVAc with no hydrolysis (**B1** and **B6**) were fit, fixing $\chi$ = 0 (Figure 2.38a, 2.39a, 2.40a). The statistical step length for hPVAc and dPVAc was constrained to be identical. The s.l.d. contrast was allowed to float from the predictive value, showing a slight decrease (likely due to lower density or voids within the samples), with values of 5.20 and 5.43 × $10^{-6}$ $Å^{-2}$ for blends **B1** and **B6**, respectively. The statistical step length and power law parameters were fit next. The fit statistical step lengths for the two isotopic blends were very similar (2187 Å and 2197 Å), corresponding to $R_g$ values of 43.6 Å for blend **B1** and 43.8 Å for blend **B6**. A mean value of 2192 Å was then applied to dPVAc across all other blends (Figure 2.38b-e), allowing $R_g$ for hPVAc to float independently. Fits for 75%D 25%H are shown in Figure 2.38 while fits for 25%D 75%H are shown in Figure 2.39.

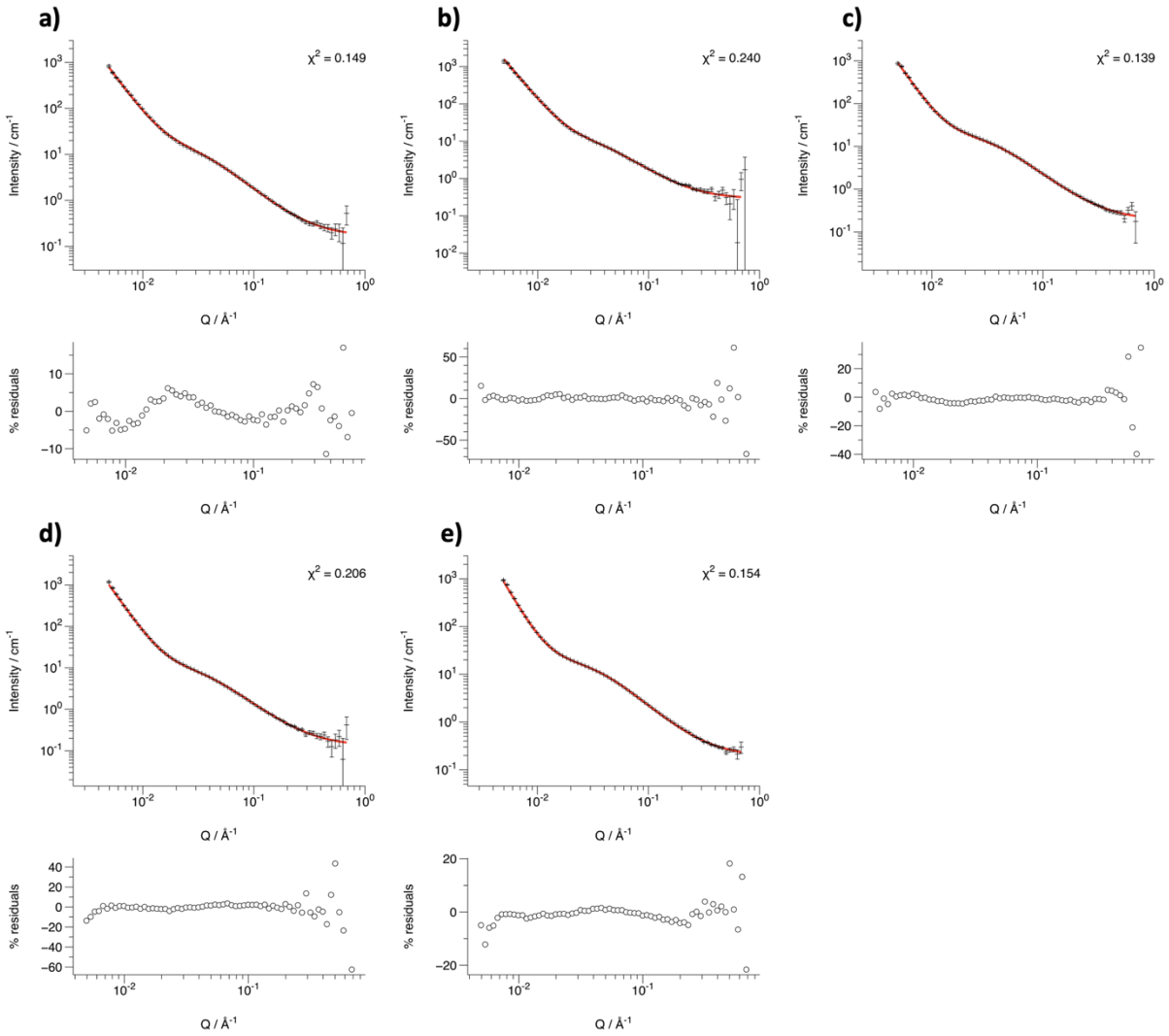


Figure 2.38: Blends **B1**-**B5**, majority D, fit to combined power law and binary blend random phase approximation model. Red line is predicted fit, crosses are experimental data. a) – e) = blends **B1**-**B5**.

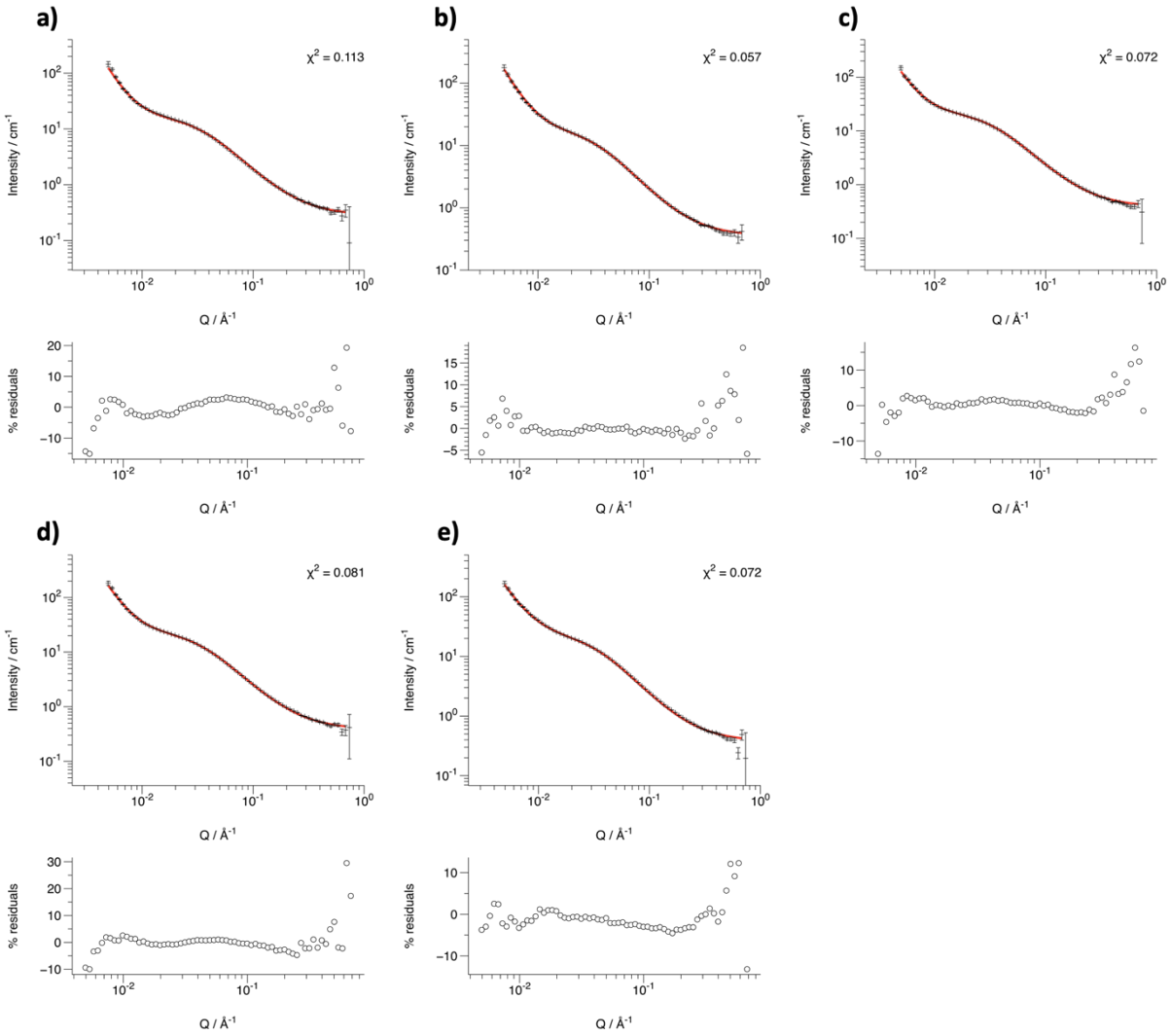


Figure 2.39: Blends **B6**-**B10** fit to combined power law and binary blend random phase approximation model. Red line is predicted fit, crosses are experimental data. a) – e) = blends **B6**-**B10**.

By fitting the data, the $R_g$ and $\chi$ parameters for both polymers in the blend were determined. It was assumed that the $R_g$ of the dPVAc remained unchanged as the DH of hPVAc was varied, and so it was kept at an average value, as shown in Figure 2.40a. It is observed that, for both sets of blends, the $R_g$ of hydrogenous PVAc decreases from the initial value measured for 0% DH blends as DH% increases, seen in Figure 2.40b. This suggests a slight chain collapse as the disparity between samples increases, which was also observed for solution samples, with chains decreasing in size as DH% increased (Figure 2.21). This can be explained by earlier hypotheses suggesting that the removal of bulky acetate groups

allows for better chain packing, thus leading to a reduction in size. The experimentally determined values of $\chi$ and $R_g$ are shown in Figure 2.41, 2.42 , as well as Table 2.10.

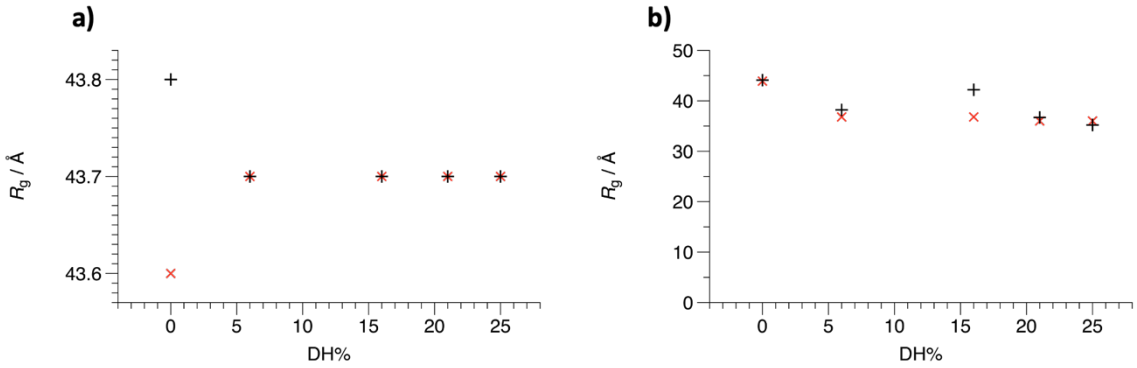


Figure 2.40: Radii of gyration for a) dPVAc, showing average value applied derived from DH 0% samples, and b) hPVAc. Red crosses = blends **B1**-**B5**, marjority dPVAc, black crosses = blends **B6**-**B10**, majority hPVAc.

Table 2.10: Summary of paramaters calculated for polymer blends **B1**-**B10**.

| D% | Blend | DH% | $R_g$ hPVAc / Å | $R_g$ dPVAc / Å | $\chi \times 10^4$ |
|---|---|---|---|---|---|
| 75 | **B1** | 0 | 43.9 | 43.6 | 0.0 |
| | **B2** | 6 | 36.8 | 43.7 | 5.0 |
| | **B3** | 16 | 36.8 | 43.7 | 12.0 |
| | **B4** | 21 | 36.0 | 43.7 | 15.0 |
| | **B5** | 25 | 36.0 | 43.7 | 20.0 |
| 25 | **B6** | 0 | 44.1 | 43.8 | 0.0 |
| | **B7** | 6 | 38.2 | 43.7 | 11.0 |
| | **B8** | 16 | 42.2 | 43.7 | 11.0 |
| | **B9** | 21 | 36.7 | 43.7 | 13.9 |
| | **B10** | 25 | 35.2 | 43.7 | 18.0 |

The results show that $\chi$ increases linearly with the DH of the hydrogenous PVAc (Figure 2.41). This linear increase suggests that, as hydrolysis proceeds, the difference in chemical composition between the two polymers leads to increasing incompatibility. The positive values of $\chi$ throughout the experiment indicate that the interaction between deuterated and partially hydrolysed hPVAc is repulsive, promoting phase separation. This trend becomes more pronounced with increasing DH, as the hydrolysis process introduces polar hydroxyl groups into the hydrogenous PVAc, while the deuterated PVAc retains its non-polar acetate groups. The increase in polarity mismatch drives the rise

in $\chi$ and reflects a growing thermodynamic tendency for phase separation between the two polymers. These findings are consistent with the expectation that partially hydrolysed PVA/c becomes less compatible with deuterated PVAc due to their diverging chemical nature. It is noted that the relationship between DH and $\chi$ is similar for both sample compositions (D:H 75:25 and 25:75), although the red dataset (Figure 2.41, 75% D blends) had lower neutron background due to the higher deuterium content. For a symmetrical 50:50 vol:vol blend, phase separation is expected when the product of the Flory-Huggins interaction parameter χ and the degree of polymerisation exceeds 2.[42, 69] This criterion is derived from the Flory-Huggins theory, which describes the thermodynamics of polymer blends. According to the theory, the critical value of χ for phase separation in a binary polymer blend is given by $\chi_c = 2/DP$.[69] Given that DP is approximately 330 for these polymers, the critical value of χ for phase separation is calculated to be 2/330, or ~0.006. This means that if χ exceeds ~0.006, the blend will undergo phase separation due to unfavourable interactions between the polymer chains.[42] For the current system, it appears that this χ value would be reached when the difference in DH between the polymers is approximately 75%. The trends observed in this work present opportunities to experimentally validate computational modelled PVA-PVAc phase behaviour such as that reported by Patukova *et al.*[70] which emphasises the importance of polymer blockiness in PVA systems on the predicted phase behaviour.

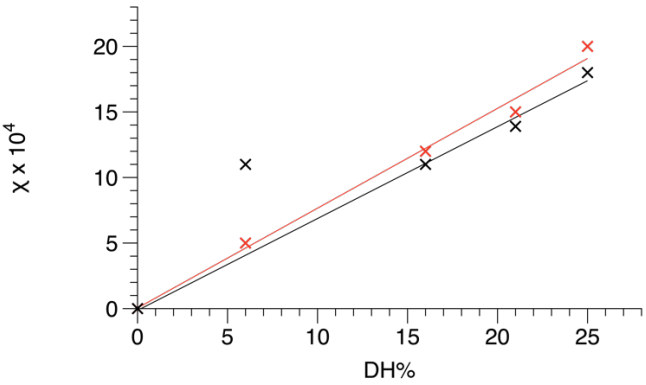


Figure 2.41: DH% dependence of the $\chi$ interaction parameter for polymer blends studied. Red crosses = blends **B1**-**B5**, 75% dPVAc, black crosses = blends **B6**-**B10**, 75% hPVAc. Black cross at 5% DH exluded from fit.

From an applied perspective, these results are useful when considering the bilayer systems in SUD pods, where at least two layers of part hydrolysed PVA film are used to seal liquid contents within the capsule, and the polymer chains must entangle rapidly. If naturally phase separating polymers are utilised, then the polymer seal will either fail to form or begin to segregate and phase separate during product storage. These results emphasise the importance that DH has on phase separation, particularly for the higher molecular weight polymers used in industry and shows that even at low DH% a positive interaction parameter arises, indicating the eventual tendency for polymer phase separation. Although a simplified system to mimic the complex industrial polymers used to make these films, it highlights the importance of evaluating polymer compatibility in some way to ensure film components are miscible. In some brands of SUD pods, there is a third polymer layer in the middle of the cavity, allowing the number of chambers within the pod to be doubled. Typically, the polymers in these films do not match the composition of the outer films, being modified to improve barrier properties between liquid-liquid compartment contents. It is therefore crucial that the compatibility of these different polymers be measured before determining them suitable for use in packaging material.

## 2.4 Conclusions and future work

In conclusion, this two-part investigation into PVA and PVAc has explored both single-component polymer solutions and dual-component polymer blends to assess the impact of DH on polymer properties. Part acetylated PVA polymers through targeted acetylation were synthesised, enabling the creation of a PVA library with systematic DH variation for solution-state SANS experiments. These studies successfully determined the polymer $R_g$ as a function of DH at various solution concentrations, revealing a reduction in polymer size with increasing DH (removal of acetate groups). Further analysis showed polymer chain aggregation, seemingly independent of chain ends or the solution environment. Disruption of hydrogen bonds reduced aggregation, suggesting that inter- or intrachain

interactions are responsible. This was further examined using dynamic light scattering (DLS) and rheology.

For PVAc, a methodology was developed to control the production of highly (but partially) acetylated materials through base-catalysed hydrolysis, allowing targeting of DH and creating a series of partially hydrolysed polymers. Deuterated PVAc was also synthesised via PET-MADIX with good control and blended with the partially hydrolysed series, enabling solid-state analysis of PVAc chain dimensions and phase behaviour. As in the solution-state experiments, chain dimensions decreased with increasing DH. Additionally, varying the DH in a single-component PVAc blend increased the positive interaction parameter. While these model materials were within the single-phase region and suitable for RPA analysis with SANS, they could demonstrate that phase separation could ultimately be driven by the DH disparity between components.

These findings have significant practical applications in simulations and sealing models for the production of SUD films, offering substantial value to both the scientific community and laundry detergent manufacturers. By improving the prediction of film compatibility in detergent capsule sealing mechanisms, this work enables more efficient and reliable production processes, reducing material waste and enhancing the performance of detergent capsules. For manufacturers, this translates to cost savings, improved product consistency, and the ability to innovate with new formulations that were previously challenging to seal effectively. For the broader scientific community, this research provides a deeper understanding of polymer interactions within PVAc systems, particularly with components of the same degree of polymerisation. This is a notable achievement, as it represents the first instance where SANS has been used to determine the polymer interaction parameter in such a system. While similar data exists for other polymer systems, this work fills a critical gap in the literature and opens new avenues for research into PVA compatibility and film behaviour. This work directly addresses the need for advanced materials characterisation techniques to support

the development of next-generation detergent products. It underscores the importance of understanding polymer interactions at a fundamental level to drive innovation in the field, ultimately contributing to more sustainable and efficient consumer products. This research not only advances scientific knowledge but also delivers tangible benefits to industry, aligning with the broader goals outlined at the outset of this thesis

To build upon this work, it would be worthwhile to analyse solutions of non-carboxylate containing end group PVAs via SANS to investigate whether this reduces or eliminates the high-intensity low-*Q* scattering observed for all existing solution samples. Similarly, it would be of interest to examine a sample before and after the addition of GuHCl, which, in DLS experiments, appeared to suppress aggregation. Another promising avenue for future exploration would be the use of Spin-Echo Small-Angle Neutron Scattering (SESANS), which can probe larger length scales up to 18 microns on LARMOR, to investigate polymer chain aggregation and structure more completely.

It would also be interesting to follow the chain structure evolution during acetylation using SANS, to understand whether the polymer chain expands or changes as acetylation makes it compatible with the solvent. Such experiments could elucidate the relationship between chemical modification and chain conformation, providing insights into the role of solvent-polymer interactions in determining chain structure. This line of inquiry could be particularly relevant for studying systems with varying DH or in blends with components of differing solubilities, as it would highlight the interplay between molecular interactions and phase behaviour. Expanding the study to include these approaches could provide a deeper understanding of the observed phenomena and open new pathways for future research.

## 2.5 Experimental methods

All reagents were purchased from commercial suppliers (Sigma-Aldrich, Acros Organics, Fluorochem, Alfa Aesar, Fisher Scientific or TCI) and were used without further purification. Deuterated vinyl acetate was purchased from Polymer Source (Montreal, Canada). Monomer was passed over a basic alumina plug to remove inhibitor.

Dried solvents were obtained from in-house SPS (Innovative Technology PureSolv MD 5 solvent purification system) or were purchased from Sigma Aldrich in Sure Seal bottles and maintained under Ar atmosphere. Flash chromatography was typically carried out using a Teledyne Combiflash NextGen 300+ system. TLC was conducted using 2 cm x 5 cm aluminium backed plates coated with silica matrix (0.2 mm) and fluorescent indicator (254 nm). Visualisation of TLC was carried out using a UV lamp.

Solution-state NMR spectra were recorded at 298 K on either: a Bruker Avance III-HD-400 spectrometer with operating frequencies of 400.07 MHz for $^{1}$H, 100.60 MHz for $^{13}$C; a Bruker Avance III-HD-400 spectrometer with operating frequencies of 400.07 MHz for $^{1}$H, 100.60 MHz for $^{13}$C; a Bruker Neo-400 spectrometer with operating frequencies of 400.20 MHz for $^{1}$H, 100.63 MHz for $^{13}$C; a Varian Inova-500 with operating frequencies of 500.13 MHz for $^{1}$H, 76.66 MHz for $^{2}$H, 125.76 MHz for $^{13}$C. Spectra were processed using MestReNova (V 15.0.1) software. $^{1}$H NMR Chemical shifts were referenced to residual non-deuterated solvent peaks within the NMR solvent; $CHCl_3$ (δH = 7.26 ppm), $CH_3OH$ (δH = 3.31 ppm), DMSO (δH =2.50 ppm).[71] $^{2}$H NMR Chemical shifts were referenced to -deuterated solvent peaks within the NMR solvent; $CDCl_3$ (δH = 7.26 ppm).[71] The multiplicity of $^{1}$H and $^{2}$H signals are indicated as: s = singlet; d = doublet; t = triplet; q = quartet; quint. = quintet; sex. = sextet; sept. = septet; m = multiplet; br = broad; and combinations thereof. Coupling constants (*J*) are quoted in Hz and are reported to the nearest 0.1 Hz. Chemical shifts for $^{13}$C NMR spectra were referenced to deuterated solvent peaks in the NMR solvent; $CDCl_3$ (δC = 77.16 ppm), $CD_3OD$ (δC = 49.00 ppm), DMSO-$d_6$ (δC = 39.52 ppm).[71]

All mass spectrometry was carried out using tandem Acquity UPLC (Waters Ltd) and a TQD with ESI mass spectrometer (set to $EI^+$ mode and $EI^-$ mode where appropriate). The UPLC was equipped with an Acquity UPLC BEH $C_{18}$ 1.7 µm (2.1 mm x 50 mm) column, and mobile phase composition of $H_2O$ containing formic acid (0.1% v/v): methanol mobile phase (gradient elution; t = 0 min, 95% : 5%, t = 4 min, 5% : 95%), set at 0.6 mL/min.

Organic gel permeation chromatography (GPC) was conducted with THF (GPC Grade, Stabilised with 0.025% butylated hydroxytoluene, Fisher Scientific) eluent on an Agilent 1260 instrument equipped with a differential refractive index (dRI) detector, a dual-angle light scattering detector (15° and 90°), a viscometer and a pair of PL gel 5 µm Mixed D 300 × 7.5 mm columns with a guard column (Polymer Laboratories Inc.) in series at 35 °C, 1 mL/min. Molecular weights were determined through universal calibration using the Agilent Infinity software. Samples were made up at 5 mg/mL in THF (GPC grade, Fisher Scientific) and passed through a 0.2 µm nylon syringe filter prior to analysis.

Aqueous GPC was conducted in $NaNO_3$ (10 mM, 2 x 0.02 µm filtered) eluent on an Agilent 1260 instrument equipped with a dRI detector, a dual-angle light scattering detector (15° and 90°), a viscometer, a variable wavelength UV detector and a pair of PL gel 8 µm PL aquagel-OH Mixed-M 300 × 7.5 mm columns with a guard column (Polymer Laboratories Inc.) in series at 35 °C, 1 mL/min. Molecular weights were determined through narrow standard calibration using the Agilent Infinity software. Samples were made up at 5 mg/mL in $NaNO_3$ (10 mM, 2 x 0.02 µm filtered) and passed through a 0.2 µm polyether sulfone syringe filter prior to analysis.

Infra-red spectra were acquired using a Perkin Elmer Spectrum Two FT-IR spectrometer equipped with a diamond µATR attachment. Spectra were recorded from a range of 4,000 - 380 $cm^{-1}$. Resolution 0.5 $cm^{-1}$.

The SANS technique along with deuterated solvent contrasting was used to investigate the polymer chain dimensions in the solution state.[56] The ISIS Neutron and Muon Source, Didcot, UK LARMOR instrument was used in conventional SANS mode in the following configuration: 1.7 - ~10.0 Å neutron wavelength, sample to detector distance of 4 m and a momentum transfer range of $3.5 \times 10^{-3}$ – $7 \times 10^{-1}$ Å. Sample measurement times were approximately 90 minutes (60 μA beam current) at 25 °C. Background runs of $D_2O$ in a quartz cell was also measured and subtracted from scattering data. Direct beam transmission runs were used to scale the averaged data to an absolute cross-sectional form. All samples were measured in either 1 mm thick or 2 mm thick quartz disc-shaped banjo cells (Hellma, Müllheim, Germany). 30 w/w% polymer solutions were made in $D_2O$ and were serially diluted with $D_2O$ to access lower concentrations throughout the experiment.

The LARMOR instrument was also used to analyse solid state samples in the same configuration as above. Sample measurement times were approximately 30 minutes (20 μA beam current) at 25 °C. Polymer blends were dissolved in a minimum volume of chloroform and solution cast onto pre weighed quartz windows (20 mm ⌀) and dried at 50°C for 5 days. Samples were mounted in the neutron beam using brass gel cell holders. Direct beam transmission runs were used to scale the averaged data to an absolute cross-sectional form. Intensity data were corrected for sample thickness and transmission and placed on an absolute scale by comparison with the scattering of the secondary standard, a blend of deuteropolystyrene in hydrogenous polystyrene.

UV/Vis spectroscopy was carried out using a TECAN Spark Multimode Microplate Reader with Infinite® 200 NanoQuant plate accessory at 20 °C. Measurement range 200 – 1000 nm, 1 nm step size.

Rheology was carried out for 30% w/w polymer solutions using a TA AR2000 rheometer at 25 °C. A 25 mm ⌀ 2° cone plate was used in conjunction with Evaporation Blocker Solvent Trap to avoid loss of water from the samples, which was crucial for consistent results. Samples underwent a 2 min

temperature soak to ensure the entire sample was at 25 °C, and that any induced structure from loading the sample had time to recover. Continuous oscillation strain sweeps (0.1 – 30.0 % strain, 1Hz freq.) were first carried out to ensure subsequent frequency sweeps were conducted in the LVER. Continuous oscillation frequency sweeps were conducted at 0.5% strain beginning at 0.3 rad/s ending at 300 rad/s. Frequency sweeps were conducted in duplicate to ensure no induced structure was imparted on the sample by the measurement. The second sweep was conducted in the opposite frequency direction to the first. Stepped flow measurements were conducted between 0.1 and 35.0 rad/s.

DLS measurements (3 runs of 13 measurements) were taken on a Malvern Zetasizer µV (Malvern Panalytical Ltd, Malvern, UK) in quartz cuvettes 10 mm path length (Hellma, Müllheim, Germany). The laser wavelength on this instrument is 633 nm and scattering is detected at an angle of 90°. Samples were made up to the desired concentration in DI $H_2O$ and passed through a 0.22 µm polyether sulfone syringe filter prior to analysis. The instrument control and data processing were conducted using Malvern Zetasizer software.

### 2.5.1 Synthesis of 2-(ethoxycarbonothioyl)sulfanyl propanoic acid, EtPAX 1

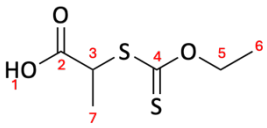


Figure 2.42: Structure of 2-(ethoxycarbonothioyl)sulfanyl propanoic acid.

Method adapted from literature.[48] Potassium hydroxide pearls (6.50 g, 11.6 mmol, 1.0 eq.) were dissolved in ethanol (63 mL) over the course of 30 min at room temperature with stirring. The solution was cooled to 0 °C and carbon disulfide (7.3 mL, 12.1 mmol, 1.0 eq.) was added dropwise over the course of 15 min, during which time a yellow precipitate formed. The solvent was removed under vacuum and a pale-yellow solid was obtained (17.0 g). The crude product, potassium ethyl xanthogenate, was used in the subsequent step without further purification. 2-bromopropionic acid (5.1 mL, 56.7 mmol, 1.0 eq.) was added dropwise to a solution of potassium ethyl xanthogenate (10.0 g, 62.4 mol, 1.10 eq.) in dry acetonitrile (40 mL) at 0 °C. The suspension was stirred at room temperature for 4 h. The colourless KBr precipitate was removed by gravimetric filtration and washed with diethyl ether (3 × 5 mL). The pale-yellow filtrate was evaporated to dryness giving a yellow oil. The crude product was then purified via CombiFlash (80 g Gold $SiO_2$ Column, ethyl acetate:hexane ramp to 0:1 to 1:1 over 5 CV). The fractions containing **1** were concentrated and the resultant pale-yellow oil recrystallised from hexane. **1** was isolated as a pale yellow crystalline solid (4.42 g, 40% yield) **m.p.** 55-57 °C. Spectra match literature report.[48] **$^1$H NMR** (*400 MHz, $CDCl_3$*) δ 10.62 (s -br, 1H, $H_1$), 4.64 (qd, *J* = 7.1, 2.0 Hz, 2H, $H_5$), 4.42 (q, *J* = 7.4 Hz, 1H, $H_3$), 1.61 (d, *J* = 7.5 Hz, 3H, $H_7$), 1.42 (t, *J* = 7.1 Hz, 3H, $H_6$). **$^{13}$C NMR** (*101 MHz, $CDCl_3$*) δ 211.89 $C_4$, 176.82 $C_2$, 70.73 $C_5$, 46.87 $C_3$, 16.63 $C_7$, 13.77 $C_6$. **LR-ESI-MS:** For $[M+H]^+$ calculated: 195.007, found: 195.119. **UV/Vis** DMSO $\lambda_{abs}$ = 283 nm.

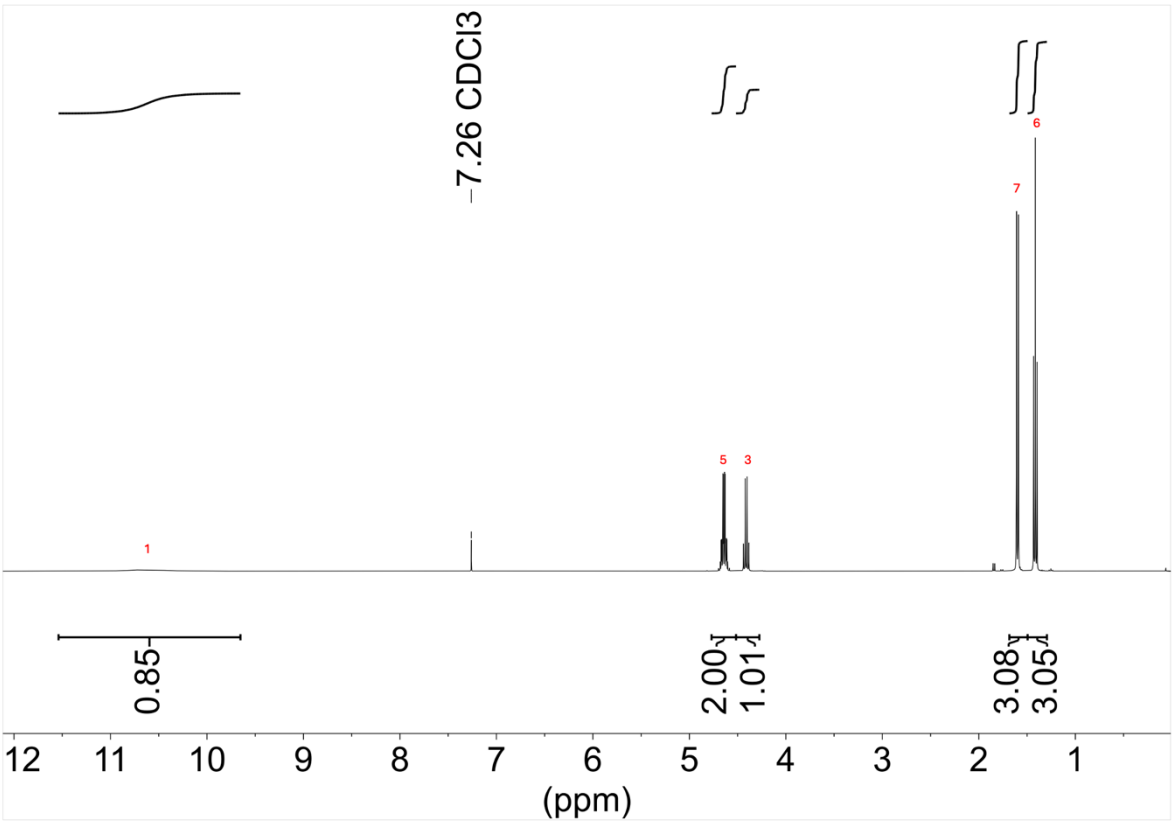


Figure 2.43: **$^{1}$H NMR** (*400 MHz, $CDCl_3$*) of 2-(ethoxycarbonothioyl)sulfanyl propanoic acid.

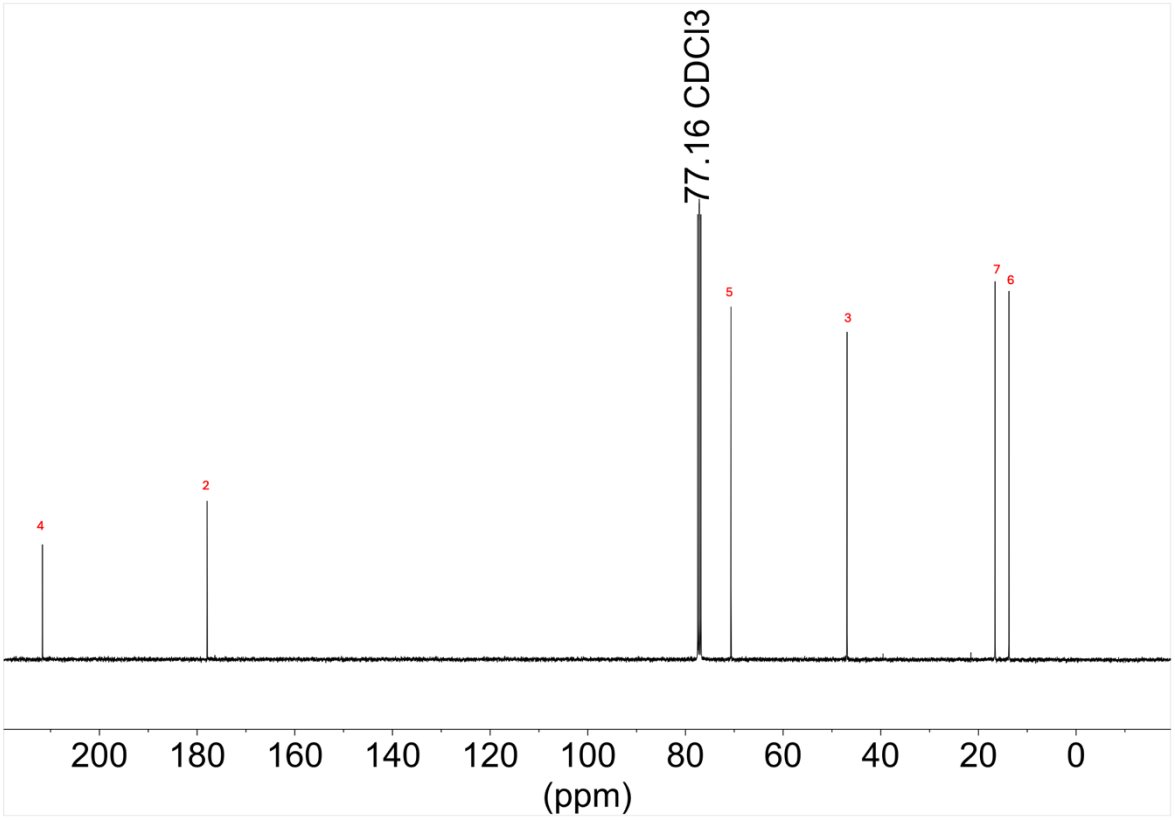


Figure 2.44: **$^{13}$C NMR** (*101 MHz, $CDCl_3$*) of 2-(ethoxycarbonothioyl)sulfanyl propanoic acid.

### 2.5.2 Synthesis of O-ethyl S-isopropyl carbonodithioate 2

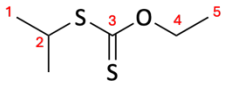


Figure 2.45: Structure of O-ethyl S-isopropyl carbonodithioate.

Method adapted from literature.[72] 2-bromopropane (3.1 mL, 33.0 mmol, 1.00 eq.) was added dropwise to a solution of potassium ethyl xanthogenate (5.82 g, 36.3 mmol, 1.10 eq.) in dry acetonitrile (30 mL) at 0 °C. The suspension was stirred at room temperature for 16 h. The colourless KBr precipitate was removed by gravimetric filtration and washed with acetonitrile (3 × 5 mL). The pale-yellow filtrate was evaporated to dryness giving a yellow oil. The crude product was then purified via CombiFlash (80 g Gold $SiO_2$ Column , ethyl acetate:hexane ramp to 0:1 to 5:95 over 5 CV). The fractions containing **2** were concentrated and the resultant pale-yellow oil (700 mg, 14% yield) with spectra matching the literature.[72] **$^1$H NMR** (*400 MHz, $CDCl_3$*) δ 4.65 (q, *J* = 7.1 Hz, 2H, $H_4$), 3.80 (hept, *J* = 6.9 Hz, 1H, $H_2$), 1.41 (t, *J* = 7.1 Hz, 3H, $H_5$), 1.38 (d, *J* = 6.9 Hz, 6H, $H_1$). **$^{13}$C NMR** (*101 MHz, $CDCl_3$*) δ 214.68 $C_3$, 69.55 $C_4$, 40.98 $C_2$, 22.40 $C_1$, 13.92 $C_5$. **LR-ESI-MS:** For $[M+H]^+$ calculated: 165.033, found: 165.128.

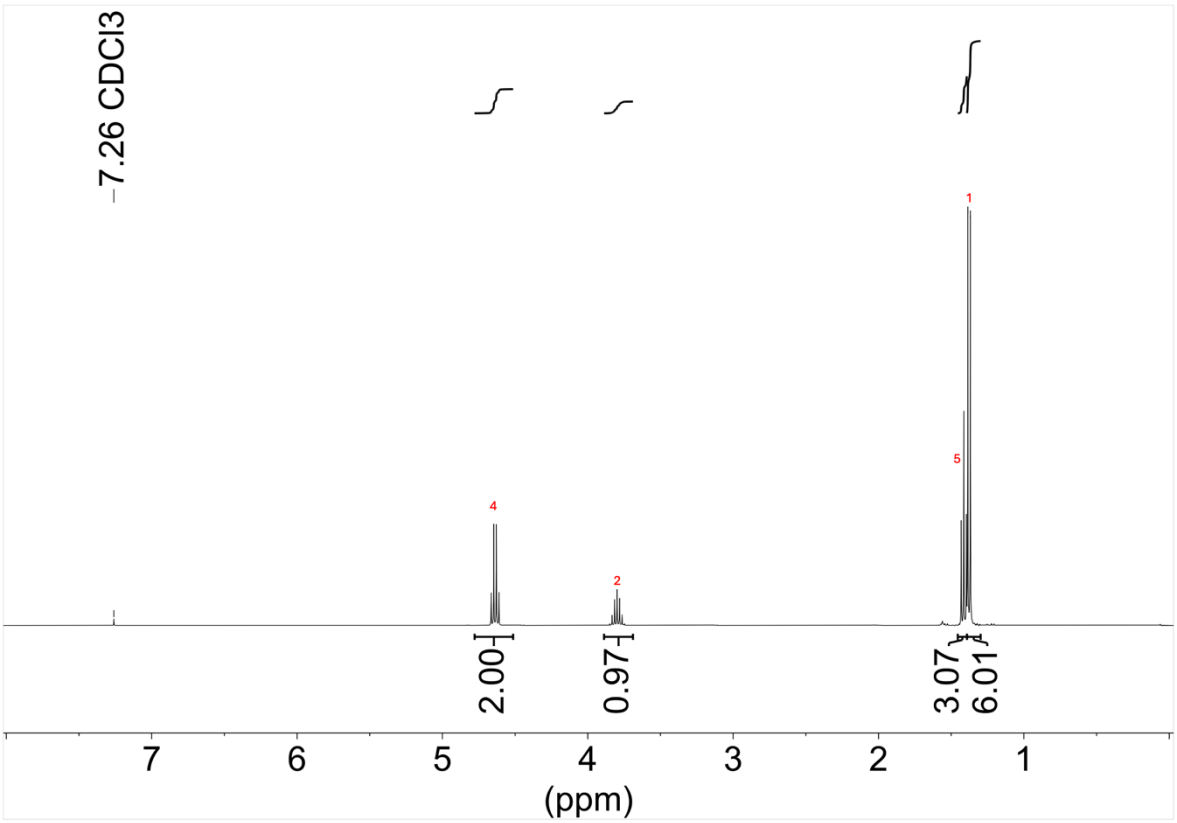


Figure 2.46: **$^{1}$H NMR** (400 MHz, $CDCl_3$) of O-ethyl S-isopropyl carbonodithioate.

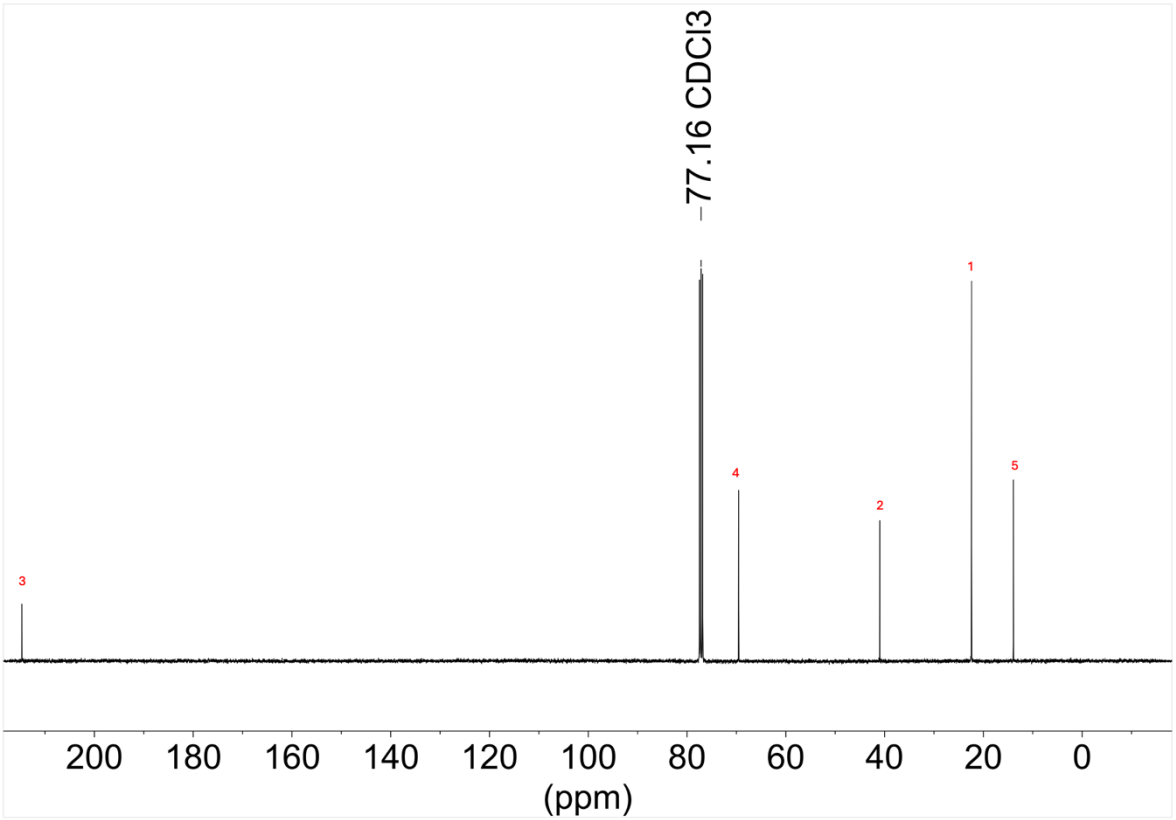


Figure 2.47: **$^{13}$C NMR** (*101 MHz, $CDCl_3$*) of O-ethyl S-isopropyl carbonodithioate.

### 2.5.3 Synthesis of COOH terminated PVAc via PET-MADIX

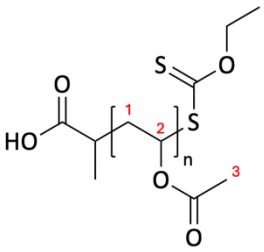


Figure 2.48: Structure of COOH terminated PVAc.

In a typical experiment, EtPAX **1** (14.3 mg, 0.07 mmol, 1.0 eq.) and $Bi_2O_3$ (6.8 mg, 0.015 mmol 0.2 eq.) were added to a solution of destabilised vinyl acetate (3.00 mL, 2.80 g, 32.5 mmol, 442 eq.) in DMSO (3 mL) and DMF (100 µL). The solution was degassed via 3 freeze pump thaw cycles before the vessel was backfilled with argon. The sealed reaction vessel was irradiated with white light (15 W Fluorescent tube, 1010 lm) at rt. The light bulb was set to 2 cm away from the Schlenk flask for the desired time. The polymer was precipitated twice into cold diethyl ether (40 mL), dialysed against acetone before drying and lyophilising from 1,4-dioxane. A colourless solid was obtained. **$^1$H NMR** (*400 MHz, $CDCl_3$*) δ 4.61 – 5.17 (m -br, 1H, *$H_2$*), 2.02 (t -br, 3H, *$H_3$*), 1.96 – 1.75 (m -br, 2H, *$H_1$*). Typical conversion to polymer >70%, calculation shown below with example (Figure 2.52, Equation 29)). Representative organic GPC chromatogram shown in Figure 2.51, typical Đ 1.15 – 1.3.

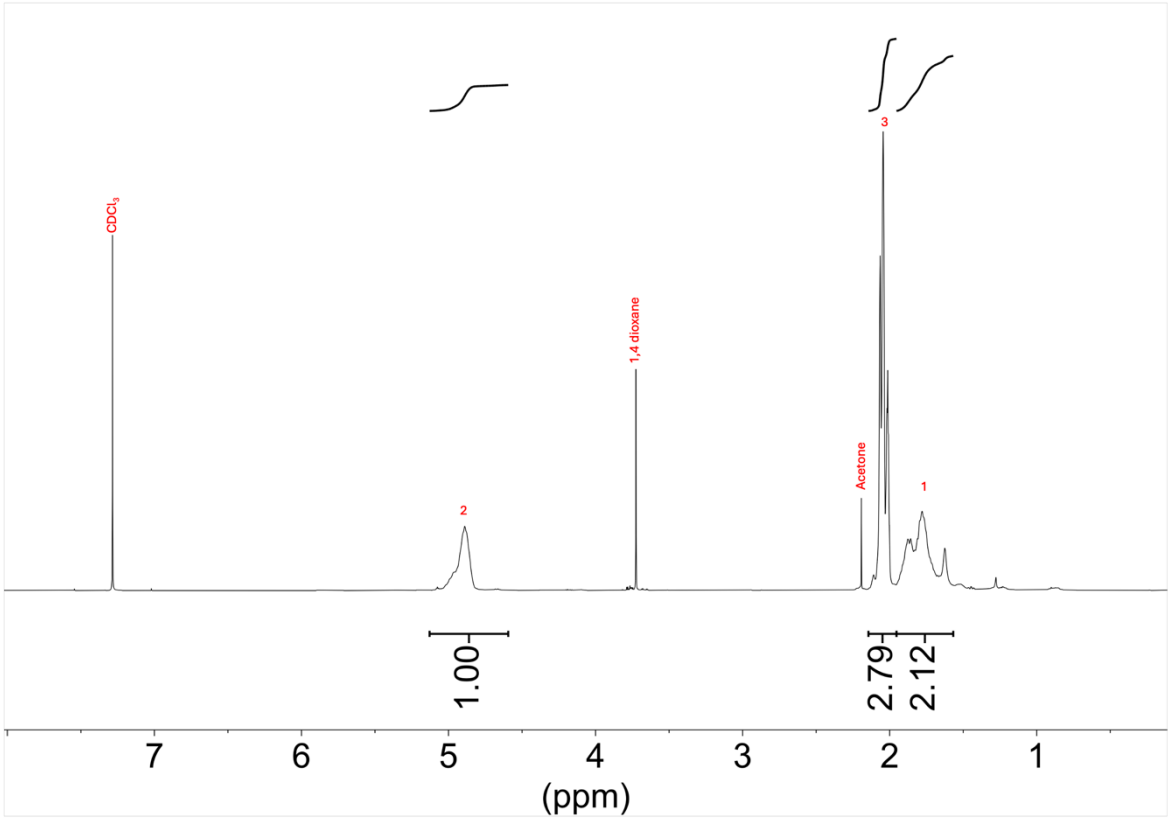


Figure 2.49: **$^{1}$H NMR** (400 MHz, $CDCl_3$) of COOH terminated PVAc.

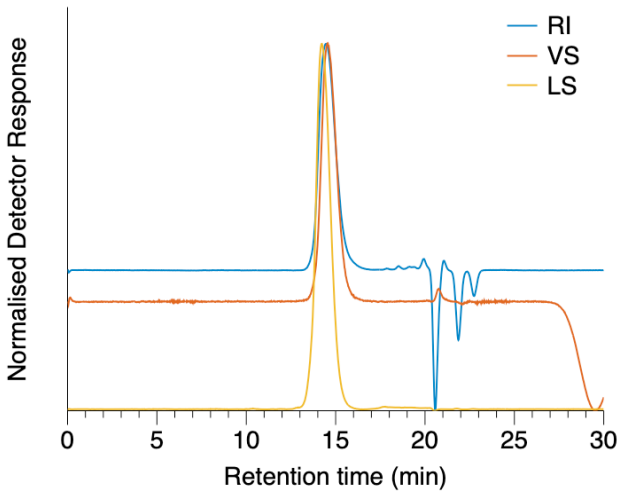


Figure 2.50: Representative GPC of COOH terminated PVAc. 5 mg/mL in THF at 35 °C, 1 mL/min. Triple detection analysis with a differential refractive index detector, a dual-angle light scattering detector (15° and 90°), a viscometer and a pair of PL gel 5 µm Mixed D 300 × 7.5 mm columns with guard column (Polymer Laboratories Inc.) in series.

**Example polymer conversion calculation**

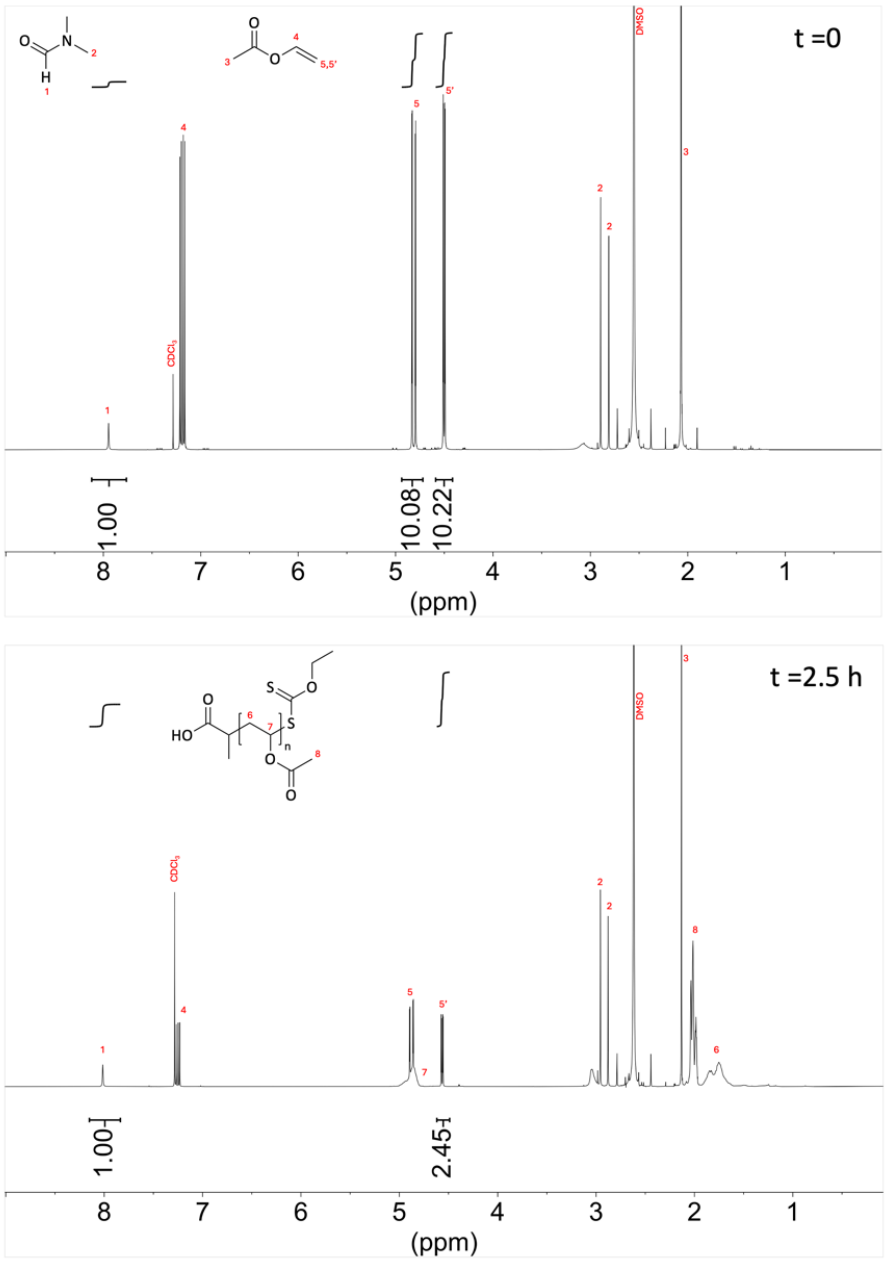


Figure 2.51: Exemplary **$^1$H NMR** spectra (*400 MHz, $CDCl_3$)* showing conversion analysis of VAc polymerisation. Integral of internal reference DMF (δ 8.00 ppm) is set to 1.00 at each time point.

$$Conversion\ \% = \left(1 - \frac{\int H_{5'}^{t=x}}{\int H_{5'}^{t=0}}\right) * 100 \qquad \text{(Equation 29)}$$

e.g.

$$Conversion\ \% = \left(1 - \frac{2.45}{10.22}\right) * 100 = 76\%$$

### 2.5.4 Synthesis of isopropyl terminated PVAc P1-iso via PET-MADIX

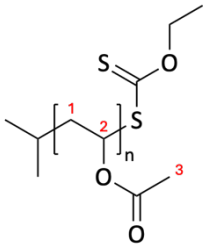


Figure 2.52: Structure of isopropyl terminated PVAc.

**2** (11.8 mg, 0.07 mmol, 1.0 eq.) and $Bi_2O_3$ (6.8 mg, 0.015 mmol 0.2 eq.) were added to a solution of destabilised vinyl acetate (2.00 mL, 2.80 g, 32.5 mmol, 453 eq.) in DMSO (2 mL) and DMF (100 µL). The solution was degassed via argon sparge for 25 mins. The sealed reaction vessel was irradiated with white light (15 W Fluorescent tube, 1010 lm) at rt. The light bulb was set to 2 cm away from the Schlenk flask for the desired time. The polymer was precipitated twice into cold diethyl ether (40 mL), dialysed against acetone before drying and lyophilising from 1,4-dioxane. **P1-iso** was isolated as a colourless solid. **$^1$H NMR** (*400 MHz, $CDCl_3$*) δ 4.78 – 5.09 (m -br, 1H, $H_2$), 1.89 – 2.21 (t -br, 3H, $H_3$), 1.96 – 1.75 (m -br, 2H, $H_1$). Conversion 90%.

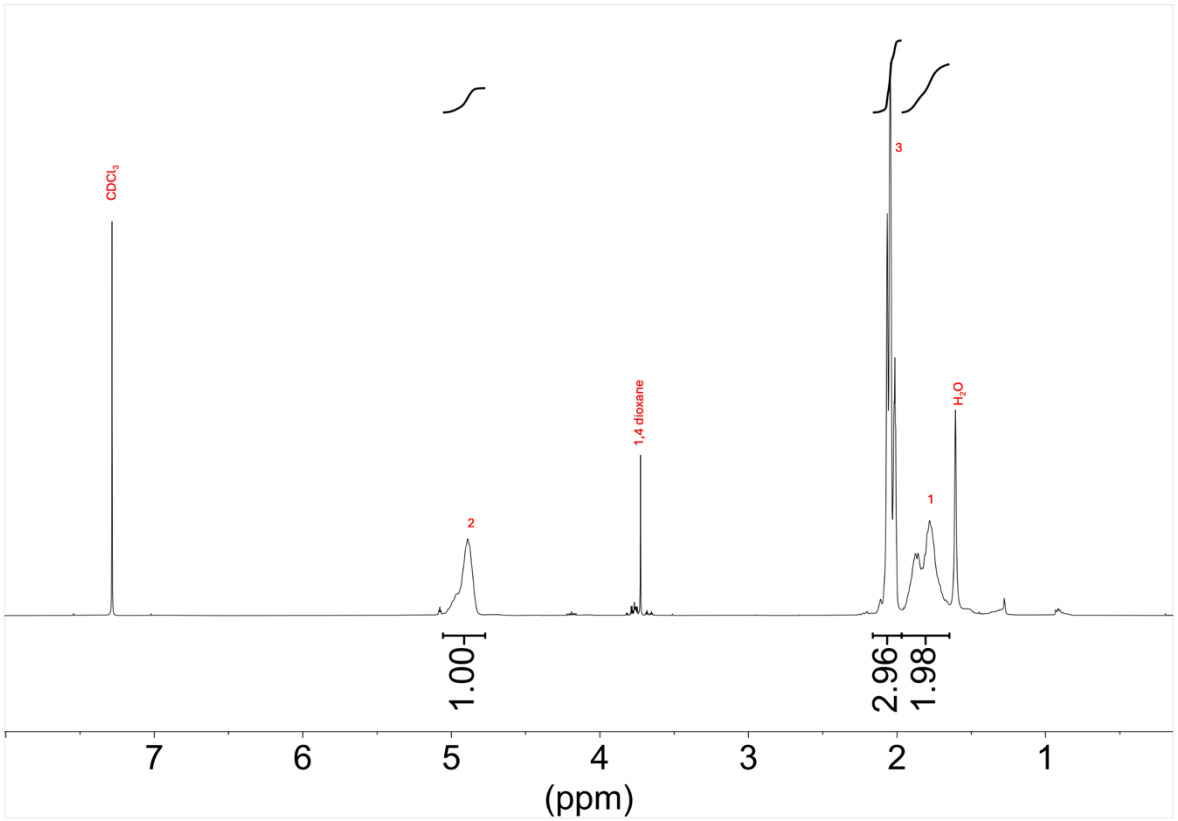


Figure 2.53: **$^1$H NMR** (400 MHz, $CDCl_3$) of isopropyl terminated PVAc.

### 2.5.5 Synthesis of deuterated PVAc P10 via PET-MADIX

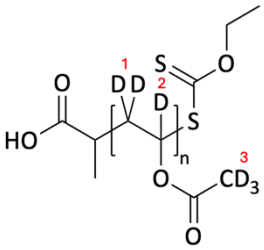


Figure 2.54: Structure of dPVAc.

EtPAX **1** (11.5 mg, 0.06 mmol, 1 eq.) and $Bi_2O_3$ (5.6 mg, 0.012 mmol, 0.2 eq.) were added to a solution of destabilised $d_6$-vinyl acetate (2.00 mL, 2.00 g, 21.71 mmol, 367 eq.) in DMSO (2 mL) and DMF-$d_7$ (100 µL). The solution was degassed via 3 freeze pump thaw cycles before the vessel was backfilled with argon. The sealed reaction vessel was irradiated with white light (15 W Fluorescent tube, 1010 lm) at rt. The light bulb was set to 2 cm away from the Schlenk flask for the desired time. The polymer was dialysed against acetone (6 changes) before drying and lyophilising from 1,4-dioxane. A colourless solid was obtained. **$^2$H NMR** (*77 MHz, $CHCl_3$*) δ 3.90 – 6.30 (s -br, 1D, *$D_2$*), 0.60 – 3.00 (s -br, 3D + 2D, *$D_3$*, *$D_1$*), Typical conversion to polymer >90%.

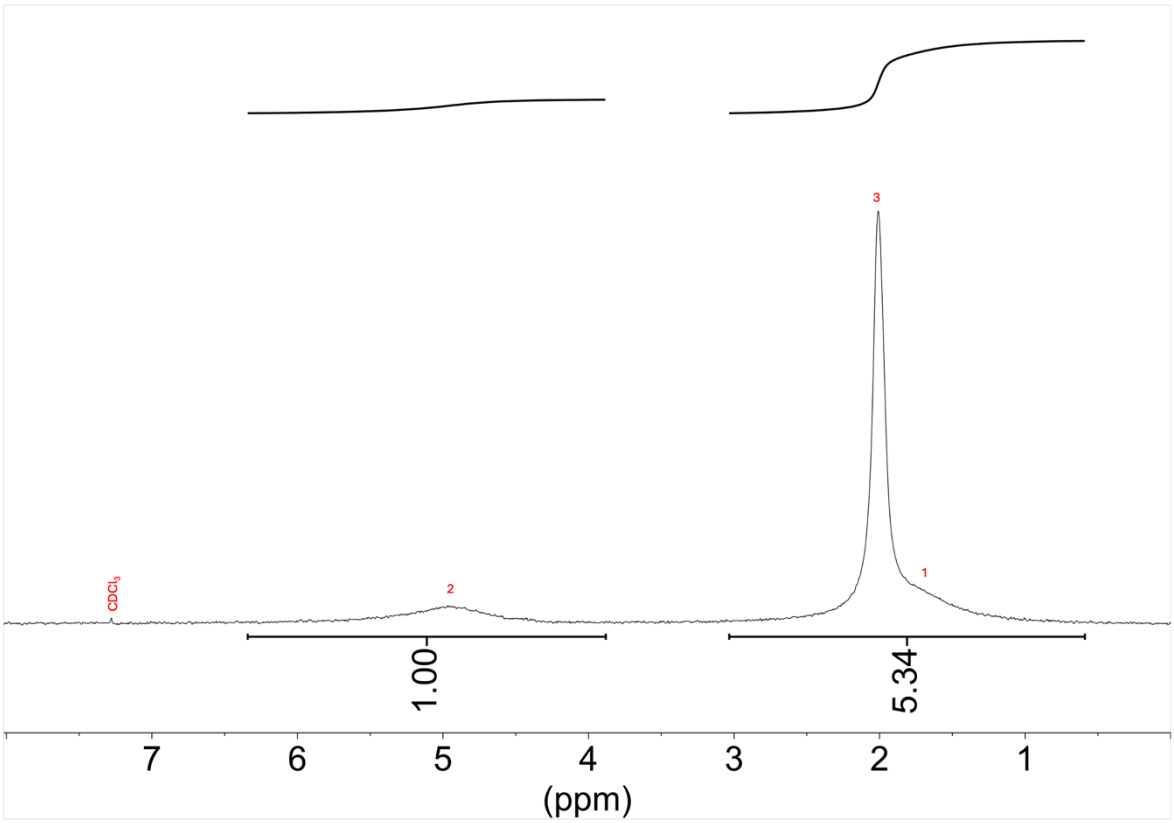


Figure 2.55: **$^{2}$H NMR** (77 MHz, $CHCl_3$) of deuterated PVAc.

### 2.5.6 Complete hydrolysis of polyvinyl acetate to polyvinyl alcohol

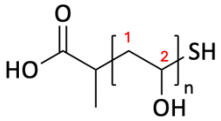


Figure 2.56: Structure of polyvinyl alcohol.

In a typical experiment, polyvinyl acetate (100 mg, $M_n$ 30,100 g mol$^{-1}$, 3.3 µmol) was dissolved in methanol (2 mL) to which sodium hydroxide (200 µL, 1M, 0.2 mmol) was added. The reaction mixture was stirred at 50 °C for 16 h. The reaction mixture was neutralised with dilute HCl (200 µL, 1M, 0.2 mmol). The reaction mixture was then dialysed against deionised water and polyvinyl alcohol was recovered via lyophilisation from water as a white spongy solid. Complete hydrolysis was confirmed by $^1$H NMR spectroscopy, with loss of the acetate resonance at ~δ 2.00 ppm indicative of complete hydrolysis. Representative characterisation data for PVA: **$^1$H NMR** (*400 MHz, $D_2O$*) δ 3.53 – 4.21 (m -br, 1H, $H_2$), 1.68–1.60 (m -br, 2H, $H_1$). Representative aqueous GPC chromatogram shown in Figure 2.59, typical Đ 1.15 – 1.3.

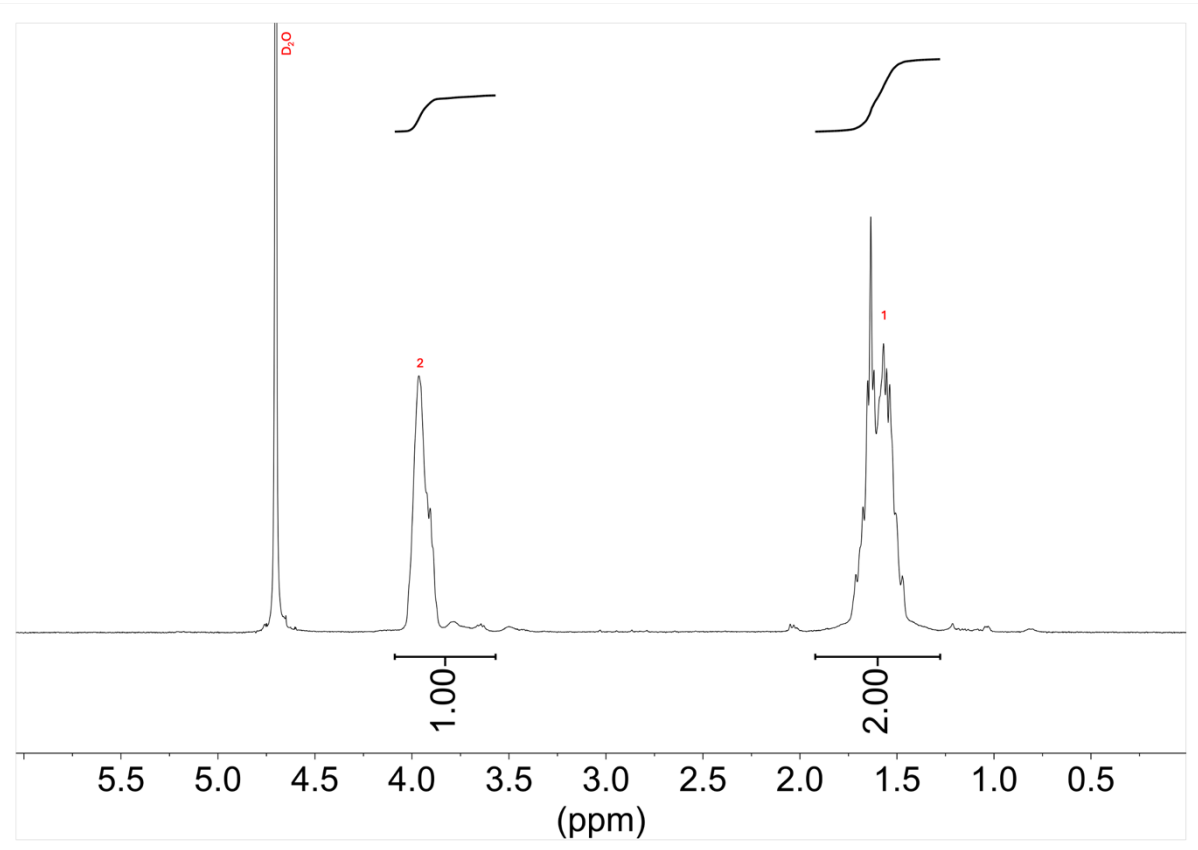


Figure 2.57: **$^1$H NMR** (400 MHz, $D_2O$) of COOH terminated PVA.

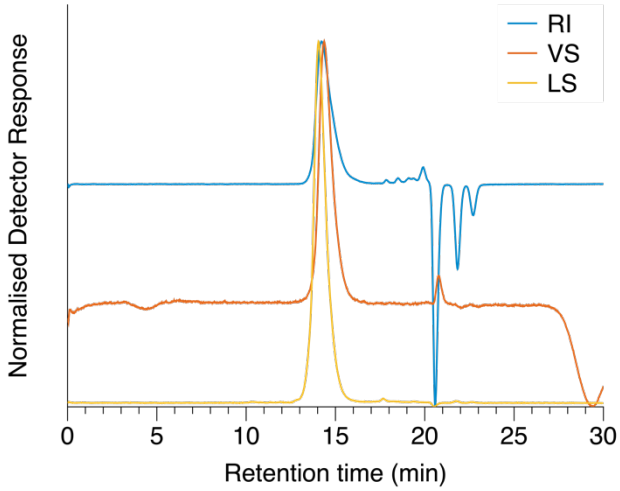


Figure 2.58: Representative GPC of COOH terminated PVA. 3 mg/mL in $NaNO_3$ (10 mM, 2 x 0.02 µm filtered) eluent on an Agilent 1260 instrument equipped with a dRI detector, a dual-angle light scattering detector (15° and 90°), a viscometer, a variable wavelength UV detector and a pair of PL gel 8 µm PL aquagel-OH Mixed-M 300 × 7.5 mm columns with a guard column (Polymer Laboratories Inc.) in series at 35 °C, 1 mL/min.

### 2.5.7 Partial hydrolysis of polyvinyl acetate to polyvinyl alcohol-co-polyvinyl acetate

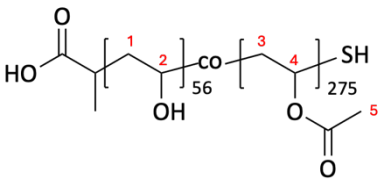


Figure 2.59: Structure of polyvinyl alcohol-co-polyvinyl acetate.

In a typical experiment, polyvinyl acetate (300 mg, $M_n$ 28,500 g mol$^{-1}$, 10.5 µmol) was dissolved in methanol (3 mL) to which dilute sodium hydroxide (150 µL, 0.1 M, 0.2 mmol) was added. The reaction mixture was stirred at 60 °C for 16 h in a sealed vial. The reaction solvent was then allowed to evaporate, and the polymer dissolved in and dialysed against deionised water. Partially hydrolysed polyvinyl acetate was recovered via lyophilisation from water. Degree of hydrolysis was determined by $^1$H NMR spectroscopy. Representative characterisation data for partially hydrolysed PVA: **$^1$H NMR** (*400 MHz, $CDCl_3$*) δ 4.72 – 5.11 (m -br, 1H, $H_4$), 1.93–2.40 (t -br, 3H, $H_5$), 0.93–1.85 (m -br, 2H, $H_1$, $H_3$).

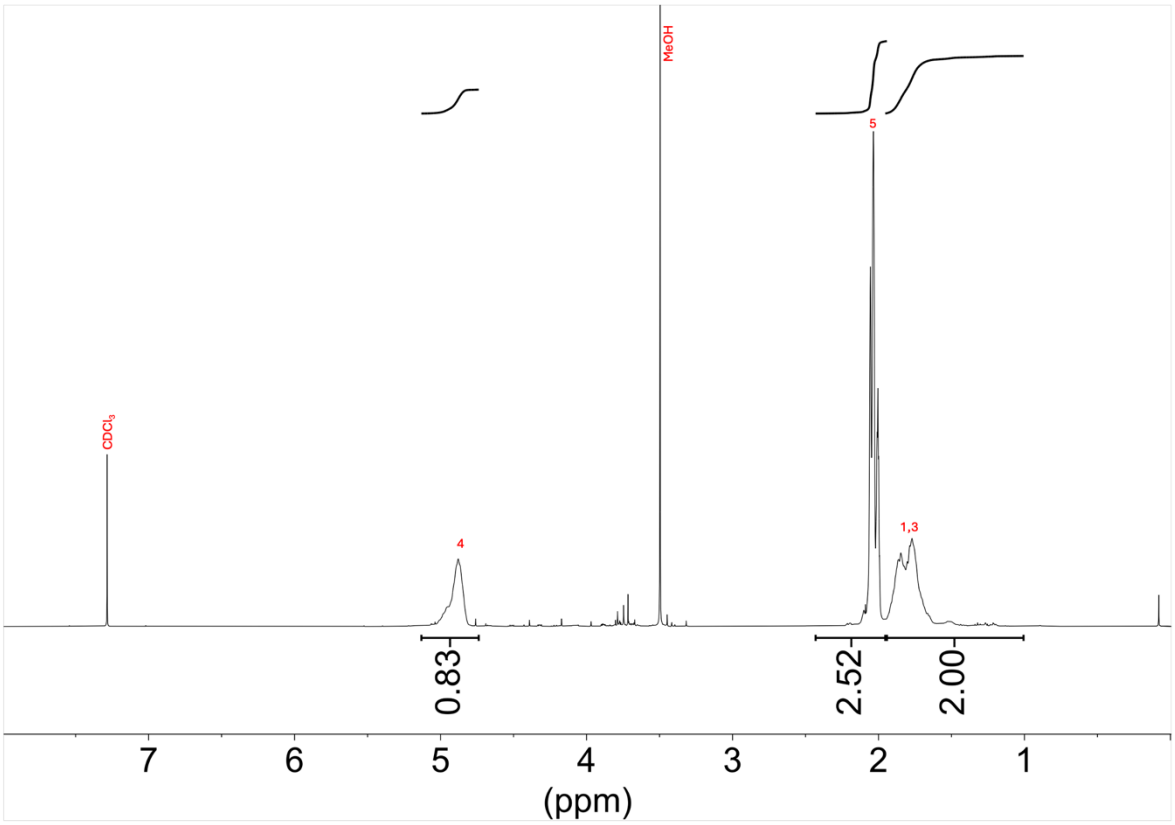


Figure 2.60: **$^1$H NMR** (*400 MHz, $CDCl_3$)* of **P7** polyvinyl alcohol-co-polyvinyl acetate produced via partial hydrolysis. Degree of acetylation = 83% as determined by peak 4, or by dividing peak 5 by 3.

Table 2.11: Summary of partially hydrolysed PVAc synthesised for solid state SANS experiment.

| **Polymer** | **Targeted DH** | **Volume base added / µL** | **Achieved DH** |
|---|---|---|---|
| **P6** | 5% | 50 | 6% |
| **P7** | 10% | 150 | 16% |
| **P8** | 15% | 350 | 21% |
| **P9** | 20% | 400 | 25% |

### 2.5.8 Acetylation of polyvinyl alcohol to polyvinyl alcohol-rand-polyvinyl acetate

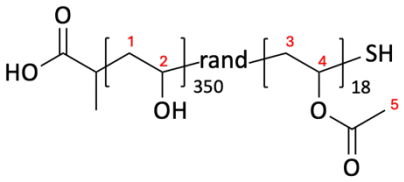


Figure 2.61: Structure of polyvinyl alcohol-rand-polyvinyl acetate.

In a typical experiment, targeting 5 mol% acetyl content, polyvinyl alcohol (300 mg, $M_n$ 16,200 g mol$^{-1}$, 18.5 µmol) was dissolved in DI $H_2O$ (4.5 mL) to which glacial acetic acid (950 µL, 15.8 mmol) and HCl (5M, 545 µL, 2.7 mmol) was added. The solution was stirred at 50 °C for 4 days. The polymer solution was dialysed against DI water (5 bulk changes) before lyophilisation of the purified reaction mixture from water yielding a white spongy solid. **$^1$H NMR** (*400 MHz, $D_2O$*) δ 4.97 – 5.37 (m -br, 1H, $H_4$), 3.44 – 4.17 (m -br, 1H, $H_2$), 2.06 – 2.21 (t -br, 3H, $H_5$), 1.31–2.05 (m -br, 2H, $H_1$, $H_3$). Reagent quantities and GPC analysis for SANS work shown in Table 2.12.

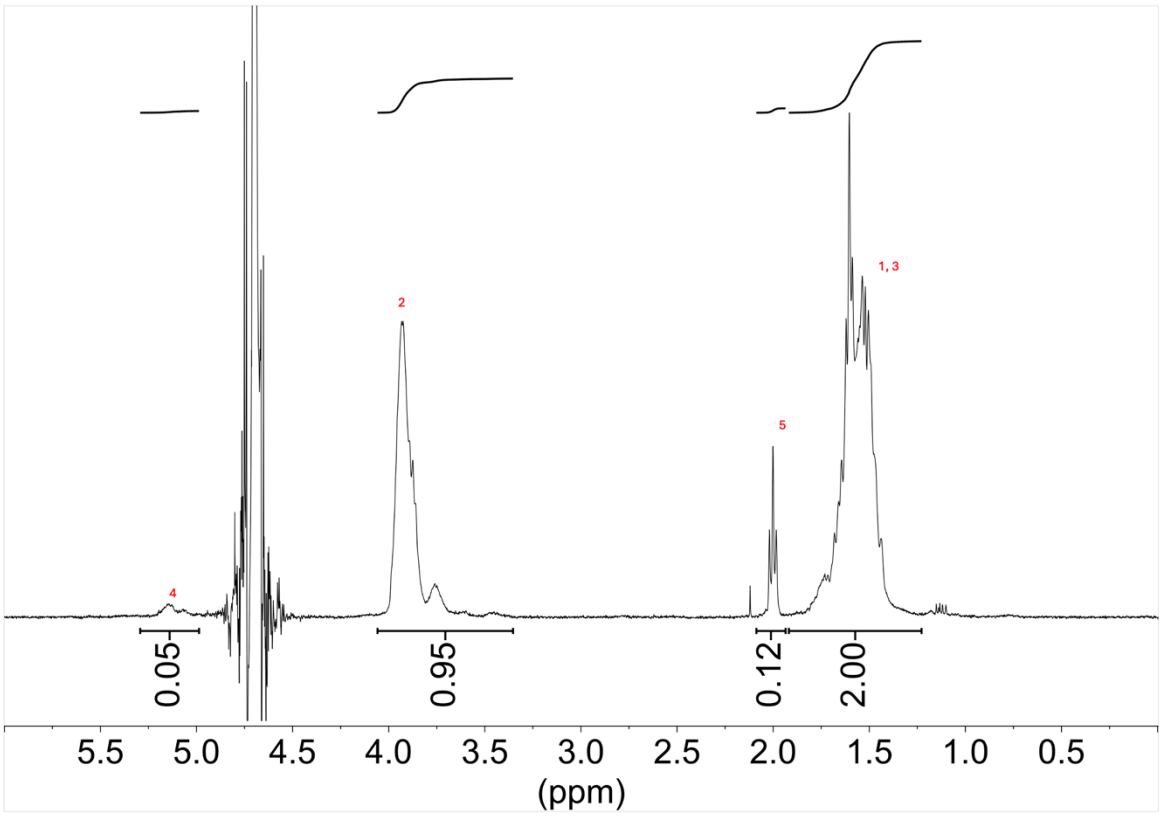


Figure 2.62: **$^1$H NMR** (*400 MHz, $D_2O$)* of **P2** polyvinyl alcohol-rand-polyvinyl acetate produced via partial reacetylation.

Table 2.12: Summary of partially acetylated PVA/c synthesised for solution state SANS experiment.

| **Polymer** | **Targeted DA** | **Volume acetic acid added / µL** | **Volume $H_2O$ added / µL** | **Volume HCl 5M added / µL** | **Achieved DA[a]** | **$M_n$[a] /gmol$^{-1}$** | **$M_n$[b] /gmol$^{-1}$** | **$M_w$[b] /gmol$^{-1}$** | **Đ[b]** |
|---|---|---|---|---|---|---|---|---|---|
| **P2** | 5% | 950 | 4505 | 545 | 4% | 15,100 | 20,800 | 25,100 | 1.21 |
| **P3** | 10% | 1900 | 3554 | 545 | 10% | 16,000 | 23,700 | 28,800 | 1.22 |
| **P4** | 15% | 2485 | 2969 | 545 | 16% | 16,800 | 32,900 | 37,400 | 1.14 |

[a]Determined by $^1$H NMR spectroscopy. [b]Determined by aqueous GPC 10 mM $NaNO_3$, 1 mL/min, narrow standard calibration.

## 2.6 References


1. B. Hammouda, S. Krueger and C. J. Glinka, *J. Res. Natl. Inst. Stand. Technol.*, 1993, **98**, 31-46.
2. L. Lautner, K. Pluhackova, N. K. H. Barth, T. Seydel, W. Lohstroh, R. A. Bockmann and T. Unruh, *Chem. Phys. Lipids.*, 2017, **206**, 28-42.
3. M. M. Castellanos, A. McAuley and J. E. Curtis, *Comput. Struct. Biotechnol. J.*, 2017, **15**, 117-130.
4. H. O'Neill, R. Shah, B. R. Evans, J. He, S. V. Pingali, S. P. Chundawat, A. D. Jones, P. Langan, B. H. Davison and V. Urban, *Methods Enzymol.*, 2015, **565**, 123-146.
5. D. P. Hoogerheide, V. T. Forsyth and K. A. Brown, *Phys. Today*, 2020, **73**, 36-42.
6. U. Betz, A. Sturm, J. F. Loeffler, W. Wagner, A. Wiedenmann and H. Hahn, *NSM*, 1999, **12**, 689-692.
7. A. J. Allen, *JACerS*, 2005, **88**, 1367-1381.
8. A. J. Allen, S. Krueger, G. G. Long, H. M. Kerch, H. Hahn and G. Skandan, *NSM*, 1996, **7**, 113-126.
9. R. Raut Dessai, J. A. E. Desa, D. Sen and S. Mazumder, *J. Alloys Compd.*, 2013, **564**, 125-129.
10. P. Strunz, G. Schumacher, R. Vaßen, A. Wiedenmann and V. Ryukhtin, *Scr. Mater.*, 2006, **55**, 545-548.
11. P. G. Sanders, J. A. Eastman and J. R. Weertman, *Acta. Mater.*, 1998, **46**, 4195-4202.
12. S. Risse, E. Hark, B. Kent and M. Ballauff, *ACS Nano*, 2019, **13**, 10233-10241.
13. J. Banhart, D. Bellmann and H. Clemens, *Acta. Mater.*, 2001, **49**, 3409-3420.
14. S. Mühlbauer, D. Honecker, É. A. Périgo, F. Bergner, S. Disch, A. Heinemann, S. Erokhin, D. Berkov, C. Leighton, M. R. Eskildsen and A. Michels, *J. Rev. Mod. Phys.*, 2019, **91**, 1-75.
15. S. Seidlmayer, J. Hattendorff, I. Buchberger, L. Karge, H. A. Gasteiger and R. Gilles, *J. Electrochem. Soc.*, 2015, **162**, A3116-A3125.
16. P. J. Flory, *J. Chem. Phys.*, 1942, **10**, 51-61.
17. M. Rubinstein and R. H. Colby, *Polymer physics*, Oxford university press, 2003.
18. P. G. d. Gennes, *Scaling concepts in polymer physics*, Cornell University Press, Ithaca [N.Y.] ;, 1979.
19. B. Hammouda, *Polym. Rev.*, 2010, **50**, 14-39.
20. N. Kardjilov, I. Manke, A. Hilger, M. Strobl and J. Banhart, *Mater. Today*, 2011, **14**, 248-256.
21. C. M. Jeffries, J. Ilavsky, A. Martel, S. Hinrichs, A. Meyer, J. S. Pedersen, A. V. Sokolova and D. I. Svergun, *Nat. Rev. Methods Primers*, 2021, **1**, 70.
22. A. J. Jackson, *Introduction to Small-Angle Neutron Scattering and Neutron Reflectometry*, 2008.
23. J. S. Higgins, H. C. Benoît and H. Benoît, *Polymers and Neutron Scattering*, Clarendon Press, 1996.
24. C. Barner-Kowollik, P. Vana and T. P. Davis, in *Handbook of Radical Polymerization*, 2002, pp. 187-261.
25. R. A. Pethrick and J. V. Dawkins, *Modern techniques for polymer characterisation / edited by R.A. Pethrick and J.V. Dawkins*, Wiley, Chichester, 1999.
26. O. Glatter and O. Kratky, *Small Angle X-ray Scattering*, Academic Press, London, 1982.
27. Sasview, sasview.org, (accessed 26/09/2024).

28. A. S. Brunacci, F. T. Kiff, R. W. Richards, R. L. Thompson and S. M. King, *Polym. J.*, 2000, **41**, 2557-2567.
29. G. ten Brinke, in *Polymer Science: A Comprehensive Reference*, eds. K. Matyjaszewski and M. Möller, Elsevier, Amsterdam, 2012, pp. 287-313.
30. K. Jain, R. Vedarajan, M. Watanabe, M. Ishikiriyama and N. Matsumi, *Polym. Chem.*, 2015, **6**, 6819-6825.
31. J. Seuring and S. Agarwal, *ACS Macro Lett.*, 2013, **2**, 597-600.
32. J. Seuring and S. Agarwal, *Macromol. Rapid. Commun.*, 2012, **33**, 1898-1920.
33. H. C. Haas, R. D. Moreau and N. W. Schuler, *J. Polym. Sci. Part A-2*, 2003, **5**, 915-927.
34. P. J. Flory, *J. Chem. Phys.*, 1941, **9**, 660-660.
35. M. L. Huggins, *J. Am. Chem. Soc.*, 1942, **64**, 1712-1719.
36. H. B. Eitouni and N. P. Balsara, in *Physical Properties of Polymers Handbook*, 2007, ch. Chapter 19, pp. 339-356.
37. M. W. Matsen and F. S. Bates, *J. Chem. Phys.*, 1997, **106**, 2436-2448.
38. M. W. Matsen and F. S. Bates, *Macromolecules*, 1996, **29**, 1091-1098.
39. L. A. Utracki and C. A. Wilkie, *Polymer Blends Handbook*, 2014.
40. T. H. Russell, B. J. Edwards and B. Khomami, *EPL*, 2014, **108**, 66003.
41. J. Dudowicz, M. S. Freed and K. F. Freed, *Macromolecules*, 2002, **24**, 5096-5111.
42. P. G. de Gennes, *Scaling Concepts in Polymer Physics*, Cornell University Press, 1979.
43. H. A. Barnes, I. o. Non-Newtonian and F. Mechanics, *A Handbook of Elementary Rheology*, University of Wales, Institute of Non-Newtonian Fluid Mechanics, 2000.
44. H. Barnes, *An introduction to rheology*, Elsevier Science Publishers, 1989.
45. C. W. Macosko, *Rheology principles*, 1994.
46. T. G. Mezger, *The Rheology Handbook: For Users of Rotational and Oscillatory Rheometers*, Vincentz Network, 2006.
47. C. A. Finch, *Polyvinyl alcohol: developments*, 1992.
48. K. Hakobyan, T. Gegenhuber, C. S. P. McErlean and M. Mullner, *Angew. Chem. Int. Ed.*, 2019, **58**, 1828-1832.
49. T. Congdon, P. Shaw and M. I. Gibson, *Polym. Chem.*, 2015, **6**, 4749-4757.
50. T. Moritani and Y. Fujiwara, *Macromolecules*, 1977, **10**, 532-535.
51. Y. I. Denisova, L. B. Krentsel', A. S. Peregudov, E. A. Litmanovich, V. V. Podbel'skiy, A. D. Litmanovich and Y. V. Kudryavtsev, *Polym. Sci., Ser. B*, 2012, **54**, 375-382.
52. A. M. Fuentes-Caparros, K. McAulay, S. E. Rogers, R. M. Dalgliesh and D. J. Adams, *Molecules*, 2019, **24**, 3855.
53. T. Sakai, in *Physics of Polymer Gels*, 2020, pp. 1-22.
54. B. Hammouda, D. Ho and S. Kline, *Macromolecules*, 2002, **35**, 8578-8585.
55. B. Hammouda, D. L. Ho and S. Kline, *Macromolecules*, 2004, **37**, 6932-6937.
56. B. Hammouda and D. L. Ho, *J. Polym. Sci. B Polym. Phys.*, 2007, **45**, 2196-2200.
57. S. M. Kimani, R. L. Thompson, L. R. Hutchings, N. Clarke, S. M. R. Billah, V. G. Sakai and S. E. Rogers, *Macromolecules*, 2014, **47**, 2062-2071.
58. A. Z. Akcasu and C. C. Han, *Macromolecules*, 1979, **12**, 276-280.
59. A. Rey, J. J. Freire, M. Bishop and J. H. R. Clarke, *Macromolecules*, 1992, **25**, 1311-1315.
60. L. J. Fetters, D. J. Lohse, D. Richter, T. A. Witten and A. Zirkel, *Macromolecules*, 1994, **27**, 4639-4647.
61. C. Tanford, *Adv. Protein Chem.*, 1968, **23**, 121-282.
62. C. Boyer, J. Liu, V. Bulmus and T. P. Davis, *Aust. J. Chem.*, 2009, **62**.
63. M. E. Sears, *Sci. World J.*, 2013, **2013**, 219840.

64. A. A. Bonapasta, F. Buda, P. Colombet and G. Guerrini, *Chem. Mater.*, 2002, **14**, 1016-1022.
65. M. Muthukumar, *Macromolecules*, 2017, **50**, 9528-9560.
66. A. Dobrynin and M. Rubinstein, *Prog. Polym. Sci.*, 2005, **30**, 1049-1118.
67. Y. I. Denisova, G. A. Shandryuk, L. B. Krentsel', I. V. Blagodatskikh, A. S. Peregudov, A. D. Litmanovich and Y. V. Kudryavtsev, *Polym. Sci., Ser. A*, 2013, **55**, 385-392.
68. O. V. Noah, A. D. Litmanovich and N. A. Platé, *J. Polym. Sci., Polym. Phys. Ed.*, 2003, **12**, 1711-1725.
69. P. J. Flory, *Principles of Polymer Chemistry*, Cornell University Press, 1953.
70. E. Patyukova, E. Xi and M. R. Wilson, *Macromolecules*, 2021, **54**, 2763-2773.
71. H. E. Gottlieb, V. Kotlyar and A. Nudelman, *J. Org. Chem.*, 1997, **62**, 7512-7515.
72. B. H. Alexander, S. I. Gertler, T. A. Oda, R. T. Brown, R. W. Ihndris and M. Beroza, *J. Org. Chem.*, 2002, **25**, 626-632.

# Chapter 3: Two component polyvinyl alcohol film interface diffusion studied via ion beam analysis

## 3.1 Introduction

Polymer interdiffusion in multilayer systems is a key factor influencing the performance of SUD pods. Understanding the diffusion behaviour at polymer-polymer interfaces is crucial for optimising the capsule seal as well as dissolution rates, and mechanical strength. This chapter explores the synthesis and characterisation of interdiffusion of PVA in a two-layer thin film system using ion beam analysis (IBA) techniques, specifically Particle Induced X-ray Emission (PIXE) and Rutherford Backscattering Spectrometry (RBS). These methods offer a cross-sectional study of the polymer interface, revealing how varying the DH impacts diffusion. RBS provides precise, quantitative measurements of diffusion through well-known cross sections, while PIXE offers stronger signals, making it ideal for detecting low bromine concentrations and mapping the distribution of synthesised PVA in a two-layer system. Together, these techniques provide a comprehensive view of interdiffusion, overcoming the limitations of other analysis methods in bilayer systems.

The system under investigation consists of two distinct PVA layers: a commercially available high molecular weight PVA layer and a lab-synthesised PVA layer modified with a brominated end group. The bromine atoms act as a detectable marker, enabling location of the synthesised polymer within the multilayer structure. By using PIXE and RBS, the diffusion depth of the brominated PVA into the commercial PVA layer can be tracked, providing insights into how the DH affects interlayer diffusion. The commercial PVA is of high molecular weight (~130 kDa, DP ~ 2,700) to allow the assumption that diffusion predominantly occurs from the PVA-Br ($M_n$ ~17 kDa, DP ~ 330) into the commercial PVA, rather than vice versa.

The subsequent sections will detail the experimental methods, data analysis approaches, and key results, highlighting the influence of polymer composition on the interdiffusion of PVA in thin film systems.

### 3.1.1 Rutherford backscattering

RBS is an ion scattering technique used to determine the composition of thin films. It is sensitive to heavy elements in a light matrix, as heavier elements possess a greater number of protons in the nucleus, making them more repulsive to an incoming proton beam, and because of their greater size, increasing the chance of deflection. This motivated the design for a brominated polymer end group label in this work. RBS works by counting the number and energy of deflected protons from a sample when irradiated by a high energy proton beam. The technique relies on Columbic repulsion between the dense positive atomic nucleus and the proton beam (Figure 3.1, in the original experiment by Rutherford and Geiger, alpha particles were used). In RBS, nuclear interactions/reactions are not considered, however, if the particle beam is of sufficient energy, then these can occur which cause more complicated backscattering, usually described as elastic backscattering, "EBS". Usually, silicon solid state detectors are used in RBS measurements for the determination of the energy of backscattered particles. The scattered ions create electron-hole pairs in the detector, which are separated by an applied electric field and create a charge pulse. The number of electron-hole pairs is proportional to the ion energy. RBS is unique in that it does not require the use of reference standards, instead, quantification is achieved due to the backscattering cross section for each element being known.

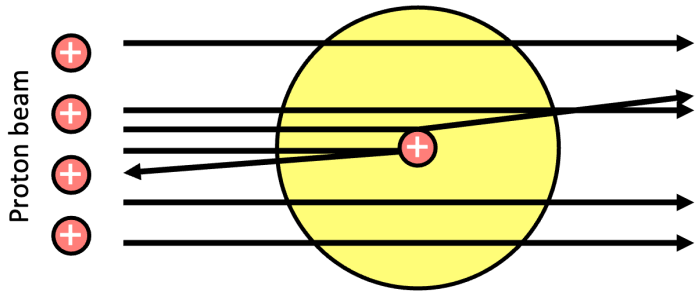


Figure 3.1: Rutherford model of the atom, with proton beam deflected as it approaches the positively charged nucleus, causing some protons to be scattered, while others pass through the atom unperturbed.

### 3.1.2 PIXE

Particle/proton induced X-ray emission (PIXE) spectroscopy is a highly sensitive technique used to study the elemental composition of materials. First developed in the 1970s,[1] PIXE utilises the interaction between high energy charged particles (usually protons or alpha particles) and a target material to induce the emission of characteristic X-rays from the atoms within the sample. The process occurs when the incident particles displace inner shell electrons, leading to electronic transitions that release energy in the form of X-rays (Figure 3.2).[2] The energy of the released X-ray is characteristic of the nuclei it originated from, providing elemental composition data for the sample. The detection system is very similar to energy dispersive X-ray analysis (EDX), which is widely used for elemental analysis in electron microscopy experiments.

PIXE is useful for detecting a wide range of elements, from sodium all the way to uranium, typically to parts per million levels or lower.[3] Furthermore, the technique is able to provide spatial resolution when combined with focussed beams (micro-PIXE) that can be raster-scanned across the samples surface to create a PIXE spectrum for each sample point.[4] From these spectra, elemental maps can be constructed, which show the variation of an element's concertation across the sample's surface. This method of scanning the sample surface to produce an elemental map is the technique exploited to image the polymer-polymer interface during this experiment, making use of elemental enrichment through chemical tagging of polymer chains.

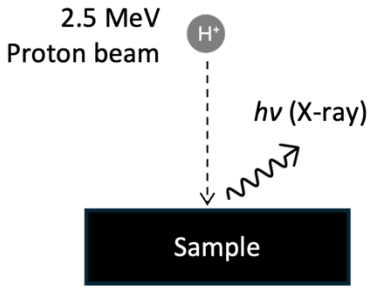


Figure 3.2: Release of an X-ray as a result of sample bombardment by 2.5 MeV proton beam.

### 3.1.3 Time of flight elastic recoil detection analysis

ToF-ERDA is used in this work to determine the bromine concentration per sample, expressed as an atomic percentage, to ensure the polymer samples retained their bromine component. Analysis involves directing a primary ion beam, for example, iodine ions, into the sample at a near-glancing angle (Figure 3.3). This interaction causes atoms from the sample to be recoiled and ejected forward. These recoiled atoms pass through two timing foils, $T_1$ and $T_2$, which serve as start and stop pulse counters, allowing the measurement of their time of flight.

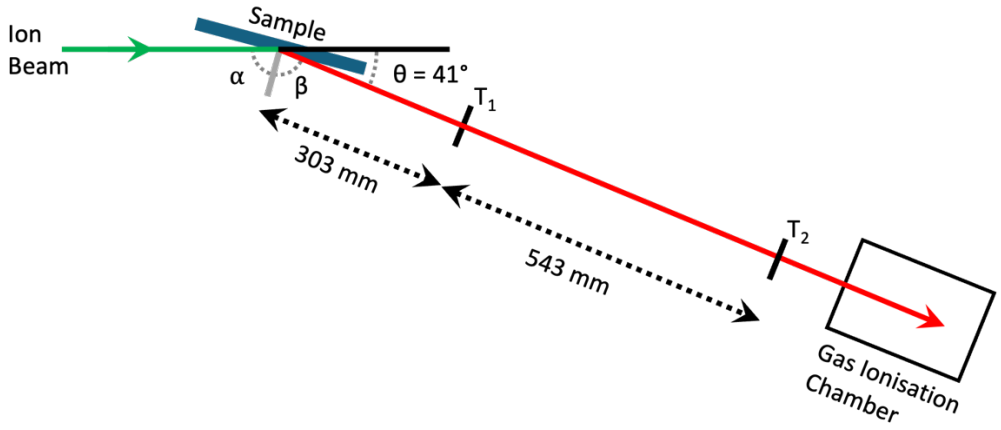


Figure 3.3: Diagram of ToF-ERDA beamline showing incident ion beam bombarding sample, ejected recoiled ions passing through the first and second timing detectors ($T_1$ and $T_2$) as well as the gas ionisation chamber which contains the energy detector. Both α (incident) and β (exit) angles = 69.5°, with θ (scattering) angle = 41°.

After passing through the timing foils, the recoiled atoms enter a gas ionization chamber through a silicon nitride (SiN) window, where their energy is measured. Since atoms of the same energy but different masses have distinct velocities (as per Equation 30), differentiation of signals from various elements within the sample is possible.

$$E = \frac{1}{2}mv^2 \qquad \text{(Equation 30)}$$

where *E* is the energy, *m* is the particle mass and *v* is the velocity.

By plotting the time of flight (ToF) of each recoiled atom against its energy, a histogram is produced where atoms of the same mass form distinct curves, separated from atoms of other masses. Additionally, forward-scattered ions can be identified in the histogram, providing further analytical insights, particularly about atoms heavier than the primary beam species.

### 3.1.4 Soluble unit dose PVA pouch manufacturing

Due to the manufacturing methods employed in the production of SUD pouches (Chapter 1, Figure 1.4), the samples analysed in this study closely mimic the form and structure of commercially available products. Specifically, the SUD pouches feature a two-layer system with an entangled polymer-polymer interface, which has been developed and equilibrated under high humidity conditions, reflecting the typical production environment. This layered structure, along with the unique interface characteristics formed during the manufacturing process, plays a critical role in the functional properties of the final product, such as barrier performance, mechanical strength, and chemical resistance.

In this chapter, these polymer-polymer interfaces are analysed using a direct approach that is specifically suited to the materials and dimensions typical of SUD pouch production. Unlike other analytical methods that may involve simplified or altered forms of the materials, such as that conducted in the FRAP chapter (Chapter 4), this technique allows for the examination of films with thicknesses that are comparable to those found in actual commercial pouches (~100 – 200 μm). As such, it provides a unique and direct assessment of the impact of DH% that, in part, governs the performance of SUD pods. By developing a heavy atom polymer labelling method, layered samples mimicking the industrial product were created, aged and analysed to examine the depth of polymer diffusion as a function of varied DH%.

To capture a DH% range of commercial interest, three degrees of hydrolysis that are used industrially were targeted. Each lab-synthesised sample would be combined with a high molecular weight

commercial polymer to provide the other component of the film. The polymers proposed to synthesise for ion beam analysis are shown (Figure 3.4).

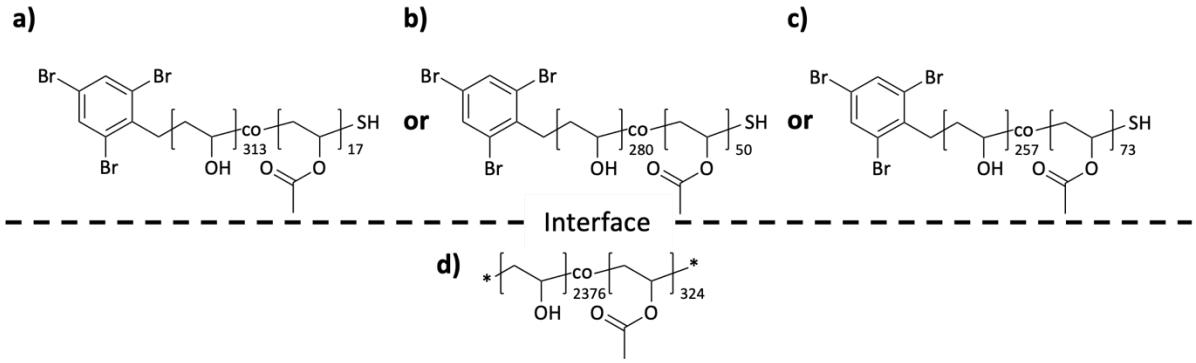


Figure 3.4: Proposed polymers for ion beam analysis. a) **P14** DH 95%, b) **P15** DH 85%, c) **P16** DH 78%, d) commercial polymer Mowiol 18-88 (Approx. DP = 2700, DH 88%).

### 3.2 Aims

This chapter aims to provide analysis of the interfaces in a library of PVA films, each with varying degrees of acetylation. The work will focus on how the level of acetylation influences the interdiffusion of a low molecular weight PVA into a high molecular weight PVA matrix. To achieve this, a combination of advanced characterisation techniques, namely Rutherford Backscattering Spectrometry (RBS) and Particle Induced X-ray Emission (PIXE) spectroscopy, will be employed. These techniques will facilitate the precise determination of bromine concentration within the cross sections of each two-component film. By analysing the bromine distribution across these films, the visualisation and quantification of the interdiffusion of bromine-tagged PVA into a high molecular weight PVA matrix will be visible. This will offer insights into the extent of diffusion in films that are aged in conditions similar to those used in soluble unit dose pod manufacturing.

Furthermore, the modification of PET-MADIX synthesised PVAs to incorporate bromine labels will serve as a critical tool for distinguishing between the different polymer layers within the films. The introduction of bromine into the polymer matrix will enable clear differentiation of the layers, facilitating an improved understanding of the interfacial regions and their influence on the overall

structure of the films. This methodology will provide a detailed picture of the interfaces of PVA-based materials, contributing to the development of PVA films for use in soluble unit dose pod manufacturing.

## 3.3 Results and discussion

Various methods were explored to design and synthesise a stable bromine-containing probe to attach to the end of polymer chains, in order to enable detection via ion beam techniques. Ultimately two methods of labelling polymer chains were attempted: end group modification post polymerisation and a brominated chain transfer agent.

To maintain an unreactive bromine species stable from substitution and elimination during the polymer hydrolysis, an aromatic system was desired to inhibit accessibility of the C-Br σ* LUMO. A further requirement for the aromatic brominated component was at least a single proton environment to enable attachment quantification via $^{1}$H NMR spectroscopy. Based on commercially available brominated raw materials, it was decided that the brominated part of the label would be of the form:

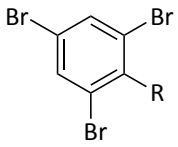


Figure 3.5: Generic brominated label structure.

### 3.3.1 End group synthesis – maleimide based bromine tag

By synthesising a maleimide functionalised end group label, the terminal thiol of the PVA chain could be exploited to provide a reactive end group suitable for Michael addition chemistry with the maleimide to occur. The route to synthesising the maleimide end group via an aliphatic amine was not trivial, with several reactions trialled prior to success (Scheme 3.1 and 3.2). It is suspected that the steric bulk of the aromatic bromine resulted in hindered accessibility to any reactive group directly

attached to the aromatic system, such as phenol and aniline derivatives. Additionally, aniline is a poor nucleophile, especially when it contains electron-withdrawing substituents like bromine. This is due to resonance involving the nitrogen lone pair, which reduces the electron density on the nitrogen and further decreases the reactivity of the aniline $-NH_2$ group.[5]

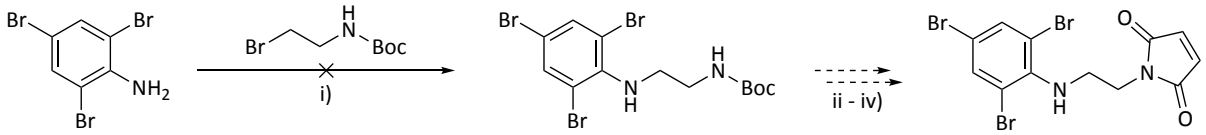


Sceheme 3.1: Failed reaction between 2,4,6-tribromoaniline and *tert*-butyl (2-bromoethyl)carbamate. i) MeCN, $Cs_2CO_3$, 78 °C, ii) 20% TFA in $CH_2Cl_2$, rt; iii) EtOH, maleic anhydride, rt; iv) $Ni(OAc)_2$, $Ac_2O$, 65 °C, 48 h.

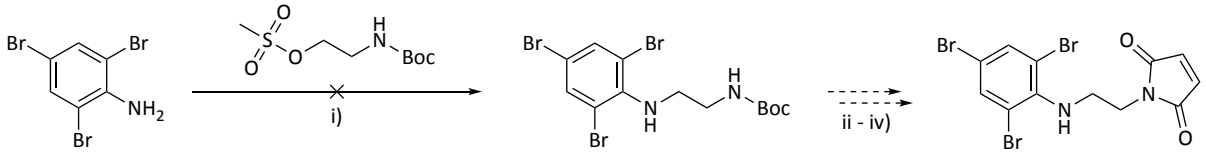


Sceheme 3.2: Failed reaction between 2,4,6-tribromoaniline and 2-((*tert*-butoxycarbonyl)amino)ethyl methanesulfonate. i) MeCN, $Cs_2CO_3$, 78 °C, ii) 20% TFA in $CH_2Cl_2$, rt; iii) EtOH, maleic anhydride, rt; iv) $Ni(OAc)_2$, $Ac_2O$, 65 °C, 48 h.

The successful reaction incorporates an amide formed from tribromobenzoic acid and a di-amine linker (Scheme 3.3) to allow subsequent reaction without the concern of steric hindrance from the bromine end of the tag.

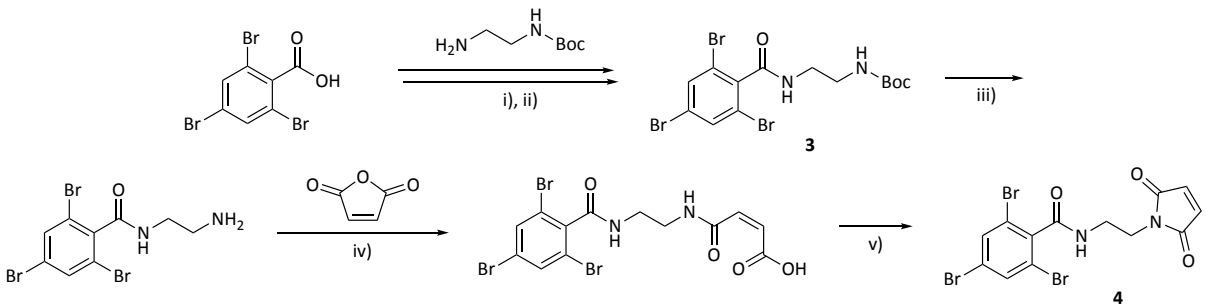


Scheme 3.3: Synthetic route to produce maleimide bromine tag (**4**) via five step synthesis. i) $PBr_5$, 90 °C, 3h (not isolated); ii) $CH_2Cl_2$, 0 °C (78% yield); iii) 20% TFA in $CH_2Cl_2$, rt (79% yield); iv) EtOH, maleic anhydride, rt; v) $Ni(OAc)_2$, $Ac_2O$, 65 °C, 48 h (64% yield).

Following successful synthesis of **4**, it was attached to a thiol terminated PVA which had been synthesised via PET-MADIX (Scheme 3.4). The PVA-SH was split into three batches for subsequent

attachments. All attachments contained TCEP·HCl to reduce formation of disulfides between polymer chains, and triethylamine to aid deprotonation of the thiol, and to neutralise the HCl from the TCEP. As the PVA had been synthesised by base hydrolysis of PVAc, all xanthate end groups were presumed to have been removed, unmasking the terminal thiol, and so no hexylamine was added as is typical for these types of end group reactions.

A variety of conditions were trialled (Scheme 3.4, Table 3.1), with varying degrees of functionalisation, likely due to the solubility of the polymer and maleimide in each reaction. The DMSO-only system yielded the highest attachment as shown in Table 3.1, with 97% attachment. The GPC traces in Figure 3.6 also confirm covalent attachment to the polymer chains as the UV peak appears at the same retention time as the polymer RI peak. As these were trial reactions, the PVA utilised was of broad Đ. It is not fully understood why, when the same PVA was utilised for each attachment, that the $M_n$ , $M_w$ and Đ vary between samples (Table 3.1), however, it is speculated that the end group tag may be influencing polymer behaviour in the size exclusion columns.

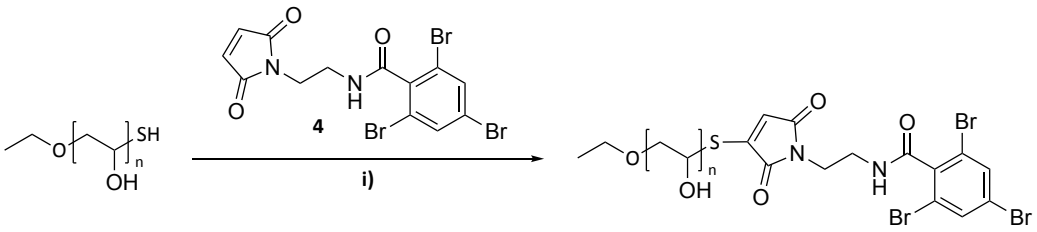


Scheme 3.4: End group attachment of **4** to PVA-SH. i) TCEP, $Et_3N$, solvent, inert atmosphere.

Table 3.1: Summary of PVA-SH with brominated end group attachments. PVA-SH DP[a] 426, $M_n$[a] 18,700. THF GPC analysis of parent PVAc pre hydrolysis: $M_n$[b] 11,900, $M_w$[b] 19,600, Đ[b] 1.65.

| Entry | Solvent(s) | End Group Attachment[a] | Aqueous GPC $\lambda_{254\ nm}$ peak[c] | $M_n$[c]/ gmol$^{-1}$ | $M_w$[c]/ gmol$^{-1}$ | Đ[c]/ gmol$^{-1}$ |
|---|---|---|---|---|---|---|
| **P11** | 1 mL DMF(dry) + 1 mL DMSO | 54% | Y | 9,500 | 19,600 | 2.10 |
| **P12** | 1 mL DMSO | 97% | Y | 5,800 | 14,300 | 2.47 |
| **P13** | 1 mL $H_2O$ + 2 mL DMSO | 56% | Y | 7,400 | 16,200 | 2.19 |

[a]determined by $^1$H NMR spectroscopy; [b]THF GPC analysis 1 mL/min 35 °C, universal calibration. [c]Aqueous GPC analysis $NaNO_3$ (10 mM) 1 mL/min 35 °C, narrow standard calibration.

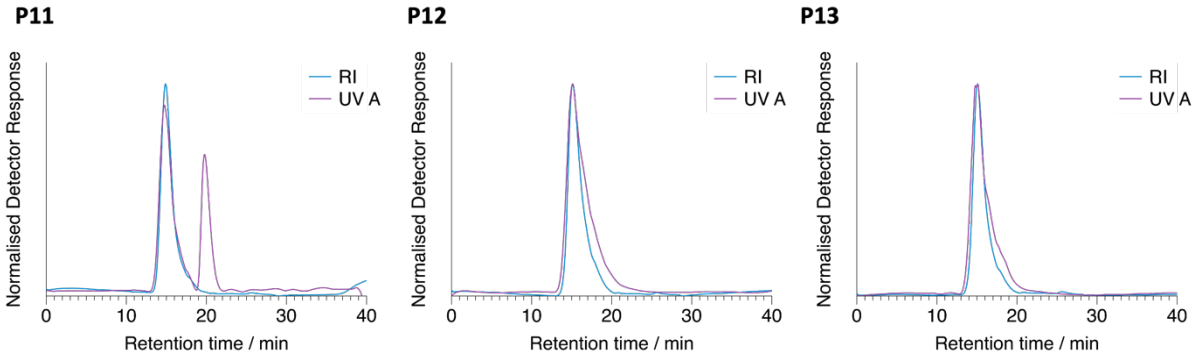


Figure 3.6: Aqueous GPC 10 mM $NaNO_3$, 1 mL/min 35 °C. UV λ = 254 nm.

Although the attachment was successful, and the polymer was labelled with almost full efficiency, the large number of synthetic steps necessary to produce the polymers made a more efficient route desirable.

### 3.3.2 End group synthesis – CTA

By synthesising a CTA that contains the heavy atom labels required for ion beam analysis detection, the synthetic route to the brominated CTA was significantly easier and cheaper, with only slight modification to existing CTA synthesis required (Scheme 3.5). The reactions proceeded in moderate yields to give the brominated CTA **6**.

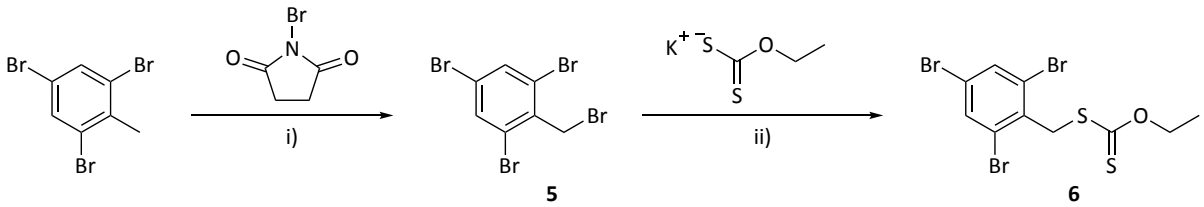


Scheme 3.5: Synthesis of **6**. i) AIBN, 85 °C, chlorobenzene (94% yield); ii) acetone, room temperature (27% yield).

Inspiration was taken from Condon *et al.* who had previously reported the successful synthesis of the non-brominated version of the aromatic CTA as well as subsequent synthesis of PVAc with reasonable molecular weight control.[6] When the PVAc acetate groups were removed according to their reported methodology[6] - treatment with hydrazine hydrate - a degradation of the aromatic bromine group was observed in the $^{1}$H NMR spectrum (Figure 3.6a,c). Use of NaOH (Scheme 3.6 ii) did not appear to cause degradation of the end group, with a singlet the only resonance present in the aromatic region, as expected for undegraded PVA-Br (Figure 3.6b).

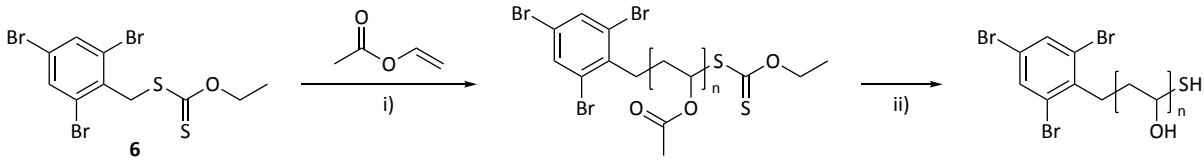


Scheme 3.6: Synthesis of bromine terminated PVA using brominated CTA **6**. i)PET-MADIX polymerisation, ii) base hydrolysis in MeOH.

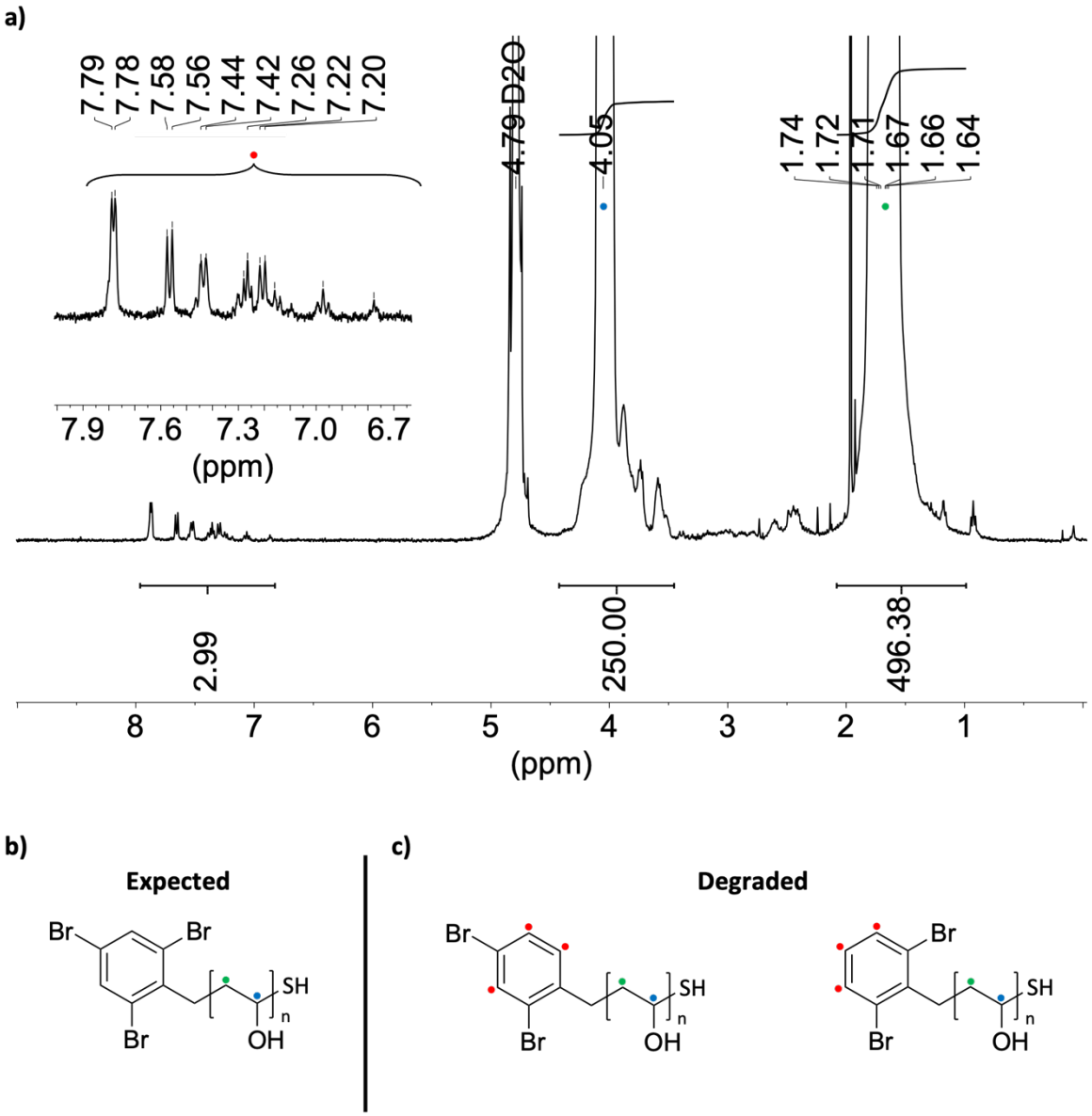


Figure 3.6: PVA-Br treated with $N_2H_4 \cdot H_2O$ a) **$^1$H NMR** (*$D_2O$, 400 MHz*) of PVA-Br following $N_2H_4.H_2O$ treatment with integrals set absolutely to polymer DP (n=250), expansion of aromatic region shows complex splitting patterns and integrates to 3H, indicating loss of one Br to yield 3 Ar-H. b) expected structure of PVA-Br with no degradation, c) Possible structures of degradation products.

Following development of a method to synthesise PVA-Br with no end group degradation, a single batch of PVA-Br was partially reacetylated to yield a series of three PVA-Br polymers as shown (Table 3.2, **P14** – **P16**), all with the same DP = 330 ($M_n^{NMR}$: 14,500 gmol$^{-1}$, DP$^{NMR}$: 330, $M_n^{GPC}$: 17,300 gmol$^{-1}$, $M_w^{GPC}$: 20,800, Đ: 1.20, *N.B.* THF GPC analysis carried out pre hydrolysis in PVAc form) . This method of synthesis was determined to be much more efficient than the end-group labelling described in Section 2.1. However, following reacetylation, the aromatic resonance appears to be split and of a greater

integral than expected (Figure 3.7). It is proposed that the splitting may be a result of the neighbouring pendent group to the aromatic end group having the possibility to be either -OH or -OAc, and there is likely a mixture present in the sample. The resonance integral being larger than expected would imply that some degradation to the end group had occurred, with lower-than-expected Br content increasing the H integral. It would also appear that the increased concentration of acetic acid through the series to achieve higher degrees of acetylation (lower DH) has had a proportional impact on the amount of damage caused to the end group, with the integral increasing down the series. This complication highlights the benefit of the maleimide end group, which could be attached post acetylation thus avoiding problems of degradation during polymer acetylation.

Table 3.2: Summary of PVA-Br series **P14** – **P16** synthesised for ion beam analysis. DP=330[a], THF GPC analysis of parent PVAc pre hydrolysis: $M_n$ 17,300, $M_w$ 20,800, Đ 1.20.

| Polymer | DH%[a] | $M_n$[a]/ gmol$^{-1}$ | ∫ Ar-H[a] (~7.9 ppm) | Structure |
|---|---|---|---|---|
| **P14** | 95 | 15,200 | 2.67 | 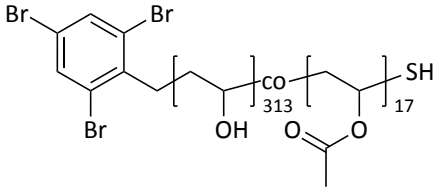 |
| **P15** | 85 | 16,200 | 2.87 | 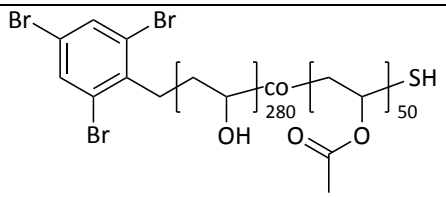 |
| **P16** | 78 | 17,600 | 2.98 | 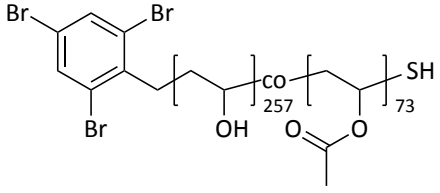 |

[a]Determined by $^1$H NMR spectroscopy. [b]Determined by THF GPC 1 mL/min, 35 °C, universal calibration, of parent PVAc before hydrolysis and reacetylation.

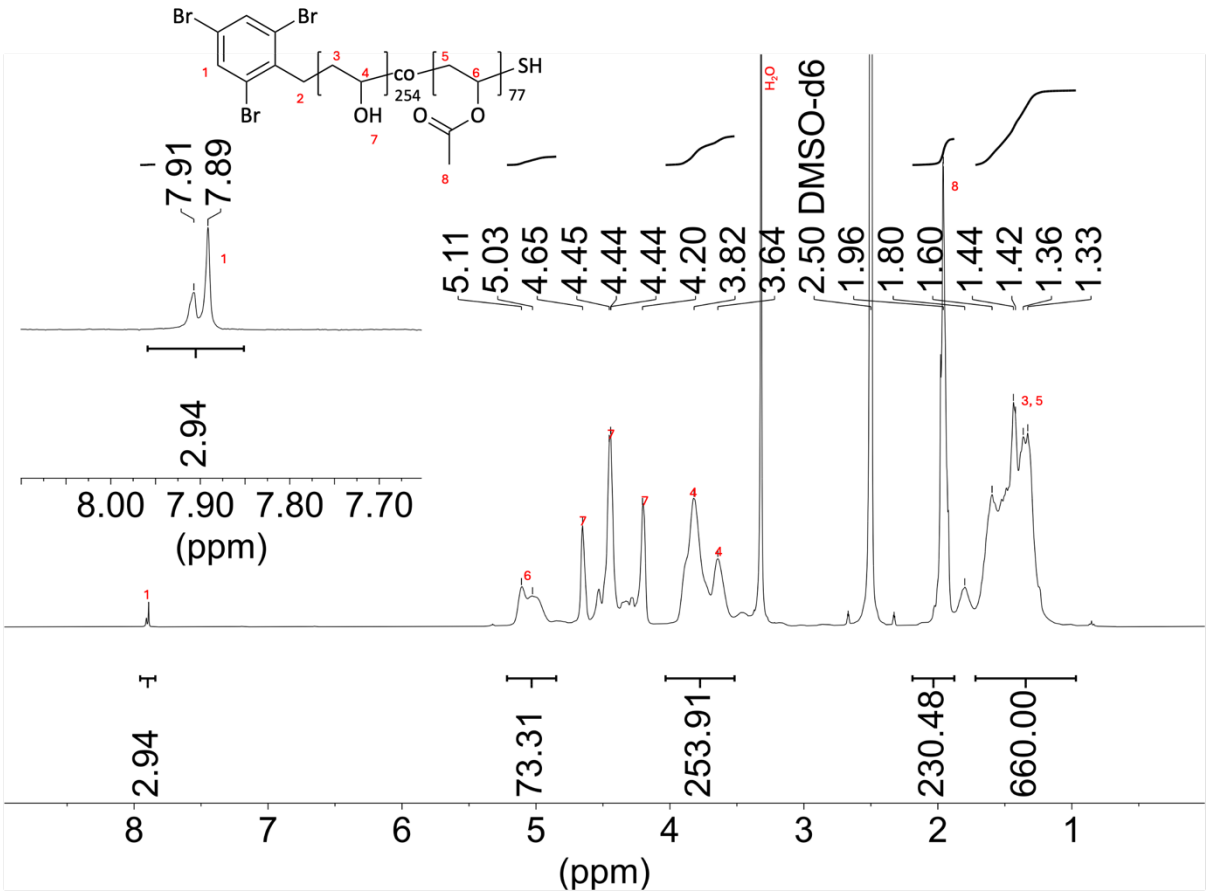


Figure 3.7: $^{1}$H NMR (DMSO-$d_6$, 400 MHz) of part hydrolysed PVA-Br (Total DP = 330,DH = 78%) **P16**. Resonances at δ 4.20 – 4.70 ppm are those of pendent OH groups, however, they were not integrated due to their labile nature and exchange with $H_2O$ in the DMSO-$d_6$. Expansion shows signal splitting in aromatic region as well as overall ∫Ar-H at a greater value than expected, indicating some end group degradation.

As time did not permit the investigation or rectification of this issue, the polymers, which nevertheless had the required labels, were used regardless and were cast into films for ion beam analysis.

### 3.3.3 Material characterisation by ToF-ERDA

To verify that the PVA-Br samples contained the expected levels of bromine, the three PVA-Br samples used to create the sandwich samples were analysed using Time-of-Flight Elastic Recoil Detection Analysis (ToF-ERDA). Samples were drop cast onto a steel sheet for analysis, yielding circular films around 50 – 300 µm thick. Samples were irradiated with a 16 MeV $^{127}I^{8+}$ ion beam and ions analysed by an energy detector in a gas ionisation chamber.

ToF-ERDA histograms (Figure 3.8a-c), depth profiles (Figure 3.8d-f) for the samples and elemental compositions (Table 3.3) were calculated using the Potku software.[7]

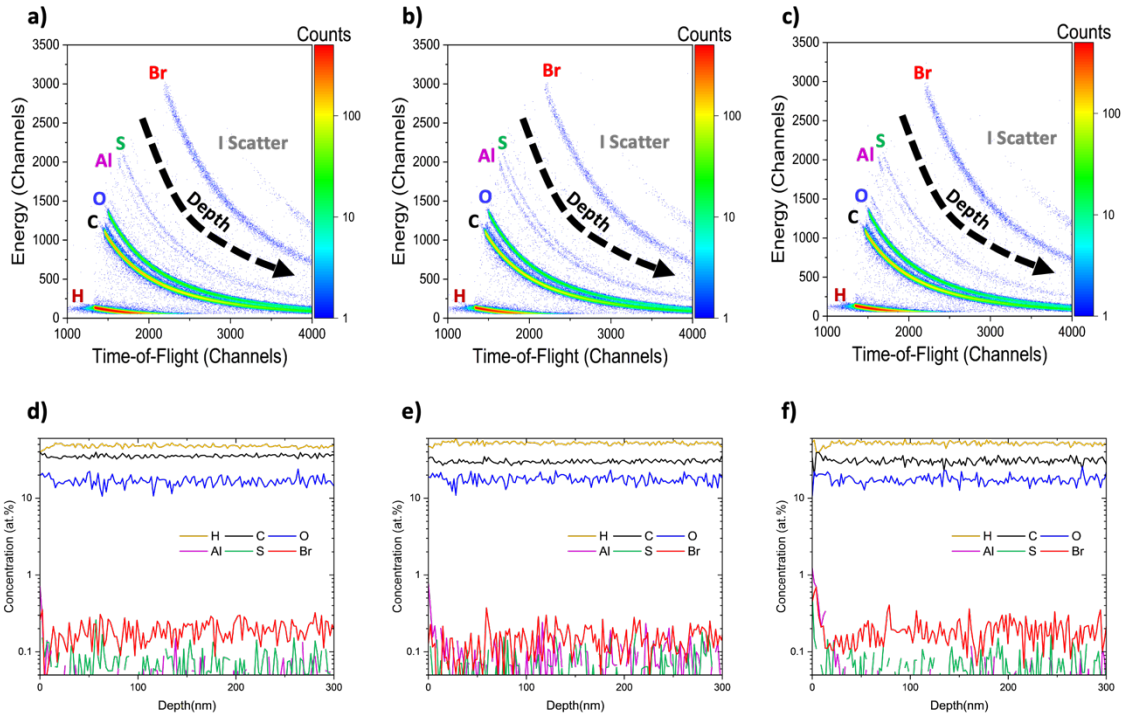


Figure 3.8: Top:ToF-ERD coincidence histograms from an incident beam of 16 MeV $^{127}I^{8+}$ and PVA-Br a) **P14** DH 95%, b) **P15** 85% and c) **P16** 78%, bottom: elemental compositions as determined by analysis of the bulk 20 – 300 nm region of the sample.

Table 3.3: Summary of ToF-ERDA elemental composition results for all PVA-Br samples in bulk layer (20 – 300 nm depth). Uncertainties for element concentrations all 5%, except H concentration which is 10% of the measured value.

| Sample - DH% | **H** | **C** | **O** | **Al** | **S** | **Br** | **$Br_{theo}$** |
|---|---|---|---|---|---|---|---|
| | **(at.%)** | **(at.%)** | **(at.%)** | **(at.%)** | **(at.%)** | **(at.%)** | **(at.%)** |
| **P14** - 95% | 47.78 | 35.34 | 16.6 | 0.03 | 0.06 | 0.19 | 0.12 |
| **P15**- 85% | 52.2 | 29.9 | 17.64 | 0.07 | 0.05 | 0.14 | 0.12 |
| **P16**- 78% | 52 | 30.5 | 17.24 | 0.02 | 0.06 | 0.18 | 0.11 |

Theoretical bromine concentration was calculated based on the molecular weight of the polymer determined by $^{1}H$ NMR and the assumption that all three bromine atoms were still present on the end group. The ToF-ERDA measurements confirmed that all samples contained bromine close to the expected amounts, although in all cases it is slightly greater in concentration than theoretically calculated. The specific cause is unknown, but there are several reasons why an overestimation of an atomic percentage can be obtained for a sample in ToF-ERDA. Multiple scattering effects can lead to

overestimation of an atom's energy level leading to incorrect identification of the species and potentially overrepresentation of certain species. Additionally, and the most likely in this instance, surface roughness or inhomogeneity within the sample can lead to inconsistent scattering angles and recoil energy distributions, which again can cause certain elements to be overrepresented in the detected signal. It was noted that by the way the metal sheets had been trimmed that there was a slight curve in all samples. Based on the $^{1}$H NMR spectroscopic analysis of the chain transfer agent and resultant polymers, it is known with confidence that there isn't any additional bromine within the samples, and as mentioned previously, slight degradation appears to have occurred, meaning the recorded bromine content should be lower than the theoretical value rather than greater.

The maximum analysis depth for this technique is ~300 nm, which is why it could not be used as the primary method of analysis for interface detection, although if there was a method of sequentially coating thinner PVA films, this technique could be explored further for sole analysis of the films.

### 3.3.4 Interface determination by PIXE and RBS spectroscopy

Analysis of three dual layer samples was carried out at the UK National Ion Beam Centre (UKNIBC), University of Surrey, Guildford, UK. The experimental work was conducted over two days of beamtime. Sample **A** is a two-layer sandwich of **P14** and commercial polymer, sample **B** is a two-layer sandwich of **P15** and commercial polymer, and sample **C** is a two-layer sandwich of **P16** and commercial polymer. Their preparation is described in the experimental Section 4. All film sandwiches were cast onto aluminium foil for ease of handling. Each film was cross sectioned using a guillotine prior to analysis to expose a fresh edge to the proton beam.

The sample was held in the beamline as shown in Figure 3.9, with commercial PVA closest to the top of the chamber. The sample was mounted such that ~1 mm polymer film protruded from the clamp to minimise interference of the clamp material with the measurement (photos of this setup are shown

in the experimental section). In this orientation, the incoming proton beam would be incident upon the interface face on as in Figure 3.11a. Spatial elemental maps are be provided by raster scanning the beam up and down across the interface.

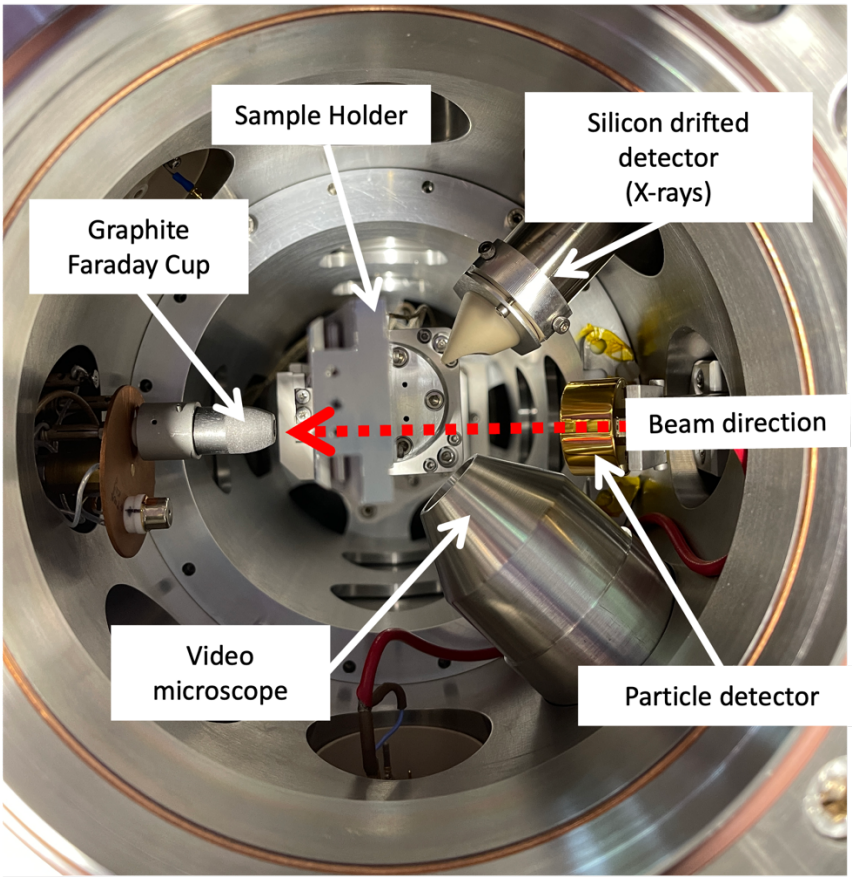


Figure 3.9: Top down view of sample chamber on the Nanobeam Line at the National Ion Beam Centre, University of Surrey, UK.

To analyse the samples, three methods were used: 2D maps, line scans, and point measurements (Figure 3.10a-c). Typically, a 2D map is performed across the region of interest to establish whether a feature is present and warrants further investigation. For this work, all maps were captured over either a 500 x 500 µm or 750 x 750 µm area with a total charge of 500 nC. Due to the charge being spread over the whole sample area, the beam damage from these kinds of measurements is typically minimal and is commonly used in archaeometry of precious samples.[8] Once a feature is identified, in this case, the polymer-polymer interface, a line scan can be conducted to collect better statistics for the sample. In this work, line scans were carried out with a total charge of 500 nC. To further improve statistics, a

line of points measurement can be taken across a feature, in this case, the interface. For this work, 200 nC per point was used.

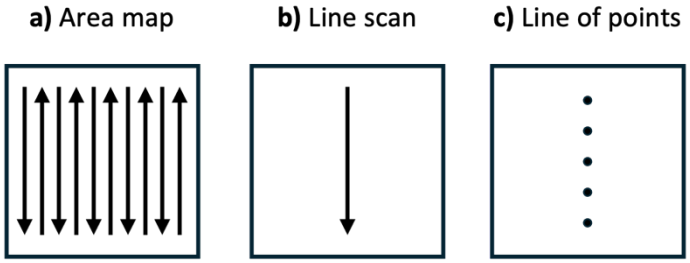


Figure 3.10: Various modes of beam scanning utilised for PIXE and RBS data collection. a) 2D area map, typically performed over a broad area to identify regions of interest. b) line scan, typically used once a ROI (region of interest) has been identified to improve the quality of the data. c) point measuremnts, used to gain the highest quality data by targeting specific points in a sample, although care should be taken to avoid beam damage.

### 3.3.5 Sample A – DH 95%

The interface in the film was successfully identified using both PIXE and RBS by generating a 500 x 500 µm area map of the freshly sliced surface (see schematic, Figure 3.11 red box, and data, Figure 3.12), showing a clear distinction in bromine and sulfur concentrations.

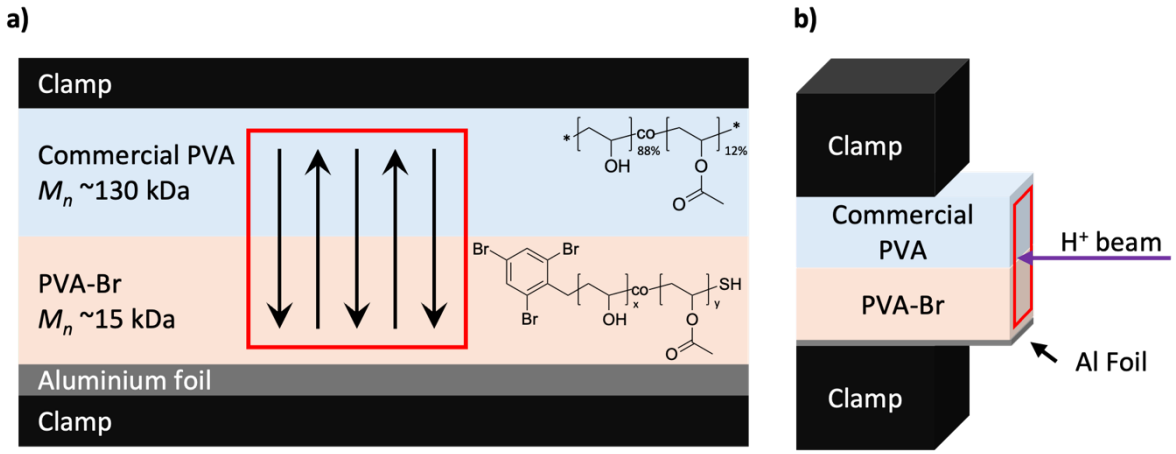


Figure 3.11: PVA sandwich clamping. a) face on view of the film interface, b) profile view showing protrusion of film from clamp to minimse interference from clamp material during the measurement. Beam scan area represented in red box with beam path depicted by black arrows.

Figure 3.12a-c shows the PIXE maps for Al, S, and Br, where the unlabelled polymer is clearly visible at the top of the S and Br maps, and the PVA-Br layer is seen at the bottom. The aluminium foil is also

visible at the bottom of the scanned region in Figure 3.12a. The RBS maps (Figure 3.12d-f) also reveal the presence of an interface, although the overall intensity is much lower compared to PIXE due to the reduced yield of proton backscattering relative to X-ray emission. Despite this difference, both techniques closely agree on the location of the interface, which appears well-defined and sharp, suggesting minimal interdiffusion between the polymers on a scale of 500 μm. Additional elemental maps are shown in the appendix, Figure 3.45.

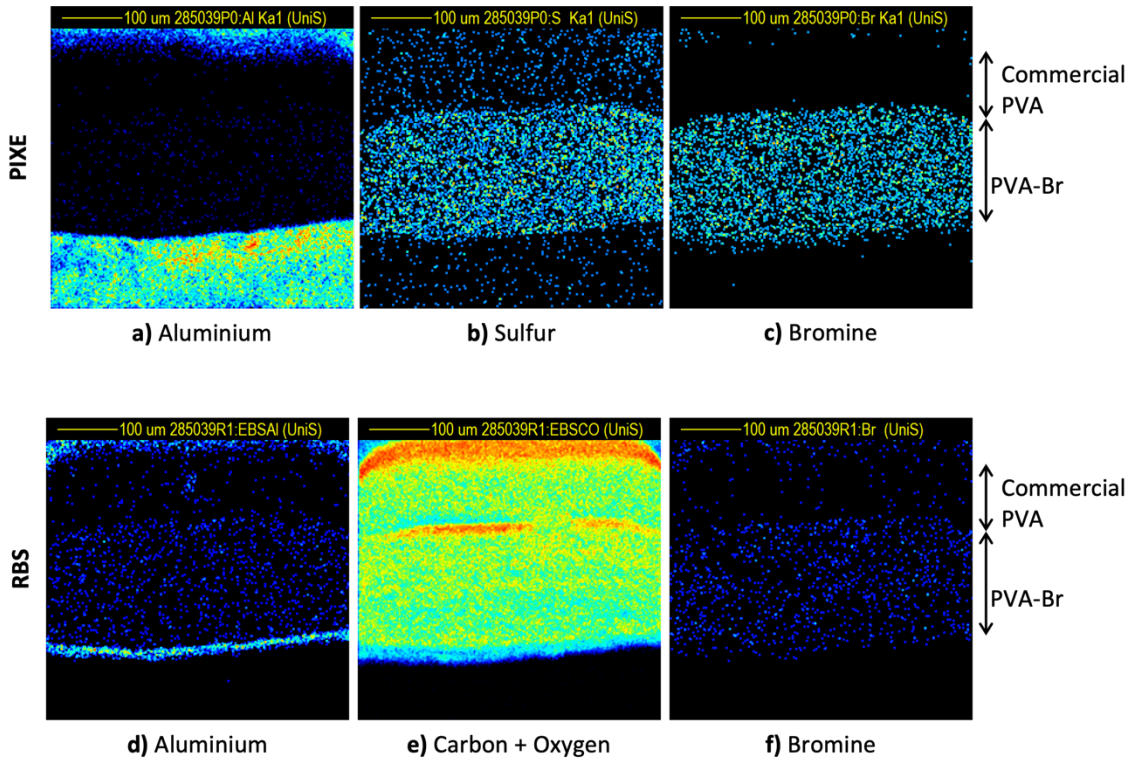


Figure 3.12: 500 x 500 μm square on interface of sample **A** (Commercial PVA + PVA-Br DH = 95%), 500 nC total charge - a-c)PIXE and d-f) RBS elemental maps.

After identifying the interface using PIXE maps, a line scan (Figure 3.13a-c) was performed to better quantify the bromine concentration across the interface, allowing for the calculation of the interfacial width. The scan (Figure 3.13b) shows an increase in both bromine (Br) and sulfur (S) concentrations as the proton beam moves from the commercial layer into the PVA-Br layer, confirming that the interface was crossed during the measurement. Additionally, the RBS spectrum (Figure 3.13c) closely aligns with the PIXE measurements for bromine concentration (Figure 3.13b), demonstrating that both techniques

agree on the position and width of the interface. The vertical lines in Figure 3.13b and c indicate the approximate interfacial region and are positioned consistently in both figures to highlight the good overlap between the two measurement techniques.

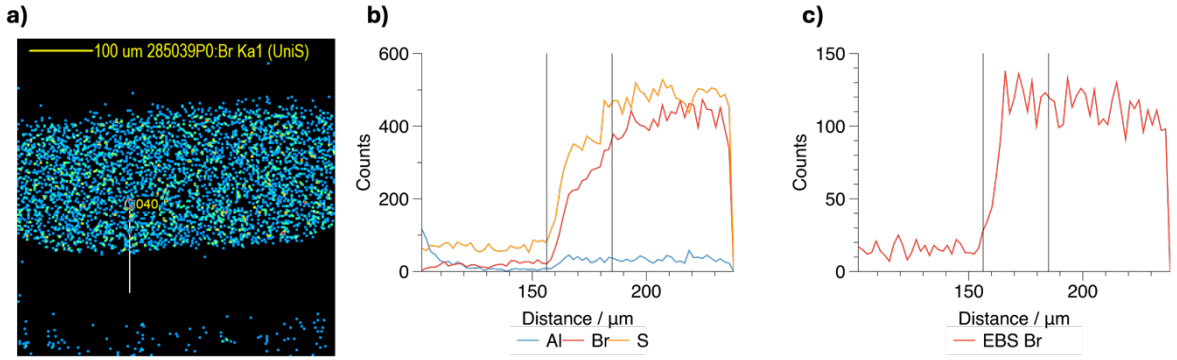


Figure 3.13: a) 2D PIXE Br map with the line scan location indicated across the interface of sample **A**. b) PIXE counts for Al, Br, and S across the interface, with distance given as the absolute value from the bottom of the image. c) RBS Br counts for the same line scan. Note that the image appears flipped due to data processing in OMDAQ for this sample. The sample is mounted with **P14** PVA-Br as the lower layer and commercial PVA as the upper layer.

The line of points measurement was the final measurement to be taken on the sample, with 5 points being measured across the interface to quantify the amount of bromine through the sample (Figure 3.14). Sulfur concentration is also seen to increase slightly, which is consistent with a transition from commercial polymer to PVA-Br. The interfacial width determined from the line scan is found to be approximately 29 µm. The rate of bromine concentration increase is given by fit of a straight line through the measurements capturing the interface, which gives a rate of concentration increase of 1566 ppm/µm for this sharp interface.

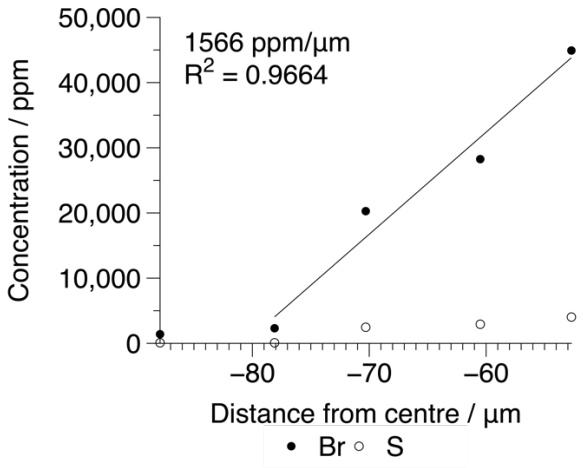


Figure 3.14: Line of points measurement of sample **A**. Elemental concentration determined by PIXE analysis. Error bars included but not seen due to small error.

### 3.3.6 Sample B – DH 85%

The second sample in the series was analysed to determine the interfacial width using a similar approach as sample **A**. PIXE maps (Figure 3.15a-c) confirmed the presence of the interface but revealed a slight defect in the lower right of sample. For this analysis, the defect was disregarded and excluded from all X-ray or proton scattering averages. The defect appears to be related to the aluminium foil, which may have deformed slightly during loading, causing shadowing of the sample from the X-ray and RBS detectors and resulting in lower intensity counts compared to the rest of the sample. Additional elemental maps are shown in the appendix, Figure 3.46.

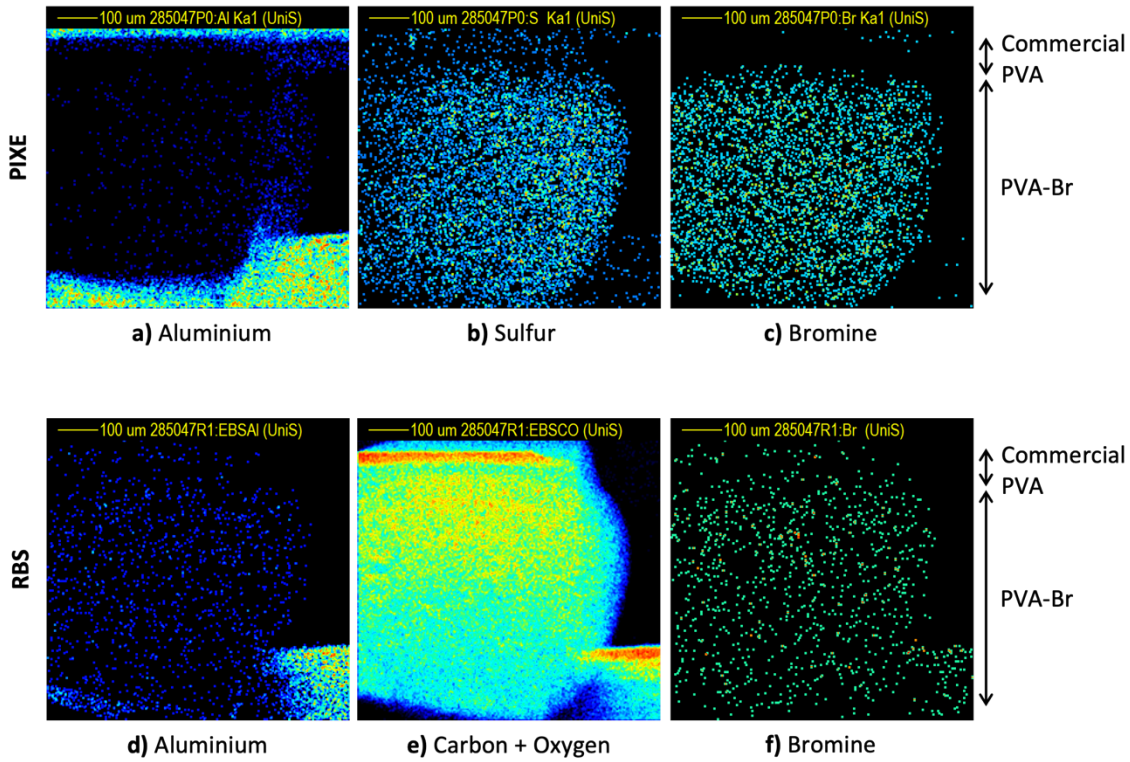


Figure 3.15: 500 x 500 µm square on interface of sample **B** (Commercial PVA + PVA-Br **P15** DH = 90%), 500 nC total charge - a-c)PIXE and d-f) RBS elemental maps. Defect in lower right corner best visualised in a) and e).

The polymer-polymer interface was captured by a line of points measurement (Figure 3.16, 10 points) which shows a general increase in bromine concentration at the union between the two films. The interface is more diffuse than that of sample **A**, implying a deeper interdiffusion of **P15** PVA-Br into the commercial matrix. This is likely due match in degree of acetylation between **P15** PVA-Br and the commercial polymer matrix, maximising the compatibility between chains. The gradient of a straight line fit between the points that most likely capture the interface shows an increase in bromine concentration at 81 ppm/µm, compared to the much sharper interface of sample **A** which increases at a rate of 1566 ppm/µm across the interface due to lower interdiffusion.

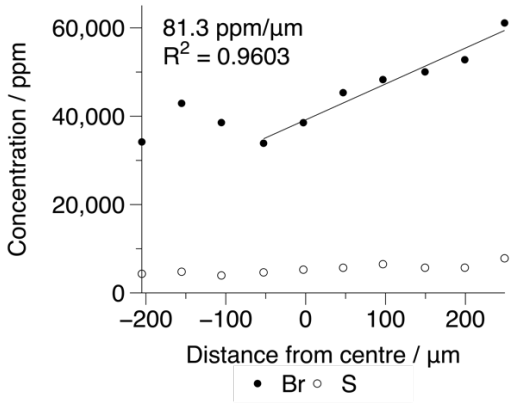


Figure 3.16: Line of points measurement of sample B. Elemental concentration determined by PIXE analysis. Error bars included but not seen due to small error.

To estimate the interfacial width without relying on a line scan (not recorded for this sample due to a software error), the PIXE map (Figure 3.17a) can be used to quantify the interface. By horizontally averaging the bromine counts from the PIXE map, an intensity profile across the interface can be generated, revealing a wider diffusion layer as acetylation increases. As shown (Figure 3.17), the diffuse region extends to approximately 100 µm in depth, compared to ~30 µm in sample **A** (Figure 3.15c). This finding aligns with the diffusion trends observed and quantified in the FRAP experiments (Chapter 4), where samples with higher DH% exhibited sharper diffusion gradients and slower diffusion rates. It also supports the idea that even at prolonged diffusion times, complete diffusion may not occur in highly hydrolysed samples due to immobile fractions caused by crystallites in the polymer, which limit full chain mobility.

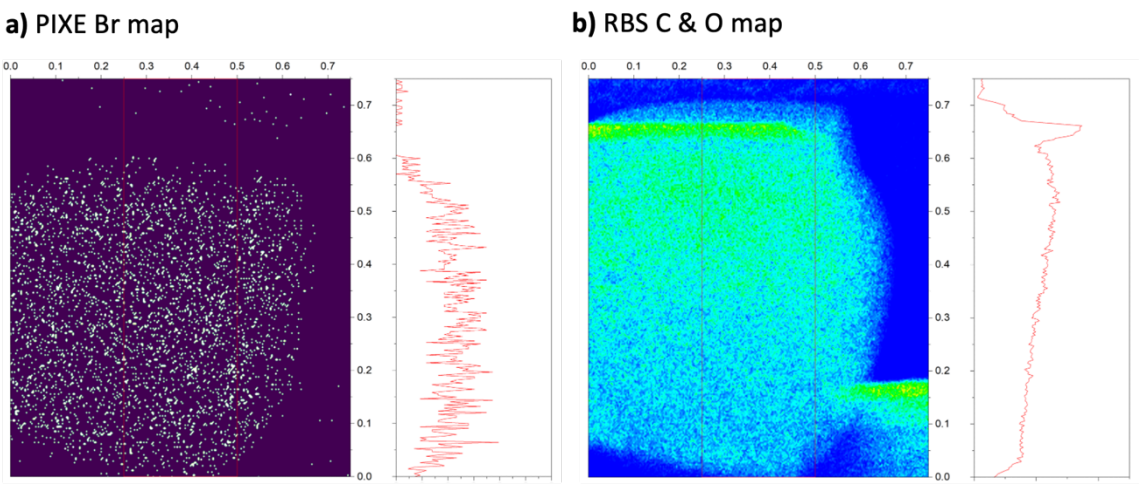


Figure 3.17: Sample **B** 750 x 750 µm a) PIXE Br map with cross sectional horizontal averages. b) RBS carbon and oxygen signal map.

### 3.3.7 Sample C – DH 78%

Sample **C** is the least hydrolysed film in the set and is therefore expected to be the most mobile. Mapping the sample with PIXE and RBS (Figure 3.18), as performed for the other samples, failed to reveal an interface, showing a uniform bromine composition throughout. Although a line scan and point measurement were conducted, severe beam damage (discussed later) rendered these measurements unusable for meaningful analysis. PVA is susceptible to beam damage, and in this instance a 2.5 MeV beam of charge density 889 nC/mm$^2$ was enough to cause significant degradation of the sample. The only method of assessing the interface for sample **C** is to consult the PIXE map (Figure 3.18) and utilise an early measurement snapshot where only 20% of the total measurement had been conducted due to the beam damage caused during measurements of this sample. 20% of the map is where the amount of beam damage is minimal and the quality of the PIXE data is high enough to produce an interface profile based on Br concentration. Additional elemental maps are shown in the appendix, Figure 3.47.

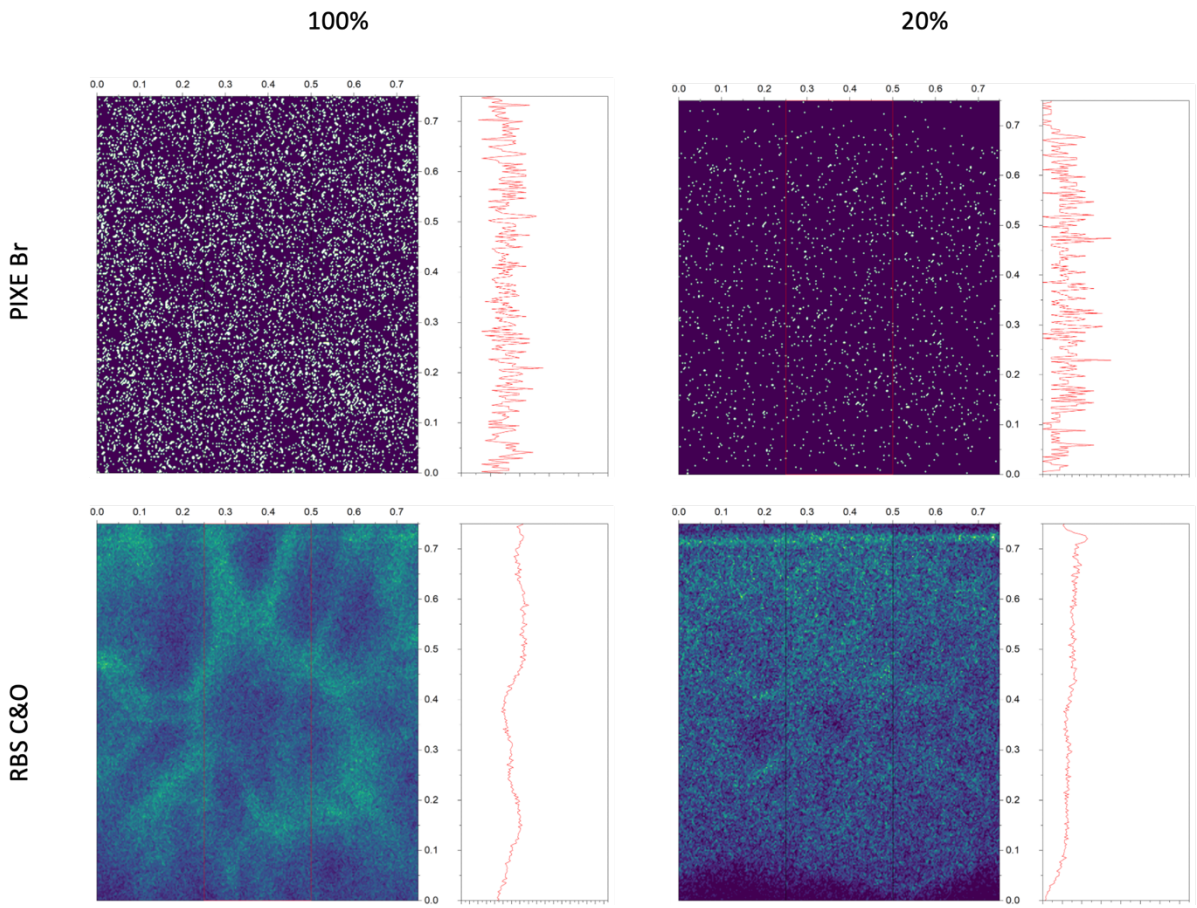


Figure 3.18: Sample **C** PIXE map at 100% and 20%, with corresponding RBS C + O spectra below, which show clear bubbling present in the later sample.

The PIXE map (Figure 3.18) provides a full cross-section of the sample, yet neither snapshot reveals a visible interface, indicating significant diffusion between the layers. This suggests that PVA-Br has fully diffused into the commercial material. The lack of an interface, even prior to beam damage, strongly supports the idea of substantial polymer interdiffusion, rather than interface destruction during measurement. Notably, bromine signals are detected, confirming the sample is above the detection limit. However, the uniform concentration of bromine throughout the sample points to a fully homogeneous mixture. This outcome is plausible given the extended diffusion period, with the interfaces allowed to diffuse at 50 °C for one week at 70% humidity (saturated KCl solutions, measured with hygrometer). Essentially, this represents a $t = \infty$ measurement, illustrating the polymer diffusion state after a duration far exceeding the diffusion time, which FRAP analysis (Chapter 4) indicates to be on the order of several hundred minutes for similar polymers.

### 3.3.8 Beam damage

It is well documented in the literature that polymers undergo structural changes when exposed to ionising radiation,[9-17] so it is unsurprising that this technique has caused visible damage to the samples. Samples **B** and **C** suffered significant beam damage from the measurement, as demonstrated by Figure 3.19. Sample **A** shows signs of moderate beam damage, with a slight bulging and browning of the sample. The beam damage appears to correlate with the DH%, with more damage caused to the samples **B** and **C** with lower DH%. This observation can be rationalised by the difference in glass transition temperature ($T_g$) between samples, with acetylation known to lower the $T_g$ of the polymer.[18]

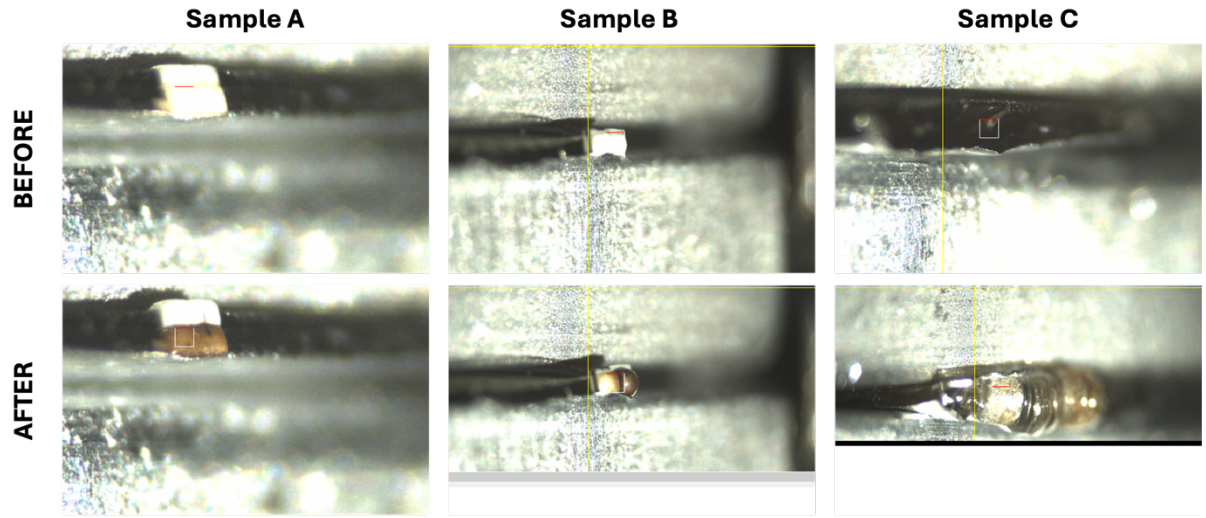


Figure 3.19: Photographs from video microscope inside sample chamber taken of each sample before and after analysis with the proton beam, showing polymer films bubbling out of the metal clamp after beam exposure.

Typically, it is heavy ion beams that cause the most damage to samples, with examples of gold and lead ion bombardment cited in the literature.[10, 13, 14] When thermal degradation is considered, acetic acid is a commonly observed degradation product, although this is typically only observed at temperatures above 400 °C, as found by pyrolysis–gas chromatography/mass spectrometry.[19] Ion beam damage occurs due to the immense energy applied to sample per unit volume. For example, consider a 2.5 MeV proton beam with a current of 100 pA which has a power of 0.25 mW; the irradiated volume for a 1.5 $\mu m^2$ beam spot where beam penetration depth is around 50 µm is 1.1 x $10^{-10}$ $cm^3$,

yielding a power density of 2.2 terawatts/$m^3$ (2.2 x $10^{12}$ W/$m^3$). When considering ion beam damage, the beam crosses the polymer, releasing huge amounts of kinetic energy into the material by exciting electrons, and breaking covalent bonds. The cascade of subsequent reactions often involves reactive radical species. Typically, polymer degradation can lead to either cross linking of polymer chains when two reactive radicals from chains in close proximity combine. Alternatively, if a reaction partner is not found in the form of a polymeric radical, scission products can abstract protons and leave as small molecules into the vacuum chamber.

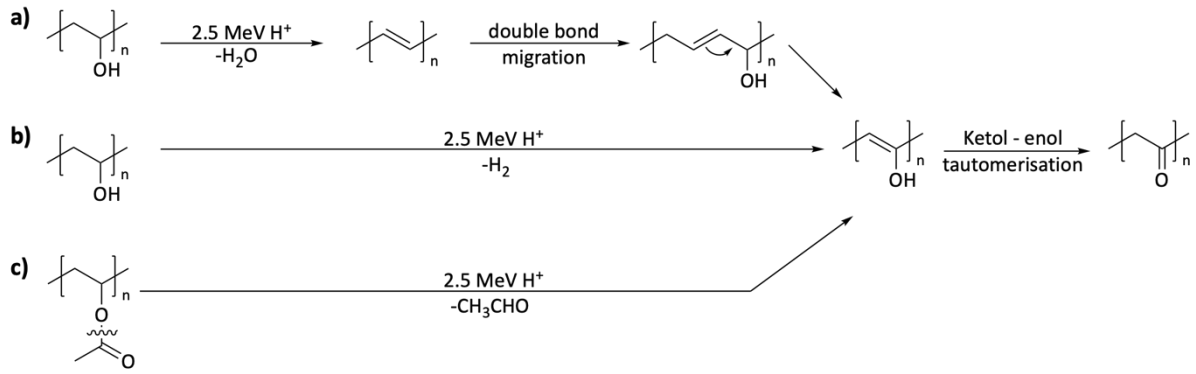


Scheme 3.7: Potential beam degradation pathways for a + b) PVA and c)PVAc.

The proposed pathways for the ion beam degradation of PVA/PVAc polymers are illustrated in Scheme 3.7, showing two possible degradation routes for PVA and one for PVAc, all ultimately resulting in the formation of a polymeric ketone. While backbone scission can occur along any point of the polymer chain during irradiation, this process is not depicted in the figure. Hossain *et al.* investigated the ion beam degradation of PVA/PVAc *in situ* using online Fourier Transform Infrared Spectroscopy (FTIR), finding evidence of these degradation pathways.[9] They observed a decrease in the –OH and –CH bands under ion irradiation, alongside an increase in a -C=O keto band. The primary fragments detected by online mass spectrometry were $H_2$ and $H_2O$. Degradation of the PVAc units was characterised by the loss of the acetate group through hydrogen abstraction from a neighbouring carbon atom, forming a C=C bond, which subsequently tautomerises into a C=O bond. Their FTIR analysis showed a decrease in acetate band intensity, supporting this degradation mechanism.

It is important to note that their study utilised high-energy gold ions, which deposit more energy per unit distance travelled than proton beams. This increased energy deposition could lead to different degradation behaviour compared to lower-energy ion irradiation as was used in this work. In light of this, the work of Lee suggests that proton beams may be more prone to causing scission and less likely to promote cross-linking.[20] Furthermore, if $H_2O$ or $H_2$ gas is formed as a result of beam damage, it is expected that the polymer-polymer interface would be disrupted by bubble formation as the gaseous products accumulate within the sample. This effect was clearly observed in samples **B** and **C**, where the RBS spectra (Figure 3.20) indicated the onset of beam damage and bubble formation as early as 30% into the completion of the RBS maps measurements.

The data collection method allowed the measurements to be “rewound”, providing snapshots from earlier time points in the experiment before significant beam damage occurred; however, this approach resulted in lower quality data due to reduced counts. Given that increasing counts would exacerbate interface damage, pursuing higher quality data at the expense of greater beam damage is counterproductive. Cooling the sample or using a larger (or closer) detector would help minimise the incident beam and, consequently, reduce beam damage, offering alternative strategies to optimise data quality while preserving sample integrity.

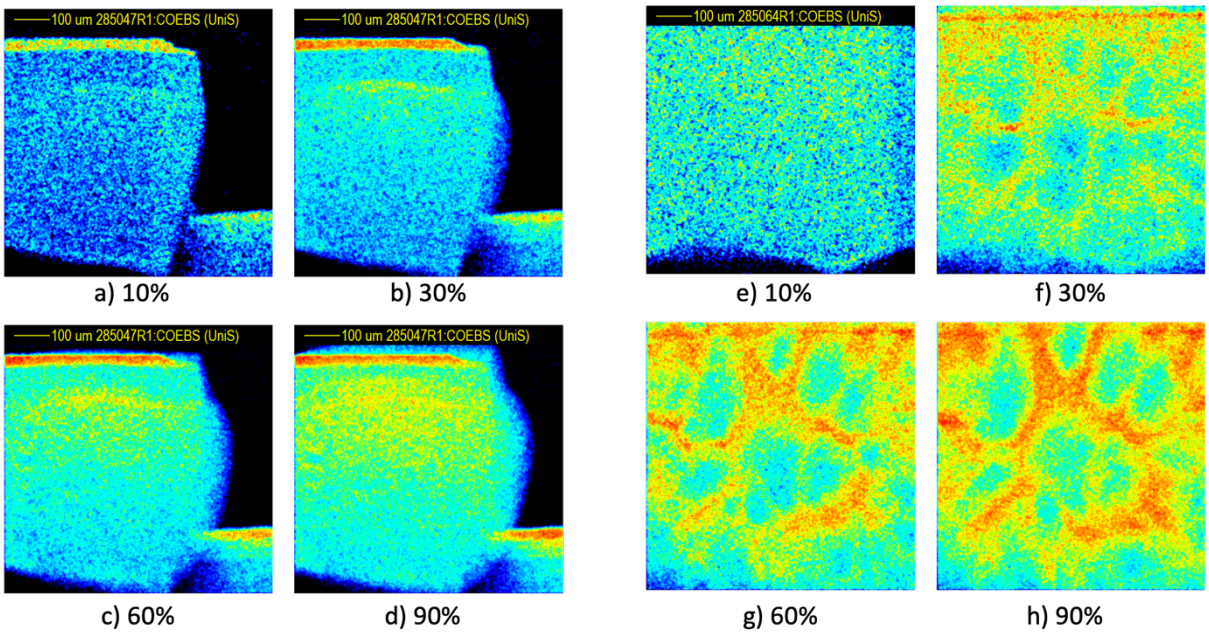


Figure 3.20: Proton beam damage caused to sample **B** (a-d) and sample **C** (e-h) visualised by RBS C+O signals, each shown at various stages of map measurement. Due to the measurement only being sensitive to C+O, the interface between PVA and PVA-Br cannot be observed.

Sample **B** (Figure 3.20a-d) shows progressive beam damage throughout the measurement, evidenced by spots of high intensity appearing in the RBS carbon and oxygen maps. These spots indicate bubble formation and film inhomogeneity, making it challenging to quantify the interfacial width as the sample's composition and structure change during measurement. Sample **C** (Figure 3.20e-h) exhibits the most severe and obvious beam damage, with bubbles forming on the order of tens of microns in diameter. For this sample, the compositional map must be analysed at the 10% measurement snapshot, resulting in lower data quality. Despite this, the interface remains difficult to observe, suggesting that diffusion was complete.

### 3.3.9 Limitations of Ion beam analysis measurements applied to PVA samples

The most obvious limitation to this technique was the high level of beam damage caused to the samples during measurements. Future experiments of this nature would benefit from cooling the samples to keep the polymer well below its glass transition temperature ($T_g$), thereby potentially reducing irradiation-induced damage. Hossain *et al.* showed through online mass spectrometry that

PVA/PVAc samples release lower intensities and fewer fragment molecules when exposed to an ion beam at lower temperature.[9] This decrease in outgassing may result from reduced beam-induced damage at lower temperatures compared to room temperature, or from volatile decomposition products becoming trapped within the polymer matrix when it is in its glassy state below its $T_g$, preventing bubbling disturbing the interface so severely.

Another limitation to the measurement was only discovered during data processing and is related to the orientation of the samples in the beamline. When analysing the RBS spectra from individual measurements, the data often deviated from the predicted fit, particularly for the line of points measurements (Figure 3.21). The high intensity of these features suggests that they are not due to weak scattering or poor signal-to-noise ratios. Instead, the observed scattering complications are likely due to limitations related to the sample geometry and the path of the beam as it exits the sample.

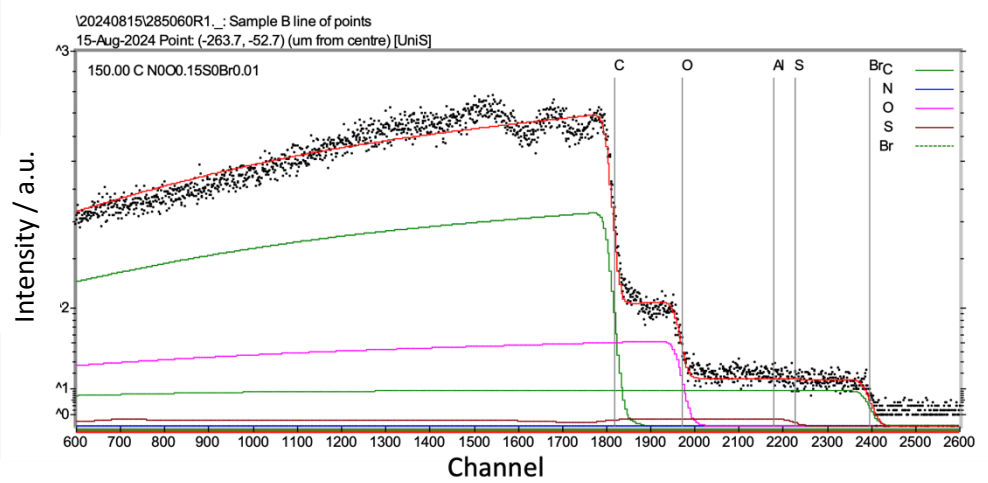


Figure 3.21: Backscattered spectrum of sample B during line of points measurement with fits for various elements shown as coloured lines. Red line = total spectra fit.

During irradiation, the sample was mounted with the interface positioned horizontally, and the particle detector was located above the plane of the interface. Particles backscattered near the interface could pass through additional layers of the sample, potentially causing secondary scattering or energy loss if

the scattered protons collide with other elements before reaching the detector. This setup is illustrated in Figure 3.22a.

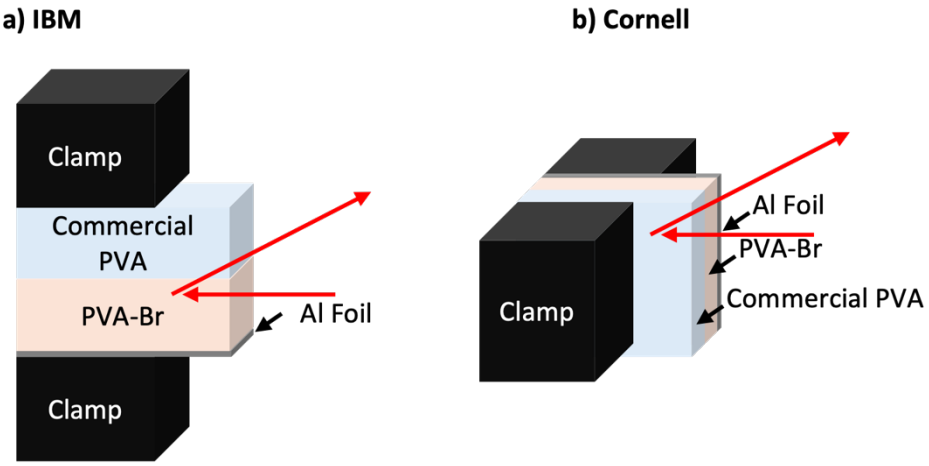


Figure 3.22: a) IBM geometry showing horizontal orientation of the sample with respect to the incoming beam and trajectory of backscattered particles to detector. b) Cornell geometry showing the same sample rotated by 90°, with verticle placment of the interface with respect to the incoming proton beam and backscattered particles traveling to the detector.

Figure 3.22 depicts two geometries: the IBM and Cornell configurations, named after the institutions, where they were first developed. In the IBM geometry that was used in these experiments, the exit path of the backscattered particles cuts through the commercial polymer layer when the particles originate from a layer beneath it. To avoid this issue, rotating the samples to adopt the Cornell geometry (shown in Figure 3.22b) would ensure that the exit path of the backscattered particles remains confined to their layer of origin. However, mounting the samples in this orientation was not feasible, so all measurements were conducted in the IBM configuration. The sample was positioned to ensure that the backscattered beam did not interact with the clamp, only with the other layers of the sample. Notably, this issue did not affect the PIXE measurements, allowing for successful elemental mapping despite the complications observed in the RBS measurements.

## 3.4 Conclusions and future work

In conclusion, this study presents an effective approach for visualising and mapping polymer-polymer interfaces using PIXE and RBS techniques. The successful incorporation of a heavy atom end group label onto polymer chains—achieved through two distinct synthesis methods—enabled the utilisation of ion beam analysis to detect polymer interdiffusion. Notably, the cost-efficient synthesis of a brominated chain transfer agent was identified as the most effective method for labelling, providing a clear and measurable bromine signal. This represents a significant advancement in the ability to map multi component polymer interfaces and could serve as a foundation for future studies investigating longer polymer chains with similar levels of bromine incorporation.

PIXE analysis proved to be the most reliable technique for assessing polymer interdiffusion, with the 2D mapping approach emerging as the optimal choice due to the fragile nature of the polymer samples under the proton beam. While intense, narrowly focused beams resulted in damage to the samples and unusable data, the 2D map provided clear results. Future experiments could refine this approach by incorporating sample cooling and using a detector with a larger surface area, minimising beam damage and enabling more precise line and point measurements for areas requiring focused analysis.

This work establishes the utility of PIXE and RBS techniques for studying polymer interfaces, offering a versatile method to analyse the impact of chain modifications, specifically the degree of hydrolysis in this instance, although there is scope to expand the work to observe the impact of other chain modifications such as molecular weight or second monomer incorporation. The results suggest that altering the degree of hydrolysis can significantly influence polymer interdiffusion, with a decrease shown to enhance polymer chain interpenetration in a polymer film of similar chemistry. These findings correlate with observations made in the FRAP chapter (Chapter 4) of this thesis, further reinforcing the importance of chain modification in controlling polymer properties.

The ability to map these interfaces in a detailed manner offers significant value to both the academic community and industries where polymer compatibility and interdiffusion are critical. Moreover, this work highlights the challenges associated with sample preparation, particularly in producing uniform films. Future efforts could focus on optimising film-casting methods, such as spin casting, to facilitate more precise top-down analysis techniques like ToF-ERDA, potentially eliminating the need for careful alignment of pristine polymer interfaces with the proton beam. While spin casting was considered impractical for this fragile polymer system, the analysed films from this work were consistent with those used industrially, demonstrating the relevance and potential applicability of this technique in real-world settings.

Ultimately, this research advances our understanding of PVA interface dynamics and provides a robust methodology for further investigation into polymer interdiffusion, with substantial implications for the development and optimisation of polymer-based materials in industrial applications involving polymeric seals.

### 3.5 Experimental methods

General experimental procedures are listed in Chapter 2 Section 4. Compounds and techniques exclusively used in this chapter are reported here.

#### 3.5.1 Synthesis of *tert*-butyl (2-(2,4,6-tribromobenzamido)ethyl)carbamate 3

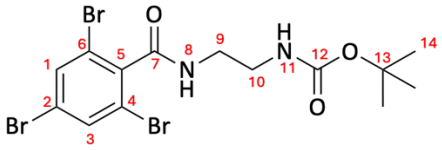


Figure 3.23: Structure of *tert*-butyl (2-(2,4,6-tribromobenzamido)ethyl)carbamate.

2,4,6-tribromobenzoic acid (1.00 g, 2.8 mmol, 2.3 eq.) was dried under vacuum in an oven dried Schlenk tube for 16 h. The vessel was placed under inert atmosphere, and $PBr_5$ (522 mg, 1.2 mmol, 1.0 eq.) was added in a single portion under a dry argon flow. The tube was vacuum/argon cycled 3× before placing into a preheated mantle at 90 °C for 3 h. Upon melting of $PBr_5$, a pale brown liquid formed, dissolving the 2,4,6-tribromobenzoic acid. Following reaction, the solution was cooled to room temperature and $CH_2Cl_2$ (anhydrous, 10 mL) was added, yielding a clear brown solution. The solution was cooled to 0 °C and *N*-boc ethylene diamine (1.77 mL, 11.2 mmol, 4.0 eq.) was added slowly to the cooled solution under an argon blanket, turning the clear brown solution chalky white with HBr evolution. Progress was followed via LC-MS and after 16 h $CH_2Cl_2$ (100 mL) was added before washing with DI $H_2O$ (100 mL). The aqueous layer was further extracted with $CH_2Cl_2$ (2 × 100 mL) and the organics combined and dried over $Na_2SO_4$ before reducing in volume. TLC analysis ($SiO_2$, 1:1 EtOAc:Hex, Figure 3.26 ) showed two spots ($R_{f\ product}$: 0.41, $R_{f\ impurity}$: 0.56). The crude was solid loaded onto celite and purified via CombiFlash (40 g Gold $SiO_2$ Column, 0:1 EtOAc:Hex to 1:0 EtOAc:Hex over 7 CV). The fractions containing **3** were combined and allowed to evaporate, yielding **3** as a white solid which was dried under vacuum (1.07 g, 78% yield). **m.p.** 198.6-199.5 °C. **$^1$H NMR** (*400 MHz, $CDCl_3$*) δ 7.69 (s, 2H, $H_{1,3}$), 6.50 (s -br, 1H, $H_8$), 4.94 (s -br, 1H, $H_{11}$), 3.58 (q, $J$ = 5.5 Hz, 2H, $H_9$), 3.41 (q -br, $J$ = 5.7 Hz, 2H, $H_{10}$), 1.42 (s, 9H, $H_{14}$). **$^{13}$C NMR** (*101 MHz, $CDCl_3$*) δ 166.32 $C_7$, 156.93 $C_{12}$, 138.87 $C_5$, 134.37 $C_{1,3}$, 123.78 $C_2$,

120.98 $C_{4,6}$, 80.11 $C_{13}$, 41.29 $C_9$, 39.98 $C_{10}$, 28.51 $C_{14}$. **HR-ESI-MS:** For $[M\text{-}Boc+H]^+$ $[C_9H_{10}Br_3N_2O]^+$ calculated: 398.8343, found: 398.8355. **IR** ν ($cm^{-1}$) 3282, 3066, 2966, 2931, 1688, 1646, 1569, 1536, 1430, 1366, 1252, 1166, 855, 740.

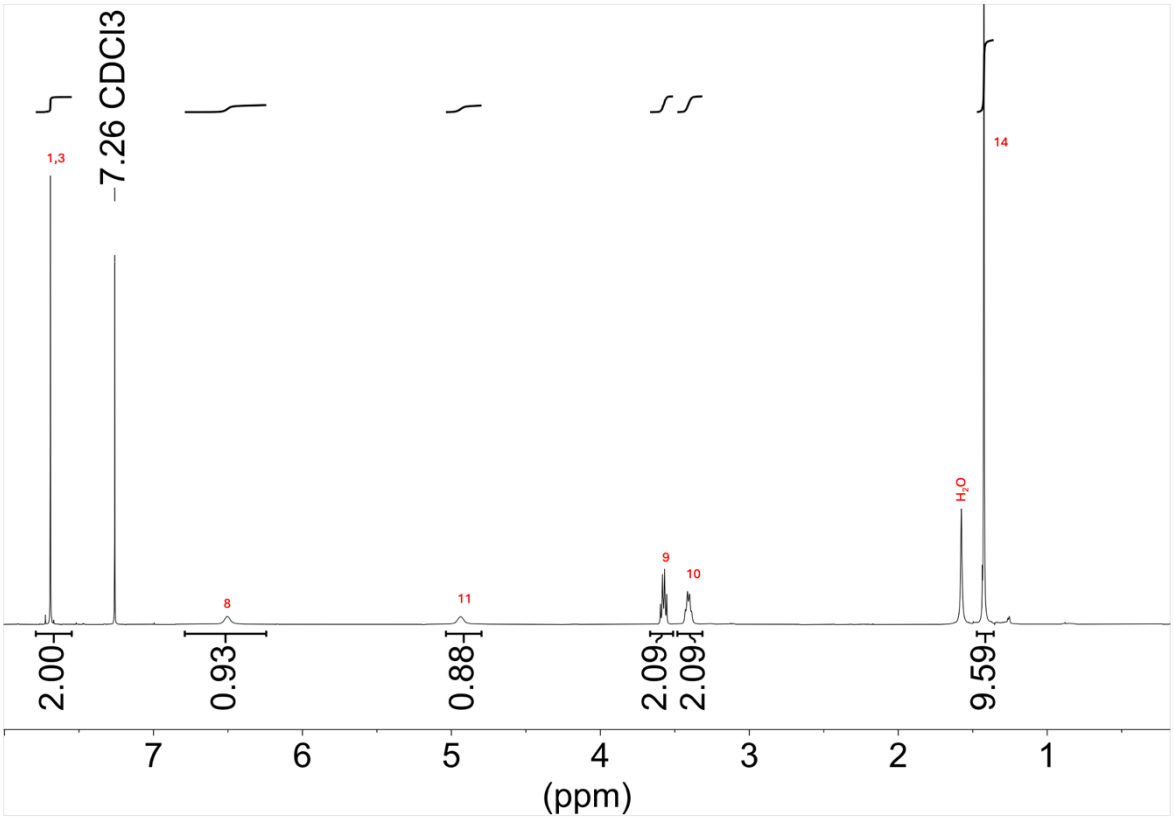


Figure 3.24: **$^1$H NMR** (*400 MHz, $CDCl_3$*) *tert*-butyl (2-(2,4,6-tribromobenzamido)ethyl)carbamate.

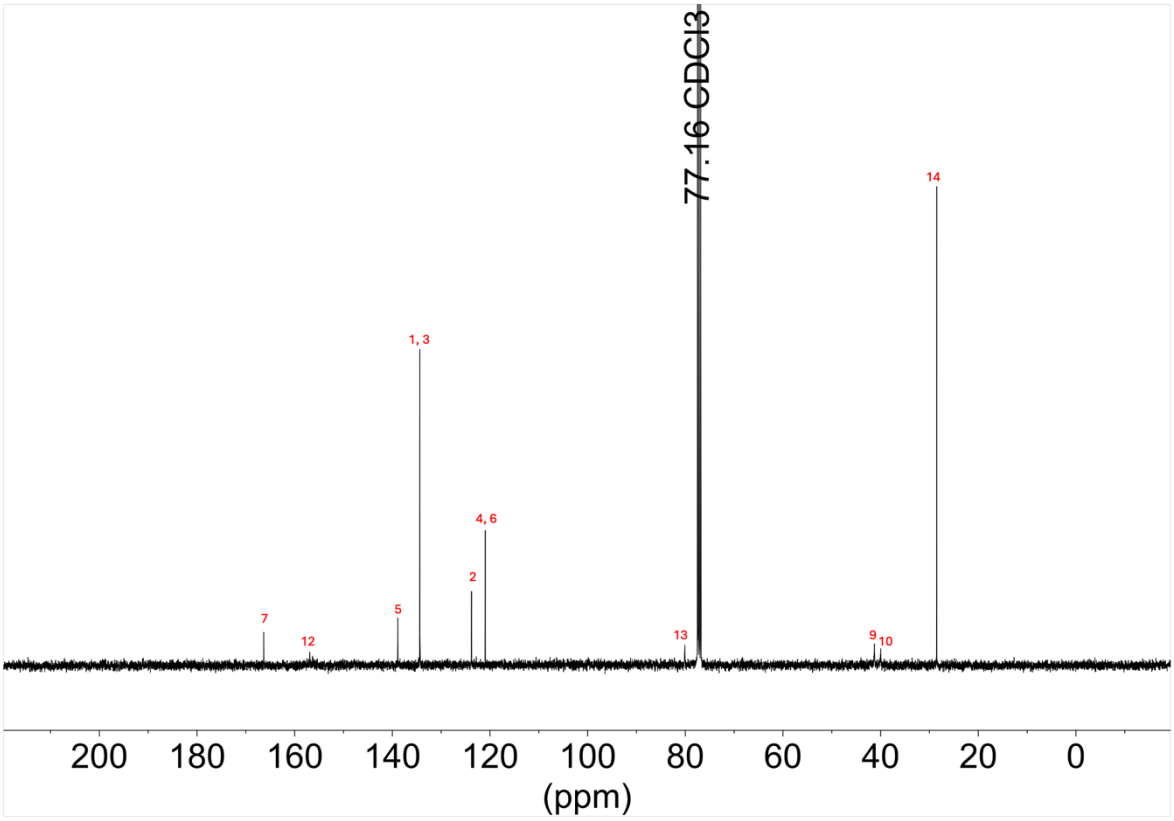


Figure 3.25: **$^{13}$C NMR** (*101 MHz, $CDCl_3$*) *tert*-butyl (2-(2,4,6-tribromobenzamido)ethyl)carbamate.

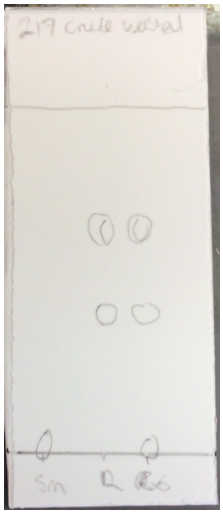


Figure 3.26: TLC analysis of reaction ($SiO_2$ 1:1 EtOAc:Hexane). Sm = starting material (2,4,6-tribromobenzoic acid) $R_f$ = 0.06, R = reaction mixture (*tert*-butyl (2-(2,4,6-tribromobenzamido)ethyl)carbamate) $R_{f\ product}$: 0.41, $R_{f\ impurity}$: 0.56, Cs = co-spot.

### 3.5.2 Synthesis of 2,4,6-tribromo-*N*-(2-(2,5-dioxo-2,5-dihydro-1*H*-pyrrol-1-yl)ethyl) 4

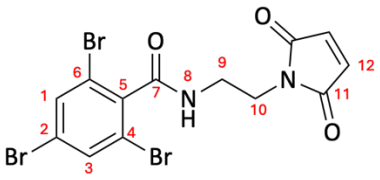


Figure 3.27: Structure of 2,4,6-tribromo-*N*-(2-(2,5-dioxo-2,5-dihydro-1*H*-pyrrol-1-yl)ethyl).

**3** (1.00 g, 2.0 mmol) was dissolved in 20% v/v trifluoroacetic acid in $CH_2Cl_2$ (20 mL) and stirred for 3 h, after which LC-MS analysis suggested complete removal of the protecting group based on a change in retention time on the chromatogram and corresponding mass identification. The solvent was removed, yielding *N*-(2-aminoethyl)-2,4,6-tribromobenzamide as a clear orange oil (632 mg, 79 % yield). **LR-ESI-MS:** Expected $[M+H]^+$ 398.834, Found 398.996.

The deprotected amine product was carried straight to the next step without further characterisation or purification. *N*-(2-aminoethyl)-2,4,6-tribromobenzamide (631 mg, 1.6 mmol, 1.0 eq.) was dissolved in EtOH (anhydrous, 25 mL), followed by addition of maleic anhydride (462 mg, 4.7 mmol, 3.0 eq.). The reaction was stirred at room temperature for 36 h with monitoring by LC-MS until consumption of the amine was complete. After the reaction, the solvent was evaporated and the residue suspended in acetone (20 mL). Nickel (II) acetate (7.0 mg, 0.04 mmol, 0.03 eq.) and $Et_3N$ (1.2 mL, 8.0 mmol, 5.1 eq.) were added at which point the white suspension dissolved. Acetic anhydride (756 µL, 8.0 mmol, 5.1 eq.) was added under stirring and the mixture was heated to 65 °C for 48 h. The mixture darkened from the clear yellow solution to black over several hours. The reaction was cooled to room temperature and the solvent evaporated before dissolving in $CH_2Cl_2$ and washing with DI $H_2O$ (3 × 100 mL). The aqueous layer was extracted with $CH_2Cl_2$ and the organics were combined, dried over $Na_2SO_4$ and reduced in volume, yielding a brown oil. Crude LCMS analysis showed presence of product. The crude was solid loaded onto celite and purified via CombiFlash (40 g Gold $SiO_2$ Column, 60 mL/min, 0:1 EtOAc:Hex to 3:2 EtOAc:Hex over 7 CV). The fractions containing **4** were combined and isolated as an off white solid (483 mg, 64 % yield). **m.p.** 173.8 – 175.1 °C. **$^1$H NMR** (*400 MHz, $CDCl_3$*) δ 7.69 (s, 2H,

*H*$_{1,3}$), 6.75 (s, 2H, *H*$_{12}$), 6.16 (s - br, 1H, *H*$_8$), 3.87 – 3.80 (m, 2H, *H*$_{10}$), 3.75 – 3.70 (m, 2H, *H*$_9$). **$^{13}$C NMR** (*101 MHz, CDCl*$_3$) δ 170.96 *C*$_{11}$, 166.05 *C*$_7$, 138.62 *C*$_5$, 134.42 *C*$_{1,3}$, 123.93 *C*$_2$, 120.90 *C*$_{4,6}$, 39.41 *C*$_{10}$, 37.06 *C*$_9$. **HR-ESI-MS:** For $[C_{13}H_9Br_3N_2O_3+H]^+$ calculated: 478.8242, found: 478.8255. **IR** ν (cm$^{-1}$) 3288, 3072, 2934, 1702, 1649, 1568, 1536, 1408, 1291, 1168, 1102, 858, 827, 738, 697, 575.

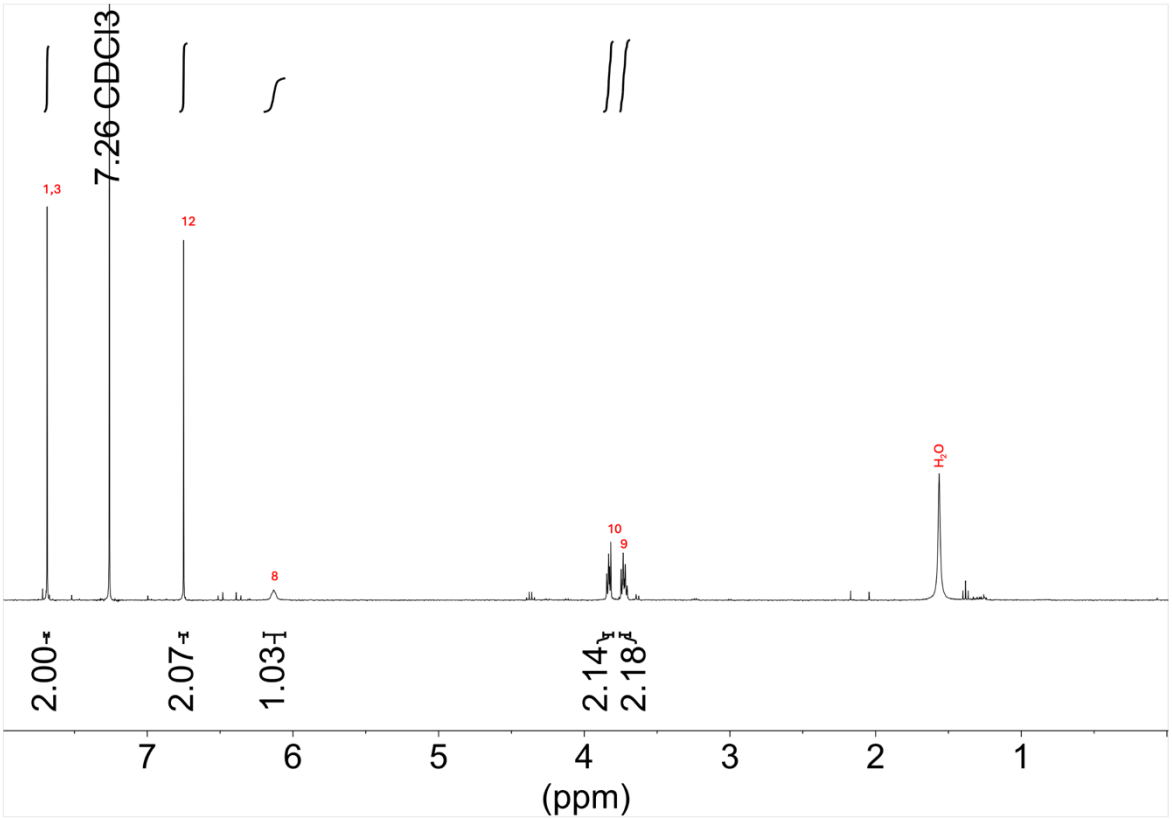


Figure 3.28: **$^1$H NMR** (*400 MHz, CDCl*$_3$) 2,4,6-tribromo-*N*-(2-(2,5-dioxo-2,5-dihydro-1*H*-pyrrol-1-yl)ethyl).

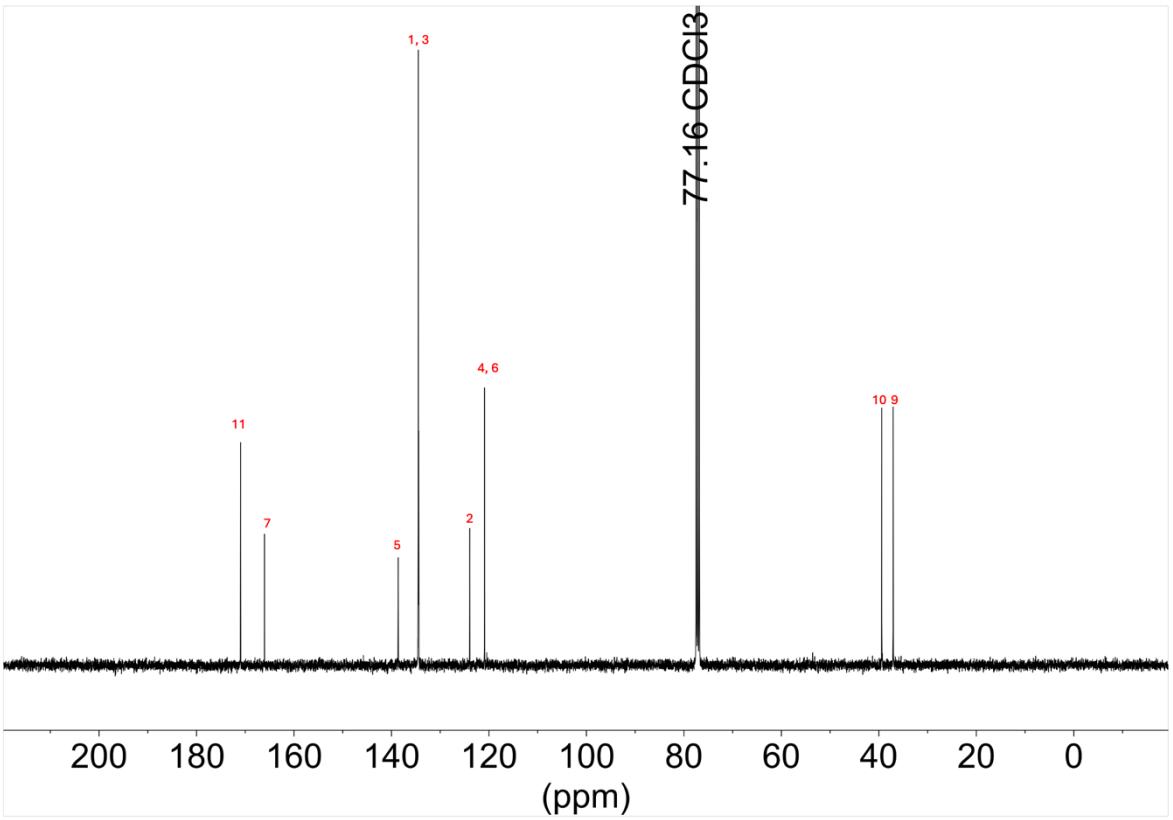


Figure 3.29: **$^{13}$C NMR** (*101 MHz, $CDCl_3$*) 2,4,6-tribromo-*N*-(2-(2,5-dioxo-2,5-dihydro-1*H*-pyrrol-1-yl)ethyl).

### 3.5.3 Synthesis of 2,4,6-tribromobenzyl bromide 5

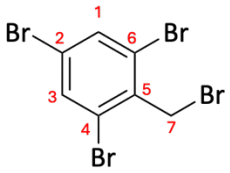


Figure 3.30: Structure of 2,4,6-tribromobenzyl bromide.

Modified from a literature method to omit $CCl_4$.[21] *N*-bromosuccinimide was recrystalised from hot water and dried under high vacuum overnight before use. Tribromotoluene (5.00 g, 15.2 mmol, 1 eq.), *N*-bromosuccinimide (3.11 g, 17.5 mmol, 1.5 eq.) and AIBN (25 mg, 0.2 mmol, 0.01 eq.) were dissolved in chlorobenzene (80 mL) and sparged with argon for 30 min. The solution was heated to 85 °C at which point the solution turned clear red in colour. The reaction was stirred under argon for 45 h, after which time TLC analysis ($SiO_2$, 100% hexane, $R_{f\ product}$: 0.57, $R_{f\ starting\ material}$ 0.86, Figure 3.31) showed consumption of all tribromotoluene and formation of a new product spot. The reaction solution was filtered to remove the insoluble succinimide byproduct. The filtrate was washed with saturated sodium bicarbonate solution (1 × 100 mL) and organics dried over $Na_2SO_4$ before evaporation to yield **5** as a while solid (5.82 g, 94% yield). Characterisation matched that reported in the literature.[21] **$^1$H NMR** (*400 MHz, $CDCl_3$*) δ 7.75 (s, 2H, $H_{1,3}$), 4.79 (s, 2H, $H_7$). **$^{13}$C NMR** (*101 MHz, $CDCl_3$*) δ135.67 $C_{4,6}$, 135.27 $C_{1,3}$, 125.99 $C_5$, 123.34 $C_2$, 33.19 $C_7$. The intermediate was taken to the next stage without further characterisation.

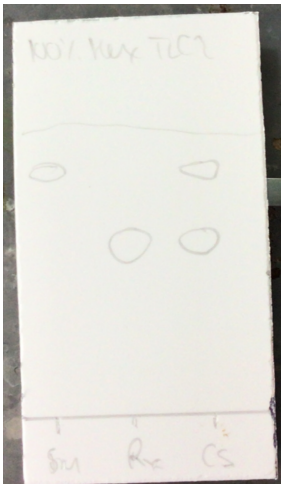

Figure 3.31: TLC analysis of reaction ($SiO_2$ 100% Hexane). Sm = starting material (2,4,6-tribromotoluene) $R_f$ = 0.86, Rx = reaction mixture (2,4,6-tribromobenzylbromide) $R_f$ = 0.57, Cs = co-spot.

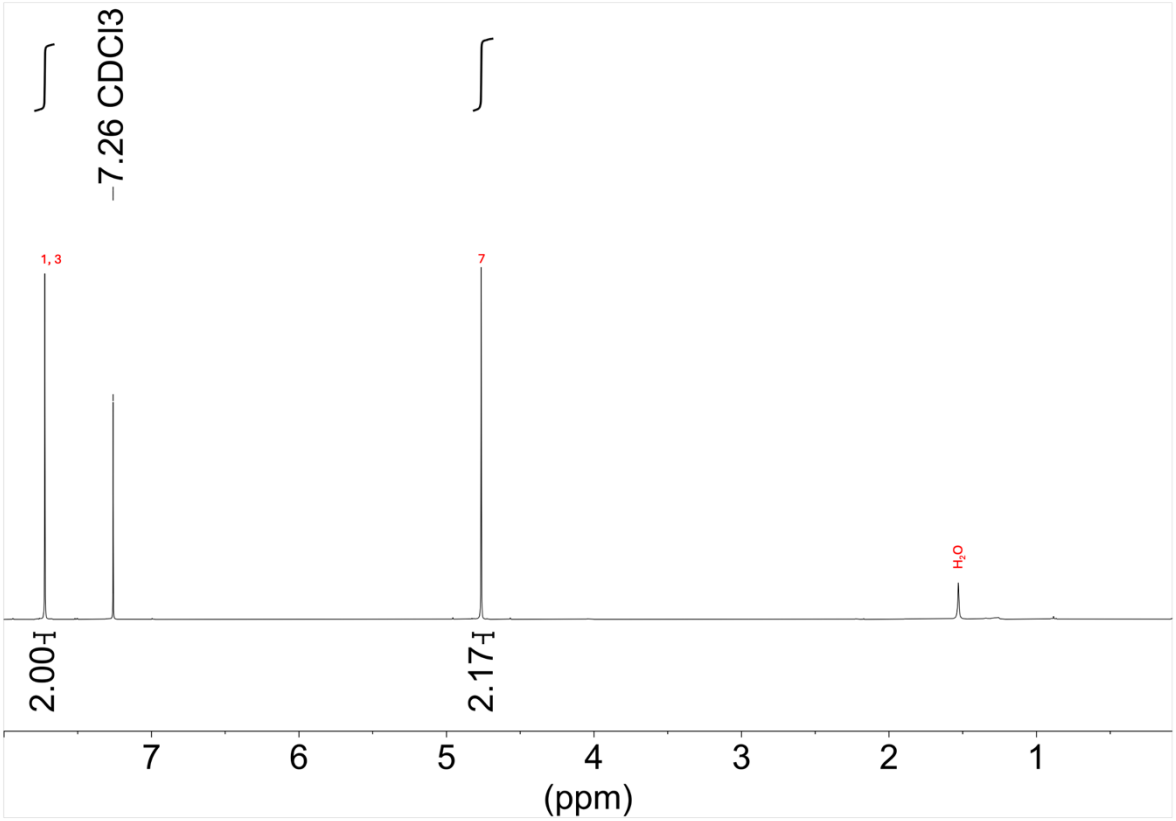


Figure 3.32: **$^1$H NMR** (*400 MHz, $CDCl_3$*) 2,4,6-tribromobenzyl bromide.

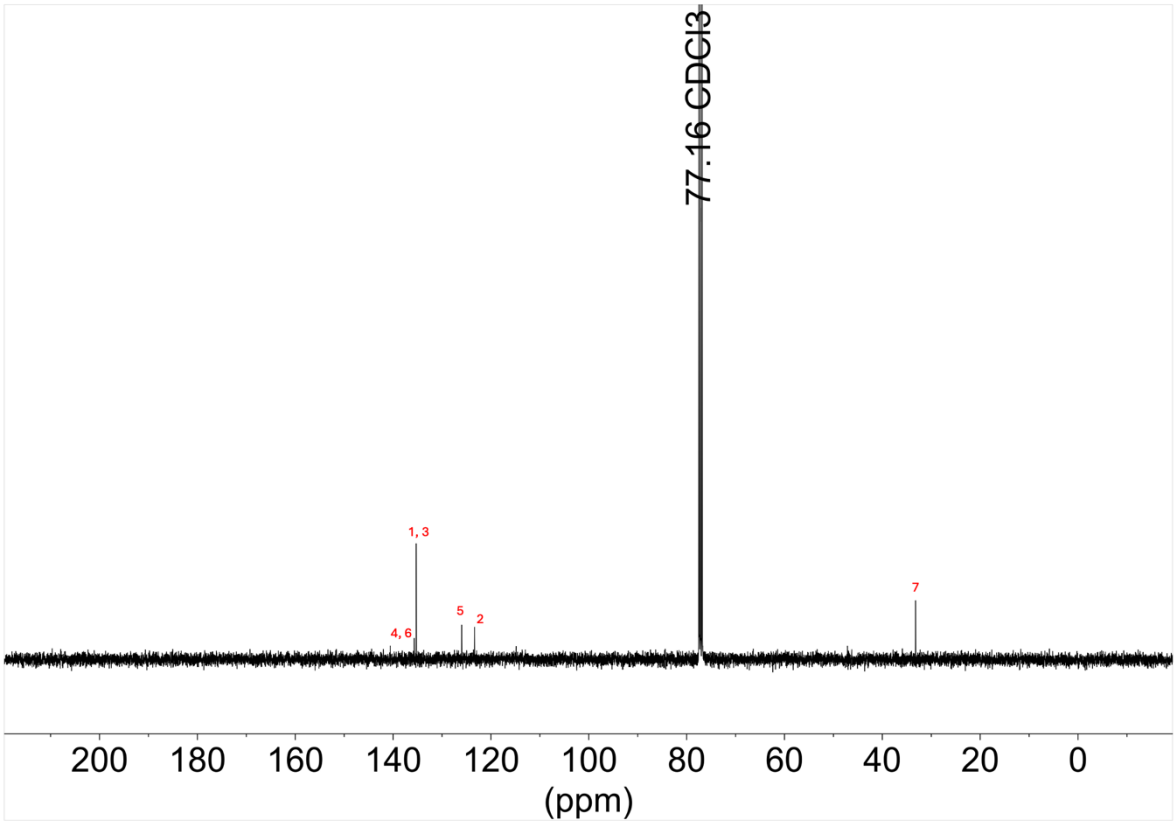


Figure 3.33: **$^{13}$C NMR** (*101 MHz, $CDCl_3$*) 2,4,6-tribromobenzyl bromide.

### 3.5.4 Synthesis of *O*-ethyl *S*-(2,4,6-tribromobenzyl) carbonodithioate 6

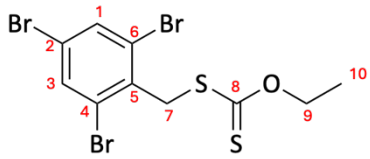


Figure 3.34: Structure of *O*-ethyl *S*-(2,4,6-tribromobenzyl) carbonodithioate.

**5** (5.82 g, 14.3 mmol, 1.0 eq.) was dissolved in in acetone (15 mL) at 40 °C with stirring. Potassium ethyl xanthogenate (2.50 g, 15.7 mmol, 1.1 eq.) was added in one portion to the stirred mixture, turning the clear orange solution to a brown solution with colourless precipitate. The suspension was stirred at room temperature for 1 h, after which TLC analysis showed consumption of all starting material and product formation ($SiO_2$, 100% hexane, $R_{f\ product}$: 0.40, Figure 3.35). The colourless KBr precipitate was removed by gravimetric filtration and washed with acetone (3 × 5 mL). The clear brown filtrate and combined acetone washings were evaporated to dryness giving a brown oil. The crude product was then purified via CombiFlash (80 g Gold $SiO_2$ Column, 100% hexane). The fractions containing **6** were combined and allowed to evaporate, yielding **6** as a colourless crystalline solid (1.72 g, 27% yield) **m.p.** 61.4 - 62.4 °C. **$^1$H NMR** (*400 MHz, $CDCl_3$*) δ 7.71 (s, 2H, $H_{1,3}$), 4.71 (m, $J$ = 7.2 Hz, 4H, $H_7$, $H_9$), 1.45 (t, $J$ = 7.1 Hz, 3H, $H_{10}$). **$^{13}$C NMR** (*101 MHz, $CDCl_3$*) δ 212.88 $C_8$, 135.05 $C_{1,3}$, 133.35 $C_5$, 126.36 $C_{4,6}$, 122.68 $C_2$, 70.45 $C_9$, 42.09 $C_7$, 13.99 $C_{10}$. **HR-ESI-MS:** For $[C_{10}H_9Br_3OS_2+CH_3OH]^+$ calculated: 478.7985, found: 478.7992. **UV/Vis** $CHCl_3$ $\lambda_{abs}$ = 290 nm. **IR** ν ($cm^{-1}$) 2981, 1562, 1532, 1432, 1371, 1220, 1111, 1044, 857, 829, 733.

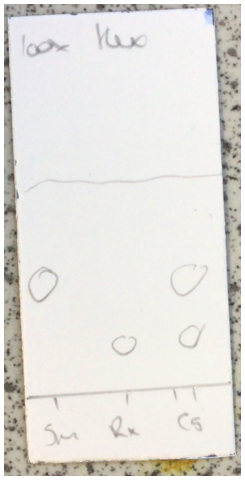


Figure 3.35: TLC analysis of reaction ($SiO_2$ 100% Hexane). Sm = starting material (2,4,6-tribromobenzyl bromide) $R_f$ = 0.57, Rx = reaction mixture (*O*-ethyl *S*-(2,4,6-tribromobenzyl) carbonodithioate) $R_f$ = 0.40, Cs = co-spot.

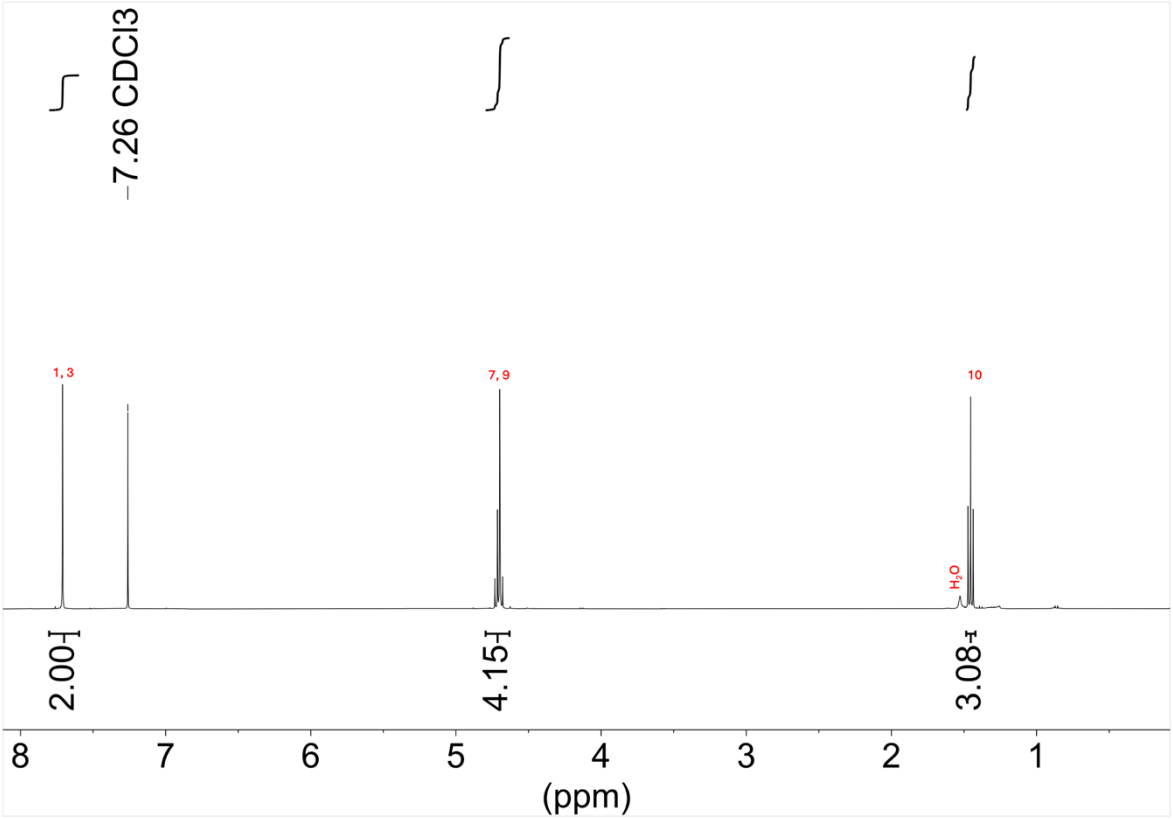


Figure 3.36: **$^1$H NMR** (*400 MHz, $CDCl_3$*) *O*-ethyl *S*-(2,4,6-tribromobenzyl) carbonodithioate.

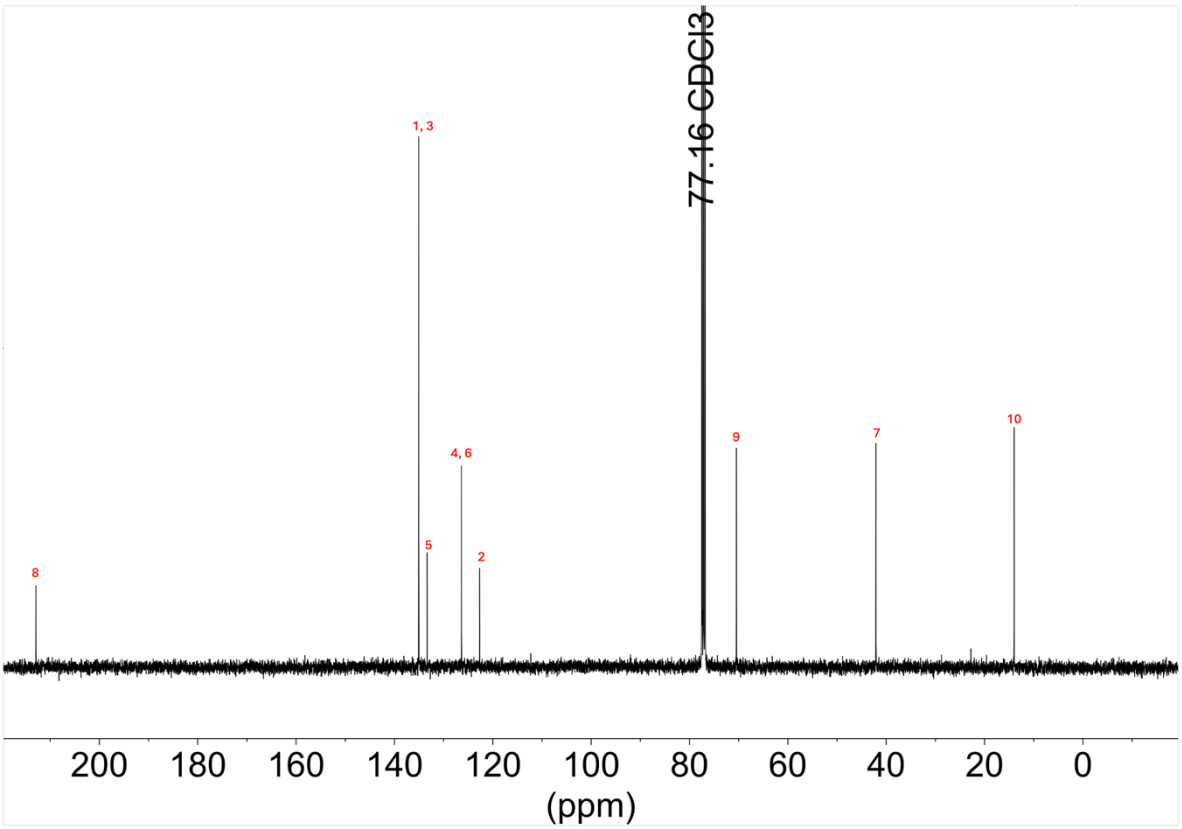


Figure 3.37: **$^{13}$C NMR** (*101 MHz, $CDCl_3$*) *O*-ethyl *S*-(2,4,6-tribromobenzyl) carbonodithioate.

### 3.5.5 Synthesis of PVAc-Br

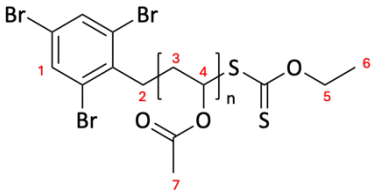


Figure 3.38: Structure of PVAc-Br.

**6** (27.8 mg, 0.06 mmol, 1 eq.) and $Bi_2O_3$ (5.8 mg, 0.01 mmol, 0.2 eq.) were added to a solution of destabilised vinyl acetate (2.0 mL, 1.87 g, 21.7 mmol, 350 eq.) in DMSO (2 mL) and DMF (100 µL). The solution was deoxygenated via argon sparge for 30 min. The sealed reaction vessel was irradiated with white light (15 W Fluorescent tube, 1010 lm) at rt. The light bulb was set to 2 cm away from the Schlenk flask. The reaction was monitored by $^1$H NMR spectroscopy to determine conversion and quenched by immersion in $N_2$(l) and subsequent oxygen exposure when conversion reached 89%. The polymer was precipitated 3 × into cold diethyl ether (40 mL) and then dialysed against acetone (4 bulk changes) before drying and lyophilising from 1,4-dioxane. A colourless brittle solid was obtained. **$^1$H NMR** (*400 MHz, $CDCl_3$*) δ 7.67 (s, 2H, $H_1$), 4.75 – 5.07 (s br, 312H, $H_4$), 1.92 – 2.12 (t -br, 940H, $H_7$), 1.54 – 1.92 (s -br, 673H, $H_3$). **GPC**: THF, $M_n$: 17,300 gmol$^{-1}$, $M_w$: 20,800 gmol$^{-1}$, Đ: 1.20.

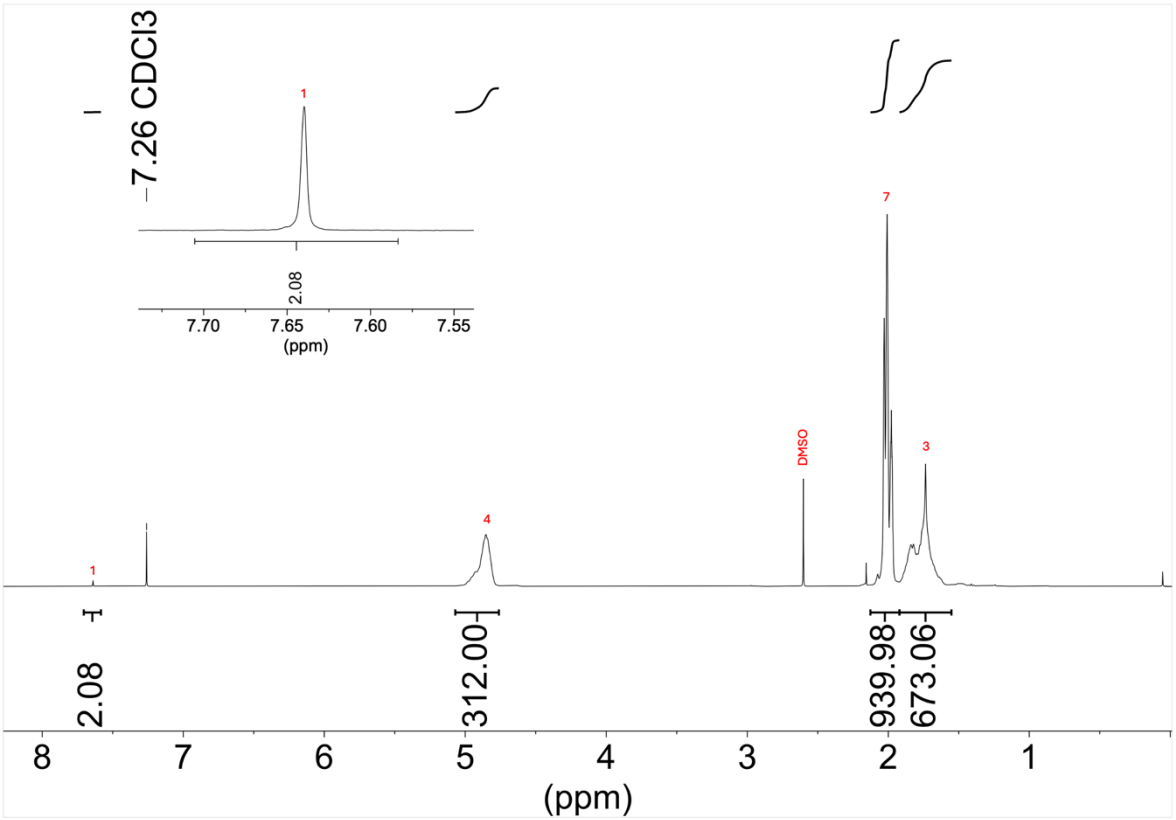


Figure 3.39: **$^{1}$H NMR** (*400 MHz, $CDCl_3$*) PVAc-Br.

### 3.5.6 Full hydrolysis of bromine tagged polyvinyl acetate to polyvinyl alcohol

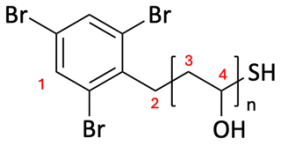


Figure 3.40: Structure of PVA-Br.

Bromine tagged polyvinyl acetate (900 mg, $M_n$ 26,800 gmol$^{-1}$, 33.6 µmol) was dissolved in a methanol (10 mL) to which sodium hydroxide (7.5 mL, 1M) was added. The reaction mixture was stirred at 50 °C for 16 h. The reaction mixture was neutralised with dilute HCl (7.5 mL, 1M). The reaction mixture was then dialysed against deionised water (5 bulk changes) and polyvinyl alcohol was recovered via lyophilisation from water as a white spongy solid (typical yield 90 – 100%). Full hydrolysis was confirmed by $^1$H NMR spectroscopy. **$^1$H NMR** (*400 MHz, $D_2O$*): δ 7.84 (s, 2H, *$H_1$*), 3.66 – 4.31 (br, 312H, *$H_4$*), 1.86–1.50 (br, 645H, *$H_3$*).

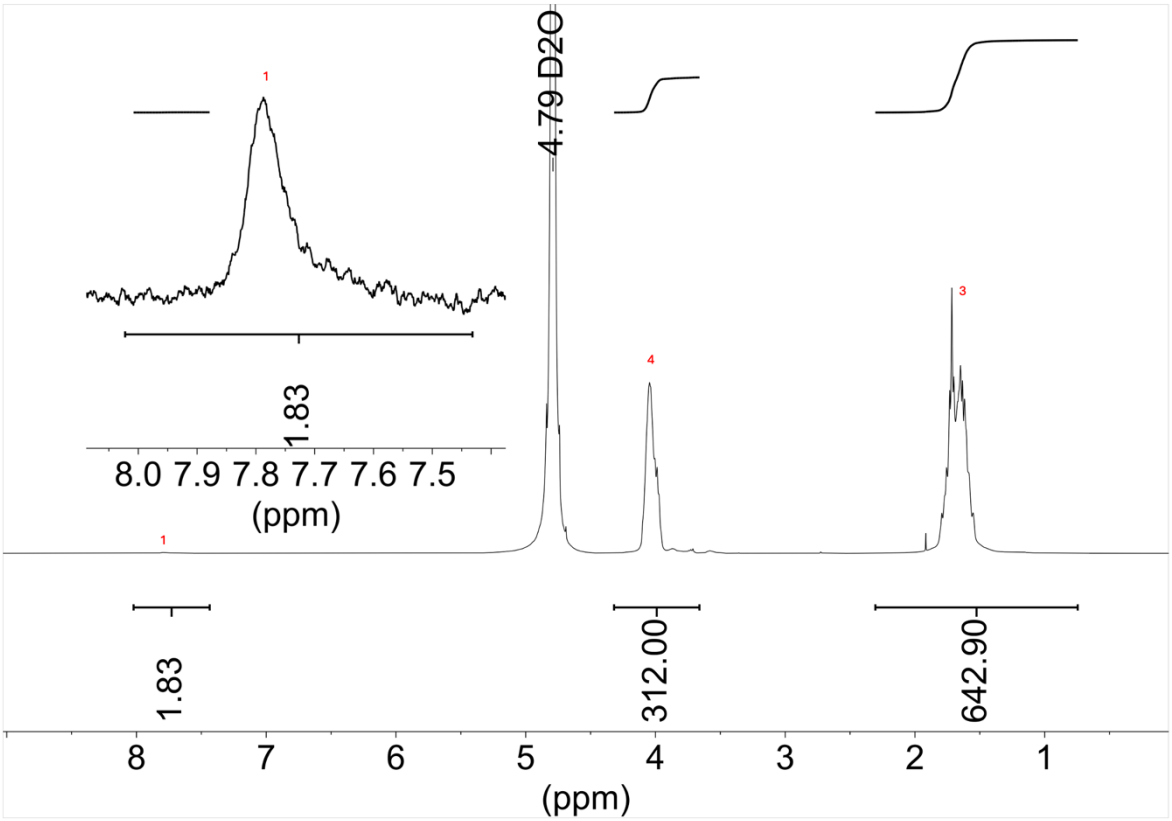


Figure 3.41: **$^1$H NMR** (*400 MHz, $D_2O$*) PVA-Br.

### 3.5.7 Acetylation of bromine tagged polyvinyl alcohol to polyvinyl alcohol-co-(vinyl acetate)

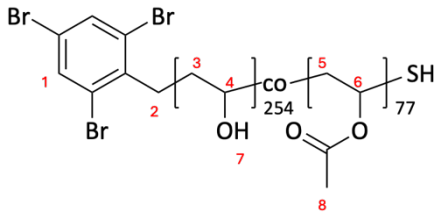


Figure 3.42: Structure of bromine tagged polyvinyl alcohol to polyvinyl alcohol-co-(vinyl acetate).

In a typical experiment, targeting 20 mol% acetyl content, bromine terminated polyvinyl alcohol (600 mg, $M_n$ 14,520 g mol$^{-1}$, 41.3 µmol) was dissolved in DI $H_2O$ (4998 µL) to which glacial acetic acid (5910 µL) and HCl (5M, 655 µL) was added. The solution was stirred at 50 °C for 2 days. The polymer solution was dialysed against water (5 bulk changes) before lyophilisation of the purified reaction mixture from water yielding a white spongy solid. Typically, close to quantitative yield was achieved. **$^1$H NMR** (*400 MHz, DMSO-$d_6$*): δ 7.89 (s, 2H, $H_1$), 4.79 – 5.21 (br, 73H, $H_6$), 3.51–4.01 (br, 254H, $H_4$), 1.87–2.18 (br, 230H, $H_8$), 0.97–1.72 (br, 660H, $H_3$, $H_5$).

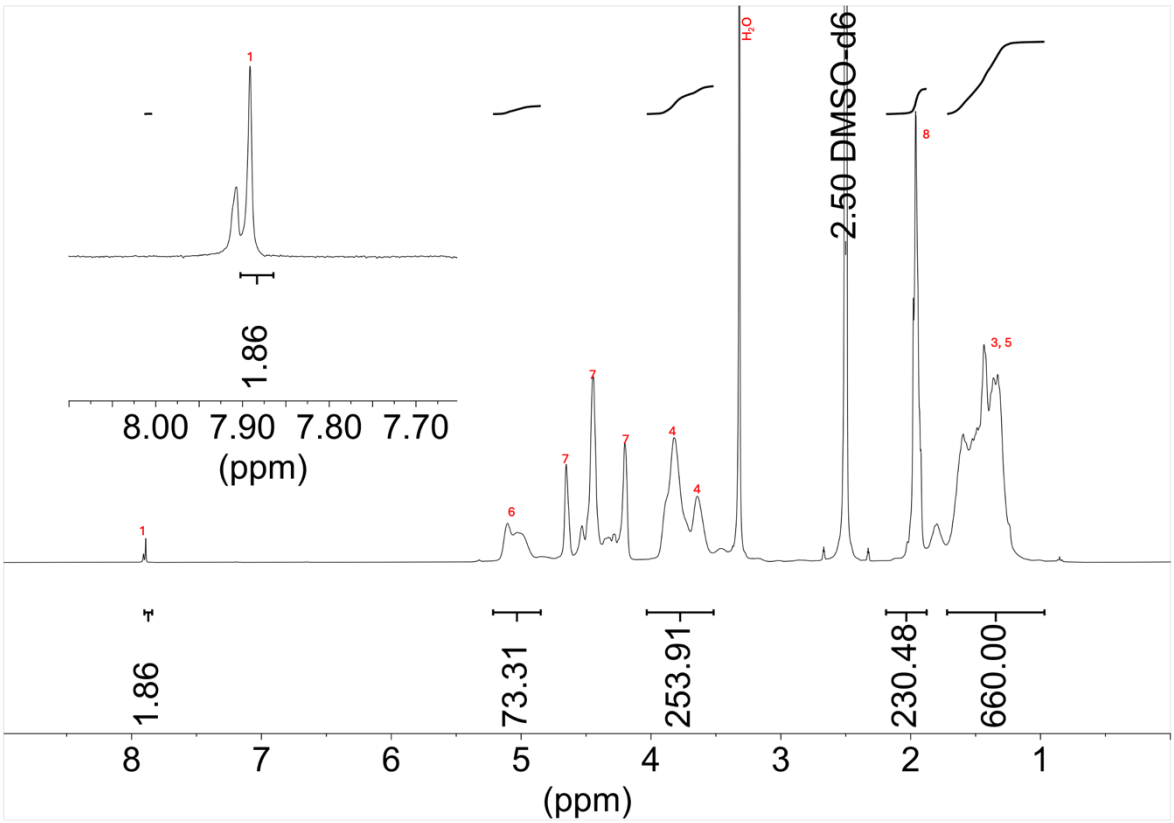


Figure 3.43: **$^1$H NMR** (*400 MHz, DMSO-$d_6$*) Bromine tagged polyvinyl alcohol-co-(vinyl acetate) DA=22%.

Table 3.4: Summary of partially acetylated PVA synthesised for ion beam analysis.

| **Polymer** | **Targeted DA** | **Volume acetic acid added / µL** | **Volume $H_2O$ added / µL** | **Volume HCl 5M added / µL** | **Achieved DA[a] (number of OAc units)** | **$M_n$[a] / gmol$^{-1}$** |
|---|---|---|---|---|---|---|
| **P14** | 5% | 1950 | 8958 | 655 | 5% (17) | 15,200 |
| **P15** | 12% | 4167 | 6741 | 655 | 15% (50) | 16,600 |
| **P16** | 20% | 5910 | 4998 | 655 | 22% (73) | 17,600 |

[a]Determined by $^1$H NMR spectroscopy.

### 3.5.8 Film Preparation

PVA-Br (**P14**-**P16**) films were cast from 20 w/v% solutions made up of polymer, DI $H_2O$ and glycerol (20 w/w% relative to polymer) into PDMS moulds (51 x 24 mm) lined with aluminium catering foil. The foil was present avoid any issues of film adhesion during manipulation once dried.

Additionally, a commercial polymer film was cast from high molecular weight PVA (Mowiol 18-88, $M_w$: 130 kDa, DH: 88%). The commercial polymer was made up to 10% w/v in solution with DI $H_2O$ with 20% w/w glycerol added with respect to polymer mass. Films were cast into PDMS moulds lined with 0.2 mm thick aluminium sheets. Both sets of films were dried at 70% humidity (saturated KCl solutions), 50 °C for 2 days, yielding clear colourless films for the commercial polymer, and clear golden films for the PVA-Br. It was noted that the lower the DH% of the PVA-Br film, the tackier and softer it appeared.

Dry film thickness was then determined for each film by use of a digital coating thickness gauge. A six-point average was taken for commercial films, and a three-point average for PVA-Br due to the size of the film relative to that of the probe. Film pairings and thicknesses are shown in Table 3.5.

Table 3.5: Summary of sandwich film compositions showing component thickness and structural representation of PVA-Br component.

| Sample | Composition | Average Thickness / µm | Structure PVA-Br |
|---|---|---|---|
| **A** | Mowiol 18-88 DH 88% | 121 | 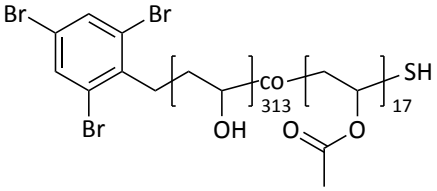 |
| | **P14** - PVA-Br DH 95% | 192 | |
| **B** | Mowiol 18-88 DH 88% | 99 | 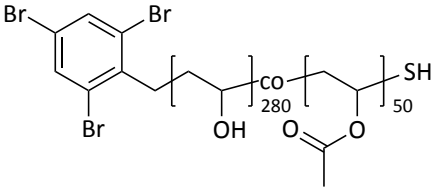 |
| | **P15** - PVA-Br DH 85% | 264 | |
| **C** | Mowiol 18-88 DH 88% | 58 | 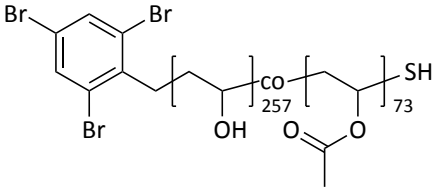 |
| | **P16** - PVA-Br DH 78% | 219 | |

Films were then combined to create a sandwich of PVA-Br and commercial PVA, and equilibrated at 50 °C, 70% humidity (saturated salt solutions) and with a 100 g weight placed on top of each film to encourage polymer interdiffusion for one week before transferring to the National Ion Beam Facility in Surrey, UK. Sample transfer from Durham to Surrey was not humidity/temperature controlled.

After transportation, the thicker aluminium backing sheet (from the commercial polymer casting) was removed from the sample to improve the ease of cutting of the film. Immediately prior to analysis, a cross-sectional slice of the film was taken with a guillotine and the film slice mounted to expose a fresh edge to the proton beam (Figure 3.23).

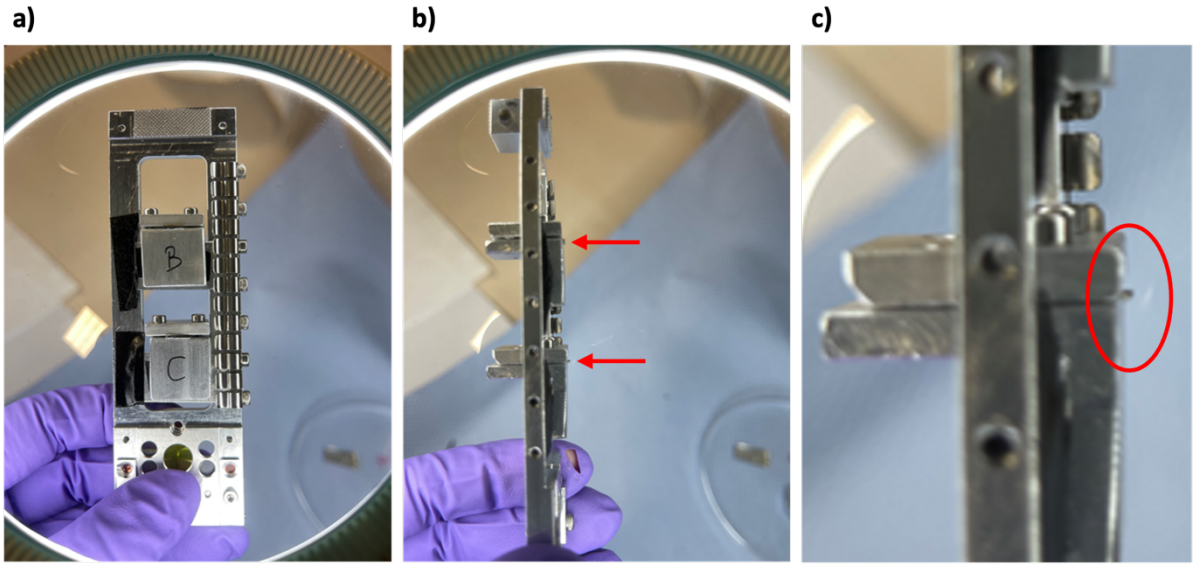

Figure 3.44: Sample holder setup for nanobeam line. Samples clamped in position with adjustable metal blocks. a) head on view of samples, b) side on view of samples with red arrows showing protrusion from metal blocks, c) zoomed in region of central image showing protrusion more clearly.

### 3.5.9 RBS and PIXE analysis

The X-ray and RBS detectors of the nanobeam line were calibrated by use of a BCR126A (Lead Glass) standard at the beginning of each day of experiments, and each time the chamber was opened. The use of the BCR glass as a standard for PIXE and backscattered measurements is described by Grime *et al.*[22] The measurement of this standard allows for energy calibration and determination of the X-ray detector efficiency as well as the set geometry parameters for all subsequent measurements for both detectors.[22, 23] The software OMDAQ compares the measured elemental concentrations against the known concentrations, with a ratio of 1:1 desired, and a measurement within 10% of the standard deviation accepted. Samples were measured using 2.5 MeV (nominal beam energy) $H^+$ beam at normal incidence on the nanobeam line. Elastically backscattered protons were detected using a passivated implanted planar silicon (PIPS) charged particle detector with an active area of 150 $mm^2$ mounted at 20° exit angle (β) (scattering angle (θ) of 160°). A silicon drifted detector (SDD) with active area of 80 $mm^2$, mounted at a central angle of 135° to the beam direction in the horizontal plane and with a sample to detector distance which can be varied between 40 mm and 90 mm. The X-ray detector was

fitted with a 130 µm beryllium foil and a sampling cone to X-ray signals from the chamber from entering the detector. Beam spot size was approximately ~1.5 × 1.5 µm, as measured using a 75 × 75 µm scan area on the copper grid. OMDAQ-3 was used to collect and later to process the data.

### 3.5.10 ToF-ERDA analysis

Measurements were taken using the ToF-ERDA beamline at UKNIBC using a 16 MeV $^{127}I^{8+}$ beam. Both incident and exit angles = 69.5°, with scattering angle = 41°. To convert from thin film units (1 TFU = $10^{15}$ atoms/cm$^2$) output by the instrument to nm, a density assumption was required for PVA. 1.19 g/cm$^3$ was used for all samples regardless of acetylation content. The conversion was then made by Equation 31.

$$t[nm] = t[TFU]\frac{10^{22}\,M_n}{\rho n N_A} \qquad \text{(Equation 31)}$$

where $t$ is thickness, $M_n$ is polymer molecular mass determined by $^1$H NMR spectroscopy including end groups, $\rho$ is density, $n$ is atoms per molecule, $N_A$ is Avogadro's constant.

Analysis was carried out with the Potku software to calculate depth profiles of each element.

### 3.6 References


1. T. B. Johansson, R. Akselsson and S. A. E. Johansson, *Nucl. Instrum. Methods*, 1970, **84**, 141-143.
2. S. A. E. Johansson and T. B. Johansson, *Nucl. Instrum. Methods*, 1976, **137**, 473-516.
3. K. Ishii, *Quantum Beam Sci.*, 2019, **3**, 12.
4. E. F. Garman and G. W. Grime, *Prog. Biophys. Mol. Biol.*, 2005, **89**, 173-205.
5. J. Clayden, N. Greeves and S. Warren, *Organic Chemistry*, OUP Oxford, 2012.
6. T. Congdon, P. Shaw and M. I. Gibson, *Polym. Chem.*, 2015, **6**, 4749-4757.
7. K. Arstila, J. Julin, M. I. Laitinen, J. Aalto, T. Konu, S. Kärkkäinen, S. Rahkonen, M. Raunio, J. Itkonen, J. P. Santanen, T. Tuovinen and T. Sajavaara, *Nucl. Instrum. Methods Phys. Res. B*, 2014, **331**, 34-41.
8. L. T. Gibson, in *Encyclopedia of Analytical Science (Second Edition)*, eds. P. Worsfold, A. Townshend and C. Poole, Elsevier, Oxford, 2005.
9. U. H. Hossain, T. Seidl and W. Ensinger, *Polym. Chem.*, 2014, **5**, 1001-1012.
10. T. Seidl, O. Baake, U. H. Hossain, M. Bender, D. Severin, C. Trautmann and W. Ensinger, *Nucl. Instrum. Methods Phys. Res. B*, 2012, **272**, 400-404.
11. T. Seidl, A. Plotnikov, E. Mustafin, R. Lopez, D. Severin, E. Floch, C. Trautmann, A. Golubev, A. Smolyakov, D. Tommasini and W. Ensinger, *Polym. Degrad. Stabil.*, 2012, **97**, 2396-2402.
12. E. Balanzat, N. Betz and S. Bouffard, *Nucl. Instrum. Methods Phys. Res. B*, 1995, **105**, 46-54.
13. D. Severin, E. Balanzat, W. Ensinger and C. Trautmann, *J. Appl. Phys.*, 2010, **108**, 024901.
14. D. Severin, W. Ensinger, R. Neumann, C. Trautmann, G. Walter, I. Alig and S. Dudkin, *Nucl. Instrum. Methods Phys. Res. B*, 2005, **236**, 456-460.
15. J. Davenas, I. Stevenson, N. Celette, S. Cambon, J. L. Gardette, A. Rivaton and L. Vignoud, *Nucl. Instrum. Methods Phys. Res. B*, 2002, **191**, 653-661.
16. T. Steckenreiter, E. Balanzat, H. Fuess and C. Trautmann, *Nucl. Instrum. Methods Phys. Res. B*, 1997, **131**, 159-166.
17. A. Chapiro, *Nucl. Instrum. Methods Phys. Res. B*, 1995, **105**, 5-7.
18. R. J. Fong, A. Robertson, P. E. Mallon and R. L. Thompson, *Polymers*, 2018, **10**, 1036.
19. S. Wei, V. Pintus and M. Schreiner, *J. Anal. Appl. Pyrolysis*, 2012, **97**, 158-163.
20. E. H. Lee, *Nucl. Instrum. Methods Phys. Res. B*, 1999, **151**, 29-41.
21. Y. Li, J. M. Wang, J. L. Kan, F. Li, Y. Dong and Y. B. Dong, *Inorg. Chem.*, 2022, **61**, 2455-2462.
22. G. W. Grime, O. B. Zeldin, M. E. Snell, E. D. Lowe, J. F. Hunt, G. T. Montelione, L. Tong, E. H. Snell and E. F. Garman, *J. Am. Chem. Soc.*, 2020, **142**, 185-197.
23. G. W. Grime, *Nucl. Instrum. Methods Phys. Res. B*, 1996, **109-110**, 170-174.

## 3.7 Appendix

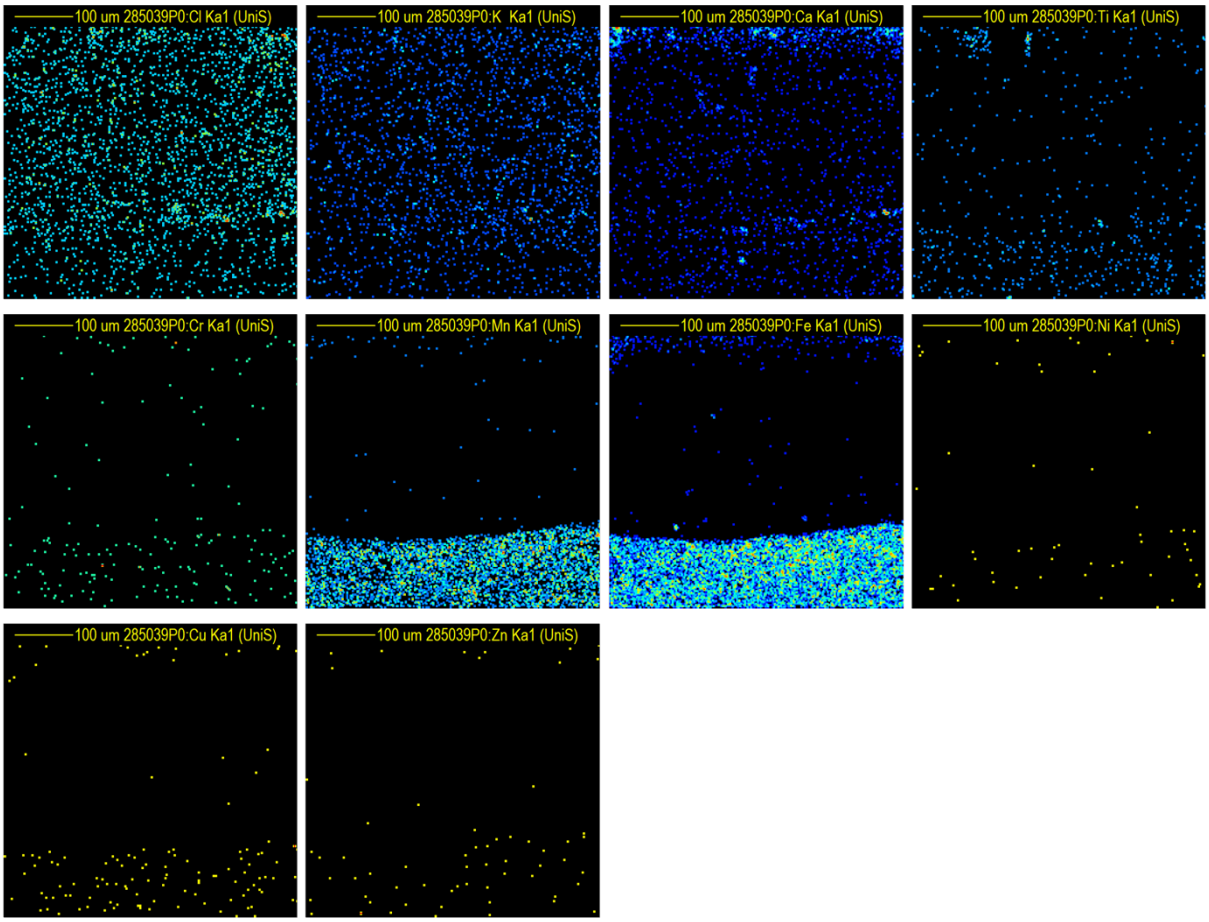


Figure 3.45: Sample **A** PIXE maps for other elements present in the X-ray spectra. Some of these are from the aluminium alloy sample holder.

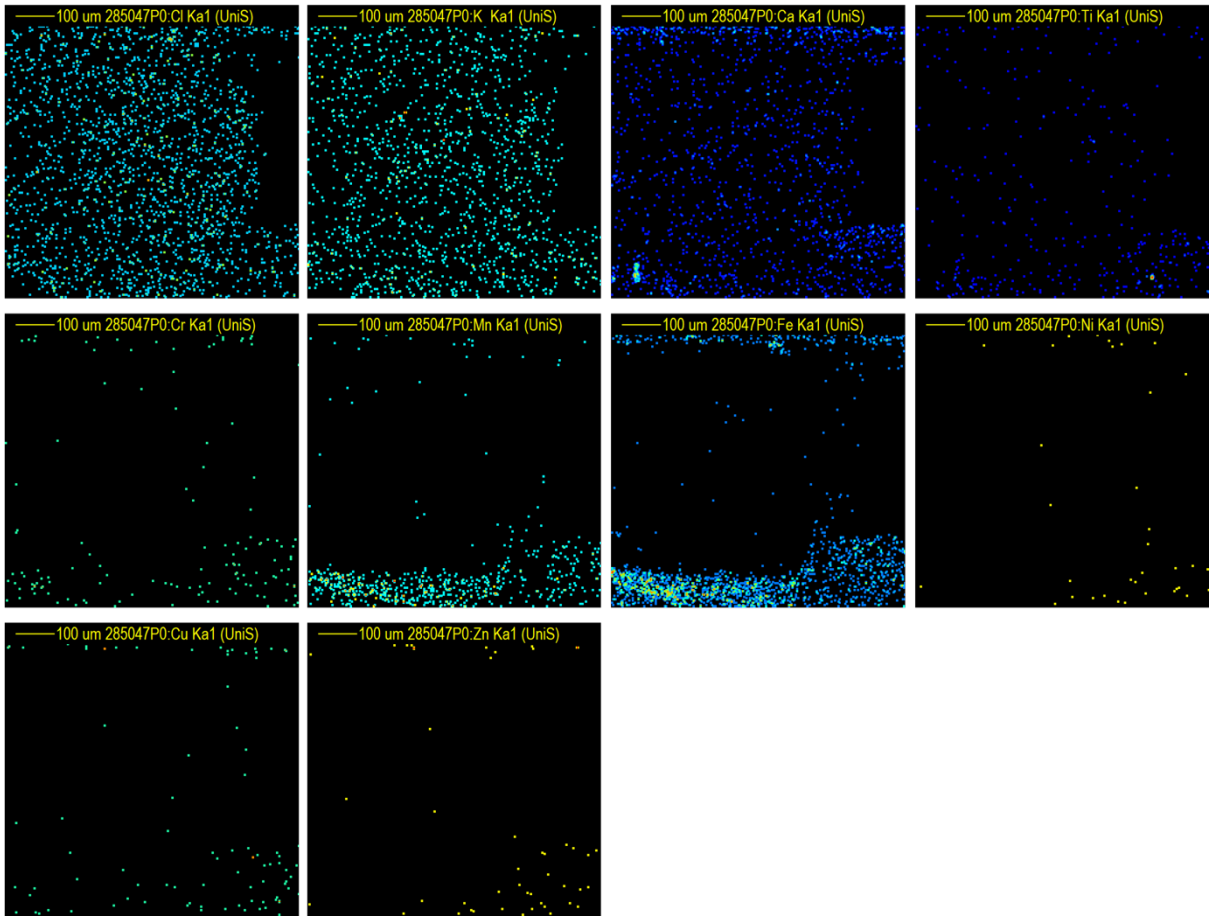


Figure 3.46: Sample **B** PIXE maps for other elements present in the X-ray spectra. Some of these are from the aluminium alloy sample holder.

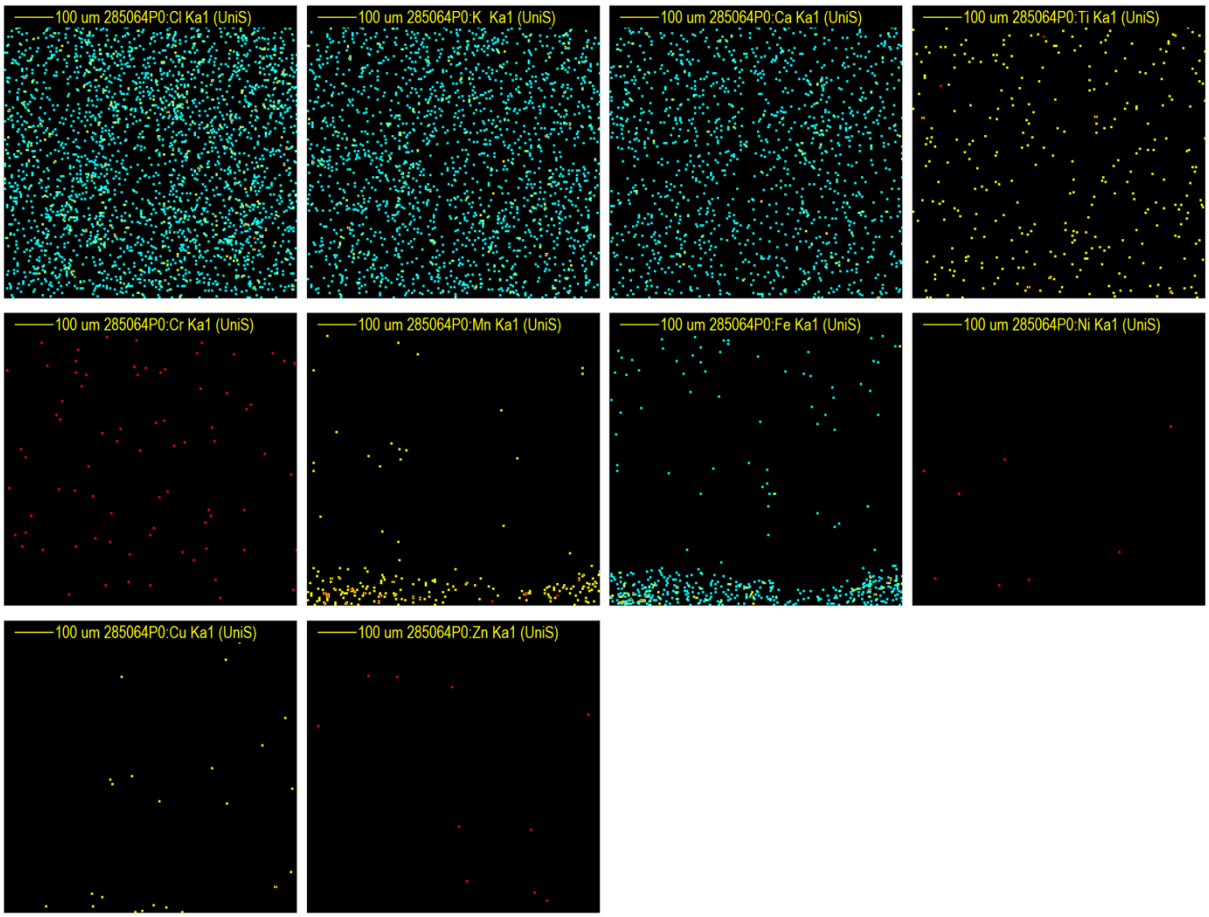


Figure 3.47: Sample **C** PIXE maps for other elements present in the X-ray spectra. Some of these are from the aluminium alloy sample holder.

# Chapter 4: A fluorescent end group label for time resolved polyvinyl alcohol diffusion measurement via fluorescent microscopy

## 4.1 Introduction

Polymer diffusion is a key factor which impacts both the manufacturing and use mechanisms of SUD pods, with chain mobility governing entanglement between the two layers of PVA film as they are combined to seal in the contents of the pod on the production line. Similarly, in the reverse process, the diffusion of polymer chains into aqueous washing media and the disentanglement of the chains within the film impacts the release rate of the pod contents. It is therefore important to characterise and assess the diffusion of polyvinyl alcohol in thin films to assess the impact of polymer structure on diffusion rate.

The complexity of polymer diffusion processes arises due to the wide variety of factors that can influence the behaviour of polymers, elements such as molecular weight, chain structure, concentration, and temperature. [1-4] Polymers diffuse more slowly than small molecules in solution, as a consequence of their large size and complex entanglements. There are a variety of models for diffusion in polymeric systems,[5] although they usually describe the movement of a solvent or small molecule diffusant, using techniques such as NMR[6] and fluorescence correlation spectroscopy (FCS).[7] Models for polymer entanglement and self-diffusion have garnered computational,[8] theoretical,[9, 10] and experimental attention,[11, 12] and although the systems heavily vary depending on the nature of the polymer, solvent, state and temperature, diffusion coefficients are often several orders of magnitude lower than their small molecule counterparts.[6] As well as in SUD pod manufacture, the diffusion of polymers plays a critical role in many other applications, including drug delivery, material processing, and understanding the dynamics of polymer blends and composites. The study of polymer diffusion helps in predicting the behaviour and performance of polymer-based materials in real-world applications.

In order to investigate the mobility of polymer chains using Fluorescence recovery after photobleaching (FRAP), a fluorescently labelled suite of polymers closely matching the materials in

SUD pod manufacture were designed (Figure 4.1). The model materials consisted of a series of PVA/PVAc polymers with varying DH, covering the range around commercially available options (DH 95 - 78%), and a fluorescent dye to facilitate observation of diffusion through light microscopy. In the manufacturing process of SUD pods, the PVA film is plasticised with glycerol to enhance chain mobility and allow fast entanglement to seal the pods, and so it was included in the films analysed in this work. Polymer molecular weight, as well as Đ, and environmental factors including temperature and humidity are kept constant during this work. The only aspect of the polymer systematically varied for this investigation is the polymer DH, which is known to impact chain crystallinity.[13] While this system is a simplification of real world polymer systems used in SUD formulations, it allows the isolation of the effect of DH on diffusion behaviour, and the acquisition of information to better inform computational models of this process.

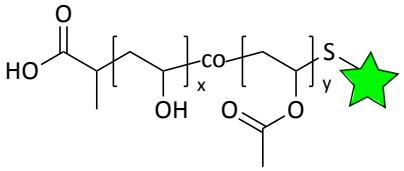


Figure 4.1: General polymer chain structure proposed for use in this work x=100, 95, 90 or 85%, y=(100-x)%. Green star reporesents photobleachable fluorescent end group label.

Studies of diffusion in polymer systems via fluorescence have been reported in the literature - Weiss *et al.* use FCS with fluorescently labelled dextrans to investigate diffusion in the cytoplasm;[14] Richbourg *et al.* utilise fluorescent microscopy to analyse fluorescently labelled dextrans and poly(ethylene glycol) diffusivity in PVA hydrogels with varying levels of cross linking.[15] Diffusion kinetics of rhodamine B in PVA thin films was investigated as a function of surfactant concentration by Majerczak *et al.*[16] Fluorescence-based approaches have been used to study the diffusion processes of macromolecules,[17, 18] but literature specifically focusing on synthetic polymers is limited. Most studies use commercially available FITC-labelled dextrans and PEG,[17, 19, 20] while reports involving other types of fluorescently labelled polymers are rare. Instead, most research describes polymer systems doped with small-molecule fluorophores.[16, 21]

### 4.1.1 FRAP Microscopy

FRAP is a microscopy technique developed by Axelrod *et al.* in 1979 to study the mobility of proteins in living cells.[22] It is widely used to investigate the movement of fluorescent species, including polymers, within a sample on the micrometre scale.[23] The method involves irreversibly bleaching a specific area of the fluorescently labelled sample with a short, high-intensity laser pulse (Figure 4.2 Stage 2), resulting in a local decrease in fluorescence intensity within the bleached region. Following bleaching, the fluorescence intensity is monitored over time as it recovers due to the diffusion of unbleached molecules into the bleached area and the diffusion of bleached molecules out (Figure 4.2 Stages 3 and 4).[24-26]

The rate of fluorescence recovery is then analysed using appropriate mathematical models to determine diffusion rates. If the sample is large compared to the photobleached area, the fluorescence intensity eventually returns to its initial level, and any discrepancy indicates an immobile fraction, which may result from barriers such as crosslinked matrices or other chemical or physical constraints. FRAP is suitable for studying diffusion rates in polymer films and only requires a low molecular-weight fluorescent label.

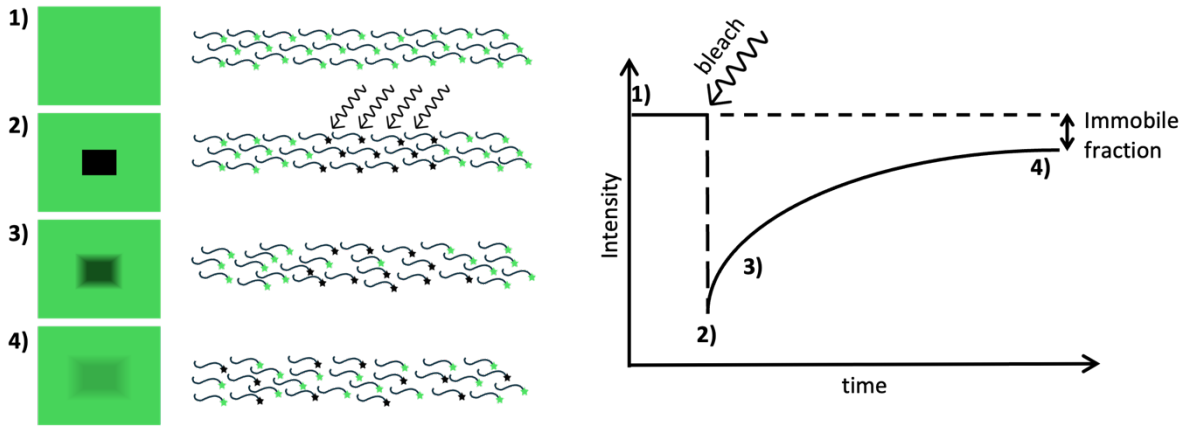


Figure 4.2: Main stages of the FRAP process showing 1) prebleach, 2) photobleaching, 3) fluorescence recovery, 4) steady state fluorescence recovered.

For FRAP to be effective, fast photobleaching is required to ensure that the timescale of bleaching is short compared to that of the diffusion.[23] This prevents new unbleached molecules diffusing in during the bleaching step. When a fluorophore is excited from the ground singlet state ($S_0$) to the excited state ($S_1$), this energy can be dissipated in several ways (Figure 4.3), including through non radiative decay back to the ground state, by the emission of light as fluorescence, or through inter-system crossing to the excited triplet state ($T_1$). [27] Fluorophores in the triplet excited state can either emit light as phosphorescence, or go on to react with oxygen or other molecules,[28, 29] leading to a non-fluorescent, photobleached product.[27] Intense light sources or longer exposure times are often necessary to induce the photobleaching required for FRAP microscopy (Figure 4.3). Bleaching of fluorophores is irreversible due to the photochemical alteration of the molecule.[28, 29]

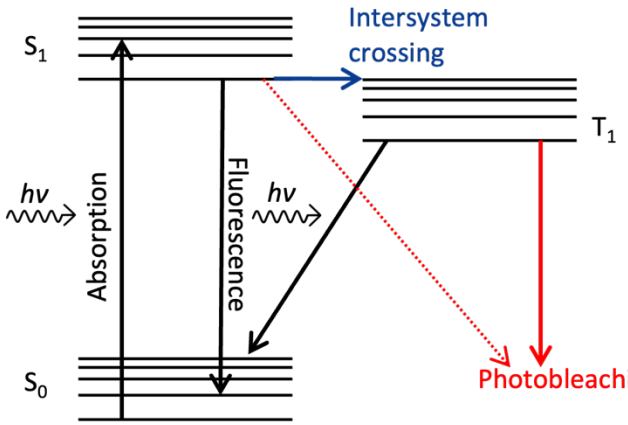


Figure 4.3: Jabłoński diagram of a fluorophore with a three-level system. Following excitation from the singlet ground state $S_0$ to the singlet excited state $S_1$, the excess energy can be lost through several mechanisms. Photobleaching of the fluorophore mainly happens from the long-lived triplet state $T_1$.

To carry out a FRAP experiment, a confocal fluorescence microscope is usually employed. Confocal microscopy was first invented in 1957 by Marvin Minsky, becoming a commonplace research technique by the 1980s.[30] Confocal microscopy differs from widefield microscopy in that it scans the field of view and illuminates only a single 'pixel' at a time, rather than entire sample volume at once.[31] It also incorporates an pinhole which filters out of focus light, improving the image resolution (Figure 4.4a and b).

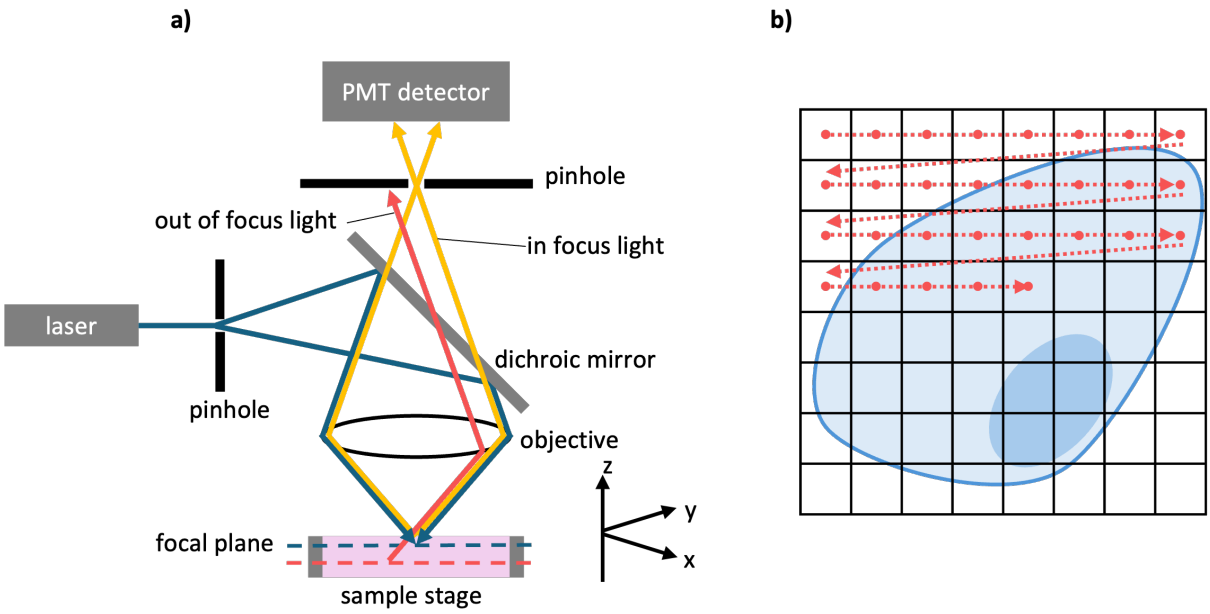


Figure 4.4: a) Confocal laser scanning microscope (CLSM) setup, showing light focused through an objective to a specific point in the sample x,y plane, pinholes used to filter out light from out of focus z planes. B) Schematic of pixel-by-pixel beam raster path.

One of the key practical considerations when designing a FRAP experiment is the choice of fluorescent probe. It is preferential to use a small molecule fluorophore for this work as to not influence the diffusion behaviour of the polymers themselves by attachment. The probe should also have a functional handle that provides a simple route to functionalising a polymer and be able to be photobleached under normal confocal laser conditions.

The most commonly used probes for FRAP (Figure 4.5) include green fluorescent protein (GFP)[32] in biological systems, and fluorescein. Fluorescein isothiocyanate (FITC, R=NCS) is a commonly available reactive form of fluorescein which is further functionalised through the isothiocyanate handle. GFP is typically found in cell biology to label specific proteins in a living cell – GFP is not exogenously added to the cell, but instead the gene sequence is added to the genome to be expressed with a protein of interest. Other probes used in fluorescent microscopy include nitrobenzofurazan (NBD), pyrenedecanoyl derivatives, 1,6-diphenyl-1,3,5-hexatriene (DPH) and cyanines, although not all of these are suitable for FRAP due to their photostability.

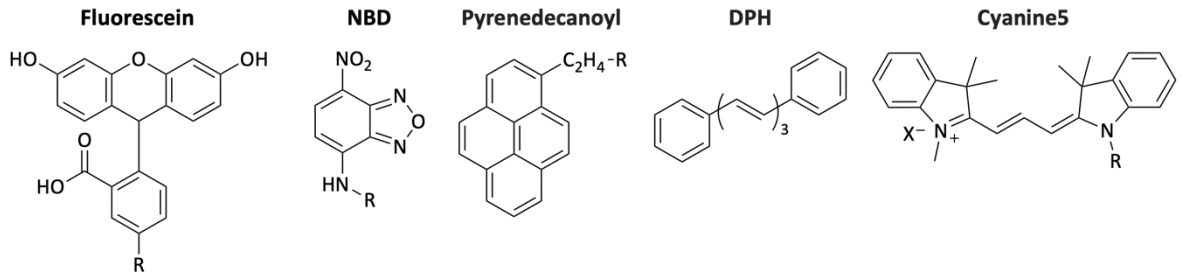

Figure 4.5: Various fluorescent molecules frequently used in microscopy. R is a handle for further functionalisation.

For this experiment, NBD was chosen as the fluorescent label due to its ease of incorporation into existing polymer end group chemistry, low cost, and small molecular size. NBD displays an excitation peak at 467 nm and an emission peak at 539 nm and so is suitable for excitation and bleaching with a 488 nm laser. Furthermore, it has good water solubility for an organic fluorophore, which was a requirement to ensure the tagged polymer film was homogenous. It is suitably susceptible to photobleaching for a FRAP experiment. NBD is a widely used fluorescent label in investigations on biological systems,[33] typically in lipid systems. NBD fluorophores have three absorbance bands in the visible and near UV region, at ~470, 306-360 and 225 nm (Figure 4.6).[34] As a visible light CLSM is used, only the absorbances in the visible region are discussed. The first absorption peak near 470 nm is due to an intramolecular charge-transfer (ICT) type transition,[34, 35] the 330 nm absorbance band corresponds to a $\pi \rightarrow \pi^*$ transition.[34] The maximum emission $\lambda_{max}$ of NBD-labelled PVA lies at 540–560 nm. The absorbance $\lambda_{max}$ and fluorescence intensity as well as emission $\lambda_{max}$ are sensitive to the polarity and hydrogen bonding capability of the environment.[34, 36-38]

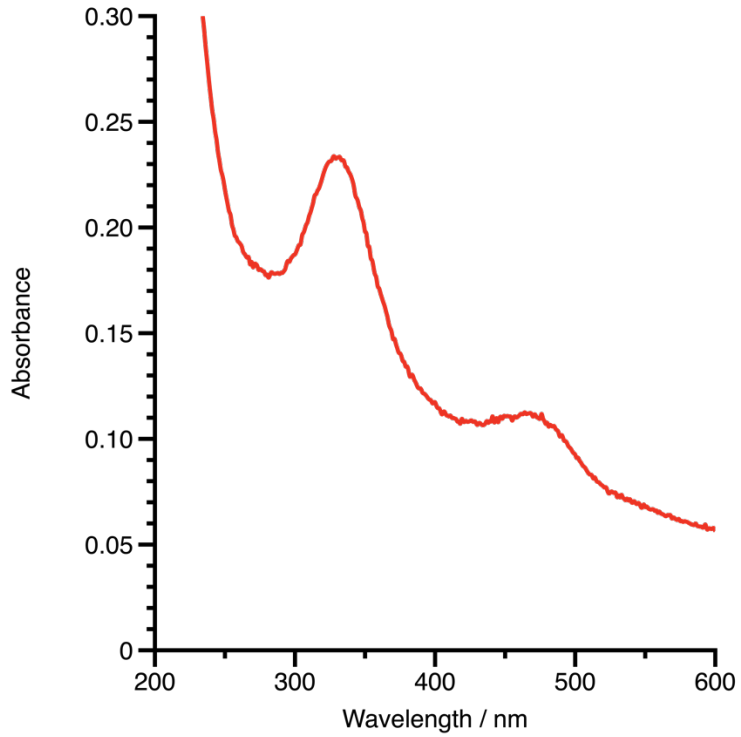

Figure 4.6: UV-Vis absorbance spectrum of PVA-NBD ($H_2O$, 0.05 mg/mL).

Compared to other techniques discussed in this thesis, such as SANS and ion beam analysis,[39] confocal microscopy is more easily accessible given the relatively low instrument cost and ease of use. Unlike ion beam measurements, where the sample is held in a vacuum, FRAP may be conducted at atmospheric conditions, enabling a dynamic system to be monitored in real time. The time-resolved diffusion data gained by FRAP experiments provides an insight into the time-dependence of polymer chain migration as a function of polymer structure. This also enables sample environment variation such as humidity and temperature.

During FRAP analysis, a lot of assumptions and simplifications are made to treat the fluorescence data with mathematical models. One of the biggest assumptions made is the 2D nature of diffusion. Most models are built on the assumption of diffusion only in two dimensions in the plane of observation, but do not account for diffusion of unbleached molecules from above or below the focal plane contributing to the fluorescence recovery. This is mainly due to the mathematical complexity of the 3D bleach profile. Efforts can be made to circumvent this in reality: either ensuring the sample is

sufficiently thin compared to the axial extent of the photobleaching beam so that it is bleached uniformly through the entire depth of the sample. Alternatively, a low numerical aperture objective can be used to result in an almost cylindrical bleach profile (Figure 4.7) with uniform bleaching at an extended distance through the z plane. This means that fluorophores above and below the focal plane are bleached, and that the observed recovery is only a result of 2D diffusion.

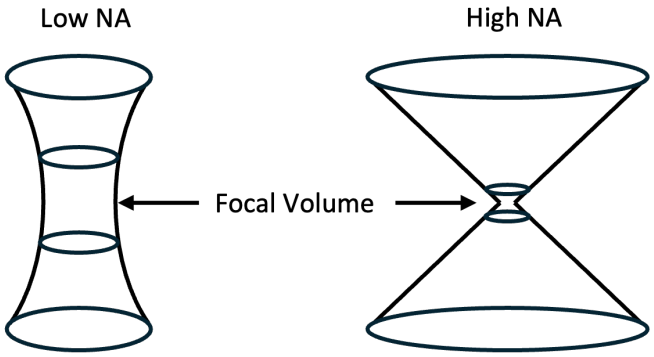

Figure 4.7: Difference in bleach volume dependent on the numerical aperture of the objective lens.

Most FRAP models assume that photobleaching is instantaneous to enable diffusion during the photobleach stage to be neglected. If this is not the case, and diffusion occurs during bleaching, the bleached area will be larger and less defined than expect, which will impact the quantitative interpretation of the fluorescence recovery.[40, 41] Meyvis *et al.* suggest, as a rule of thumb, that the bleach time should be no more than 5% of the characteristic recovery time, τ.[42]

Another issue that FRAP experiments are susceptible to is photobleaching of the sample during collection of the recovery images. This must be corrected for if the FRAP analysis is to be quantitative as the overall intensity of the image series will decrease with time due to the continued irradiation by the low power laser to collect the recovery images. This can be done by collecting a second background region of interest (ROI), either in a separate part of the field of view away from the bleach region (Figure 4.8a) or placed such that the bleach region and any subsequent diffusion is captured (Figure 4.8b). The later method assumes the background ROI to be sufficiently large that bleached

fluorophores will not diffuse out, allowing the assumption of constant fluorescence within the background, despite local diffusion.

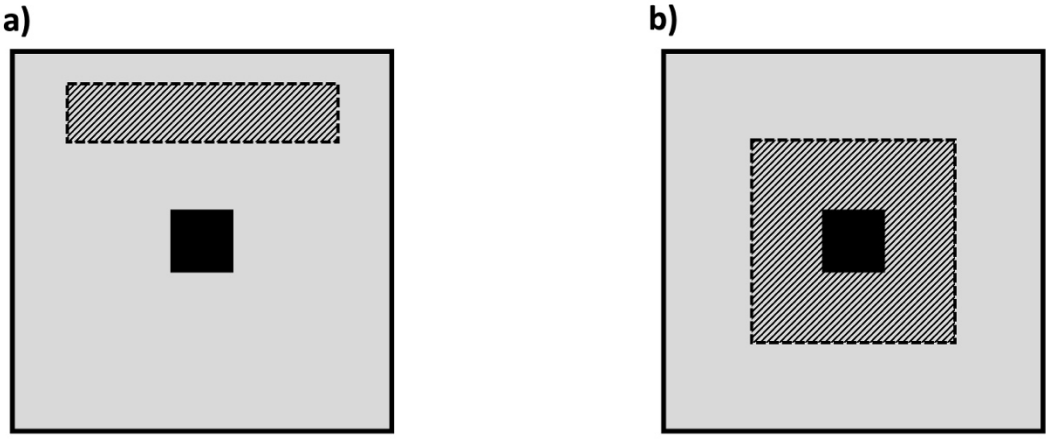


Figure 4.8: Schematic illustration of the background reference region selection. a) Selection of the reference region at sufficient distance from the bleach region. b) Selecting a reference region which encompases the bleach region and a sufficiently large perimeter to allow assumptuon that fluorescence within the background reference boundary is constant during the recovery process.

## 4.2 Aims

The aim of this chapter is to investigate the impact of PVA degree of hydrolysis on polymer diffusion dynamics in commercially relevant thin films. To achieve this, a suite of fluorescently tagged PVA polymers with varying degrees of hydrolysis, closely resembling the industrial materials used in SUD pods (Figure 4.9) will be produced. Controlled acetylation to produce a library of PVAs of commercial relevance as well as attachment of a photo bleachable fluorescent tag will enable the study of polymers in a plasticised film in real time. These polymers will then be imaged in FRAP microscopy experiments at humidity which mimics the manufacturing process.

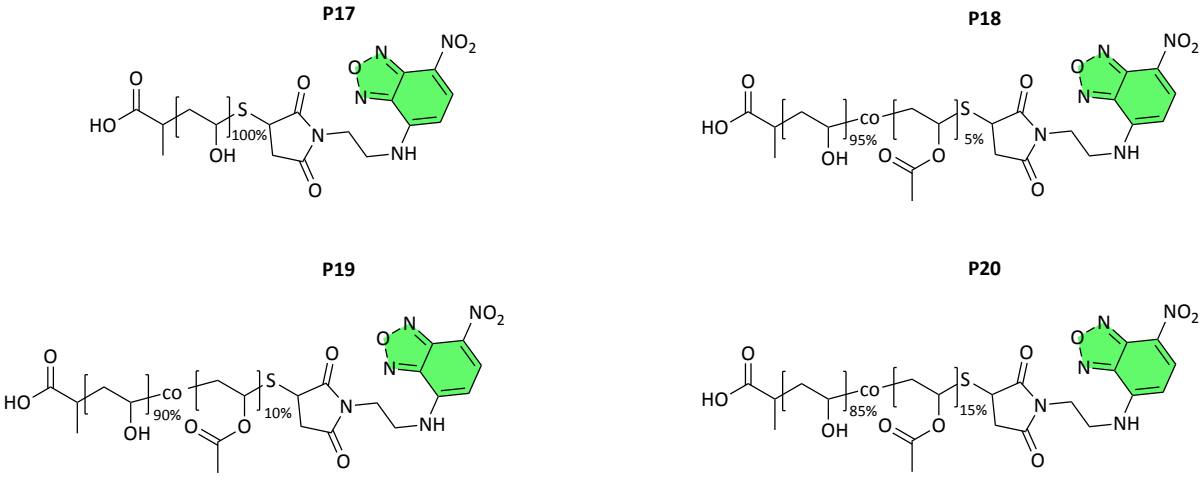


Figure 4.9: Structures of materials for FRAP analysis **P17**-**P20**. DP[a] = 295. $M_n$[a] = 13,000 for **P17**. [a]Determined by $^1$H NMR spectroscopic polymer conversion analysis, described in Chapter 2 experimental.

## 4.3 Results and discussion

### 4.3.1 Polymer and tag synthesis

To enable FRAP analysis of the polymer system, a method of fluorescently labelling a polymer chain with the NBD fluorophore was required. To enable isolation of the impact of degree of acetylation on diffusion dynamics, the degree of polymerisation of polymer chains was kept constant by using the same batch of PVA to synthesise all the subsequent polymer derivatives to be analysed, and fluorescent labelling conducted in the final stage.

PVA for use in this work was synthesised via PET-MADIX polymerisation (Scheme 4.1i). Vinyl acetate was first polymerised to polyvinyl acetate which was then hydrolysed to yield polyvinyl alcohol (Scheme 4.1 ii). Acetyl functionality was then re-introduced to the polymer chains, reducing the DH% as hydroxyl pendent groups were acetylated (Scheme 4.1 iii). The part-acetylated PVAs were then reacted at their thiol terminus with a maleimide to incorporate an amine terminal functional group. The terminal amine was then reacted with NBD-Cl to yield fluorescent PVA molecules (Scheme 4.1 iv).

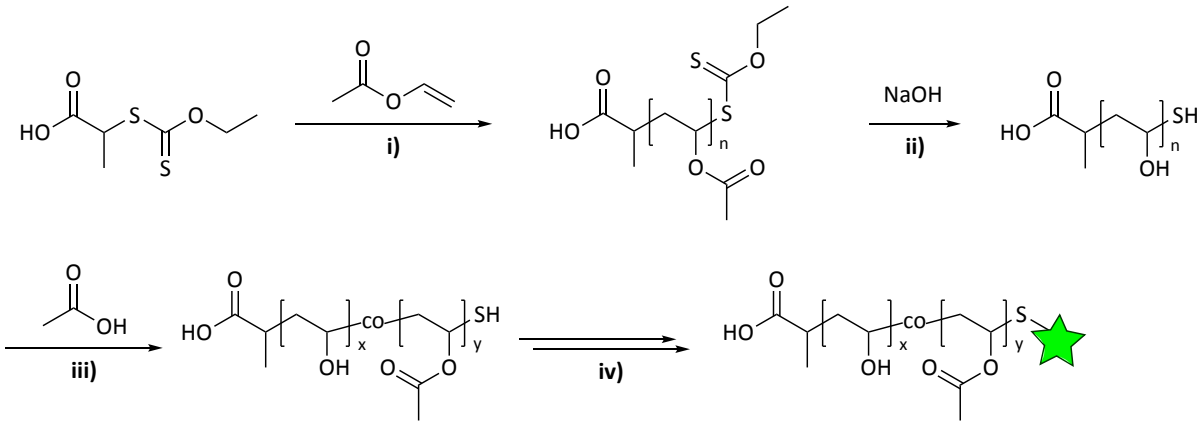


Scheme 4.1: synthetic route to NBD labelled part hydrolysed PVA. i) PET-MADIX polymerisation, DMSO, hv, inert atmosphere; ii) hydrolysis in MeOH; iii) reacetylation, AcOH, $H_2O$, HCl(cat); iv) fluorescent labelling end group chemistry, discussed below.

#### 4.3.1.1 Route 1 – maleimide and end group modification

The initial attempt of labelling the polymer involved synthesis of a small molecule fluorescent maleimide label, which, following purification and characterisation, would be reacted with the polymer through exploitation of thiol end group chemistry. This method is preferred as it allows full spectroscopic analysis of the tag prior to addition to the polymer, at which point it is more difficult to analyse with techniques such as $^1$H NMR spectroscopy due to the covalent attachment to polymer chains making effective concentration of the tag molecule lower. Additionally, $^1$H NMR resonances of macromolecules are typically broad, which often mask those of small molecules.

Reaction of commercially available NBD-chloride with **8** (synthesised via literature procedure)[43] failed (Scheme 4.2). Characteristic peaks in the $^1$H NMR spectrum of the expected product were not present, and the product did not appear to be fluorescent, indicating degradation had occurred. Control experiments with different amine nucleophiles did give the expected substituted products, indicating the issue with this reaction was potentially due to the maleimide functionality.

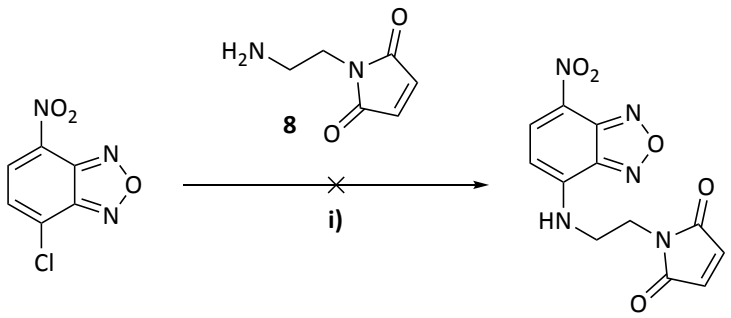


Scheme 4.2: The failed synthesis of maleimide functionalised NBD from commercial NBD-Cl precursor and **8**. i) MeCN, $K_2CO_3$, 50 °C.

Following the failed synthesis, my colleague Dr Kate Leslie successfully synthesised **NBD-Mal** (Figure 4.10), which was then used in this work.

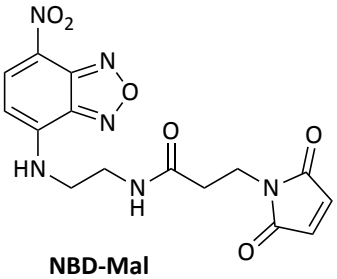


**NBD-Mal**

Figure 4.10: Structure of NBD-Mal synthesised by Dr Kate Leslie.

Attachment to thiol terminated PVA was attempted under standard reducing conditions (Scheme 4.3). Unfortunately, this also appeared to degrade the fluorescent tag, with the resultant polymer solution turning from green to dull pink in colour and becoming non-fluorescent in nature. Moreover, the aromatic resonance observed in the $^1$H NMR was at a higher chemical shift than expected, with a low integral value equating to approximately 7% attachment (determined by setting the δ 4.00 ppm polymeric CH signal to the polymer DP).

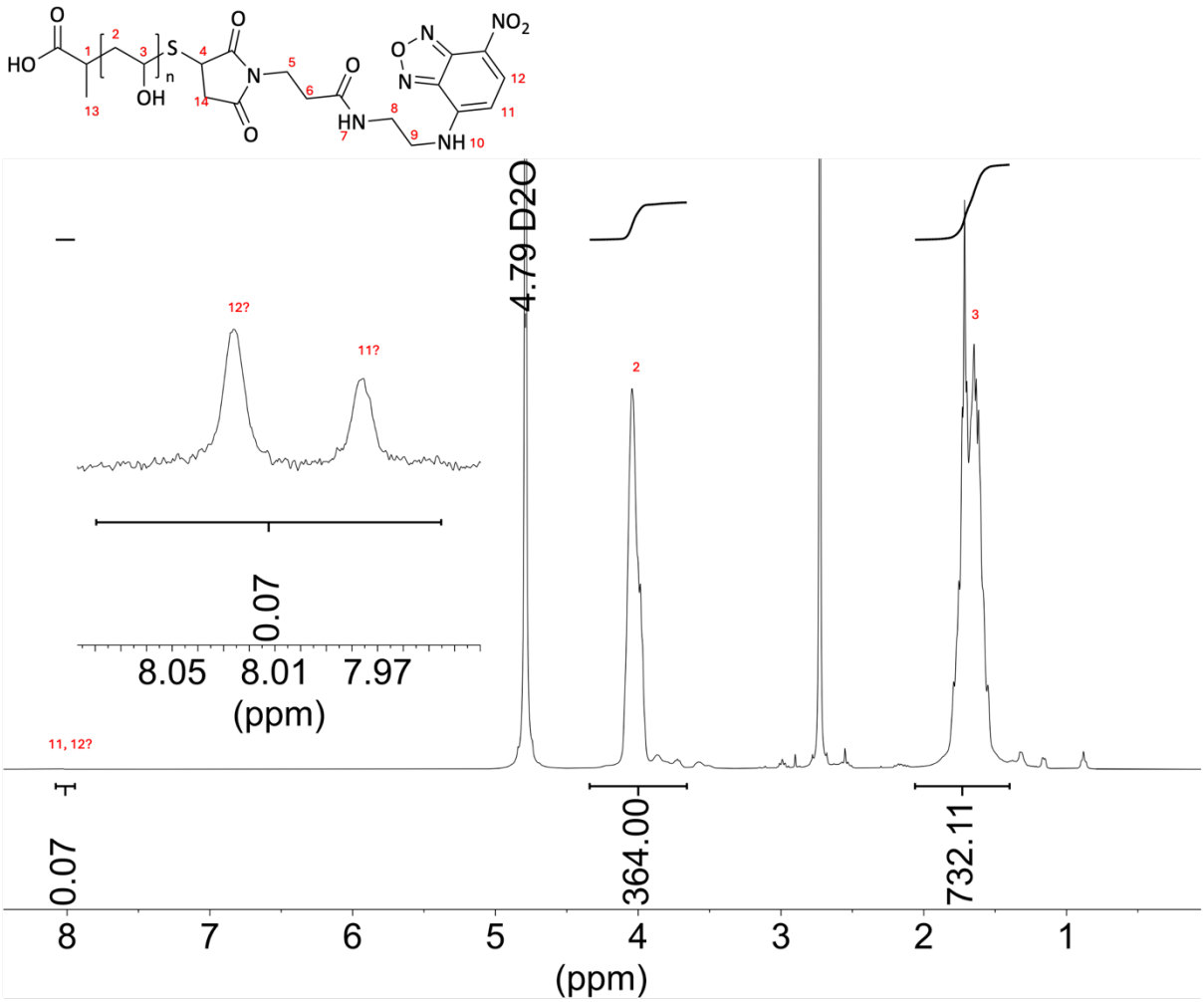


Figure 4.11: $^{1}$H NMR (400 MHz, $D_2O$): **PVA-NBD failed synthesis** showing Ar-H δ 7.19 (s - br, 1H), Ar-$H_{NBD}$ δ 6.65 (s - br, 1H), $OH_{poly}$ δ 4.46 (t - br, 1H), $CH_{poly}$ δ 3.90 (m - br, 1H), polymer $CH_{2\ poly}$ δ 1.39 (m - br, 2H). Integrals set to polymer DP = 295 on CH proton to establish end group attachment.

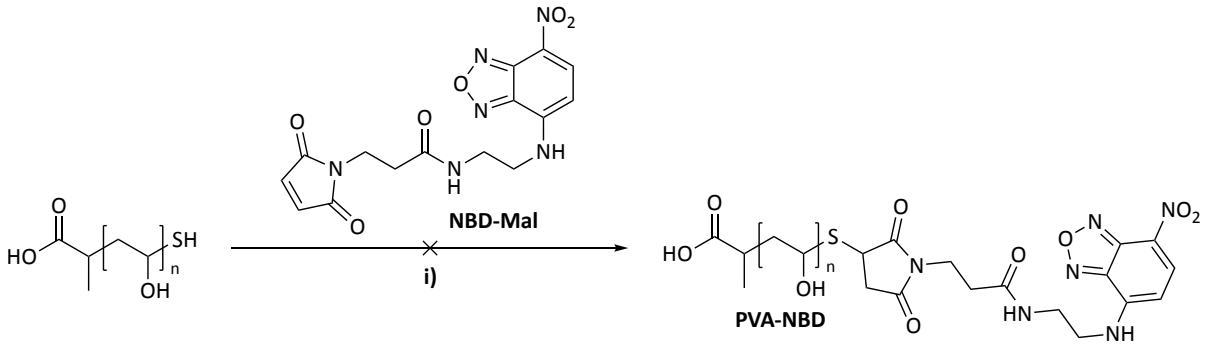


Scheme 4.3: Attempted synthesis of **PVA-NBD** from **NBD-Mal**. i) DMSO, $CH_3(CH_2)_5NH_2$ , $Et_3N$, TCEP (tris(2-carboxyethyl)phosphine), inert atm.

It was hypothesised that the TCEP reducing agent used in end group attachments to prevent disulfide formation between polymer chains may have inadvertently also been reducing the NBD nitro group to an amine, which would result in the loss of fluorescence as the donor acceptor system between the

amine and nitro groups would no longer be present (Figure 4.12). A similar reduction of nitro groups by dithiothreitol (DTT) has been reported in the literature.[44] Additionally, several biological studies purposely utilise NBD labelled lipids to study the reduction to its nonfluorescent product 7-amino-2,1,3-benzoxadiazol-4-yl (ABD).[45-48]

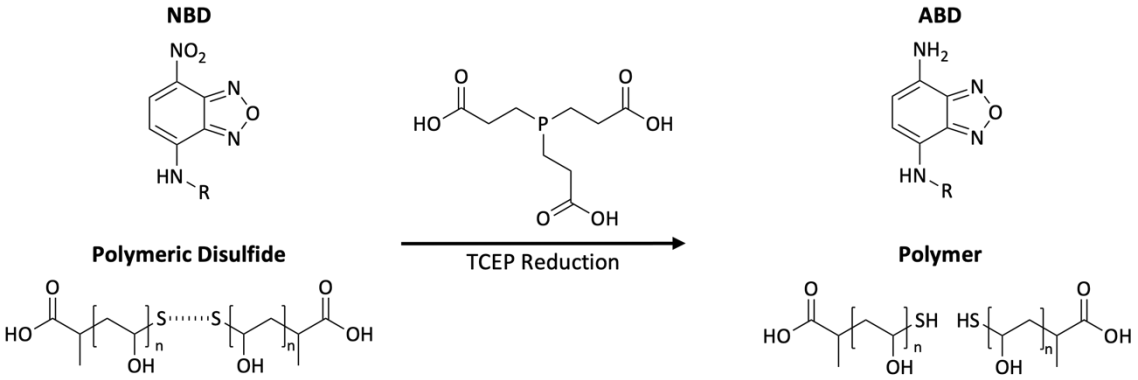


Figure 4.12: Upper) TCEP reduction of NBD to ABD and lower) disulfide groups on fluorophore and polymer chains respectively.

#### 4.3.1.2 Route 2 – NBD-Cl addition to amine functionalised PVA

In order to separate the thiol conjugation step and reducing conditions from the NBD fluorophore, the label was built up stepwise on the polymer chain (Scheme 4.4). This means any residual TCEP could be removed prior to addition of NBD, preventing unintended reduction of the nitro group. This method of synthesis yielded max. 19% attachment of the fluorophore, which, while low, was sufficient for FRAP experiments in a thin film. Attachment is calculated by setting the polymer integrals based on the degree of polymerisation and evaluating the integral of the NBD aromatic protons against their theoretical value, as shown in Figure 4.14.

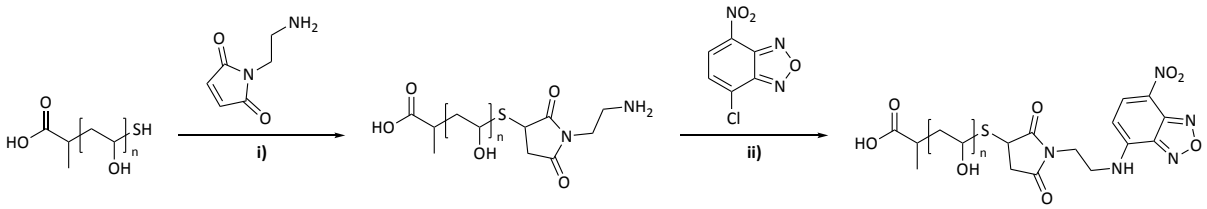


Scheme 4.4: Stepwise reaction to attach NBD to a thiol terminated PVA. i) DMSO, $CH_3(CH_2)_5NH_2$, $Et_3N$, TCEP. ii) MeCN, $K_2CO_3$, 50 °C.

To confirm whether the fluorophore was covalently bonded to the polymer chain, and not just present in the sample as an unattached small molecule, aqueous GPC coupled to a UV detector was used to verify the successful covalent attachment of NBD by confirming that the fluorescence signal peak sensitive only to NBD fluorescence with $\lambda_{ex}$ = 467 nm, coeluted with the polymer refractive index (RI) peak (Figure 4.13b).

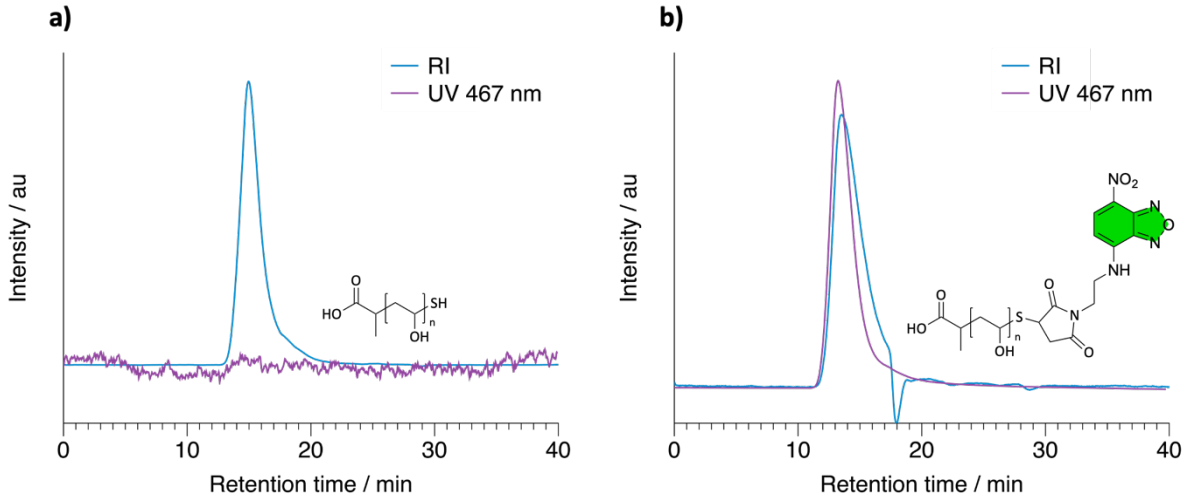


Figure 4.13: a) Pre NBD functionalisation chromatogram, b) Post NBD functionalisation chromatogram for **P17**. 5 mg/mL in $NaNO_3$ (10 mM), 35 °C, 1 mL/min. Analysis via differential refractive index detector and UV-Vis detector.

$^1$H NMR spectroscopy showed small broad aromatic resonances which matched those of the NBD starting material (Figure 4.14) .

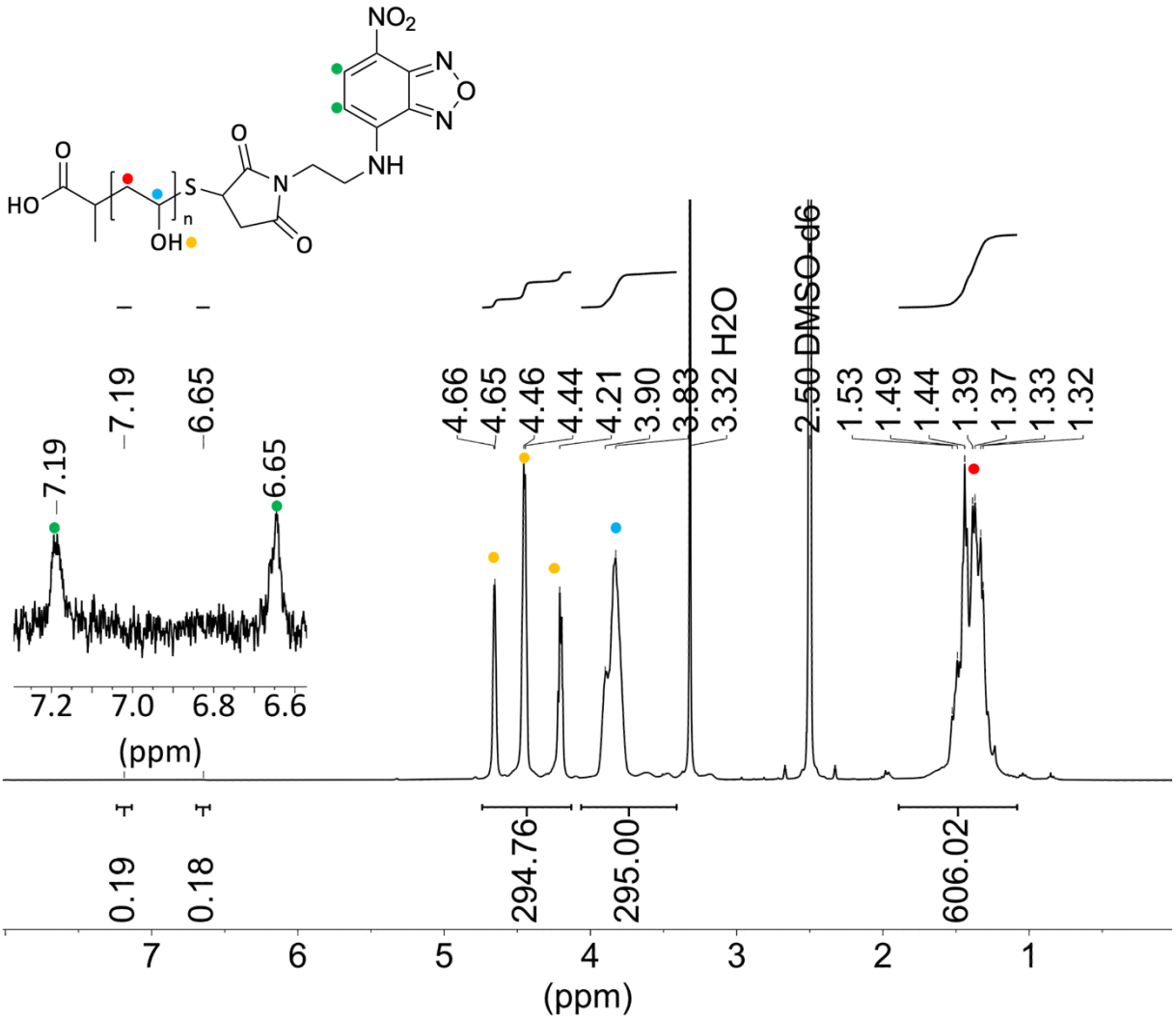


Figure 4.14: **$^{1}$H NMR** (*400 MHz, DMSO-$d_6$*): **P17** showing Ar-$H_{NBD}$ δ 7.19 (s -br, 1H), Ar-$H_{NBD}$ 6.65 (s -br, 1H), $OH_{poly}$ 4.15 – 4.71 (t - br, 1H), $CH_{poly}$ 3.32 – 4.10 (m - br, 1H), polymer $CH_{2\ poly}$ δ 1.32 – 1.53 (m - br, 2H). Integrals set to polymer DP = 295 on CH proton to establish end group attachment.

Following successful development of methodology to attach the fluorescent dye, the whole series of PVA polymers with varying degrees of hydrolysis were labelled. The labelling proceeded with yields from 9-19%, as determined by $^{1}$H NMR spectroscopy (Table 4.1).

Table 4.1: Summary of PVA series used in FRAP analysis with DH%[a] and degree of attachment of the fluorescent label.[a] PVA DP[a] = 295, THF GPC of parent PVAc pre hydrolysis: $M_n$[b] 31,000, $M_w$[b] 36,700, Đ[b] 1.18.

| Polymer | DH%[a] | Fluorophore Attachment[a] | $M_n$[a]/ gmol$^{-1}$ | $M_n$[c]/ gmol$^{-1}$ | $M_w$[c]/ gmol$^{-1}$ | Đ[c] | Structure |
|---|---|---|---|---|---|---|---|
| **P17** | 100 | 19% | 13,000 | 11,400 | 18,700 | 1.64 | 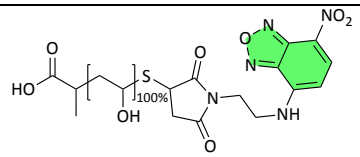 |
| **P18** | 95 | 12% | 13,600 | 15,100 | 18,400 | 1.22 | 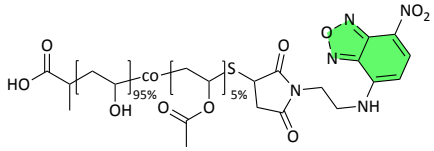 |
| **P19** | 90 | 15% | 14,200 | 13,600 | 18,200 | 1.34 | 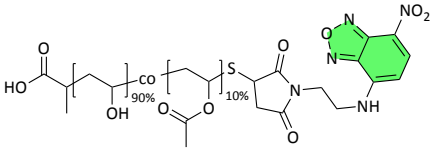 |
| **P20** | 85 | 9% | 14,800 | 16,500 | 20,000 | 1.21 | 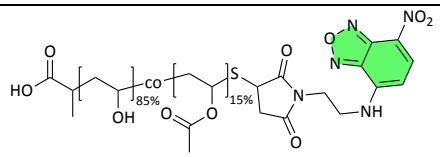 |

[a]Determined by $^1$H NMR spectroscopy. [b]THF GPC 1 mL/min, 35 °C, universal calibration. [c]Aqueous GPC $NaNO_3$ (10 mM), 1 mL/min, 35 °C, narrow standard calibration.

### 4.3.2 FRAP Microscopy

**P17**-**P20** were spin-cast onto glass slides and FRAP performed on a confocal laser scanning microscope. More detail about sample preparation can be found in the experimental methods section. Images were acquired by irradiation of the zoomed-in bleach spot with an unattenuated 488 nm laser for 2 minutes, followed by image collection with reduced intensity laser power every 3 minutes for a 42-minute period, or 1.5 minutes for a 28.5-minute period, depending on the rate of recovery. Each sample was analysed in triplicate in different spots as to not impact results by photobleaching from previous experiments. Samples were analysed at 24 ± 2 °C at 70 ± 2% RH (relative humidity).

#### 4.3.2.1 Data Processing

FRAP is a powerful technique which, when executed with appropriate care and control over experimental conditions, can provide quantitative information about system kinetics if the system is analysed with a suitable model.[23] There are numerous models developed to analyse FRAP data, each with their own assumptions about experimental procedure and sample behaviour.[23, 41, 49] In almost all cases, it is difficult to ensure the FRAP experiment is entirely inclusive of all aspects of the model assumptions. Due to the rectangular nature of the bleached spot, coupled with the slow diffusion of polymer samples compared to those the technique is usually used for, the data processing was achieved by following parts of several methods as appropriate. The data processing and fitting is described below. FRAP analysis is described in two main stages: 1) the raw image processing to normalise within a dataset and to correct for sample fading during the measurement, and 2) the fitting of the fluorescence data to both empirical and theoretical models, with limitations of each method and the experiment itself discussed.

Before further analysis of the data, the sample recovery data was normalised to the fluorescence before bleaching, and corrected for intensity fluctuations and photo bleaching during imaging using the ImageJ software.[50] Normalisation to the pre-bleach intensity was performed by dividing intensity measured at every pixel in the recovery images by the corresponding pixel value in the pre-bleach image (Equation 32). To limit the corresponding amplification of noise, the pre-bleach image was first smoothed by a 15 by 15-pixel median filter.

$$I_{corrected}(t) = \frac{I(t)}{I(prebleach)} \qquad \text{(Equation 32)}$$

where $I(t)$ is the raw pixel intensity within the frame and $I(prebleach)$ is the pixel intensity of the pre bleach frame post 15 x 15 pixel median smooth filter (Figure 4.15).

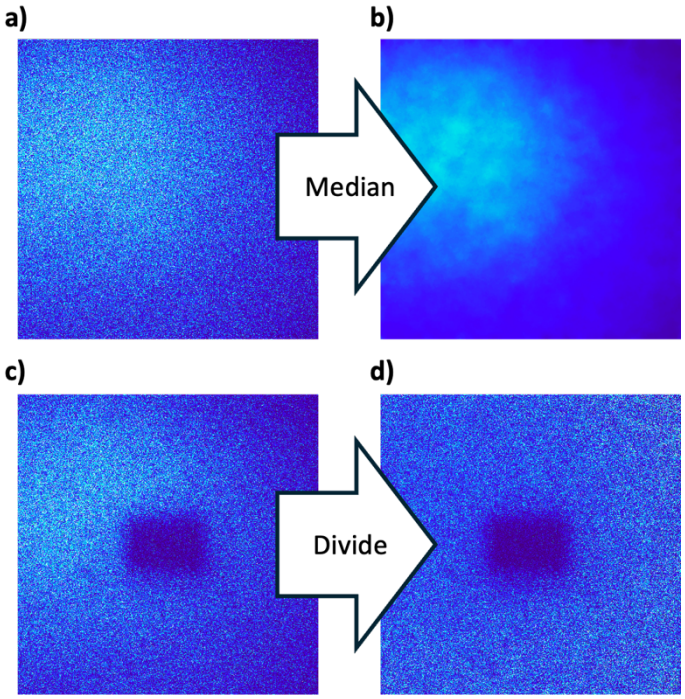

Figure 4.15: Image correction workflow. All images shown with lookup table (LUT) applied to clearly visualise transformations. a) Original prebleach image, b) 15 x 15 px median smooth filter applied to a), c) original post bleach image, d) each pixel of c) divided by each pixel of b).

Correction for laser fluctuations and bleaching during imaging was performed by dividing the mean intensity of the bleached square ROI of each recovery image by the mean intensity from a reference background region in the same image (Equation 33).

$$I(t) = \frac{I_{ROI}(t)}{I_{bk}(t)} \qquad \text{(Equation 33)}$$

where $I_{ROI}(t)$ is the mean intensity of the region of interest (Figure 4.15 ROI1), and $I_{bk}(t)$ is the mean intensity of the background region (Figure 4.16 ROI2) of the frame at time $t$.

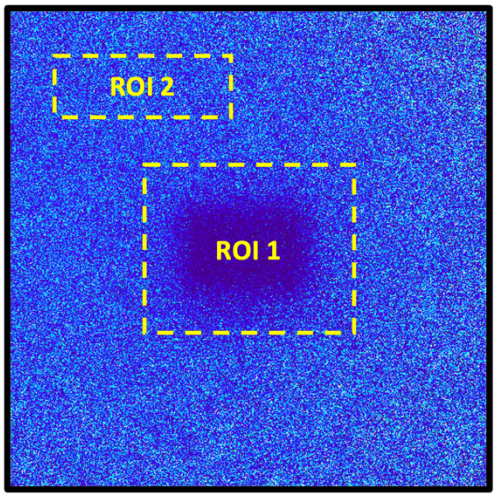


Figure 4.16: ROI 1 – bleach ROI. ROI 2 – background ROI. To correct for background fade and laser fluctuation, data extracted from ROI 1 is divided by the area mean of ROI 2 at each time frame.

This treatment produced datasets similar to those shown in Figure 4.16a, where the fluorescence intensity in the photobleached area recovers over the course of the experiment. This can be visualised by plotting the average intensity profile along the rectangle analysis cross-section (Figure 4.17b).

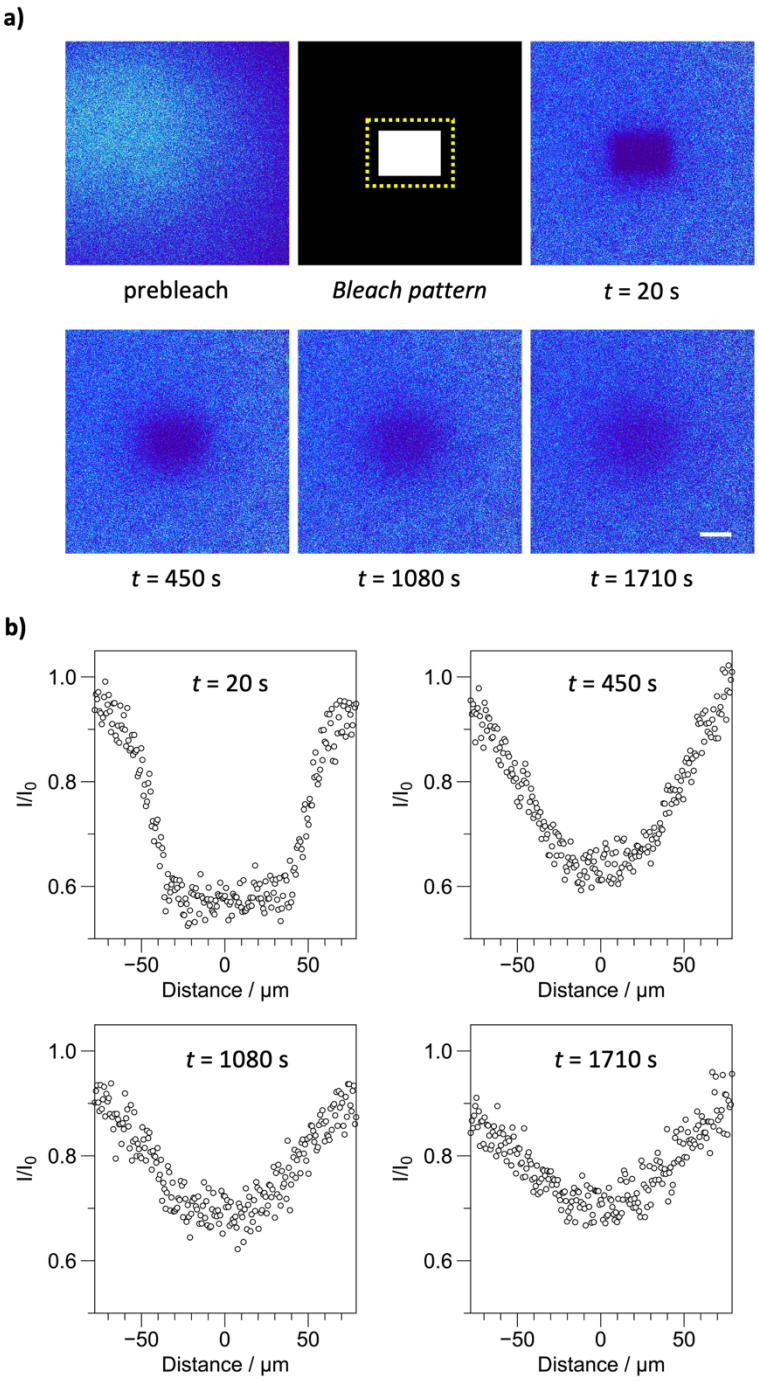


Figure 4.17: a) A FRAP experiment peformed on part acetylated PVA/c (**P19**, DH=90%) in a solution of glycerol 20 w/w%. PVA/c $M_n$: 13 kDa. The first image shows the sample before bleaching. The photobleaching is executed in a rectangular pattern illustrated in the second image. The yellow dashed line around the white rectangular bleach area denotes the region that was taken into account for the subsequent plotting. The subsequent images show fluorescent recovery. The scale bar represents 50 µm. b) Spatial profiles of the normalised fluorescence recovery along the x-direction through the photobleached region. The intensity $I/I_0$ is an average of the vertical pixels at each x coordinate.

#### 4.3.2.2 Empirical equation data fitting

The typical shape of a FRAP intensity recovery curve can be described by a simple exponential of the form (Equation 34).[51]

$$\frac{I(t)}{I_0} = 1 - be^{-t/\tau} \quad \text{(Equation 34)}$$

where $I_0$ is the initial fluorescence intensity, $I(t)$ is the fluorescence intensity in the photobleached region after time $t$ after photobleaching, $\tau$ is a characteristic recovery time that is related to the recovery half-life through Equation 35, and $b$ is the fraction of bleached fluorophores.

By fitting experimental FRAP recovery curves to Equation 34, it is possible to compare recovery half-life values and make statements about the rate of diffusion. It is important to remember that the use of Equation 34 is a pragmatic approach with no robust underpinning theory.[52] Care should be applied when using this approach, as the recovery half-life typically depends on the size and shape of the photobleached region, as well as the extent of photobleaching, and Equation 34 contains no spatial information. This type of analysis therefore comes with the caveat of only being able to compare half-lives if they were determined from experiments with exactly the same bleach region and extent of photobleaching. An example of this mono-exponential fit is shown in Figure 4.18.

$$t_{1/2} = \tau \ln(2) \quad \text{(Equation 35)}$$

To improve the fit to the experimental data, a second term can be included in the equation to describe different diffusion rates (Equation 36), either from a secondary diffusing species, or from initial diffusion of the polymer being a different rate to the bulk of the recovery time scale (Figure 4.18).

$$\frac{I(t)}{I_0} = 1 - b_1 e^{-t/\tau_1} - b_2 e^{-t/\tau_2} \quad \text{(Equation 36)}$$

This analysis was performed on the acquired dataset to produce single and double-exponential fits for all recoveries (Table 4.2, 4.3). These fits are visualised in Figure 4.18, where solid lines represent the single exponential fits and dotted lines the double-exponential.

Table 4.2: Single exponential fit parameters for all FRAP profiles. Duplicate polymer entries indicate repeat FRAP experient of the same film at sufficient distance from any previous photobleached zone. SE is standard error.

| Entry | Polymer | DH% | b | τ / min | $\tau_{1/2}$ / min | SE b | SE τ | $R^2$ | RMSE |
|---|---|---|---|---|---|---|---|---|---|
| **1** | **P17** | 100 | 0.45 | 276.0 | 191.3 | 0.005 | 38.8 | 0.79 | 0.010540 |
| **2** | **P17** | 100 | 0.41 | 254.5 | 176.4 | 0.008 | 50.4 | 0.66 | 0.014670 |
| **3** | **P18** | 95 | 0.57 | 138.9 | 96.3 | 0.011 | 16.9 | 0.84 | 0.021200 |
| **4** | **P18** | 95 | 0.56 | 120.8 | 83.7 | 0.007 | 8.5 | 0.94 | 0.013620 |
| **5** | **P18** | 95 | 0.54 | 130.9 | 90.7 | 0.006 | 9.0 | 0.94 | 0.012070 |
| **6** | **P19** | 90 | 0.45 | 41.7 | 28.9 | 0.003 | 0.9 | 0.99 | 0.006211 |
| **7** | **P19** | 90 | 0.46 | 48.7 | 33.8 | 0.004 | 1.5 | 0.98 | 0.008219 |
| **8** | **P19** | 90 | 0.47 | 40.9 | 28.3 | 0.003 | 0.8 | 0.99 | 0.005801 |
| **9** | **P20** | 85 | 0.54 | 53.3 | 36.9 | 0.003 | 1.2 | 0.99 | 0.006908 |
| **10** | **P20** | 85 | 0.53 | 57.1 | 39.6 | 0.005 | 2.0 | 0.98 | 0.009982 |
| **11** | **P20** | 85 | 0.55 | 70.5 | 48.9 | 0.004 | 2.1 | 0.98 | 0.007412 |

Table 4.3: Double exponential fit parameters for all FRAP profiles. Duplicate polymer entries indicate repeat FRAP experiment of the same film at sufficient distance from any previous photobleached zone. SE is standard error.

| Entry | Polymer | DH% | $b_1$ | $b_2$ | $\tau_1$ / min | $\tau_{1\,1/2}$ / min | $\tau_2$ / min | $\tau_{2\,1/2}$ / min | SE $b_1$ | SE $b_2$ | SE $\tau_1$ | SE $\tau_2$ | $R^2$ | RMSE |
|---|---|---|---|---|---|---|---|---|---|---|---|---|---|---|
| 1 | **P17** | 100 | 0.05 | 0.43 | 3.4 | 2.4 | 483.0 | 334.8 | 0.005 | 0.004 | 0.7 | 65.3 | 0.98 | 0.003161 |
| 2 | **P17** | 100 | 0.07 | 0.39 | 2.3 | 1.6 | 507.7 | 351.9 | 0.006 | 0.003 | 0.4 | 79.8 | 0.98 | 0.003814 |
| 3 | **P18** | 95 | 0.14 | 0.48 | 7.8 | 5.4 | 501.8 | 347.8 | 0.014 | 0.015 | 1.3 | 212.6 | 0.99 | 0.004598 |
| 4 | **P18** | 95 | 0.08 | 0.52 | 4.6 | 3.2 | 167.9 | 116.4 | 0.004 | 0.004 | 0.6 | 7.3 | 1.00 | 0.002511 |
| 5 | **P18** | 95 | 0.06 | 0.51 | 3.6 | 2.5 | 168.9 | 117.1 | 0.005 | 0.004 | 0.7 | 8.3 | 1.00 | 0.003415 |
| 6 | **P19** | 90 | 0.05 | 0.41 | 6.6 | 4.6 | 50.8 | 35.2 | 0.023 | 0.025 | 3.0 | 5.4 | 1.00 | 0.003271 |
| 7 | **P19** | 90 | 0.05 | 0.44 | 3.0 | 2.1 | 56.5 | 39.2 | 0.005 | 0.005 | 0.7 | 1.8 | 1.00 | 0.003016 |
| 8 | **P19** | 90 | 0.03 | 0.45 | 4.8 | 3.3 | 44.8 | 31.1 | 0.017 | 0.018 | 3.7 | 3.4 | 1.00 | 0.004630 |
| 9 | **P20** | 85 | 0.04 | 0.53 | 3.0 | 2.1 | 58.5 | 40.5 | 0.007 | 0.007 | 1.3 | 2.3 | 1.00 | 0.004355 |
| 10 | **P20** | 85 | 0.06 | 0.51 | 2.8 | 1.9 | 67.4 | 46.7 | 0.006 | 0.005 | 0.6 | 2.3 | 1.00 | 0.003639 |
| 11 | **P20** | 85 | 0.04 | 0.53 | 2.4 | 1.7 | 79.6 | 55.2 | 0.004 | 0.003 | 0.6 | 2.1 | 1.00 | 0.002875 |

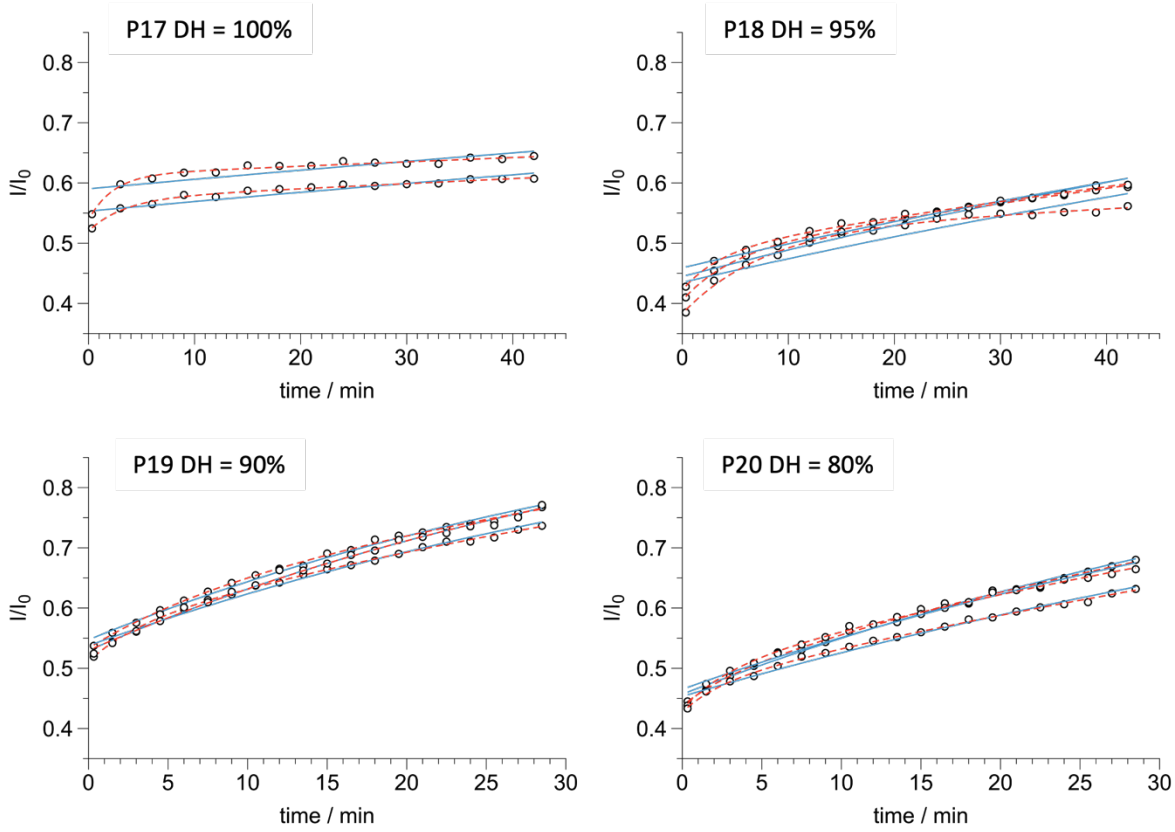


Figure 4.18: FRAP recovery profiles for **P17** – **P20** fit to both single (solid blue line) and double exponential (dashed red line) empirical equations. **P17** and **P18** were monitored every 3 mins for 42 mins, **P19** and **P20** every 90 s for 28.5 mins due to their faster recovery.

Including a second exponential improves the fit significantly. This effect is the largest for **P17**, with the more acetylated materials better described than the single exponential. This may be a result of fully hydrolysed PVA being more semicrystalline in nature than **P20** with a lower DH (added acetylation). **P17** is therefore the most likely in the series to contain a large crystalline component (Figure 4.19b) as well as some amorphous regions, which likely have varying diffusion kinetics, with the crystalline regions expected to diffuse at a much lower rate than the amorphous regions of the chains. Conversely, lowering DH supresses crystallisation of the chains, resulting in a larger proportion of amorphous polymer (Figure 4.19a).

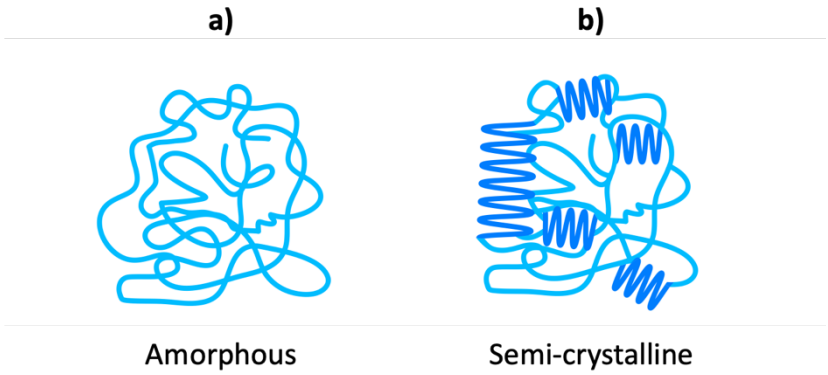


Figure 4.19: Representation of a) fully amorphous and b) semi polymer chains.

Comparing the recovery profiles for the polymer series (Figure 4.19), it is evident that reducing degree of hydrolysis increases the rate of fluorescence recovery. It is noted that the extent of photobleaching varies slightly between samples, which may be due to inconsistent film thickness or fluctuations in the laser intensity during the bleach. Nevertheless, the rate of recovery increases through the series, which implies that polymer mobility is increased as a function of acetylation. To relatively quantify this effect, $\tau$ values were evaluated as shown in Figure 4.20.

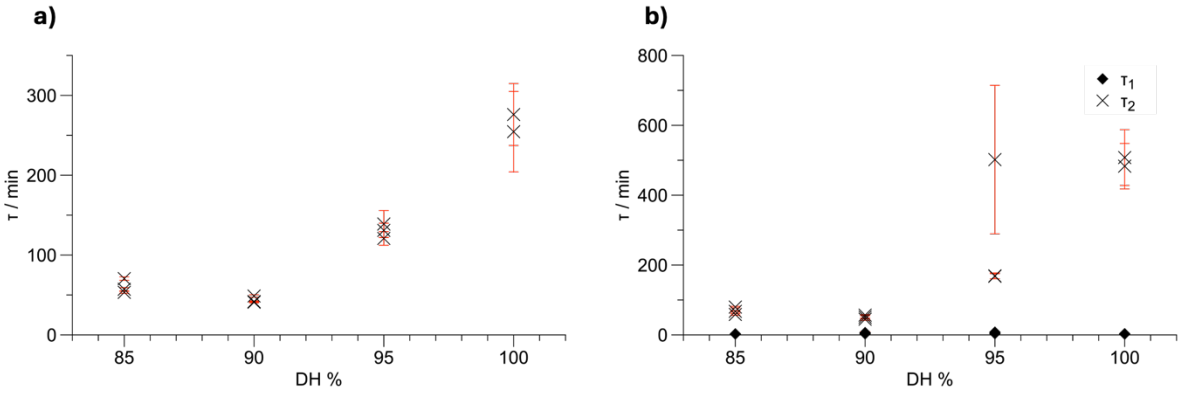


Figure 4.20: Characteristic recovery times of **P17** (DH 100%) – **P20** (DH 85%) fit to a) single exponential and b) double exponential equations.

Figure 4.20a shows that even though the fits to single exponential equations fail to capture the initial timepoints of the recovery data well, there is still a clear observable trend in the relationship between DH and $\tau$. The longest recovery times are those of **P17**, DH 100%, where the polymers are most

crystalline. This makes sense as the crystallinity will hinder polymer diffusion in this highly hydrogen bonded system. Decreasing DH also decreases recovery time to a point, where it is then seen that between 85 and 90% DH there is little difference between recovery times. It can be expected that there is a limit on the benefit of decreasing DH has on recovery time, as increasing the acetyl content of the polymer indefinitely will cause solubility issues, which would begin to hamper diffusion.

The same trend is observed in the dual exponential fits (Figure 4.20b), with $\tau_2$ increasing with increasing DH. $\tau_1$ is seen to be small and linear, and typically has a value of ~ 3 mins, which would encompass the duration between the first two measurement points of the profile. All $\tau_1$ values have a low contribution ($b_1$) to the overall fit (Table 4.3). It is presumed that the $\tau_2$ exponential fit for Table 4.3 entry 3 is an outlier due to the large standard error and uncharacteristically large recovery time.

#### 4.3.2.3 Theoretical equation data fitting

To improve upon the semi-quantitative recovery times acquired from fitting to Equation 34, the images were fit to more complex diffusion models. In this method, the intensity profile of the bleach spot edge is fit to a Gaussian curve, as described by Seiffert *et al.,*[53] which uses the analytical solution to the diffusion equation (Fick's second law, Equation 37), and explicitly refers to the distance diffused.

$$I(x,t) = I_0 - A(t)\, e^{-\frac{x^2}{2\omega^2}} \qquad \text{(Equation 37)}$$

where *I* is the fluorescence intensity at position *x* and time *t* post photo bleach, $I_0$ is the pre recovery fluorescence intensity, $\omega$ is the Gaussian width, *D* is the diffusion coefficient and *A(t)* is the depth of the 'dip' in intensity post bleaching.

All images were processed following the same method as for the empirical analysis, with normalisation of the prebleach measurement with 15 x 15-pixel median blur applied. Each column of pixels in the

ROI is vertically averaged to improve the signal to noise. This average is then normalised to a background ROI to account for fluctuating laser power and sample fading during measurement.

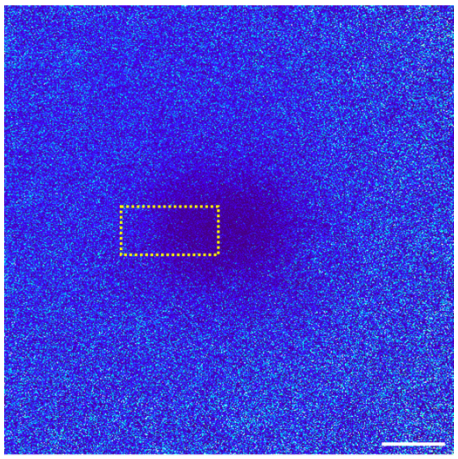

Figure 4.21: Representative ROI for Fickian analysis. **P19** (DH=90%) at time 180 s. Scale bar is 50 µm.

To analyse microscope images via Equation 37, a large rectangular ROI was selected (Figure 4.21), with centre placed on the edge of the bleached spot as to capture the maximum and minimum fluorescence intensity. Care was taken to avoid the horizontal edges of the bleach spot, as including these would mean diffusion was occurring in two dimensions rather than only one, which would complicate analysis. Had the bleach spot been circular in nature, a radial average could have been applied. The vertically averaged intensities for each column at each time point was then fit to a Gaussian (Figure 4.22a) of the form Equation 37. Calculating the Gaussian width, $\omega$, at each time point, $t$ (Figure 4.22b), allows the use of Equation 38 to extract the diffusion constant, $D$.

$$\omega^2 = 2Dt \qquad \text{(Equation 38)}$$

The diffusion of **P1** (DH 100%) was of such a low rate and high background that the fluorescence intensity profiles did not fit well, meaning diffusion coefficients were unable to be calculated for this polymer. When forced to fit to a Gaussian by holding the Gaussian minimum, the errors in $\omega$ were large, and the values formed straight horizontal line implying essentially no diffusion on the timescale

of the experiment. This is supported by the large $\tau$ value calculated by the empirical fit (>250 mins on an experiment of time scale 42 mins).

The analysis was completed for **P18**, **P19** and **P20**, which showed similar diffusion coefficients for **P19** and **P20**, and a drop-off in the rate of diffusion for **P18** (Figure 4.22d, Table 4.4). This trend is similar to that observed in the exponential fitting method.

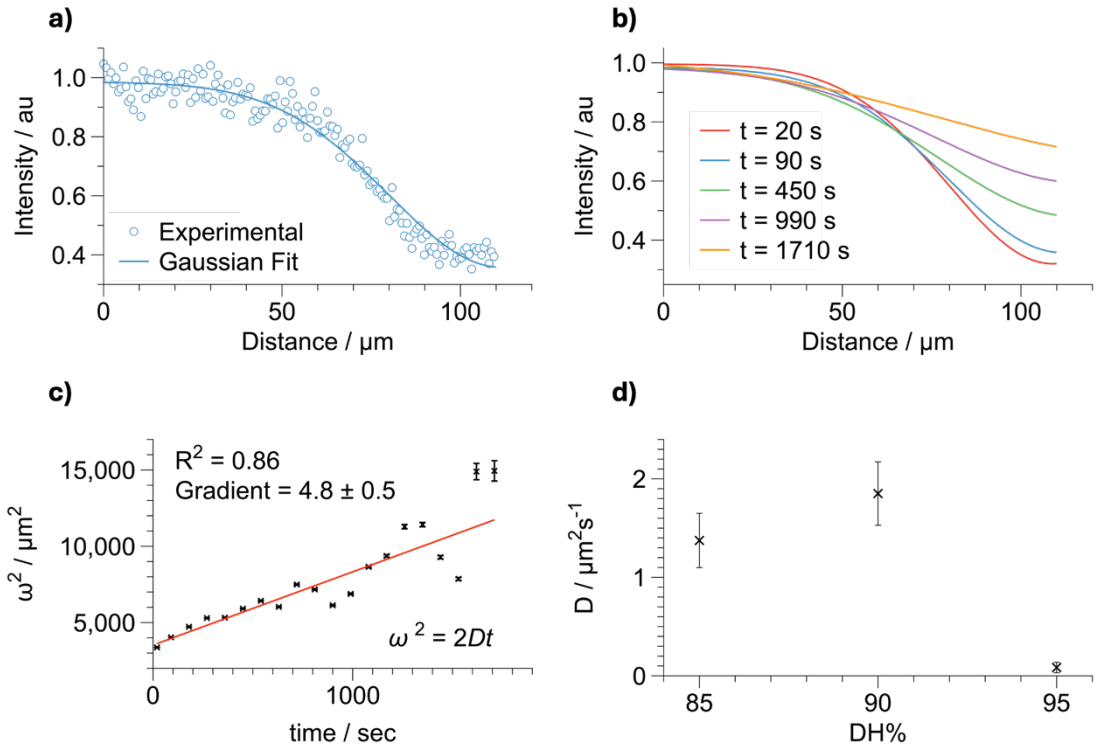


Figure 4.22: Fickian diffusion analysis of **P18**-**P20**. a) – c) shown for **P19** as example. a) Gaussian fit to normalised and background corrected FRAP profile (t=90 s), b) Gaussian fits of **P19** at various time frames showing increasing Gaussian width with time, c) Increase in $\omega^2$ with time $t$ with linear fit to extract diffusion constant D, d) Average diffusion constant as a function of DH% with standard error.

Table 4.4: Extracted diffusion coefficients from Fickian analysis of **P18**-**P20**.

| Polymer | DH% | D / µm$^2$s$^{-1}$ |
|---|---|---|
| **P18** | 95 | 0.08±0.05 |
| **P19** | 90 | 1.85±0.32 |
| **P20** | 85 | 1.37±0.28 |

The diffusion rates extracted for PVA are of a similar order of magnitude to those found in the literature for small molecule tracers in PVA films. Van Keuren *et al.* reported D values in the order of 3 – 6 x $10^{-3}$ $um^2s^{-1}$ for glycerol-plasticised polyvinyl alcohol films doped with rhodamine B.[54] However, the PVA used in that study had a significantly higher molecular weight (>150 kDa) compared to the PVA used in this chapter (~15 kDa). This suggests that diffusion rates should decrease with increased polymer entanglement at higher molecular weights, which aligns with the expectation that the *D* is inversely proportional to molecular weight squared, as described by Thompson *et al*.[55] Based on this relationship, it can be predicted that for commercial polymers of larger molecular weight, such as 100 kDa, the diffusion coefficient would decrease proportionally. For example, *D* for a 100 kDa polymer is predicted to be approximately $(15/100)^2 \approx 1/40$ of the measured value for the smaller polymer. Therefore, the diffusion rate for a 100 kDa PVA polymer would be expected to be significantly slower. From this, we can also estimate the time required for the polymer to diffuse sufficiently to form an entangled interface. To achieve a diffusion width of around 10 nm—a likely minimum for forming an entangled interface—the contact time would need to be extended significantly for larger molecular weight polymers. Additionally, Majerczak *et al.* reported similar diffusion rates for rhodamine B tracer in 25 wt. % glycerol-plasticised PVA films (~0.5 – 1.3 $\mu m^2s^{-1}$), as were found here for 20 wt. % glycerol-plasticised fluorescent polymer chains.[16] However, the molecular weight of the PVA in their study (30 – 70 kDa, DH% 87-90) again differs from that used in this chapter, which is much lower (~15 kDa). Furthermore, all of these experiments used polymer matrices doped with free fluorescent dyes, rather than dyes covalently bonded to the polymer chains themselves, introducing the possibility of multiple simultaneous diffusion processes. Modelling becomes complex when deconvoluting the diffusion of free dyes from that of the polymer chains. It would be intriguing to compare the diffusion coefficients from the experiment conducted in this study with those from a similar experiment using the same polymer series without fluorescent tags, whilst incorporating free fluorescent tags into the matrix.

While a limited number of polymer DH were studied, the range appears to capture essentially immobile polymer chains for the most hydrolysed samples, as well as reasonably mobile chains for

those with lower DH%. It would appear that for the application of SUD pods, and for manufacturing methods where the polymer-polymer interface is formed and required to seal sufficiently after tens of seconds before allowing to further strengthen for a period of days, the most suitable materials are those with DH% between 85 and 90%. Materials with a DH greater than 95% will likely fail to entangle when a polymer-polymer interface is made, even with plasticisation and high humidity.

### 4.3.3 Limitations of this experiment

Although this work has shown the potential scope for FRAP analysis of fluorescently labelled polymers, it has several limitations which are discussed below. Should this work be repeated, it would be beneficial to modify the original experimental approach to address these shortcomings.

Humidity and temperature are known to impact the kinetics of PVA diffusion,[56] and so it would be beneficial to the experiment if better control was exercised over these variables. During this work, ambient laboratory temperature was used, which varied through the course of the day (24 ± 2 °C). Relative humidity was controlled in the pre-experiment conditioning by means of saturated KCl solutions in an airtight environment, and during imaging by placing small plates of salt solution on the microscope stage. The microscope was sealed as well as possible with clingfilm and a hygrometer was utilised to monitor the relative humidity throughout imaging, which was recorded for each sample at the beginning and end of each recovery. Although humidity stayed within a 4% range (70 ± 2% RH), further control of humidity could benefit the set-up. A control experiment where **P20** was measured at 45% RH (ambient) compared to 70% RH, and large differences in the recovery time was observed (Table 4.5), further emphasising the need for effective humidity control. NBD fluorescence was also observed to vary as humidity dropped during the experiment, highlighting the importance of background correction for each image.

Table 4.5: Comparison of **P20** DH 85% at 45% RH and 70% RH. Analysis via both exponential fits and Gaussian fitting.

| | | **45% RH** | **70% RH** |
|---|---|---|---|
| **Single Exponential Fit** | $\tau$ | 85.1 mins (↑41%) | 60.3 mins |
| **Double Exponential fit** | $\tau_1$ | 6.4 mins (↑137%) | 2.7 mins |
| | $\tau_2$ | 120.1 mins (↑75%) | 68.5 mins |
| **Gaussian fit** | $D$ | 0.25 μm/s$^{-1}$ (↓82%) | 1.37±0.28 μm/s$^{-1}$ |

Increasing the degree of polymer labelling would improve the signal to noise in imaging, reducing the background noise and improving fits. The impact of increased fluorophore content on the polymer should be evaluated to ensure polymer behaviour is not impacted by greater labelling efficiency. It may be beneficial to optimise experimental procedures to reduce the time required to bleach the sample. This experiment required 2 minutes of bleaching, which resulted in some amount of polymer diffusion occurring in and out of the bleached region before the first recovery measurement was taken, limiting the ability to monitor diffusion from a true $t_0$. This was especially noticed for faster diffusing polymers, with the shape of the initial measurement of the bleach region becoming less defined as samples were more acetylated. To further increase confidence in the statistics acquired for the experiment, a greater number of repeats per polymer film would be required, and a model to explicitly include the diffusion that occurs during the bleaching stage would improve the accuracy of the measurement. This would help identify outliers more clearly, as well as reducing error in the data collected.

## 4.4 Conclusions and future work

In conclusion, this work presents a novel method for evaluating polymer mobility in thin, plasticised films, specifically focusing on commercially relevant, partially and fully hydrolysed PVA, using Fluorescence Recovery After Photobleaching (FRAP). This approach has proven effective not only in establishing relative trends within the polymer series but also in quantifying absolute diffusion rates.

A method for fluorescently labelling PVA synthesised via PET MADIX was developed, ensuring that the fluorescent label remained intact throughout the synthesis process.

The analysis of recovery times within a fixed window facilitated a relative comparison across the polymer library, revealing a positive correlation between the degree of hydrolysis (DH) and the length of characteristic recovery times. Further evaluation using single and dual-component exponential fitting confirmed these trends. Fickian diffusion model fitting was employed to calculate absolute diffusion coefficients for the polymer library, excluding the most hydrolysed sample, which diffused at too slow a rate to quantify using this method. The extracted diffusion coefficients were consistent with the relative trends observed from empirical fits. These findings suggest that multiple factors likely influence the rate of diffusion, with the solubility of the polymer in aqueous systems potentially counteracting the reduction in polymer crystallinity as acetylation increases.

This work demonstrates that FRAP can serve as a proof of concept for comparing polymer diffusion rates. The use of a commonly accessible confocal microscope, without the need for complex computational modelling, makes this approach a promising tool for studying polymer mobility. However, it is clear that the experimental method would benefit from further refinement to improve the reliability of the calculated data.

Based on the findings of this chapter, it is apparent that for sufficiently rapid polymer entanglement on the manufacturing timescale of seconds—such as when polymer films are pressed together in the presence of plasticiser and high humidity to seal SUD pods—a partially hydrolysed PVA is optimal, particularly with a DH of up to 85%. Although further decreasing DH could enhance chain mobility, there is a threshold beyond which acetylation may favour phase separation of the polymer, ultimately inhibiting solubility and diffusion. While evidence of this trend was observed in this work, additional samples with varying DH are required to confirm whether this pattern persists.

This approach marks a significant advancement in the field, offering a novel, accessible, and effective method for investigating polymer diffusion in thin films, particularly for PVA. The use of FRAP for evaluating synthetic polymer mobility in this context is a new contribution to the literature and holds important implications for the development and optimisation of polymer-based materials in industrial applications.

## 4.5 Experimental methods

General experimental procedures are listed in Chapter 2 Section 4. Compounds and techniques exclusively used in this chapter are reported here.

### 4.5.1 Synthesis of *tert*-butyl (2-(2,5-dioxo-2,5-dihydro-1*H*-pyrrol-1-yl)ethyl)carbamate 7.

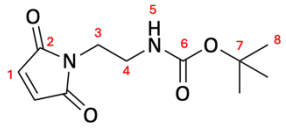


Figure 4.23: Structure of *tert*-butyl (2-(2,5-dioxo-2,5-dihydro-1*H*-pyrrol-1-yl)ethyl)carbamate.

Adapted from Bai *et al.*[43] Maleic anhydride (6.00 g, 61.2 mmol, 2.2 eq.) was dissolved in anhydrous $CH_2Cl_2$ (60 mL) and cooled to 0 °C. *N*-boc ethylene diamine (4.44 g, 27.7 mmol, 1.0 eq.) was dissolved in anhydrous $CH_2Cl_2$ (60 mL) and added dropwise to the cool maleic anhydride solution and stirred overnight at room temperature. After the reaction, $CH_2Cl_2$ was evaporated, and the white residue was dissolved in acetone (120 mL) giving a clear colourless solution. Nickel acetate (150 mg, 0.6 mmol, 0.02 eq.) and acetic anhydride (10.60 mL, 112.2 mmol, 4.0 eq.) and triethylamine (1.60 mL, 11.4 mmol, 0.4 eq.) were added to the solution with stirring. The mixture was heated to 65 °C for 2 days. After approximately 1 hour the solution had turned from a clear pale-yellow solution to black. The reaction was monitored via TLC (1:1 ethyl acetate:hexane, $R_f$ = 0.32, Figure 4.26). After the reaction, the mixture was cooled to room temperature and the acetone removed giving a thick black liquor which was poured over ice water (400 mL) and stirred for 30 mins. A black precipitate was collected by sinter filtration and washed with DI $H_2O$ (2 × 50 mL). After drying, the crude product was solid loaded onto celite and purified via CombiFlash (80 g Gold $SiO_2$ Column, ethyl acetate:hexane ramp to 0:1 to 1:0 over 10 CV). The fractions containing **7** were concentrated and the resultant white solid dried under high vacuum for several days. (3.92 g, 16.3 mmol, 60 % yield). **$^1$H NMR** (*400 MHz, $CDCl_3$*) δ 6.71 (s, 2H, $H_1$), 4.73 (s, 1H, $H_5$), 3.66 (t, *J* = 5.5 Hz, 2H, $H_3$), 3.33 (q, *J* = 5.8 Hz, 2H, $H_4$), 1.40 (s, 9H, $H_8$). **$^{13}$C NMR** (*101 MHz, $CDCl_3$*) δ 170.90 $C_2$, 156.03 $C_6$, 134.26 $C_1$, 79.56 $C_7$, 39.43 $C_3$, 38.07 $C_4$, 28.39 $C_8$. **LR-ESI-**

**MS:** For $[M\text{-Boc}+H]^+$ calculated: 141.066, found: 141.098, For $[M+Na]^+$ calculated: 263.101, found: 263.217. Spectroscopic data were consistent with literature reports.[57]

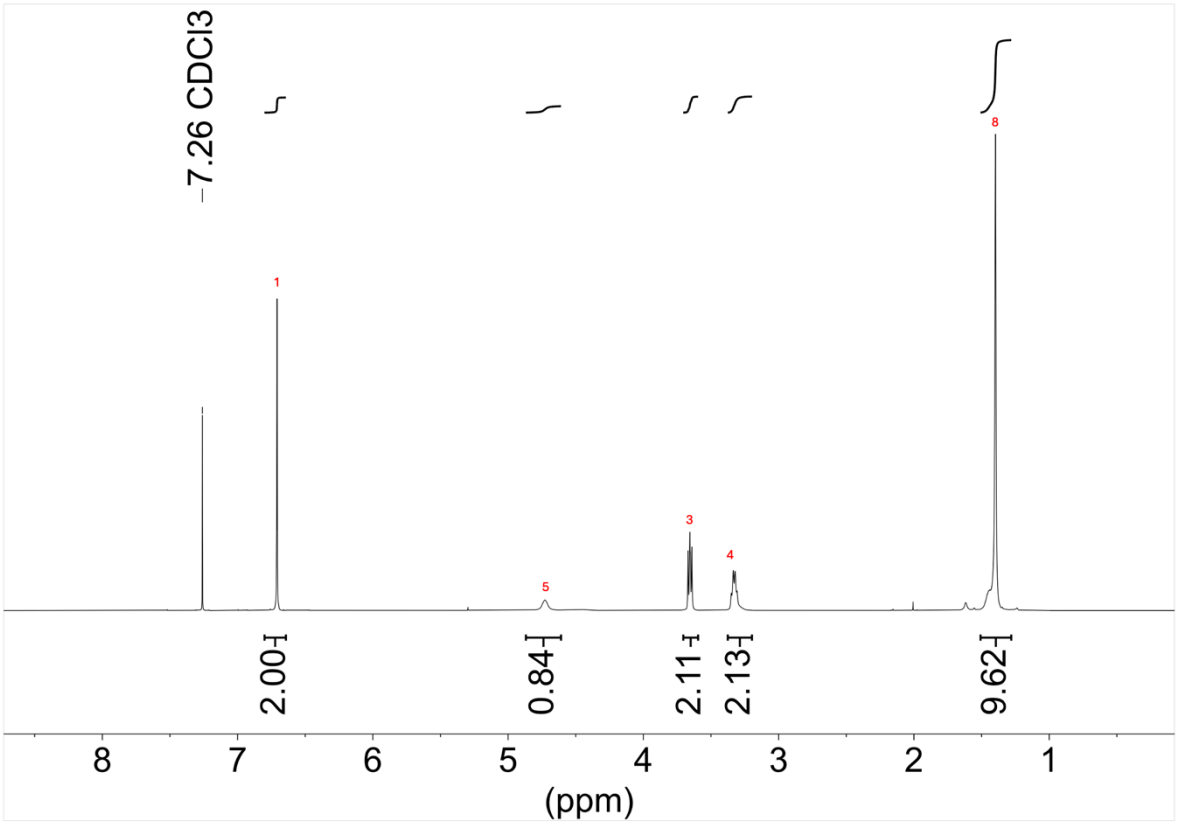


Figure 4.24: **$^1$H NMR** (*400 MHz, $CDCl_3$*) of *tert*-butyl (2-(2,5-dioxo-2,5-dihydro-1*H*-pyrrol-1-yl)ethyl)carbamate.

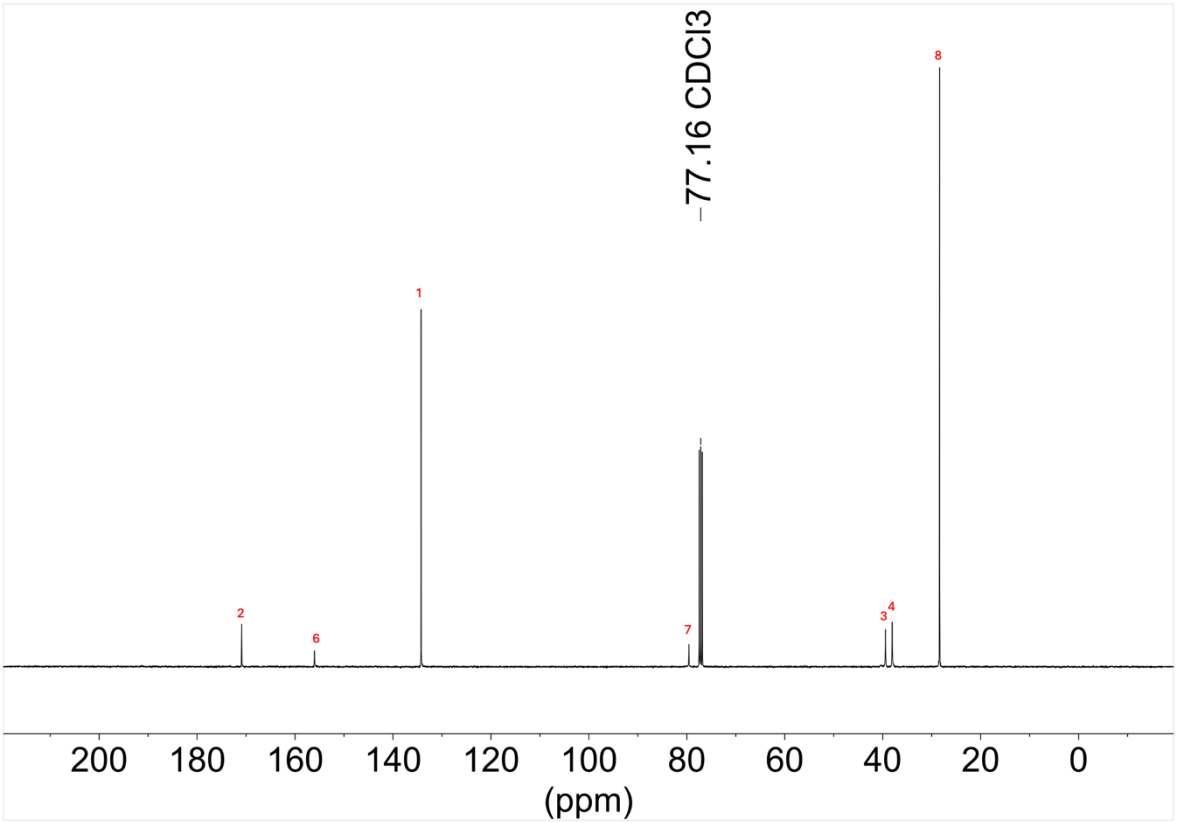


Figure 4.25: **$^{13}$C NMR** (*101 MHz, $CDCl_3$*) of *tert*-butyl (2-(2,5-dioxo-2,5-dihydro-1*H*-pyrrol-1-yl)ethyl)carbamate.

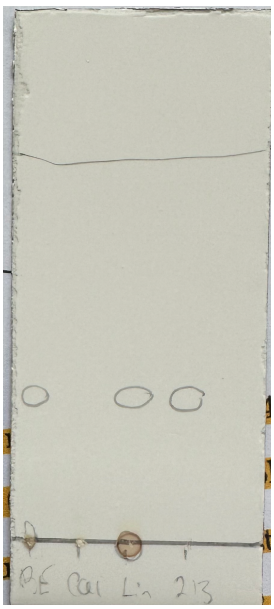

Figure 4.26: TLC analysis ($SiO_2$, 1:1 EtOAc:Hexane) of various reactions synthesising *tert*-butyl (2-(2,5-dioxo-2,5-dihydro-1*H*-pyrrol-1-yl)ethyl)carbamate in parallel. Same product spot observed at $R_f$ = 0.32 in each reaction. Black impurity does not move from baseline.

### 4.5.2 Synthesis of 2-(2,5-dioxo-2,5-dihydro-1*H*-pyrrol-1-yl)ethan-1-aminium trifluoroacetate 8

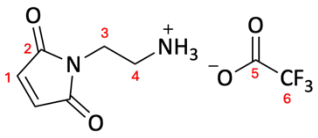

Figure 4.27: Structure of 2-(2,5-dioxo-2,5-dihydro-1*H*-pyrrol-1-yl)ethan-1-aminium trifluoroacetate.

Adapted from Bai *et al.*[43] **7** (3.18 g. 13.2 mmol) was dissolved in 20% v/v trifluoroacetic acid in $CH_2Cl_2$ (20 mL) and stirred for 2.5 h. Following the reaction, $CH_2Cl_2$ was removed, and the resulting yellow oil precipitated into $Et_2O$, yielding **8** as a white crystalline solid (3.01 g, 11.8 mmol, 90% yield). **$^1$H NMR** (*400 MHz, $D_2O$*) δ 6.93 (s, 1H, $H_1$), 3.86 (t, $J$ = 5.7 Hz, 1H, $H_3$), 3.26 (t, $J$ = 5.8 Hz, 1H, $H_4$). **$^{13}$C NMR** (*101 MHz, $CDCl_3$*) δ 172.65 $C_2$, 134.72 $C_1$, 38.41 $C_3$, 35.04 $C_4$. **LR-ESI-MS:** For $[M\text{-}COOCF_3+H]^+$ calculated: 141.066, found: 141.087. Spectroscopic data were consistent with literature reports.[57]

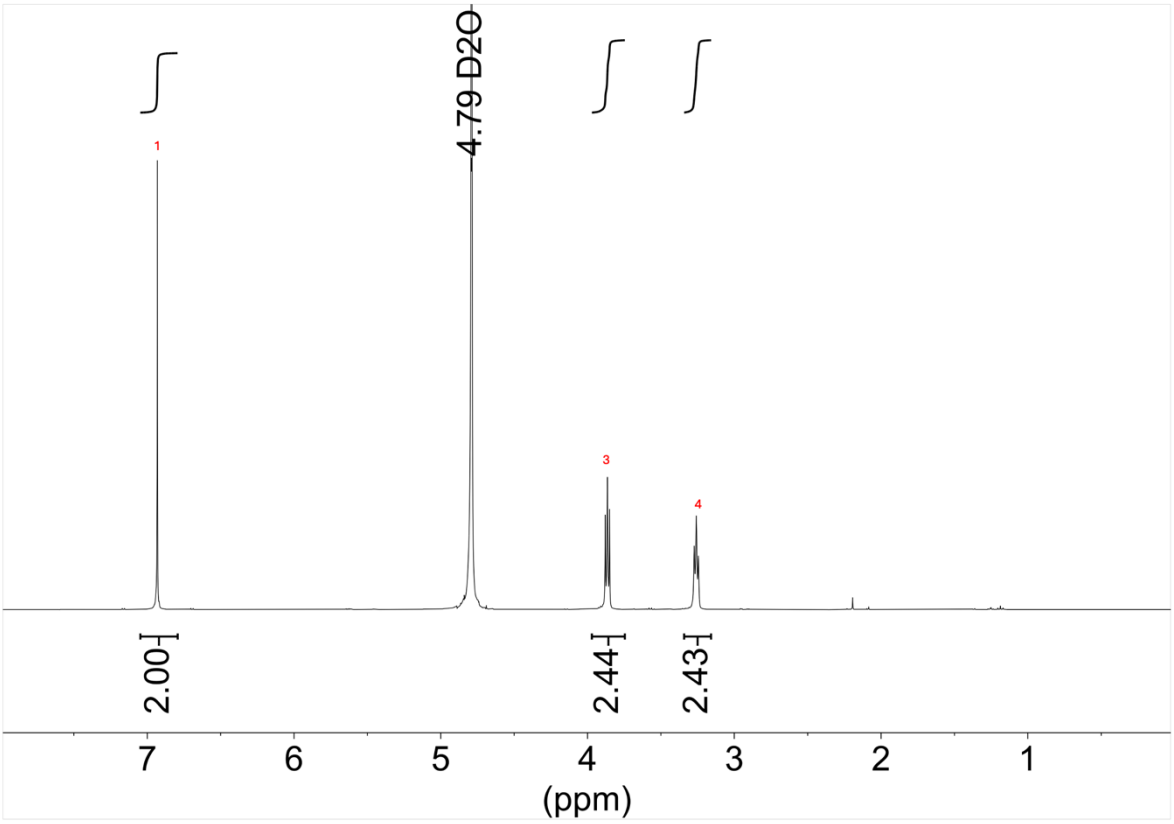


Figure 4.28: **$^1$H NMR** (*400 MHz, $D_2O$*) of 2-(2,5-dioxo-2,5-dihydro-1H-pyrrol-1-yl)ethan-1-aminium trifluoroacetate.

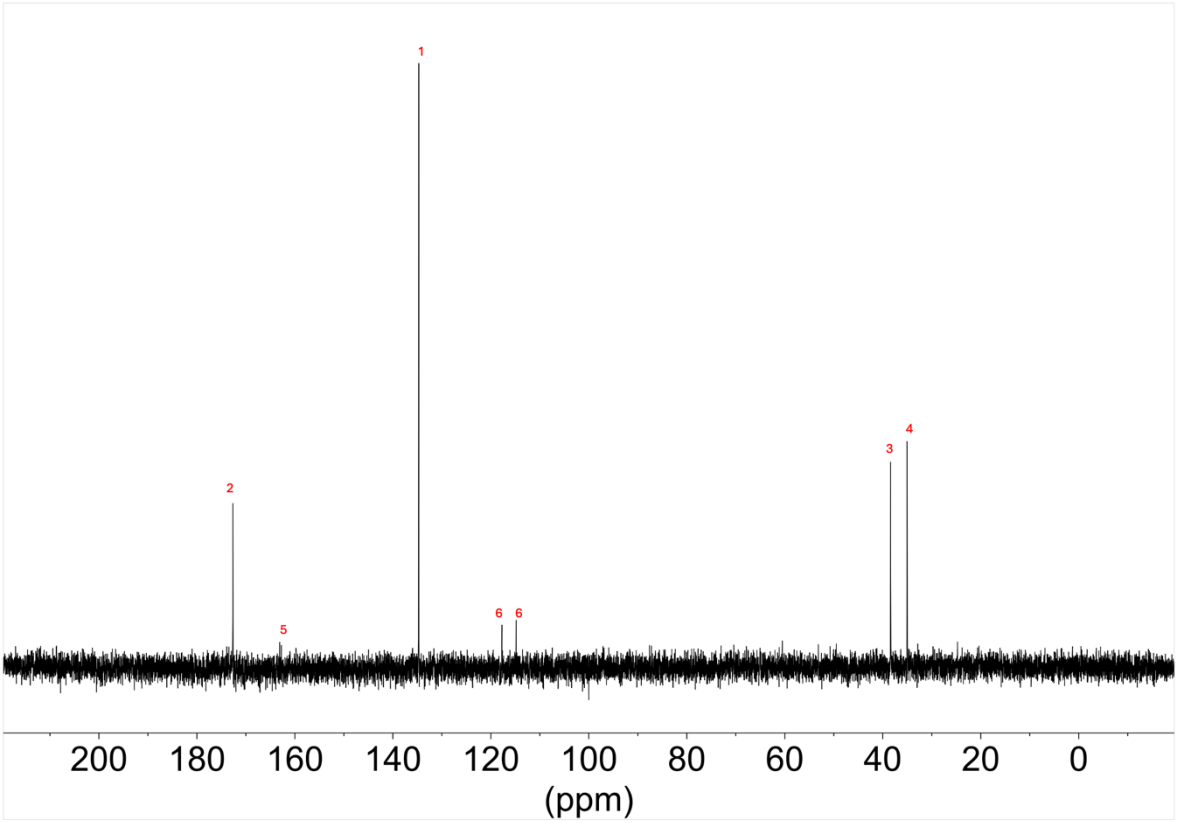


Figure 4.29: **$^{13}$C NMR** (*101 MHz, $D_2O$*) of 2-(2,5-dioxo-2,5-dihydro-1H-pyrrol-1-yl)ethan-1-aminium trifluoroacetate. TFA resonances show $^{13}$C-$^{19}$F coupling.

### 4.5.3 End group attachment of 1-(2-aminoethyl)-1*H*-pyrrole-2,5-dione to PVA

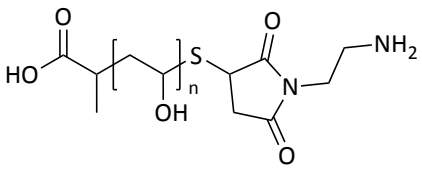


Figure 4.30: Structure of 1-(2-aminoethyl)-1*H*-pyrrole-2,5-dione terminated PVA.

Thiol terminated PVA (100 mg, $M_n$ ~13 kDa, 7.7 µmol, 1.0 eq.) was dissolved in DMSO (1 mL) with gentle heating and deoxygenated via argon sparging for 15 minutes, giving a straw-coloured clear solution. Tris(2-carboxyethyl)phosphine hydrochloride (4.4 mg, 15.5 µmol, 2.0 eq.) was added with continued sparging. Sparging was stopped and triethylamine (8.2 µL, 61.5 µmol, 8.0 eq.), hexylamine (5.1 µL, 38.5 µmol, 5.0 eq.) and **8** (7.8 mg, 30.8 µmol, 4.0 eq.) were added with stirring yielding a clear orange solution. The reaction was stirred at room temperature overnight before dialysis against $H_2O$ (5 changes) and lyophilisation to give a white spongy solid. The product was carried forward without further purification or analysis.

### 4.5.4 End group attachment of NBD-Cl to amine terminated PVA

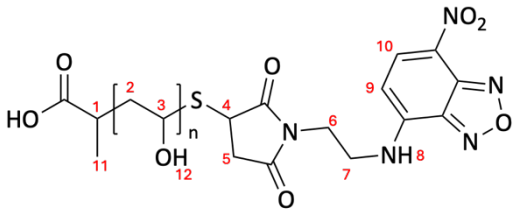


Figure 4.31: Structure of NBD terminated PVA.

Amine terminated PVA (100 mg, $M_n$ ~13 kDa, 7.7 µmol, 1.0 eq.) was dissolved in anhydrous dimethylacetamide (2 mL) with gentle heating. NBD-Cl (15.3 mg, 76.9 µmol, 10 eq.) and $K_2CO_3$ (10 mg, 76.9 µmol, 10 eq.) were added giving a clear orange solution which turned dark green after approx. 3 h. The reaction was wrapped in foil and stirred overnight. Following the reaction, the polymer solution was precipitated into cold acetone (2 × 40 mL) before dialysis against $H_2O$ (6 changes) and lyophilisation yielding a brown spongy solid (typically ~90 mg recovered). For partially acetylated PVA-NBD, the same procedure was followed with end group modification following acetylation procedure. Representative characterisation data for NBD-PVA: **$^1$H NMR** (*400 MHz, DMSO-$d_6$*): δ 7.20 (s -br, 1H, $H_{10}$), 6.66 (s -br, 1H, $H_9$), 3.30 – 4.19 (m -br 1H, $H_3$), 1.68 – 1.60 (m -br 2H, $H_2$). NBD attachment determined by $^1$H NMR spectroscopy (setting polymeric CH to DP): 19%. **UV/Vis** $H_2O$ $\lambda_{abs}$ = 328 nm, 473 nm.

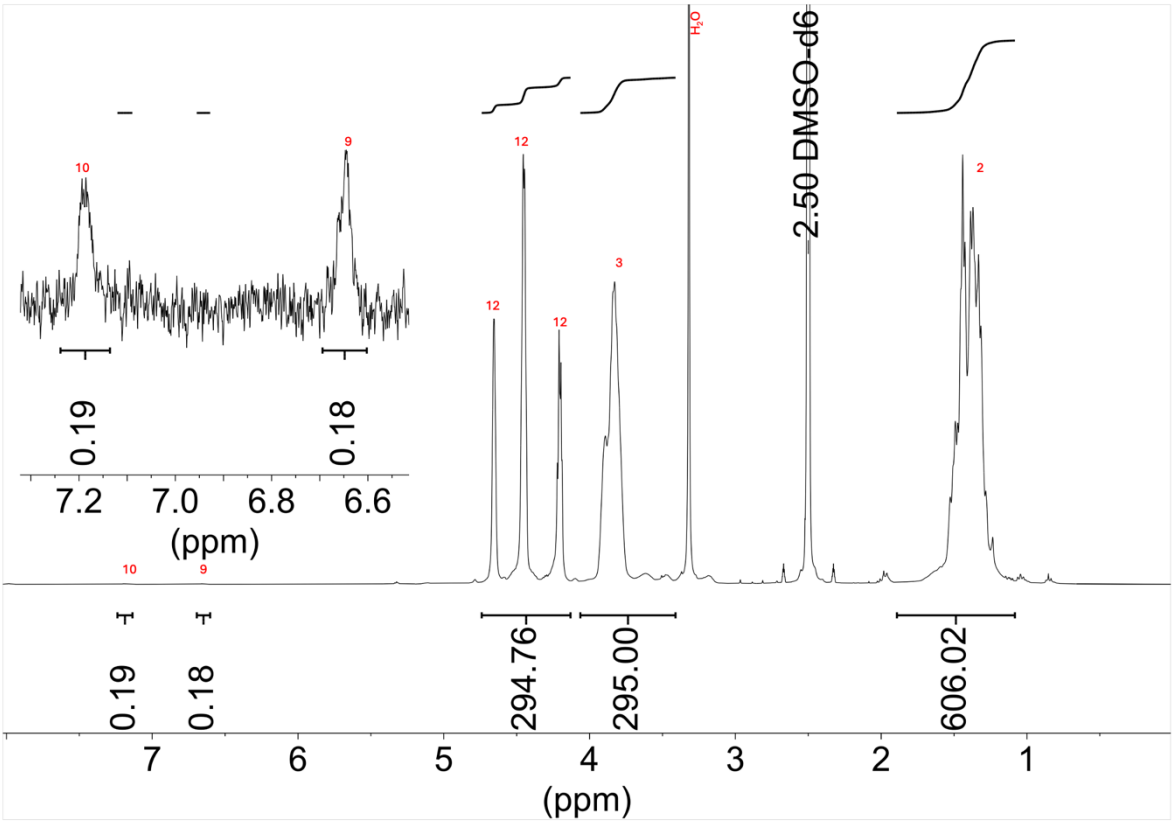


Figure 4.32: **$^{1}$H NMR** (*400 MHz, DMSO-$d_6$*) PVA-NBD.

**UV-Vis spectroscopy**

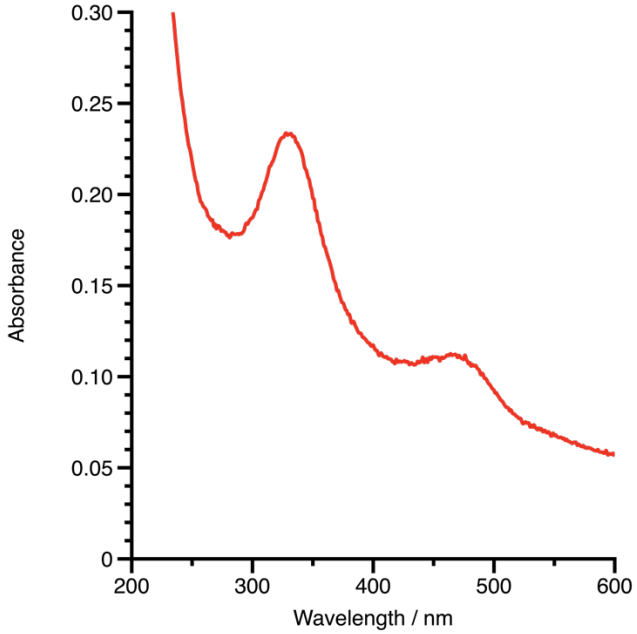


Figure 4.6: **UV/Vis** absorption spectrum of PVA-NBD 0.05 mg/mL in DI $H_2O$.

**GPC** with UV-Vis detection was used to verify the successful covalent attachment of NBD by confirming that the absorbance peak at λ = 467 nm, corresponding to the NBD label, coeluted with the polymer refractive index peak (Figure 4.33).

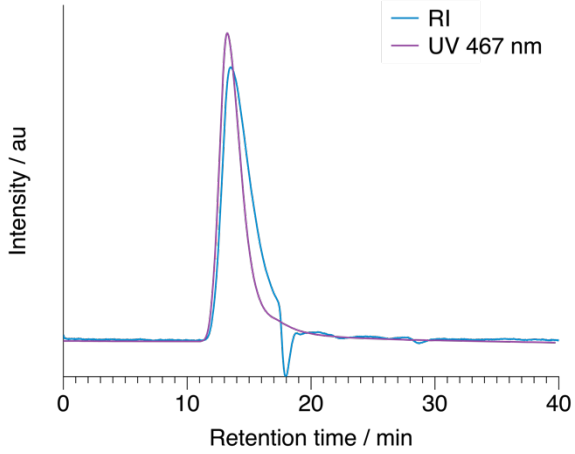


Figure 4.33: Representative GPC of PVA-NBD 5 mg/mL in 10 mM $NaNO_3$ at 35 °C, 1 mL/min. Triple detection analysis with a differential refractive index detector, a dual-angle light scattering detector (15° and 90°), a viscometer, UV-Vis detector and a pair of PL aquagel-OH 5 µm 300 × 7.5 mm columns with guard column (Polymer Laboratories Inc.) in series.

### 4.5.5 Film casting procedure for FRAP experiments

Polymers were made up as 5 w/v % solutions in 20% v/v glycerol MilliQ water. Glass microscope slides were cleaned with acetone prior to spin coating 100 µL polymer solution (1000 rpm, 60 s). Coated slides were equilibrated at room temperature at 70% RH for 24 h before imaging (Saturated KCl solutions in sealed chamber).

### 4.5.6 Imaging procedure

PVA-NBD films were imaged using a Nikon C1 series confocal microscope equipped with a Melles Griot 488 nm laser 35-IMA-410-019 Argon laser and a 515/30, 590/50 nm and 650LP detectors. Imaging was carried out in a humidity-controlled environment 70 ± 2% RH at 24 ± 2 °C (Microscope stage wrapped in clingfilm with saturated KCl solutions in petri dishes placed either side of the objective lens). Prebleach measurements were taken using a 4-scan average and 1 × field zoom magnification. Bleaching was achieved using 120 scans at 6 × field zoom magnification, 2 ND (neutral density) filters

removed. Recovery images were captured either every 90 s or every 180 s (depending on sample) using 4 scans and 1 $\times$ field zoom magnification, 1 ND filter removed, for a total of either 28.5- or 42-min post bleach.

## 4.6 References


1. H. Lee and L. A. Archer, *Polymer*, 2002, **43**, 2721-2728.
2. G. Wypych, *Handbook of Plasticizers*, ChemTec Publishing, 2004.
3. M. Hesami, W. Steffen, H. J. Butt, G. Floudas and K. Koynov, *ACS Macro Lett.*, 2018, **7**, 425-430.
4. C. Hubert, E. Malcor, I. Maurin, J. M. Nunzi, P. Raimond and C. Fiorini, *Appl. Surface Sci.*, 2002, **186**, 29-33.
5. L. Masaro and X. X. Zhu, *Prog. Polym. Sci.*, 1999, **24**, 731-775.
6. J. M. Petit, X. X. Zhu and P. M. Macdonald, *Macromolecules*, 1996, **29**, 70-76.
7. K. K. Senanayake, E. A. Fakhrabadi, M. W. Liberatore and A. Mukhopadhyay, *Macromolecules*, 2019, **52**, 787-795.
8. A. Karatrantos, R. J. Composto, K. I. Winey, M. Kröger and N. Clarke, *Polymers*, 2019, **11**, 876.
9. P. G. de Gennes, *J. Chem. Phys.*, 1971, **55**, 572-579.
10. H. Fujita and Y. Einaga, *Polym. J.*, 1985, **17**, 1131-1139.
11. B. Hanley, S. Balloge and M. Tirrell, *Chem. Engin. Commun.*, 1983, **24**, 93-113.
12. C. Xuexin, X. Zhongde, E. Von Meerwall, N. Seung, N. Hadjichristidis and L. J. Fetters, *Macromolecules*, 1984, **17**, 1343-1348.
13. H. Ochiai, H. Fujii, M. Watanabe and H. Yamamura, *Polym. J.*, 1974, **6**, 396-402.
14. M. Weiss, M. Elsner, F. Kartberg and T. Nilsson, *Biophys. J.*, 2004, **87**, 3518-3524.
15. N. R. Richbourg and N. A. Peppas, *Macromolecules*, 2021, **54**, 10477-10486.
16. K. Majerczak, Z. Shi, Z. Zhang and Z. J. Zhang, *Prog. Org. Coatings*, 2023, **185**, 107833.
17. A. S. Verkman, *Trends Biochem. Sci.*, 2002, **27**, 27-33.
18. A. B. Houtsmuller and W. Vermeulen, *Histochem. Cell Biol.*, 2001, **115**, 13-21.
19. A. S. Braegelman, R. C. Ollier, B. Su, C. J. Addonizio, L. Zou, S. L. Cole and M. J. Webber, *ACS Appl. Bio. Mater.*, 2022, **5**, 4589-4598.
20. M. D. Burke, J. O. Park, M. Srinivasarao and S. A. Khan, *Macromolecules*, 2000, **33**, 7500-7507.
21. E. Van Keuren and W. Schrof, *Macromol. Rapid Commun.*, 2003, **23**, 1138-1140.
22. D. Axelrod, D. E. Koppel, J. Schlessinger, E. Elson and W. W. Webb, *Biophys. J.*, 1976, **16**, 1055-1069.
23. N. Loren, J. Hagman, J. K. Jonasson, H. Deschout, D. Bernin, F. Cella-Zanacchi, A. Diaspro, J. G. McNally, M. Ameloot, N. Smisdom, M. Nyden, A. M. Hermansson, M. Rudemo and K. Braeckmans, *Q. Rev. Biophys.*, 2015, **48**, 323-387.
24. K. Braeckmans, L. Peeters, N. N. Sanders, S. C. De Smedt and J. Demeester, *Biophys. J.*, 2003, **85**, 2240-2252.
25. D. E. Wolf, *Biophys. J.*, 1992, **61**, 487-493.
26. A. Lopez, L. Dupou, A. Altibelli, J. Trotard and J. F. Tocanne, *Biophys. J.*, 1988, **53**, 963-970.
27. J. R. Lakowicz, in *Principles of Fluorescence Spectroscopy*, Springer US, Boston, MA, 2006.
28. L. A. Deschenes and D. A. Vanden Bout, *Chem. Phys. Lett.*, 2002, **365**, 387-395.
29. D. S. English, A. Furube and P. F. Barbara, *Chem. Phys. Lett.*, 2000, **324**, 15-19.
30. M. Minsky, *Scanning*, 1987, **10**, 128-138.
31. J. Jonkman and C. M. Brown, *J. Biomol. Tech.*, 2015, **26**, 54-65.
32. R. Y. Tsien, *Annu. Rev. Biochem.*, 1998, **67**, 509-544.

33. A. Chattopadhyay, *Chem. Phys. Lipids*, 1990, **53**, 1-15.
34. S. Fery-Forgues, J.-P. Fayet and A. Lopez, *J. Photochem. Photobiol. A*, 1993, **70**, 229-243.
35. P. A. Paprica, N. C. Baird and N. O. Petersen, *J. Photochem. Photobiol. A*, 1993, **70**, 51-57.
36. D. Lancet and I. Pecht, *Biochemistry*, 1977, **16**, 5150-5157.
37. S. Lin and W. S. Struve, *Photochem. Photobiol.*, 1991, **54**, 361-365.
38. S. Saha and A. Samanta, *J. Phys. Chem. A*, 1998, **102**, 7903-7912.
39. R. Fong, Phd Thesis, Durham University, 2020.
40. J. Braga, J. M. Desterro and M. Carmo-Fonseca, *Mol. Biol. Cell*, 2004, **15**, 4749-4760.
41. M. Weiss, *Traffic*, 2004, **5**, 662-671.
42. T. K. Meyvis, S. C. De Smedt, P. Van Oostveldt and J. Demeester, *Pharm. Res.*, 1999, **16**, 1153-1162.
43. N. Bai, K. Saito and G. P. Simon, *Polym. Chem.*, 2013, **4**, 724-730.
44. A. S. Soderling, L. Hultman, D. Delbro, P. Hojrup and K. Caidahl, *J. Chromatogr. B*, 2007, **851**, 277-286.
45. J. I. Alakoskela and P. K. Kinnunen, *Biophys. J.*, 2001, **80**, 294-304.
46. J. C. McIntyre and R. G. Sleight, *Biochemistry*, 1991, **30**, 11819-11827.
47. P. Williamson, E. M. Bevers, E. F. Smeets, P. Comfurius, R. A. Schlegel and R. F. Zwaal, *Biochemistry*, 1995, **34**, 10448-10455.
48. M. Langner and S. W. Hui, *Chem. Phys. Lipids*, 1993, **65**, 23-30.
49. H. Deschout, J. Hagman, S. Fransson, J. Jonasson, M. Rudemo, N. Loren and K. Braeckmans, *Opt. Express*, 2010, **18**, 22886-22905.
50. C. A. Schneider, W. S. Rasband and K. W. Eliceiri, *Nat. Methods*, 2012, **9**, 671-675.
51. H. G. Kapitza, G. McGregor and K. A. Jacobson, *Proc. Natl. Acad. Sci. U.S.A.*, 1985, **82**, 4122-4126.
52. J. Crank, *The Mathematics of Diffusion*, OUP, Oxford, UK, 1979.
53. S. Seiffert and W. Oppermann, *J. Microsc.*, 2005, **220**, 20-30.
54. E. Van Keuren and W. Schrof, *Macromolecules*, 2003, **36**, 5002-5007.
55. R. L. Thompson, M. T. McDonald, J. T. Lenthall and L. R. Hutchings, *Macromolecules*, 2005, **38**, 4339-4344.
56. A. Noorjahan and P. Choi, *Chem. Eng. Sci.*, 2015, **121**, 258-267.
57. T. L. Foley, A. Yasgar, C. J. Garcia, A. Jadhav, A. Simeonov and M. D. Burkart, *Org. Biomol. Chem.*, 2010, **8**, 4601-4606.

**Conclusions**

This thesis provides a comprehensive and detailed investigation into the structure-property relationships of polyvinyl alcohol (PVA) and polyvinyl acetate (PVAc) systems, with a particular focus on the effects of the degree of hydrolysis (DH) on polymer phase and diffusion behaviour. By employing a combination of solution-state and solid-state techniques, such as small-angle neutron scattering (SANS), dynamic light scattering (DLS), rheology, ion beam analysis (PIXE, RBS), and fluorescence recovery after photobleaching (FRAP), this work has made several important contributions to the understanding of polymer interactions and phase behaviour.

The research highlights the critical role of DH in determining polymer properties such as chain dimensions, aggregation behaviour, and phase stability. Specifically, the results show that the radius of gyration ($R_g$) of PVA decreases with increasing DH, and aggregation is influenced by inter- and intrachain interactions rather than solution environment. Furthermore, the study introduces a novel methodology to predictably control the DA of PVA through controlled acid-catalysed reacetylation and base hydrolysis, allowing for precise material synthesis for analysis of chain dimensions and phase separation behaviour. It was found that phase separation in PVAc blends was impacted by DH disparity, highlighting the need for controlling polymer blending and compatibility for various industrial applications.

One of the major parts in this work is the application of SANS to determine the Flory-Huggins interaction parameter ($\chi$) for PVAc blends of identical degree of polymerisation (DP). This research fills a gap in the literature, as similar analyses have been conducted in other polymer systems, but not for PVA/PVAc. These findings have practical implications for predicting film compatibility, particularly for soluble unit dose (SUD) film production, and can aid in improving sealing mechanisms in detergent capsule formulations.

Additionally, the application of advanced techniques such as PIXE and RBS allowed for the visualisation and mapping of polymer-polymer interfaces, providing insight into how DH influences interdiffusion at the polymer interface. The results showed that decreasing DH enhances the interdiffusion of polymer chains, although this effect is subject to a limiting threshold beyond which further reduction in DH may lead to phase separation as explored in the SANS chapter.

The FRAP experiments demonstrated that DH also significantly impacts polymer mobility in thin plasticised films. Polymer chains with lower DH exhibited faster diffusion rates, which could be leveraged in optimising polymer formulation and manufacturing processes. The method developed here to evaluate synthetic polymer diffusion offers a valuable tool for future studies of polymer systems and can be adapted for a variety of other materials and environments.

In summary, this thesis advances the understanding of how chemical modifications—specifically the degree of hydrolysis—affect polymer phase behaviour, interfacial diffusion, and mobility in thin films. The findings have practical implications for the development and optimisation of SUD films, offering potential solutions to key manufacturing challenges in the home and laundry care industry. Moreover, the methodologies utilised here, such as the use of SANS for determining $\chi$ and the application of FRAP for polymer diffusion analysis, present methodologies for exploring polymer systems in other contexts. The insights gained from this work not only contribute to improving detergent capsule formulations but also establish a framework for future investigations into polymer behaviour, with applications spanning multiple industries, including packaging, biomedical, and materials science.

Ultimately, the results from this research offer a deeper understanding of the complex interplay between polymer chemistry, structure, and properties. The methodologies and findings can inform the development of computational models for predicting interface behaviour in polymer film systems and provide a pathway for innovation in polymer-based products across a wide range of sectors.

**Future Work**

Several areas from this thesis could benefit from further investigation. Of the SANS work undertaken during this PhD, the following could be further studied. Investigation of non-carboxylate containing PVA solutions via SANS should explore the behaviour of PVA solutions without carboxylate-containing end groups to determine whether the high-intensity low-Q scattering observed in current samples is reduced or eliminated. This would help isolate the contribution of end groups to polymer chain aggregation. Additionally, building on dynamic light scattering (DLS) results that showed GuHCl suppressed aggregation, it would be valuable to analyse the effect of GuHCl addition on PVA chain conformation and interactions via solution state SANS. Such experiments could clarify the role of hydrogen bonding in aggregation behaviour. Employing Spin Echo SANS (SESANS) could provide insights into the aggregation and structure of PVA and PVAc chains on larger length scales, up to around 18 µm in size, which would allow for detailed analysis of polymers and further investigation into the factors which impact the aggregation observed. Investigating how the polymer chain conformation changes during acetylation using SANS could provide deeper understanding of the relationship between chemical modification and chain structure. Such studies could explore solvent-polymer interactions and their impact on chain expansion and phase behaviour by monitoring an acetylation reaction in real time.

Extending the ion beam analysis methodology to longer polymer chains with similar bromine incorporation would help to understand how molecular weight influences interdiffusion and interface dynamics. Future work could also focus on optimising sample preparation techniques to minimise damage and improve mapping precision. Further FRAP analysis with expanded polymer libraries would improve confidence in the results obtained in this work. More samples with varying DH should be evaluated using FRAP to assess how chain mobility changes with increased acetylation, as well as collection of more data points to improve detection of outliers. Such studies would help identify the optimal DH range for achieving desired diffusion properties in SUD film applications. This work would

also benefit from automation in data processing, which was conducted manually and was time consuming.